Politecnico di Bari

UNIVERSITÀ DEGLI STUDI DI PALERMO

DiFC
DIPARTIMENTO DI FISICA E CHIMICA - DiFC

BARI – ITALY
11-13 JUNE
SiO2018

BOOK OF ABSTRACTS

UNIVERSITÉ JEAN MONNET SAINT-ÉTIENNE

UNIVERSITÉ FRANCO ITALIENNE | UNIVERSITÀ ITALO FRANCESE

ROHDE&SCHWARZ

DEI DIPARTIMENTO DI INGEGNERIA ELETTRICA E DELL'INFORMAZIONE

Anritsu envision : ensure

SCIENTIFIC AND SOCIAL PROGRAM

TIME	MONDAY	TIME	TUESDAY	TIME	WEDNESDAY
	DEFECTS- RADIATION EFFECTS I		NANOSTRUCTURES		2D AND ADVANCED DIELECTRICS MATERIALS
09,00-09,20	Welcome (Chairs)	09,00-09,30	**Lorenzi - Keynote**	09,00-09,30	**Agnello - Keynote**
09,20-09,50	**Skuja - Keynote**	09,30-09,50	Carbonaro	09,30-09,50	Monteduro
09,50-10,10	Trukhin	09,50-10,10	Ortelli	09,50-10,10	Stesman
10,10-10,30	Boukhalov	10,10-10,30	Korobova	10,10-10-30	Faggio
10,30-10,50	Alessi	10,30-10,50	Nazarov	10,30-10,50	Corpino
10,50-11,30	Coffe Break	10,50-11,30	Coffe Break	10,50-11,30	Coffe Break
	DEFECTS- RADIATION EFFECTS II		DEVICES-MODELING II		DIELECTRICS MATERIALS FOR HEALTHCARE, ENERGY,ENVIRONMENT
11,30-12,00	**D'Amico - Keynote**	11,30-12,00	**Paillet - Keynote**	11,00-11,30	**Ciminelli - Keynote**
12,00-12,20	Cannas	12,00-12,30	**Cardillo - Keynote**	11,30,11,50	Mescia
12,20-12,40	De Michele	12,30-12,50	Spagnolo	11,50-12,10	Kajihara
12,40-13,00	Faraj	12,50-13,10	Elliott	12,10-12,30	Best presentation award
13,00-13,20				12,30-12,50	Concluding remarks
13,20-15,00	Lunch	13,10-14,30	Lunch	12,50-14,00	Lunch
	FIBERS-SENSORS				
15,00-15,30	**Di Francesca - Keynote**	14,30-16,00	Poster session		
15,30-15,50	Al Helou	16,00-16,30	Coffe Break		
15,50-16,10	Benabdesselam				
16,10-16,30	Ju	17,00-23,00	TRIP/Social diner		
16,30-16,50	Tomyshev				
16,50-17,30	Coffe Break				
	DEFECTS-MODELING I				
17,30-18,00	**Giacomazzi - Keynote**				
18,00-18,20	Mady				
18,20-18,40	Tsarev				

BARI – ITALY
11-13 JUNE
SiO2018

CONFERENCE SPONSORS

de' remi facemmo ali
1990
POLITECNICO DI BARI
Politecnico
di Bari

UNIVERSITÀ
DEGLI STUDI
DI PALERMO
DiFC
DIPARTIMENTO DI FISICA E CHIMICA - DiFC

UNIVERSITÉ
JEAN MONNET
SAINT-ÉTIENNE

UNIVERSITÉ FRANCO ITALIENNE
UNIVERSITÀ ITALO FRANCESE

Anritsu
envision : ensure

ROHDE&SCHWARZ

CONFERENCE PATRONAGE

DEI
DIPARTIMENTO DI
INGEGNERIA ELETTRICA
E DELL'INFORMAZIONE

DETAILED PROGRAM

Monday, June 11

08:00-11:00	Conference registration desk open
09:00-09:20	Welcome and opening remarks *Luciano Mescia and Marco Cannas, Conference chairs*
09:20-10:50	**DEFECTS – RADIATION EFFECTS I** *Chair: Y. Ouerdane*
09:20-09:50	Optical properties of intrinsic and chlorine-related defects in O_2-containing SiO_2 glass and in α-quartz *L. Skuja, University of Latvia , Latvia (Invited)*
09:50-10:10	Photoluminescence and Electron Spin Resonance of Silicon Dioxide Crystal with Rutile Structure (Stishovite) *A. Trukhin, University of Latvia, Latvia*
10:10-10:30	Non-stoichiometric defects in metal-doped SiO_2 *D.W. Boukhvalov, Ural Federal University, Russia*
10:30-10:50	Radiation Effects on Aluminosilicate Optical Fibers in the Ultraviolet and Near-Infrared Domains *A. Alessi, University of Lyon, France*
10:50-11:30	**Coffee Break**
11:30-13:00	**DEFECTS – RADIATION EFFECTS II** *Chair: R. Lorenzi*
11:30-12:00	Ultrafast laser 3D photo-inscription of bulk chalcogenide glasses for photonic applications in the mid-IR *C. D'Amico. University of Lyon, France (Invited)*
12:00-12:20	Luminescence efficiency of Si/SiO_2 nanoparticles produced by laser ablation *M. Cannas, University of Palermo, Italy*
12:20-12:40	Pulsed X-ray Radiation Responses of Solarization-Resistant Optical Fibers *V. De Michele, University of Lyon, France*
12:40-13:00	Growth of gold nanoparticles in a glass matrix by continuous laser irradiation *R. Faraj, University of Lyon, France*
13:20-15:00	**Lunch**

15:00-16:50 **FIBERS-SENSORS**
Chair: A. Stesmans

15:00-15:30 Phosphosilicate Optical Fibers for Distributed Dose Measurement at CERN
D. Di Francesca, CERN , Switzerland (Invited)

15:30-15:50 Low Dose and Low Dose rate measurements of X-rays using Copper-doped Sol-gel Silica Glass
N. Al Helou, University of Lille, France

15:50-16:10 Investigation by TSL of the properties of some potential fibred-OSL dosimeters
M. Benabdesselam, Université Côte d'Azur, France

16:10-16:30 Temperature Dependence of Faraday Effect of Germano-silicate Glass Optical Fiber Doped with CdSe and CdMnTe particles
S. Ju, Gwangju Institute of Science and Technology, South Korea

16:30-16:50 Combined planar-fiber surface plasmon resonance sensor
K. A. Tomyshev, Kotel'nikov Institute of Radioengineering and Electronics of RAS, Russia

16:50-17:30 **Coffee Break**

17:30-19:00 **DEFECTS – MODELING I**
Chair: A. Alessi

17:30-18:00 Color centers in P-doped silica: generation, conversion mechanisms, and optical properties
L. Giacomazzi, University of Nova Gorica and SISSA , Italy (Invited)

18:00-18:20 Modeling of the RIA in silica-based optical fibers: contribution of the photoionization of radiation-induced trapped states
F. Mady, Université Côte d'Azur, France

18:20-18:40 Numerical Modeling of Novel Sensor Element Based on Abnormal Blocking by Periodic Grating Strips over Si/SiO_2 wire waveguide
A. Tsarev, Novosibirsk State University, Russia

Tuesday, June 12

09:00-10:50 **NANOSTRUCTURES**
Chair: L. Skuja

09:00-09:30 Charge transport in oxide-in-oxide nanostructured silica-based dielectrics
R. Lorenzi, University of Milano-Bicocca, Italy (Invited)

09:30-09:50 A Photoluminescence Study of Microwave Synthesized Carbon-dots Dispersed in Water and in Mesoporous Silica
C. M. Carbonaro, University of Cagliari, Italy

09:50-10:10 Silica coating as "safer by molecular design" strategy to control nano-TiO_2 photoreactivity
S. Ortelli, ISTEC-CNR, Italy

10:10-10:30 Formation of SiO_2 Dendritic Structures during Annealing of Silicon on Insulator Wafers
N. Korobova, National Research University of Electronic Technology, Moscow, Russia

10:30-10:50 Fumed Silica as Morphological Template for the Synthesis of Luminescent Carbon Nanodots
A. N. Nazarov, Lashkaryov Institute of Semiconductor Physics NASU, Ukraine

10:50-11:30 **Coffee Break**

11:30-13:00 **DEFECTS – MODELING II**
Chair: L. Giacomazzi

11:30-12:00 Radiation effects simulation for materials in microelectronics and optoelectronics
P. Paillet, CEA-DAM-DIF, France (Invited)

12:00-12:30 HEMT Sensitivity to Optical Radiation: Distinguishing Microwave Noise Aspect
E. Cardillo, University of Messina , Italy (Invited)

12:30-12:50 Damping mechanisms of piezoelectric quartz tuning forks used in photoacoustic spectroscopy for gas sensing
V. Spagnolo, Polytechnic University of Bari, Italy

12:50-13:10 The origin of radiation tolerance in amorphous $Ge_2Sb_2Te_5$ phase-change random-access memory material
S. R. Elliot, University of Cambridge, UK

13:10-14:30 **Lunch**

14:30-16:00 POSTER SESSION

P01 Relaxation of the UV-induced defects in H2-loaded Er-doped fibers
A.P. Bazakutsa, Kotel'nikov Institute of Radioengineering and Electronics of RAS, Russia

P02 Synthesis and optical properties of Bismuth-doped sol-gel derived phosphosilicate Glasses
H. El Hamzaoui, University of Lille, France

P03 Multiphysics Numerical Model of Rare Earth-Doped Cladding-Pumped Fiber Amplifiers for Space Missions
M.A. Chiapperino, Polytechnic University of Bari, Italy

P04 Structural Evolution in Thermally Treated Preforms of Slip Cast Silica Ceramics as Revealed from FTIR Reflectance Study
A. Chmel, Polytekhnicheskaya of St-Petersburg, Russia

P05 Proton radiation responses of pure or doped multimode optical fibers
S. Girard, University of Lyon, France

P06 Non-Conductive Graphene-Based Derivative as Interlayer in Graphene/n-Si Schottky Barrier Solar Cells
A. Gnisci, University "Mediterranea" of Reggio Calabria, Italy

P07 Glass Formation Ability and Glass Structure of Chalcogenide Systems
V. Minaev, National Research University of Electronic Technology of Moscow, Russia

P08 First Principles Study of the Influence of the Local Steric Environment on the Incorporation and Migration of NO in a-SiO_2
N. V. Mistry, University College London, UK

P09 Spatial distributions of NBOHCs in electron and γ-ray irradiated germanosilicate optical fibers
I. Reghioua, University of Lyon, France

P10 Heavily Er^{3+}-doped distributed feedback silica-based fiber laser
A.M. Smirnov, Kotel'nikov Institute of Radioengineering and Electronics of RAS, Russia

P11 Electronic structure and optical absorption in Gd-implanted silica glassesser
A. F. Zatsepin, Ural Federal University, Russia

16:00-16:30 Coffee Break

17:00-23:00 Trip and Social Dinner at Alberobello

Wednesday, June 13

09:00-10:50 **2D AND ADVANCED DIELECTRICS MATERIALS**
Chair: C. M. Carbonaro

09:00-09:30 Graphene – SiO_2 interaction from composites to doping
S. Agnello, University of Palermo, Italy (Invited)

09:30-09:50 Functional Oxides for nano-eletronics and spintronics
A. G. Monteduro, University of Salento, Italy

09:50-10:10 Thermal stability and temperature dependent ESR characteristics of the as acceptor in geological $2H\text{-}MoS_2$
A. Stesmans, University of Leuven, Belgium

10:10-10:30 Carbon dots dispersed on graphene/SiO_2/Si: a morphological study
G. Faggio, University "Mediterranea" of Reggio Calabria, Italy

10:30-10:50 Enhancement of Carbon Dot Emission with Au Nanoparticles
R. Corpino, University of Cagliari, Italy

10:50-11:30 **Coffee Break**

11:30-13:00 **DIELECTRICS MATERIALS FOR HEALTCARE, ENERGY, ENVIRONMENT**
Chair: M. Cannas

11:30-12:00 Integrated photonic and plasmonic microresonators for label-free biosensing and trapping at nanoscale
C. Ciminelli, Polytechnic University of Bari, Italy (Invited)

12:00-12:20 Fractional-Calculus-Based electromagnetic tool to study pulse propagation in arbitrary dispersive dielectrics
L. Mescia, Polytechnic University of Bari, Italy

12:20-12:40 Cosolvent-free synthesis of polysilsesquioxane liquids and polysilsesquioxane-based organic-inorganic hybrid glasses
K. Kajihara, Tokyo Metropolitan University, Japan

12:40-13:10 Award ceremony for the best talks given by young researchers and concluding remarks
Luciano Mescia and Marco Cannas, Conference chairs

13:10-14:30 **Lunch**

MONDAY

SESSION

DEFECTS - RADIATION EFFECTS I

Optical properties of intrinsic and chlorine-related defects in O_2-containing SiO_2 glass and in α-quartz.

Linards Skuja[*], Nadège Ollier[**], Koichi Kajihara[***]

[*]Institute of Solid State Physics, University of Latvia
8 Kengaraga str., LV1063, Riga, Latvia
[**] Laboratoire des Solides Irradiés, Université Paris Saclay,
UMR 7642 CEA-CNRS Ecole Polytechnique, Palaiseau, France
[***] Department of Applied Chemistry, Graduate School of Urban Environmental Sciences,
Tokyo Metropolitan University, 1-1 Minami-Osawa, Hachioji, Tokyo 192-0397, Japan

ABSTRACT

Defects and impurities contributing to the deep-UV and vacuum-UV optical absorption in SiO_2 are briefly surveyed and new data are presented. Singlet luminescence of interstitial O_2 molecules, activated by energy transfer from interstitial Cl_2 was observed, indicating their proximity. Irradiation by F_2 laser gives rise to Raman band at 953 cm^{-1} due to formation of interstitial ClClO molecules. Isochronal annealing correlates this band to an optical absorption band at 4.7 eV, which is different from similarly placed absorption bands of NBOHCs and interstitial ozone. The parameters of the band are close to those of ClClO molecules in inert gas matrices.

Vacuum-UV absorption of high-purity synthetic α-quartz irradiated by 2.5 MeV electrons up to 1.4×10^{19} e^{-}/cm^2 was studied. Apart from oxygen vacancy (SiODC(I)) band at 7.6 eV, two weaker overlapping bands at around 6.4 and 7.2 eV were found and tentatively assigned to interstitial oxygens in the form of peroxy linkages.

PACS Keywords: glasses, quartz (42.70Ce), luminescence of molecules (33.50.-j) and glasses (78.55.Qr), point defects (61.72.J-), ultraviolet spectroscopy 78.40.-q.

1 INTRODUCTION

Synthetic silica glass is the most-widely used optical material for ultraviolet (UV) applications, in particular, for deep UV (DUV) and vacuum UV (VUV) ranges. Accordingly, a large number of studies have been dedicated to finding of the origins of UV optical absorption (OA). Since many OA bands overlap there, this is a formidable problem. The main well-established intrinsic UV-VUV OA bands in silica are due to oxygen vacancies ("ODC(I)")[1], dangling Si bonds (E'- centers) [2], oxygen dangling bonds ("NBOHC") [3], divalent Si ("ODC(II)") [4,5]. However, exact parameters of peroxy radical OA band in silica are still absent. Moreover, there are no experimental data on OA of one of the most basic intrinsic defects in SiO_2 – the interstitial oxygen, which is thought to exist in peroxy linkage (POL) form. Only theoretical calculations are available, predicting weak deep-UV OA bands [6-9]. The present work reports the first experimental data on the optical absorption of oxygen interstitials.

Apart from intrinsic defects, impurities common to the (otherwise) "high purity" synthetic SiO_2: hydrogen and chlorine - also contribute to the deep UV OA. Network-bound SiCl and SiOH groups give OA near the fundamental absorption edge, while Cl_2 molecules give rise to near UV OA band, often present in "dry" optical fiber waveguides. Our recent work [10] indicated formation of chlorine oxides in irradiated Cl_2-containing silicas. These molecules have strong and until now neglected UV absorption bands, and are studied in the present work.

2 EXPERIMENTAL

It was realized early-on that even in highest-purity silicas many hard-to-distinguish OA bands overlap in the deep UV region, obscuring the possibly underlying weaker POL OA band. As anion part of the elementary Frenkel pair, POLs should be present both in glassy and crystalline forms of SiO_2, while the interfering OA of dangling bond-type defects should be absent in crystalline SiO_2. Therefore, high-purity α-quartz monocrystals were selected (Asahi Glass/Tokyo Denpa, 2×10^{15} Al, 2×10^{15} Li, 1×10^{15} Na per cm^3). They were irradiated at the room temperature by 2.5 MeV electrons to dose 3.6 GGy (1.4×10^{19} e^{-}/cm^2). Their OA was measured using McPherson 234/302 monochromator, with resolution 1 nm.

Formation of Cl oxides was studied in synthetic "dry" silica sample having $\sim10^{17}..10^{18}$ cm^{-3} interstitial Cl_2 and O_2 molecules, irradiated by $\sim10^{20}$ 7.9 eV photons/cm^2. Samples with different Cl_2 and O_2 contents (10^{16} to 10^{18} molecules/cm^3) were used in energy-transfer experiments.

3 RESULTS AND DISCUSSION

3.1 Energy transfer from interstitial Cl_2 to O_2 molecules

Interstitial O_2 in SiO_2 is detected by 0.974 eV (1272 nm) photoluminescence (PL) from its lowest singlet state $^1\Delta_g$. It can be excited resonantly or, more efficiently, to the next O_2 term $^1\sum^+_g$ (1.62 eV). There are no other higher energy O_2 excited states until ≈6eV. However, O_2 PL band was detected with 355 nm pulsed laser or 370 nm UV LED CW excitation. The measured lifetime, τ=845 ms was close to the case of 1.62 eV excitation (861 ms @295K). O_2 PL intensity did not correlate with the PL of NBOHCs. It correlated with the product of O_2 and Cl_2 concentrations in the sample, indicating energy transfer $Cl_2 \rightarrow O_2$ and small distances between some part of the interstitial molecules.

3.2 Optical absorption of chlorine oxides

7.9 eV photon irradiation of SiO_2 glass, containing both interstitial O_2 and Cl_2, gives rise to a sharp low-intensity Raman band at 955 cm^{-1} due to interstitial ClClO molecules [10]. The sample was isochronally annealed (20 C-800 C, step 100 C) and Raman and OA spectra were monitored. Initial OA band peaked at 4.75 eV and was significantly destroyed at 200 C, without affecting Cl_2 OA or 955 cm^{-1} Raman band intensities. This stage can be attributed to the destruction of interstitial O_3. In the interval 300 - 400 C, the 955 cm^{-1} Raman band and a large component of the OA around 4.8 eV were destroyed, and the 3.76 eV OA of interstitial Cl_2 increased in intensity. The destroyed OA component (peak 4.7 eV, fwhm 1.04 eV) is very similar to the low-energy UV band of NBOHC (4.8 eV, fwhm=1.05 eV). However the intensity of NBOHC PL changes relatively little in this T interval. Therefore, the 4.7 eV (fwhm=1.04 eV) OA component can be assigned to ClClO molecules in SiO_2. Cl oxides can significantly contribute to UV attenuation in Cl-containing silicas.

3.3 Optical absorption of peroxy linkage

High-dose (3.6 GGy) 2.5 MeV e^- irradiation of pure α-quartz induced an intense short-wavelength OA band due to SiODC(I) – oxygen vacancy band at 7.6 eV. Its amplitude, estimated from the wing, was ≈100 cm^{-1}, corresponding [1] to 1.4×10^{18} centers/cm^3, implying that a similar number of POLs must be present. This band was flanked by a wide, ≈2 cm^{-1} high shoulder at 6.2 eV, smoothly descending to <0.2..0.1 cm^{-1} intensity for $\hbar\omega$<4.2 eV. OA band at 5.8 eV, characteristic to E'-centers in silica or neutron irradiated quartz, was not found. Using the exact spectral parameters of the 7.6 eV band [11], the remaining component was approximated by 2 Gaussians, 6.4 and 7.2 eV, fwhm 2.2 and 0.7 eV, respectively. Given the high purity of the samples, the certain presence of large numbers (≈10^{18} cm^{-3}) of oxygen interstitials in the sample, and the results of calculations [6-9], this component can be tentatively assigned to OA of peroxy linkages in the SiO_2 lattice.

L.S. was supported by ERANET MyND program, N.O.- by Ecole Polytechnique, K.K. in part by Collaborative Research Project of MSL, TITech.

REFERENCES.

[1] H. Hosono, Y. Abe, H. Imagawa, H. Imai, K.Arai K, "Experimental evidence for the Si-Si bond model of the 7.6 eV band in SiO_2 glass", Phys.Rev.**B44**, 12043 (1991).

[2] R.A.Weeks, E. Sonder, "The relation between the Magnetic Susceptibility, Electron Spin Resonance and Optical Absorption of the E_1' center in Fused Silica", In: "Paramagnetic Resonance", V.2, ed. by W.Low, Academic Press, N.Y.(1963), pp. 869-79.

[3] L. Skuja, K. Kajihara, M. Hirano, H. Hosono, "Visible to vacuum-UV range optical absorption of oxygen dangling bonds in amorphous SiO_2", Phys.Rev.**B84**, 205206 (2011).

[4] L. Skuja,"Isoelectronic series of twofold coordinated Si, Ge, and Sn atoms in glassy SiO_2: a luminescence study". J. Non-Cryst. Solids, **149**, 77(1992).

[5] S.Agnello, R. Boscaino, M. Cannas, F. M. Gelardi, M. Leone, B. Boizot, "Competitive relaxation processes of oxygen deficient centers in silica", Phys.Rev.**B67**, 033202(2003).

[6] B. Stefanov, K. Raghavachari, " Photoabsorption of the peroxide linkage defect in silicate glasses. J.Chem.Phys. **111**, 8039(1999).

[7] D. Ricci, G. Pacchioni, M. A. Szymanski, A.L. Shluger,A. M. Stoneham, "Modeling disorder in amorphous silica with embedded clusters: The peroxy bridge defect center" Phys.Rev. **B64**, 224104(2001).

[8] Weizheng Wang, Pengfei Lu, Lihong Han, Chunfang Zhang, Liyuan Wu, Pengfei Guan, Rui Su, Jun Chen, "Structural and electronic properties of peroxy linkage defect and its interconversion in fused silica" J. Non-Cryst. Solids **434**, 96 (2016).

[9] B. Winkler B., L. Martin-Samos, N. Richard, L. Giacomazzi, A. Alessi, S. Girard, A. Boukenter, Y. Ouerdane, M. Valant "Correlations between Structural and Optical Properties of Peroxy Bridges from First Principles" J. Phys. Chem. **C121**, 4002 (2017).

[10] L. Skuja, K. Kajihara, K. Smits, A. Silins, H. Hosono "Luminescence and Raman Detection of Molecular Cl_2 and ClClO Molecules in Amorphous SiO_2 Matrix", J. Phys. Chem. **C121** 5261(2017).

[11] K.Kajihara, L.Skuja, H. Hosono, "Formation and annihilation of intrinsic defects induced by electronic excitation in high-purity crystalline SiO_2" J. Appl. Phys. **113**, 143511 (2013).

Photoluminescence and Electron Spin Resonance of Silicon Dioxide Crystal with Rutile Structure (Stishovite)

A.Trukhin*, A. Antuzevics*,

* Institute of Solid State Physics,
University of Latvia, LV-1063 Riga, Latvia

ABSTRACT

As received crystal of stishovite possesses electron spin resonance signal, witnessing on some defects presence in non-irradiated crystal.

Photoluminescence of as received stishovite single crystals exhibits two main bands a blue at 3 eV and an UV at 4.75 eV. Luminescence is excited in the range of optical transparency of stishovite (below 8.75 eV) and therefore ascribed to defects. Wide range of decay kinetics under pulsed excitation was observed. For blue band beside exponential decay with time constant about 17 µs an ms additional component revealed. For UV band beside fast component with time constant 1-3 ns a component with decay in tens µs was obtained. Main components (17 µs and 1-3 ns) possess usual for intra-center transitions intensity thermal quenching, whereas additional components exhibit wave-like thermal dependences.

PACS Keywords: stishovite, time resolved luminescence, radiation, recombination processes, electron spin resonance

1 INTRODUCTION

In stishovite synthetic monocrystals there are two main luminescence bands: a blue one at about 3 eV with time constants about 18 µs and an UV one at about 4.75 eV with time constant about some ns [1]. Besides, a red luminescence with series of sharp lines was observed. Its was explained as a quasimolecular luminescence center due to the presence of carbon impurity [2]. Also, OH groups are found [2].

Some peculiarities were detected in the shape of decay kinetics curve at different temperatures [2]. Also, different temperature dependences where obtained under photo and x-ray excitations [2]. The effects are interpreted as luminescence center interaction with surrounding interstitial defects, which modify properties of luminescence center. It is assumed that motion of defects modulates radiative transitions probabilities provoking deviations of kinetics curves from exponent. Charge trapping on modifiers under x-ray excitation stimulates remove of them from complex defect at temperature above 100 K [2] leading to decrease of luminescence intensity. Photoexcitation does not provide effective charge release and luminescence intensity is less dependent on temperature than that under x-ray excitation. In the present work we report about observation of additional slow decay component of stishovite luminescence and detection of ESR signal in non-irradiated sample. Decay curves in ms range of time were obtained for blue band and in µs for UV band. Spectral and thermal dependences of this additional luminescence were studied.

2 EXPERIMENTAL

Single crystals of stishovite have been grown from hydrothermal solution in the system SiO_2–H_2O under a pressure of 9–9.5 GPa within a temperature range of 1170–770 K [3]. The natural quartz crystal powder was taken as raw material. The samples under investigation were small, optically transparent single-crystals with dimensions of about 0.2-0.4·0.6·0.9 mm^3. ArF (193 nm), KrF (248 nm) and F_2 (157 nm) pulsed excimer lasers with pulse duration about 5 ns are used to excite PL.

3 RESULTS

3.1 Blue luminescence

The luminescence and decay kinetics of stishovite is presented in Figure.1.

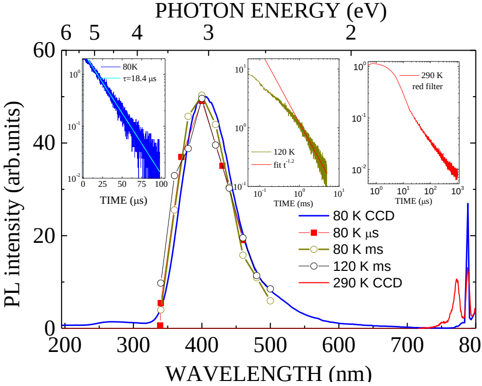

Figure 1: Time resolved photoluminescence spectra of stishovite single crystal under pulses of excimer ArF laser excitation at 120 K and 80 K. Inserts – decay kinetics curves. Left for µs time range, middle and right for ms time range. Right insert shows decay kinetics measured in the range of sharp luminescence lines ascribed to carbon related molecular center.

At 120 K a slow component appeared, see Figure 1, insert in the middle. The rights insert shows decay of PL in the range of 800 nm belonging to carbon impurity-related center. In Figure 2 the intensity of slow PL obtained by integration of decay curves at each temperature is demonstrated. The thermal dependence of time resolved intensity of 18 µs component is presented as well.

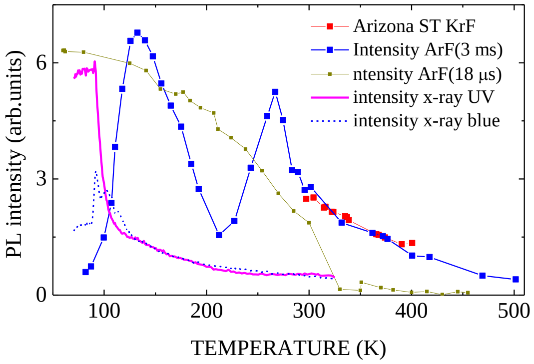

Figure 2: Time resolved temperature dependences of the blue photoluminescence of stishovite measured with photon counting method in the range of time 3 ms (big closed squares) and in the time range of 18 µs (open squares) under ArF laser excitation. Some points with the closed squares were measured for Arizona stishovite with use of KrF laser. The lines correspond to x-ray excited luminescence intensity thermal dependences (line – UV band, dash line – blue band).

3.2 UV luminescence

In Fig.7 the UV band detected by photon counting method is presented. It is seen that there is the slow component detected in the µs time range. The component of decay in ms range is not detected for UV band.

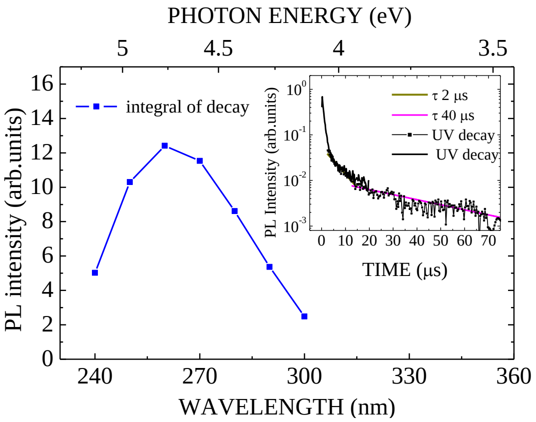

Figure 3: Time resolved luminescence spectra measured with photon counting method for UV band of stishovite single crystal. Excitation – ArF laser. Insert: measured decay curve and exponential approximation with two exponents at T= 290 K.

3.3 Electron spin resonance

For the non-irradiated stishovite crystal an angularly dependent ESR signal was detected at 77 K. The ESR spectra at some selected orientations are shown in figure 4. The observed resonance positions range from $g_{eff} \approx 2.06$ to 2.00. Previous studies on natural occurring samples of stishovite have reported a resonance at g ≈ 2.003 [4], whereas in-depth ESR studies of radiation induced defects in synthetic single crystals have identified Al-O_2^{3-}, Ti^{3+} and W^{5+} centers in stishovite [5]. No set of spin-Hamiltonian parameters from [5] is able to reproduce our experimental ESR spectra, therefore, the nature of this paramagnetic center requires further investigations.

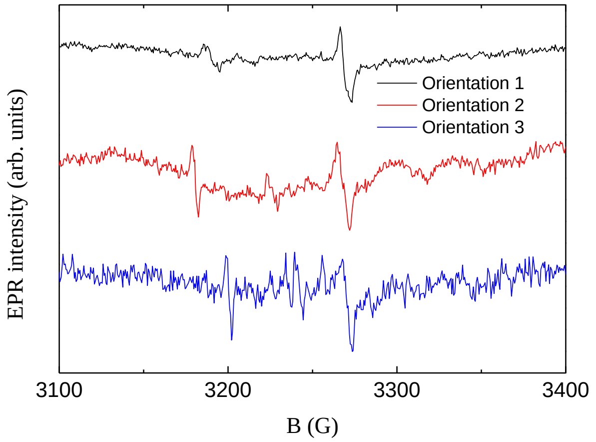

Figure 4: X-band ESR spectra of stishovite at selected crystal orientations.

4 CONCLUSIONS

It is obtained that luminescence of stishovite single crystal possesses the additional slower component in the ms range for blue band and in tens µs for UV band. The effect of additional slow component could be related to presence of OH group and/or carbon related molecular defects modifying the luminescence center, creating a complex defect. This complex configuration of defect with the nearest modifier is changing with temperature and luminescence properties are also changing with temperature. We have some distribution of luminescence center with different quantity and/or distance between luminescence center and modifier.

REFERENCES

[1] A.N. Trukhin, et al., J.Phys.: Condens. Matter, 20, 175206, 2008.

[2] A.N. Trukhin, et al., Sol. State Commun., 189, 10, 2014.

[3] L.M. Lityagina, et al., J. Cryst. Growth, 222, 627, 2001.

[4] R.A.B. Devine, et. al., Phys. Rev. B, 40, 10 1989.

[5] Y. Pan, et. al., Phys. Chem.Minerals, 39, 627, 2012.

Non-stoichiometric defects in metal-doped SiO_2

D.W. Boukhvalov[*,**], D.A. Zatsepin[**], A.F. Zatsepin[**]
[*1]Institute of Physics and Technology, Ural Federal University,
Mira Str. 19, 620002 Yekaterinburg, Russia
**Department of Chemistry, Hanyang University,
17 Haengdang-dong, Seongdong-gu, Seoul 133-791, Korea

ABSTRACT

Based on results of the combination of x-ray photoemission spectroscopy (XPS), photoluminescence measurements (PL) and theoretical modeling we have found the tendency for the formation of the combination of substitutional and interstitial defects in the metal-implanted SiO_2 matrix. In Sn-doped quartz was observed the formation of SnO_2-like structure in combination with the appearance of metallic Sn-phase. In the case of two valent zinc impurities, occur formation of Zn_2SiO_4 secondary phase. In Re-doped a-SiO_2 we detect multiple Re_xO_y structures and also clusterization of metallic rhenium. The role of oxygen vacancies also discussed.

PACS Keywords: 61.72.Bb, 71.15.Mb, 78.40.Fy, 78.70.

1 INTRODUCTION

Direct ion-doping by ion-implantation techniques was proved as a powerful technique for controllably managing embedded dopant concentration in a doped material, fabrication of non-stoichiometric defects that are used in luminescing electronic devices, and selective modification of the surface and near-surface layers of a host-material that dramatically re-builds the chemical properties of the inorganic material. The most important aspect of ion-implantation synthesis is ion-dopant allocation within the host-structure and the possibility of direct ion-replacement during the fabrication of substitutional impurities. In contrast with other conventional methods, such as molecular beam epitaxy or the sol-gel technique, when impurity incorporation into the host-structure occurs simultaneously on the stage of new matrix formation, the ion-implantation synthesis supposes “insertion” of the doping impurities into the unaffected host-structure. The situation appears to be even more complicated when multi-electron and multi-shell elements are implanted to yield wide-gape insulating matrices such as a-SiO_2. This kind of implants is significantly valuable for concrete applicative employment and also interesting for the understanding general principles of defects formation.

2 METHODS

KU-type (“wet” sintering approach) quartz glass was used as a host-matrix for ion pulsed implantation. The samples were implanted by single ion implantation, using a metal-vapor vacuum arc ion source, developed at the Institute of Electrophysics—Ural Branch of RAS. [1] XPS survey (fast wide scan) and core-level analysis of the samples under study were made using a PHI XPS Versaprobe 5000 spectrometer with an Al Kα X-Ray. The photoluminescence spectra were recorded under selective excitation with 6.5 eV at room temperature using McPherson VUVAS 1000 PL spectrometer (McPherson, USA) with a 30W deuterium light source. First-principle-based modeling using density functional theory (DFT) was performed to determine the formation energies and electronic structures of various configurations of the defects. These calculations were performed with the use of the SIESTA pseudopotential code. For the current modeling we employed the specially build $Si_{24}O_{48}$ supercell of α-quartz (Fig. 1). The presence of oxygen vacancies in the vicinity of all studied defects was also taken into account for considerations.

.

3 RESULTS

3.1 Sn-doping

The combined characterization of the electronic structure of a Sn-implanted glassy SiO_2 host-matrix before and after thermal tempering (900°C, one hour) was performed. We detect two dissimilar mechanisms of Sn-embedding into the SiO_2 host-matrix: the $Sn^{4+} \rightarrow Si^{4+}$ substitution by moving the host-atoms from stoichiometric positions into the intestinal void for samples without tempering, and the Sn-loss effect for the thermally treated host-matrices. The latter is represented by partial backward translocation of host-atoms into their stoichiometric positions simultaneously with Sn-metal clustering as interstitials in an amorphous three-dimensional glassy network of the SiO_2-host. Theoretical calculations also demonstrate favorability of the formation of substitutional Sn-defects in the presence of interstitial Si-atoms. In the absence of silicon atoms in the interstitial void, the most favorable configuration of impurities is a combination of substitutional and interstitial Sn-impurities. This rearrangement of the impurities disposition change not the only electronic structure of valence band but also provide significant changes of the optical properties that were proven by PL spectroscopy. [2]

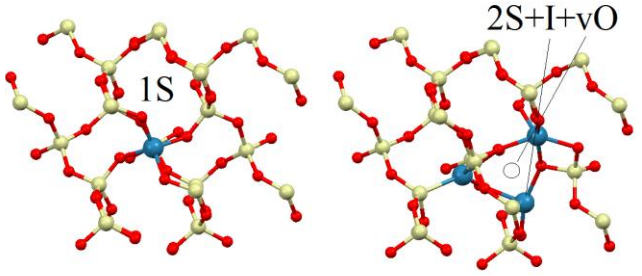

Figure 1: An optimized atomic structure of several configurations for substitutional (S) and interstitial (I) Re-defects and oxygen vacancies (vO).

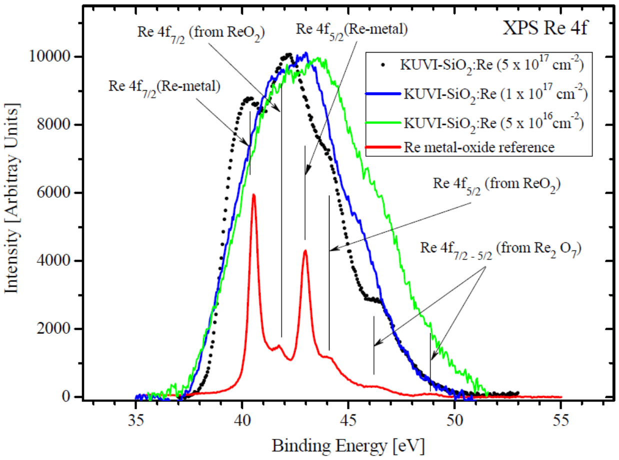

Figure 2: Normalized XPS Re 4f core-level spectra for Re-implanted KUVI-SiO$_2$ host-matrix after different implantation fluences without tempering.

3.2 Zn-doping

Similarly to the previous case, we have studied Zn-ion implanted silica glass before and after thermal annealing at 900 °C (1 h). Basing on a comparison of theory and experiment we can conclude that in as-implanted silica the stable ZnO nanoparticles are formed whereas the thermal annealing induces the formation of Zn_2SiO_4 species with strongly increased green emission. Thereby, the fabrication of luminescing Zn_2SiO_4 nanoparticles in the Zn-implanted a-SiO_2 host can be discussed as a two-step solid-state process which is including the formation of ZnO nanoparticles as an intermediate stage with the following their interaction with the glassy network of a-SiO_2 host-matrix. The observed relatively high-intensive green emission of implanted and thermally treated a-SiO_2:Zn samples might be linked with the intrinsic defects in the newly fabricated nanoscaled Zn_2SiO_4-phase. This fact seems to be very important regarding understanding the physical origin and the peculiarities of optical features of advanced photonic nanomaterials synthesized with the help of ion-beam treatment technologies. [3]

3.3 Re-doping

The The following scenarios of Re-embedding into SiO_2-host by pulsed Re-implantation were derived: (i) low Re-impurity concentration mode → the formation of combined substitutional and interstitial impurities with Re_2O_7-like atomic and electronic structures in the vicinity of oxygen vacancies; (ii) high Re-impurity concentration mode → the fabrication of interstitial Re-metal clusters with the accompanied formation of ReO_2-like atomic structures and (iii) an intermediate transient mode with Re-impurity concentration increase, when the precursors of interstitial defect clusters are appeared and growing in the host-matrix structure occur. An amplification regime of Re-metal contribution majority to the final VB structure was found as one of the sequences of intermediate transient mode. [4]

4 CONCLUSIONS

In summary, we demonstrate that implantations of multi-electron and multi-shell elements in a-SiO_2 matrix provide formation of various combinations of substitutional and interstitial defects with oxygen vacancies. Rearrangement of the configurations of the defects significantly influences optical properties of doped silica. Combining of XPS measurement and DFT modeling is the powerful tool for the ascertainment of the local configurations of the defects.

REFERENCES

[1] D.A. Zatsepin, A.F. Zatsepin, D.W. Boukhvalov, E.Z. Kurmaev, N.V. Gavrilov, N.A. Skorikov, A. von Czarnowski, H.-J. Fitting, “Octahedral conversion of a-SiO2 host matrix by pulsed ion implantation” phys. status solidi (b) 252, 2185, 2015.

[2] D.A. Zatsepin, A.F. Zatsepin, D.W. Boukhvalov, E.Z. Kurmaev, N.V. Gavrilov, “Sn-loss effect in a Sn-implanted a-SiO2 host-matrix after thermal annealing: A combined XPS, PL, and DFT study” Appl. Surf. Sci. 367, 320, 2016.

[3] D.A. Zatsepin, A.F. Zatsepin, D.W. Boukhvalov, E.Z. Kurmaev, Z.V. Pchelkina, N.V. Gavrilov, “Electronic structure and photoluminescence properties of Zn-ion implanted silica glass before and after thermal annealing” J. Non-Cryst. Solids 432, 183, 2016.

[4] 9. A.F. Zatsepin, D.A. Zatsepin, D.W. Boukhvalov, N.V. Gavrilov, V.Y. Shur, A.A. Esin, “The MRO-accompanied modes of Re-implantation into SiO2-host matrix: XPS and DFT based scenarios” J. Alloys and Comp. 728, 759, 2017.

Radiation Effects on Aluminosilicate Optical Fibers in the Ultraviolet and Near-Infrared Domains

A. Alessi*, A. Guttilla**, S. Girard*, S. Agnello**, M. Cannas**, T. Robin***, A. Boukenter*, Y. Ouerdane*

* Univ Lyon, Laboratoire H. Curien, UMR CNRS 5516,
18 rue du Pr. Benoît Lauras F-42000, Saint-Etienne, France
** Dipartimento di Fisica e Chimica, Università di Palermo,
I-90123 Palermo, Italy
*** iXBlue Photonics, Rue Paul Sabatier, F-22300 Lannion, France

ABSTRACT

Online X-ray RIA (radiation induced attenuation) has been measured for differently doped aluminosilicate optical fibers. The acquired data in the visible spectral range show the generation of absorption bands and that their generation is dose rate independent. The optical data will be completed by additional Electron Paramagnetic Resonance measurements to highlight the presence of defects attributed to Al as the Al-OHC and support the attribution of Vis-IR RIA bands to Al centers.

PACS Keywords: 61.80.-x Radiation effects in solids, 61.72.J- Point defects, 78.40.Pg Absorption spectra disordered solids, 42.81.-i Fiber optics.

1 INTRODUCTION

Aluminum doping of silica is often used for the production of rare-earth (RE) doped optical fibers a key element of optical amplifiers [1]. Furthermore, Al impurities can be present in natural silica and constitute a limit for its use in radiation-rich environments. Despite these facts only a few research studies have been performed on passive (without RE ions) aluminosilicate fibers in comparison to more usual and differently (Ge, P, and …) doped silica typologies. In this context, the study of natural silica provides evidence for relations between some of the radiation induced Al defects and optical absorption bands. In particular, at least an absorption band peaked at ~2.3 eV has been attributed to the Al-OHC, Aluminum-Oxygen-Hole-Center, ($[AlO_4]^0$) [2,3]. Another band at about 4.1 eV was attributed to the E'Al [2].

Since, in comparison to the pure silica, the Al doped silica appears to be extremely sensitive to ionizing radiation in terms of RIA, there is a growing interest to understand the Al-defect generation processes as the RIA monitoring of these fibers can be used for distributed dosimetry. This interest involves the investigation of the RIA origins in both the UV-visible and the NIR spectral domains. In the present abstract we focused our attention on the visible part of the spectrum to highlight the properties of Al-OHCs. A comparison with the behavior of the radiation induced attenuation in the NIR domain will be also presented at the conference to highlight possible impact of Al related defects in this latter spectral domain. Furthermore, since the Al-OHC defects are paramagnetic [2,3] post-irradiation Electron Paramagnetic Resonance (EPR) measurements will be performed to support the *in situ* RIA characterization.

2 EXPERIMENTAL

In the present investigation we studied different single- and multi-mode Al doped optical fibers produced by iXBlue Photonics. The Al doping level changes in the range 2-4 weight percent (%wt).

The RIA has been studied on-line during 40 keV X-ray irradiation. UV-Vis light from a DH-2000-BAL source from Ocean Optics was injected in the fiber and the light transmitted by the fiber was monitored as a function of the irradiation time using a UV-Vis detector HR-4000. Similarly, the RIA induced in the NIR spectral domain has been studied using an AQ-4303B source and a NIRQUEST spectrometer.

X-ray irradiations were performed using the Moperix machine, in which the X-ray source is constituted by a Tungsten target. The dose rate was changed from 0.07 up to 6.25 Gy(SiO_2)/s varying the operation current.

3 RESULTS AND DISCUSSION

In figure 1, we report the online RIA kinetic measured at ~530 nm (~2.34 eV) in the four single mode Al doped fibers (dose rate of 0.07 Gy/s), the data of the multi-mode fiber are not reported in the abstract. For all the samples we note a linear increase of the RIA. We also note that the four fibers feature very close RIA kinetics, suggesting the independence of the radiation effects on the aluminum concentration in the 2-4 weight percent range.

In figure 2, we report the online RIA measured at 530 nm (2.34 eV) for fiber3 as a function of the accumulated dose changing the dose rate, from 0.07 up to 6.25 Gy/s. We note that for all the employed dose rates the kinetics remain unchanged. Indeed, we observe no particular dependence of the RIA at this wavelength on the dose rate. Using the data recorded with the highest dose rate we can suggest that the RIA kinetic is linear up to a dose of ~3 kGy.

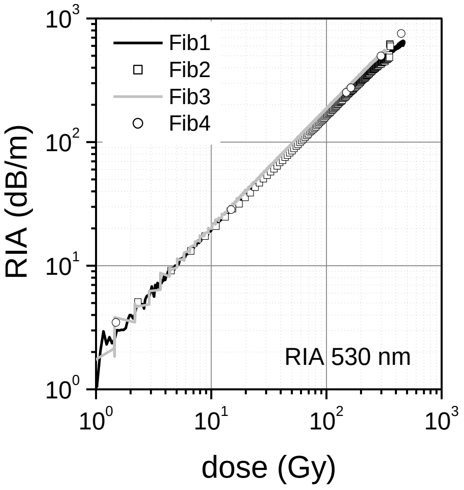

Figure 1: RIA at 530 nm measured in the four single mode investigated samples as function of the dose (at 0.07 Gy/s).

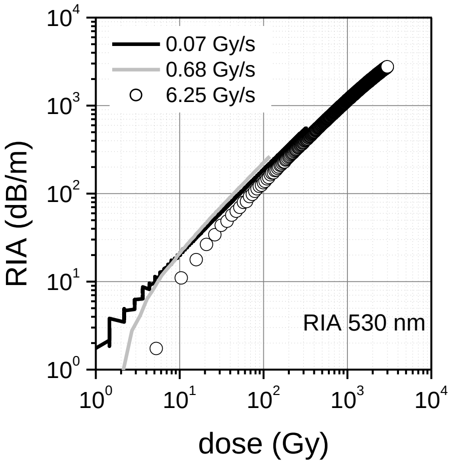

Figure 2: RIA at 530 nm measured in the fiber3 using three different dose rates.

To better identify the origin of the RIA at 530 nm we report some RIA spectra in the range from 1.5 to 3.5 eV. Such data highlight the presence of an optical absorption band at ~2.3 eV and of other components peaking at higher energies. A detailed study of the spectra will be reported to better identify the different contributions. Anyway, the presence of this band appears to be compatible with the generation of the Al-OHCs. The behavior of the RIA reported in figures 1 and 2 seems to be due to this defect type. As a consequence the Al-OHC generation does not depend on the Al-concentration or neither on the dose rate.

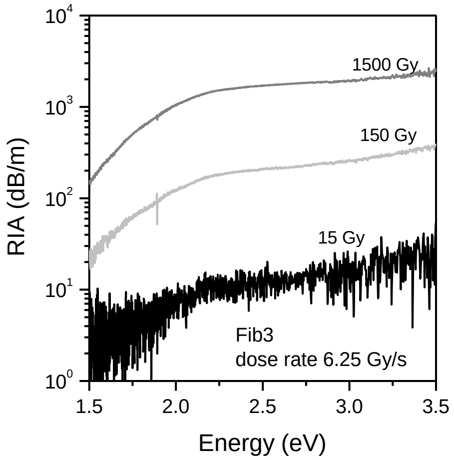

Figure 3: RIA spectra recorded at three different doses for the Fib3 irradiated at the dose rate of 6.25 Gy/s.

4 CONCLUSION

We studied the on-line RIA (radiation induced attenuation) in aluminosilicate fibers. In particular, we monitored the signal in the visible spectral range. Our data show the generation of an optical absorption band at ~2.3 eV, which can be attributed to Al-OHCs. By changing the dose rate from 0.07 to 6.25 Gy/s we did not observe any specific dependence of this parameter on the Al-OHC levels, suggesting that their generation process is not strongly affected by the dose rate. Further data recorded in the NIR and acquired through electron paramagnetic resonance technique will be presented to better understand the Al-doped fiber radiation responses at the conference.

REFERENCES

[1] M. Engholm, P. Jelger, F. Laurell, L. Norin Opt. Let., 34, 1285, 2009.
[2] H. Hosono, H. Kawazoe, Nucl. Inst. Met. Phys. B, 91, 395, 1994.
[3] A. N. Trukin, J. Teteris, A. Fedotov, D. L. Griscom, G. Buscarino, J. Non-Cryst. Solids, 355, 1066, 2009.

MONDAY

SESSION

DEFECTS - RADIATION EFFECTS II

Ultrafast laser 3D photo-inscription of bulk chalcogenide glasses for photonic applications in the mid-IR

C. D'Amico*, G. Martin**, J. Troles***, R. Stoian*

*Univ. Lyon, Univ. Jean Monnet, CNRS, LabHC- UMR 5516, 42000 St. Etienne, France
** Univ. Grenoble Alpes/CNRS, IPAG, F-38000 Grenoble, France
*** Univ. Rennes, CNRS, ISCR-UMR 6226, 35000 Rennes, France

ABSTRACT

Ultrafast laser photo-inscription is probable the most flexible technique allowing generating complex 3D optical functions in bulk glasses. Here we present some very recent results about ultrafast laser photo-inscription of bulk Chalcogenide glasses. In particular we demonstrate the possibility of building efficient and compact spectro-interferometers (linear optical functions) and saturable absorbers (nonlinear optical functions) for integrated photonic applications in the mid-IR.

PACS Keywords: ultrafast lasers, material laser processing, integrated photonics, glasses, nonlinear optics

1 INTRODUCTION

Ultrafast laser photo-inscription of bulk transparent glasses is a technique on the path of maturity for engineering material optical properties. The glass is locally and permanently modified in correspondence of the focal volume of a focused ultrashort laser beam. The permanent change correspond to a local modification of the glass refractive index, which can be either positive (local densification, type I) or negative (local expansion, type II). It is generally accompanied by specific structural changes of the microscopic glass matrix. By using both type I and type II index changes, and 3D optical design, complex optical functions can be defined, and sophisticated integrated photonic devices can be built for applications in numerous domains. Possibilities of application further increase in the mid-IR domain, ranging from gas sensing for atmospheric and astronomical measurements to process monitoring/control for industrial purposes. Because of their very large transparency spectral window, Chalcogenide (ChG) glasses represent an interesting solution for integrated photonic applications in the mid-IR.

2 MATERIAL AND METHODS

The ChG samples used for this study are a commercial Ga-La-S (ChG Southampton Ltd.) and three glasses, $As_{40}S_{60}$, $Ge_{20}As_{20}S_{60}$ and $Ge_{15}As_{15}S_{70}$ which have been synthesized in the laboratory. The laboratory samples are obtained by mixing elements in a furnace at a temperature of 800°C for 15 hours and rapid cooling to T_g-15°C, where T_g is the glass transition temperature. An annealing of 30 minutes allows a partial removal of constraints, followed by a slow cooling to room temperature. This process in general generates unrelaxed glasses with characteristic volumes higher than in the case of relaxed glasses, and therefore a lower density. The laser used to induce the local index change is an amplified Ti:Sapphire chain, which can deliver 150 fs laser pulses with a repetition rate of 100 kHz and a maximum energy per pulse of 6 µJ. The laser beam is focused into the sample by means of a 20× - 0.3 NA microscope objective. By changing the laser dose one can obtain permanent index modifications having different contrast. Positive and negative index changes appear respectively as dark and white traces to phase contrast microscopy (PCM). The response of the samples to laser radiation is studied by using post-mortem PCM and Raman analysis, and, when possible, the experimental results are compared with numerical simulations based on the Non-Linear Schrödinger Equation (NLSE).

3 RESULTS

In this section we present a list of recent results about bulk ChG photo-inscription using ultrafast lasers.

3.1 Laser-induced refractive index change in ChG glasses

In general ChG glasses can have a variety of responses to ultrafast laser radiation depending on their composition and their thermal history. An interesting example is obtained by comparing the response of $As_{40}S_{60}$ and $Ge_{15}As_{15}S_{70}$ (see Fig. 1(a)). These glasses show a completely opposite response to focused ultrafast laser beams; if the first present mainly type II positive index changes, in the second a very large window of laser dose can be defined, which gives only type I positive index changes. This different response has been attributed to Ge doping action, which increases the structural flexibility of the glass matrix [1]. Concerning the importance of the glass thermal history, we demonstrated that applying a thermal treatment can decrease the threshold for the apparition of positive index changes in some ChG glasses [2] as shown in Fig. 1(b). This opens the route to deeper studies in order to better understand how the glass matrix couples with the ultrafast laser radiation.

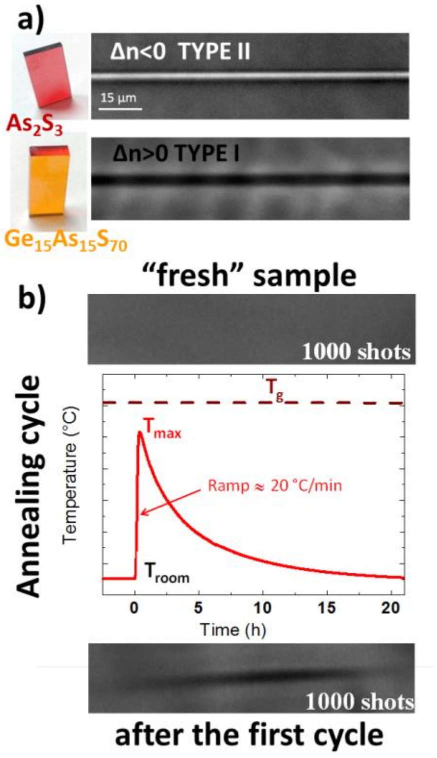

Figure 1: Opposite response of $As_{40}S_{60}$ and $Ge_{15}As_{15}S_{70}$ samples to focused ultrafast laser radiation for the same laser dose (a). Lowering the threshold of laser photo-inscription in $Ge_{20}As_{20}S_{60}$ after one annealing cycle (b).

3.2 Photo-inscription of 3D linear optical functions

Translating the sample in the three directions of the space allows generating complex 3D optical circuitry. Changing the laser dose (pulse energy and/or translation speed) allows variating the index contrasts and so optimizing the guiding efficiency in a given spectral window. Here we demonstrate an efficient large mode area guiding technique in bulk ChG in the mid-IR, based on the concept of evanescent coupling mechanism [3]. By using type I waveguide, photo-inscribed by focused Gaussian laser beams, and high-contrasted type II negative index structures, photo-inscribed using focused non diffractive Bessel beams, we demonstrate the possibility of building integrated compact spectro-interferometers, working in the mid-IR spectral range [4] (see Fig. 2(a) and 2(b)).

3.3 Photo-inscription of 3D nonlinear optical functions

An interesting characteristic of ChG glasses is their high nonlinear index n_2 (10^2 to 10^3 higher than in fused silica). This allows exciting non-invasive 3^{rd} order nonlinearities (Optical Kerr Effect) during the propagation in a pre-built waveguide by using relatively low laser pulse intensities, which remain under the threshold for local material modification. Based on this concept, we demonstrated for the first time the ultrafast laser fabrication of 3D saturable absorber structures in bulk Ga-La-S [5] (see Fig. 2(c)).

4 CONCLUSIONS

In conclusion, the ultrafast laser photo-inscription technique allows generating efficient optimized linear and nonlinear optical functions in bulk ChG glasses. Here we demonstrate the concept of 3D integrated spectro-interferometers and saturable absorbers in bulk ChG glasses, working in the mid-IR. Furthermore we demonstrate that the threshold for ultrafast laser photo-inscription can be lowered in some ChG glasses by a simple thermal treatment, opening the route for a deeper understanding of the laser induced modification process.

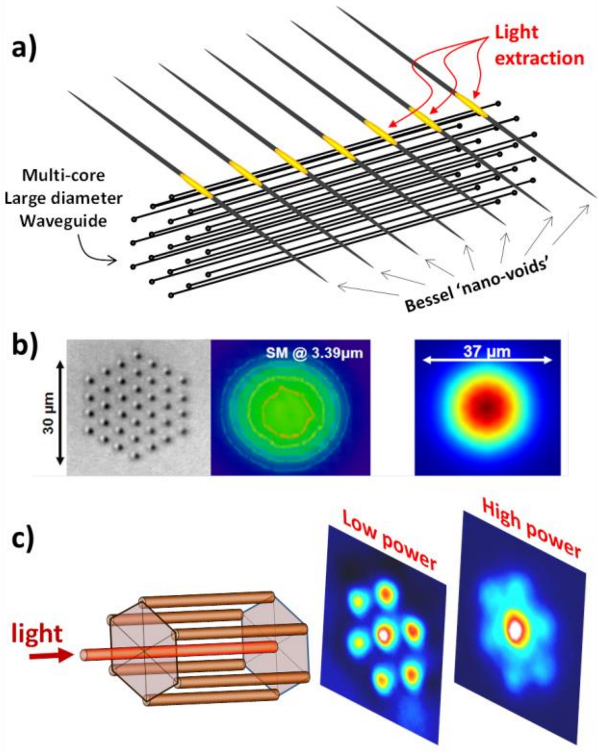

Figure 2: Integrated 3D spectro-interferometer in a bulk ChG glass, working in the mid-IR (a). Cross-section of a multi-core large diameter waveguide guiding single mode at 3.39 µm, and comparison with numerical simulations (b). Integrated 3D saturable absorber structure in bulk Ga-La-S sample (c).

REFERENCES

[1] C. D'Amico et *al*., Opt. Mat. Express 6, 1914, 2016.
[2] M. Somayaji et *al*., submitted to Optical Material.
[3] C. D'Amico et *al*., Opt. Express 22, 13091, 2014.
[4] G. Martin et *al*., Opt. Express 25, 8386, 2017.
[5] S. Minardi et *al*., Opt. Lett. 40, 257, 2015.

Luminescence efficiency of Si/SiO_2 nanoparticles produced by laser ablation

M. Cannas, P. Camarda, L. Vaccaro, F. Amato, F. Messina, T. Fiore, S. Agnello, F.M. Gelardi

*Dipartimento di Fisica e Chimica, Università degli Studi di Palermo, Italia.

ABSTRACT

Photoluminescence properties of Si(core)/SiO_2(shell) nanoparticles produced by pulsed laser ablation in aqueous solution are investigated with the purpose to highlight the microscopic processes that govern the PL stability and brightness. These systems emit a μs decaying band centered around 1.95 eV, that is associated with the radiative recombination of quantum-confined excitons generated in the Si nanocrystal core. Both the quantum efficiency and the stability of this emission are strongly dependent on the pH of the solution. They enhance in acid environment because of the H^+ passivation of nonradiative defects, located in the Si/SiO_2 interface, which causes the growth of SiH groups.

PACS Keywords: Si/SiO_2 nanoparticles, laser ablation, quantum confinement, photoluminescence, pH dependence.

1 INTRODUCTION

The visible photoluminescence (PL) of Silicon-nanocrystals (Si-NCs) is fundamental for several applications (optoelectronics, display devices, sensors, light detectors) and is, therefore, widely investigated [1]. Several works have evidenced that the PL position depends on Si particle size thus supporting the hypothesis that it originates from the radiative recombination of quantum-confined (QC) excitons [2]. On the other hand, the PL is strongly influenced by the Si surface chemistry [3]. The main processes are: i) oxidation that produces a SiO_2 shell surrounding the Si core and, consequently, luminescent defects may be introduced at the Si/SiO_2 interface; ii) doping with hydrogen (molecular, atomic, or ion) that diffuses easily in the Si/SiO_2 and interacts with interface defects.

Regardless the PL origin, the requirement of its stability and brightness motivate a huge effort to develop convenient synthesis processes or thermochemical treatments able to finely control the emission efficiency. To this aim, Pulsed Laser Ablation (PLA) is a versatile and environmentally friendly method that is normally adopted to realize a large variety of luminescent nanomaterials. In this work, we use PLA to produce Si-NC(core)/SiO_2(shell) nanoparticles in water. The influence of H^+ ions on the PL properties is studied by changing the pH of the aqueous solution in which the Si laser ablation was done. We take advantage of time-resolved experiments that are appropriate to measure spectroscopic parameters (intensity and lifetime), from which we derive how the PL efficiency and stability are dependent on the acid and basic environment of nanoparticles. Moreover, Fourier Transform Infrared (FTIR) absorption spectra are investigated to clarify the interaction processes between H^+ and Si/SiO_2 interface defects.

2 EXPERIMENTAL METHODS

Si/SiO_2 nanoparticles are synthesized by PLA of a p-type silicon wafer placed at the bottom of a vessel containing deionized water. We have used the first harmonic (1064 nm) of a 5 ns pulsed Nd:YAG laser), operating at a repetition rate of 10 Hz and 40 mJ/pulse energy, weakly focused on the Si target (spot size 2 mm). After the ablation, the solution is divided into several parts which were diluted with acid(HCl) or basic (NaOH) water solution so that the pH, measured by a benchtop pH-Meter, is varied from 1 to 10. Time resolved PL spectra are excited by a tunable laser consisting of an optical parametric oscillator pumped by the third harmonic (355 nm) of a Nd:YAG laser, analyzed by a monochromator, equipped with a grating of 300 lines/mm and blaze wavelength 500 nm, and acquired by an intensified CCD camera driven by a delay generator (PI MAX Princeton Instruments) setting the acquisition time window, T_W, and the delay, T_D, with respect to the arrival of laser pulses. The structural properties are characterized by FTIR spectra on specimens prepared by pressing a mixture of nanoparticles and KBr salt at 160 MPa.

3 RESULTS

PL spectra of Si/SiO_2 nanoparticles suspended in the colloidal solutions at different pH are reported in Fig. 1(a). In all samples, it is observed a μs decaying emission centered at 1.95 eV, which is associated with the radiative recombination of QC excitons generated in the Si-NCs [2]. The comparison among the spectra evidences that the PL intensity is strongly influenced by the acidity/basicity of the aqueous solution: it decreases by a factor of ≈20 on increasing pH from 2 to 10. A detailed picture of the normalized PL intensity as a function of pH is reported Fig. 1(b): the curve is almost flat in the two ranges pH<3.5 and 4.0<pH<9.0, while it evidences an abrupt negative change of slope for 3.5<pH<4.0 and pH>9.0. It is worth noting that this trend is well correlated with the change of PL lifetime, we deduce, therefore, that is related to the variation of quantum efficiency. Then, its enhancement in acid environment agrees with the reduction of nonradiative decay rates related to the H^+ induced passivation of Si/SiO_2 interface defects (nonradiative centers).

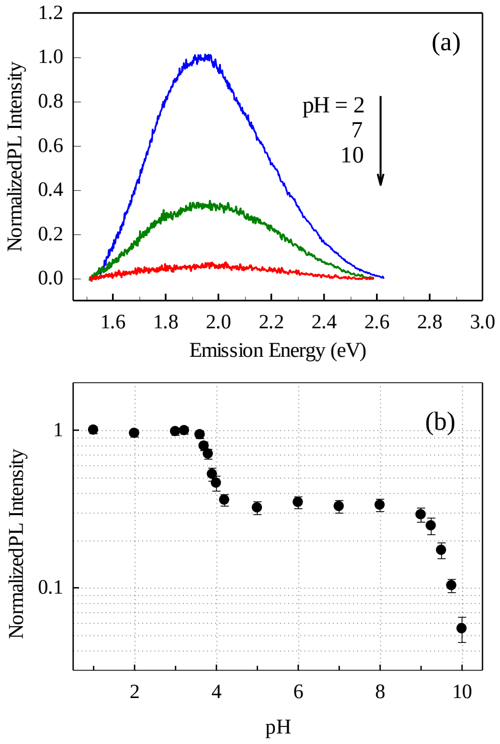

Figure 1: (a) PL spectra excited at 4.13 eV and acquired with T_W = 10 ms and T_D = 1 μs from Si-NCs in aqueous solutions with different pH. (b) PL intensity as a function of pH. In both figures, the data are normalized to the value recorded at pH=1.

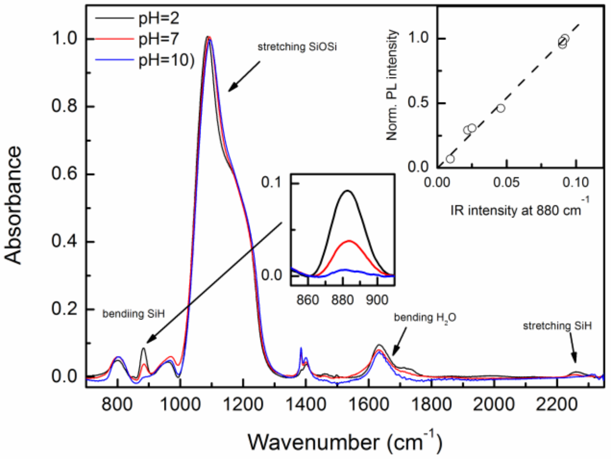

Figure 2: FTIR spectra normalized with respect to the intensity of the IR mode at 1100 cm^{-1} of Si/SiO_2 nanoparticles produced on varying the pH of aqueous solution. The first inset reports a zoom of the I band, around 880 cm^{-1}, related to SiH bending, the second shows its linear correlation with the normalized PL intensity.

To clarify this model, in Fig. 2 we report the FTIR spectra of Si/SiO_2 nanoparticles at different pH. All the samples evidence the vibration modes peculiar to SiO_2, such as the Si-O-Si stretching around 1100 cm^{-1}, consistently with the Si oxidation induced by PLA in water [4]. Hydrogen related species are observed both in the form of Si-OH and Si-H, likely originating from the Si surface. In particular, we observe that the SiH bending mode centered at 880 cm^{-1} decreases on increasing pH. Such a dependence agrees with that observed for the PL intensity, displayed in Fig.1 (b), as well demonstrated by the linear correlation between these signals. Hence, we infer that in acid environment H^+ ions passivate the nonradiative centers thus increasing the SiH concentration. The origin of these defects is connected with the structure of the Si/SiO_2 interface and could be hypothesized on the basis of previous computational works. Lee et al [5] have proposed the existence of diamagnetic defects such as distorted Si-Si bonds, which overlap with the electron density in the Si-NCs thus limiting the PL efficiency. Then, trapping of H^+ at these defect sites may explain the enhancement of PL efficiency correlated with the formation of SiH.

REFERENCES

[1] F. Priolo, T. Gregorkiewicz, M. Galli, T. F. Krauss, Nat. Nanotechnol., 9, 19, 2014.
[2] T. Schmidt, A. I. Chizhik, A. M. Chizhik, K. Potrick, A. J. Meixner, F. Huisken, Phys. Rev. B, 86, 125302, 2012.
[3] K. Dohnalova, A. N. Poddubny, A. A. Prokofiev, W. D. de Boer, C. P. Umesh, J. M. Paulusse, H. Zuilhof, T. Gregorkiewicz, Light Sci. Appl., 2, e47, 2013.
[4] L. Vaccaro, R. Popescu, F. Messina, P. Camarda, R. Schneider, D. Gerthsen, F.M. Gelardi, M. Cannas, J. Appl. Phys., 120, 024303, 2016.
[5] B. G. Lee, D. Hiller, J.-W. Luo, O. E. Semonin, M. C. Beard, M. Zacharias, P. Stradins, Adv. Funct. Mater., 22, 3223, 2012.

Pulsed X-ray Radiation Responses of Solarization-Resistant Optical Fibers

V. De Michele[*], *C. Marcandella*[**], *D. Di Francesca*[*], *P. Paillet*[**], *A. Alessi*[*], *M. Cannas****, *Y. Ouerdane*[*], *A. Boukenter*[*], *S. Girard*[*]
[*]Univ Lyon, *Laboratoire Hubert Curien, UMR CNRS 5516, 42000 Saint-Etienne, France*
[**] CEA, DAM, DIF, F-91297, Arpajon, France.
***Dipartimento di Fisica e Chimica, Università di Palermo, Via Archirafi 36, I-90123 Palermo, Italy
vincenzo.demichele@univ-st-etienne.fr

ABSTRACT

In this work, we investigate the transient Radiation Induced Attenuation (RIA) of a particular type of optical fibers called "solarization-resistant" after an ultra-short X-ray pulse. We performed on-line RIA spectra in the range (0.7 – 3.5) eV, both at room temperature (RT) and at liquid nitrogen temperatures (LNT), to characterize the metastable defects that are quickly bleached just after the X-ray pulse. Our results evidence that in the two fibers investigated, the transient RIA can be mainly explained by the generation and the post-irradiation kinetics of the self-trapped holes.

PACS Keywords: Optical fibers; Radiation effects; Transient defects; Silica.

INTRODUCTION

Transmission of high-power UV light inside a fiber can generate absorbing defects leading to a darkening phenomenon: this effect is usually called "solarization" [1,2]. To reduce this effect, several industries have developed "solarization-resistant" fibers having a better tolerance to the UV light, resulting in a more stable transmission of light with time. Furthermore, the radiation strongly affects their optical properties in this spectral region through an increase of attenuation (*Radiation-Induced Attenuation (RIA)*) explicable by the fact that most of the created defects absorb in this spectral domain. The use of the Asterix facility from the CEA Gramat [3], where the optical fibers are exposed to X-ray pulses (durations of few tens nanoseconds), allows us to study the vulnerability of optical fibers to the harsh radiation constraints (mixed pulse of X-rays, γ-rays and 14 MeV neutrons) associated with the ignition shots at megajoule class laser facilities such as LMJ in France or NIF in the US. These irradiations are then characterized by very high dose rates (> 100Mrad/s) and moderate dose (less than 100 krad(SiO_2)). In this work, we studied the RIA response to an ultra-short X-ray pulse of multimode "solarization-resistant" optical fibers at RT and LNT. The main purpose is to follow the annealing processes of the defects induced by irradiation in these optical fibers.

EXPERIMENTAL METHOD

Irradiations were performed at room temperature (RT) and liquid nitrogen temperature (LNT) using the ASTERIS X-ray pulsed generator (Gramat, France). The dose and dose rate (that can be larger than 100Mrad/s) depend on the distance of the sample from the source. In our experiment, the maximum dose value was limited to ~30 krad. We investigated two optical fiber typologies: polymicro FDP and polymicro FBP, both are step index fibers, pure silica core, high OH concentration in the core, doped clad and a high UV transmission. Samples under test consist of fiber coils with diameters of 8 cm and lengths of 10 m (for measurements in the UV – Vis spectral range) or 50 m (for measurement in the near – IR part of the spectrum) connectorized with fc-pc connectors to fiber pigtails, themselves connected to sources (DH2000 is the UV-Vis source and HL-2000 is the IR source) and detectors (HR4000 spectrometers from Ocean Optics for the UV-Vis measurements at RT and LNT; NIR512 spectrometer for RT and the NIR256 at LNT for IR measurements). The online RIA technique, used during the experiments, consists in the evaluation of the losses of transmitted light in an optical fiber during the irradiation. At the same time, a part of the optical fiber is irradiated by the X-ray pulse.

RESULTS AND DISCUSSION

Fig. 1 illustrates the RIA spectra (from ~ 0.7 eV to ~ 3.4 eV) recorded for the fiber FBP at RT after 7 krad X-ray pulsed exposure as a function of the delay from the shoot. The shape of the spectra acquired at RT appears time independent, featuring higher RIA values at higher energies. At LNT, despite the low shot dose ~ 1 krad, the detected RIA is larger. Differently from the RT data, the spectra acquired at LNT evidence a change of the spectral shape as a function of time and highlight the appearance of new absorption bands (not detected at RT). Furthermore, the comparison between the LNT and RT data shows that the recovery kinetic of the transmission properties is faster at room temperature.

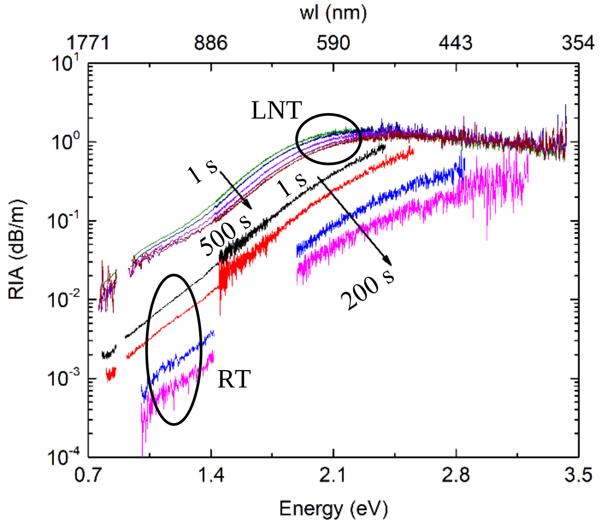

Figure 1 RIA spectra recorded for the FBP optical fiber at LNT and RT and at different times after the X-ray pulse.

In order to deeper analyze the origin of the RIA and the dynamic of the transient defect after the X-ray pulse, a quantitative analysis can be performed. In details, we used previous investigations to identify the possible RIA contributions related to different induced absorbing defects: we considered alternative sets of Gaussian curves proposed in literature [4,5]. In fig. 2a is shown the set used, in the case of the FBP fiber, to fit the experimental data at RT: as we can see that the most of the attenuation is caused by the self-trapped holes [6] (STH_1: peaked at 2.61, FWHM=1.2 eV) and by the defect related to the chlorine impurity (Cl^o: peaked at 3.26 eV, FWHM=1.2 eV). Even at low temperature, fig. 2b, the UV-Vis part of the spectrum is well fitted by the self-trapped holes contribution: in this case, are present the two types of STH (STH_1, present even at RT, and STH_2: peaked at 2.16 eV, FWHM=0.32 eV) and new bands linked to the STH strain-assisted [5] (STH_1: peaked at 1.88 eV, FWHM=0.42 eV; STH_2: peaked at 1.63 eV, FWHM=0.52 eV), which at RT could be bleached for time lower than our temporal resolution. The absence of the chlorine contribution, in fig. 2b, could be linked to its longer diffusion time caused by the low temperature. With this analysis, we conclude that the self-trapped holes represent the bigger contribution to the absorption in these two types of fiber at both temperatures. It is worth to note that the bands peaked at 2.16 eV (STH_2) and 2.61 eV (STH_1), usually called inherent [5], although rarely observed in optical fibers, are evident in the present work (observed even in [5]) and it is possible to follow the related annealing processes. Further experiments will be performed, in order to clarify the attenuation in the NIR part of the spectra, not considered yet in the fit, and to understand the role of the point defects in this contribution.

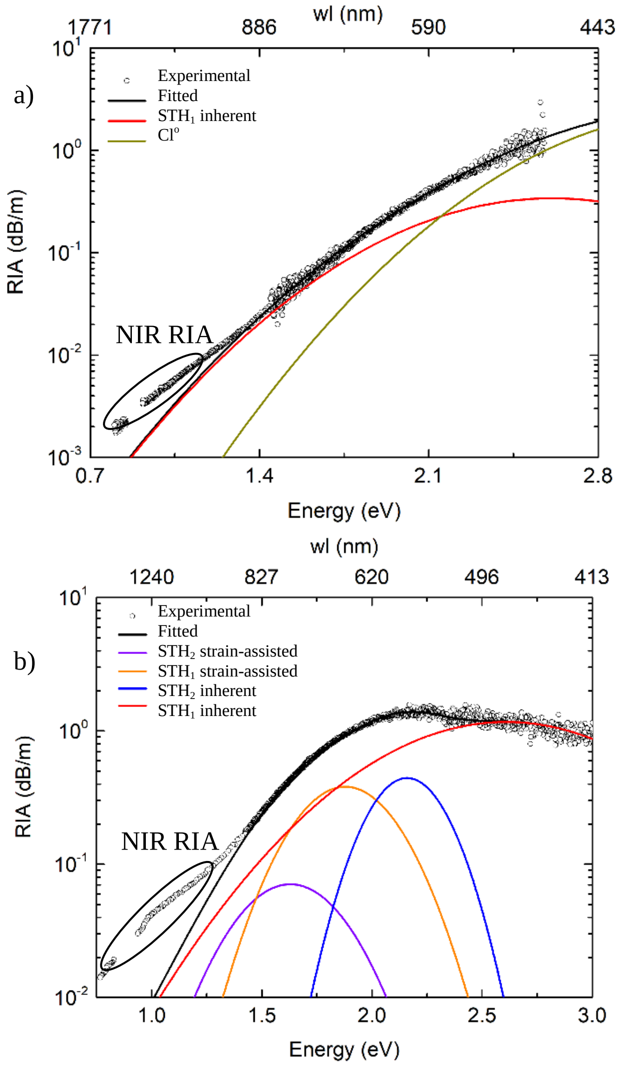

Figure 2 Decomposition of the FBP RIA spectra measured 1 s after the X-ray pulse. a) RIA decomposition at RT: open circle experimental data, black line global fit function, red line STH_1 inherent, green line chlorine. b) RIA decomposition at LNT: open circle experimental data, black line global fit function, purple line STH_2 strain-assisted, orange line STH_1 strain-assisted, blue line STH_2 inherent and red line STH_1 inherent contribution.

REFERENCES

[1] K. F. Klein, P. Schließmann, E. Smolka, G. Hillrichs, M. Belz, W. J. O. Boyle, and K. T. V. Grattan, *Sensors Actuat. B*, vol. 38–39, pp. 305–309, 1997.

[2] K.-F. Klein, S. Huettel, R. Kaminski, J. Kirchhof, S. Grimm, and G. W. Nelson, in *Proc. SPIE*, San Jose, Jan. 1998, vol. 3262C, pp. 150–160, (BiOS'98).

[3] A. Johan, B. Azaïs, C. Malaval, G. Raboisson, and M. Roche, Ann. Phys., vol. 14, pp. 379–393, 1989.

[4] S. Girard, and C. Marcandella, *IEEE Trans. Nucl. Sci.*, VOL. 57, NO. 4, (2010).

[5] P. F. Kashaykin, A. L. Tomashuk, M. Yu. Salgansky, A. N. Guryanov, and E. M. Dianov, Journal of Applied Physics 121, 213104 (2017);

[6] D. L. Griscom, Phys. Rev. B 40, 4224 (1989).

Growth of gold nanoparticles in a glass matrix by continuous laser irradiation

Rim FARAJ*, François GOUTALAND*, Nadège OLLIER*

* Univ Lyon, UJM-Saint-Etienne, CNRS, Institut d'Optique Graduate School, Laboratoire Hubert Curien
UMR 5516, F-42023, SAINT-ETIENNE, France

ABSTRACT

The Field-Assisted Solid-State Ion Exchange has been used to incorporate gold ions near the surface of a commercial soda-lime glass. The growth of gold nanoparticles by further continuous wave ultraviolet focused laser exposure has been investigated. Scanning electron microscopy reveals the formation of gold nanoparticles of diameter up to 40 nm, responsible for an absorption band, due to their localized surface plasmon resonance, centered at around 530 nm.

Keywords: Glass, ionic diffusion, field-assisted solid-state ion exchange, nanoparticles, surface plasmon resonance.

1 INTRODUCTION

Nanocomposite glasses, which contain metallic nanoparticles embedded in a glassy matrix, exhibit plasmonic properties based on the Surface Plasmon Resonance (SPR) of the nanoparticles, which are promising for numerous applications [1-2] . Their fabrication requires two subsequent steps: the first one consists in the introduction of the metal ions into the glass while the second one promotes the formation of metallic nanoparticles by subsequent appropriate heat treatment. Silver nanoparticles have been extensively studied since the silver-sodium ion exchange method allows the introduction of large amounts of silver ions into the glass. This technique is not suitable for the much larger gold ions, but the Field-Assisted Solid-State Ion Exchange (FASSIE) [3] technique can be used instead.

In this work, we successively use the FASSIE technique and continuous wave (cw) laser exposure at 244 nm to promote the formation of gold nanoparticles near the glass surface. The efficiency of the FASSIE technique is clearly demonstrated by recording the evolution of the electrical current through the glass sample. Subsequent laser exposure leads to the formation of gold nanoparticles, characterized by absorption measurements and Scanning Electron Microscopy (SEM). Gold nanoparticles of diameter of about 40 nm are observed, responsible for a SPR band centered at around 430 nm. Combining FASSIE and laser annealing opens up new perspectives for gold nanocomposite glasses.

2 EXPERIMENTAL PROCEDURE

A commercial soda-lime glass slide has been cleaned in three successive ethanol, acetone and water ultrasonic baths. A 50 nm thick gold layer has then been deposited onto the glass surface by thermal evaporation. The FASSIE method has been performed (figure 1): the glass slide is sandwiched between two polished steel electrodes and submitted to a direct electric field, ranging from 100 to 600 V/mm, while being heated in an oven at temperatures between 200 to 400 °C. The FASSIE duration was varied from 1 to 3 h, during which the electrical current across the glass was recorded.

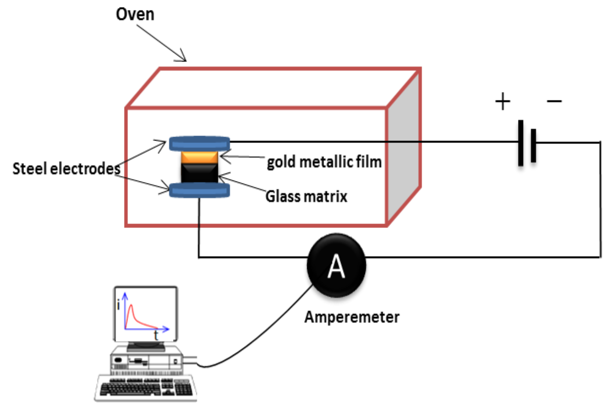

Figure 1: Schematic diagram of the of FASSIE experimental setup.

Once the glass doped with Au^{3+} ions, cw laser exposure at 244 nm has been performed with power density up to 10 kW/cm^2. This allows the growth of gold nanoparticles, which have been characterized by absorption spectroscopy and SEM.

3 RESULTS AND DISSCUSSION

Figure 2 displays the evolution of the electrical current with the FASSIE process duration. The electric field was applied once the high temperature inside the furnace was constant. This explains the delay observed in fig. 2. Two main peaks are observed in the current profile curve: the first one, that occurs almost immediately once the electric field has been applied, is attributed to the diffusion of Na^+

ions towards the anode. The second and less peak, which is delayed by roughly 800s from the first one, is due to the diffusion of the Au^{3+} ions inside the glass, which implies that the gold layer has been oxidized. Our results attest of the efficiency of the poling process to dope the glass with Au^{3+} ions.

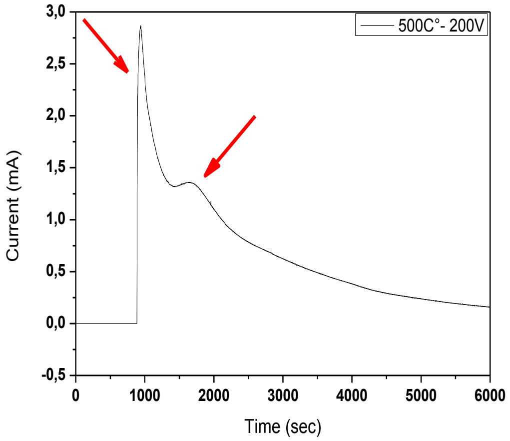

Figure 2: Current versus time profile of the sample poled for 500℃ and 200V. The two peaks indicated by arrows are due to the diffusion of Na^+ and Au^{3+} ions.

The laser exposed area of the poled sample exhibits a pink coloration, due to the SPR of gold nanoparticles [4]. The absorbance spectrum recorded through the irradiated area, which presents a band centered at around 530 nm, confirms this attribution (figure 3).

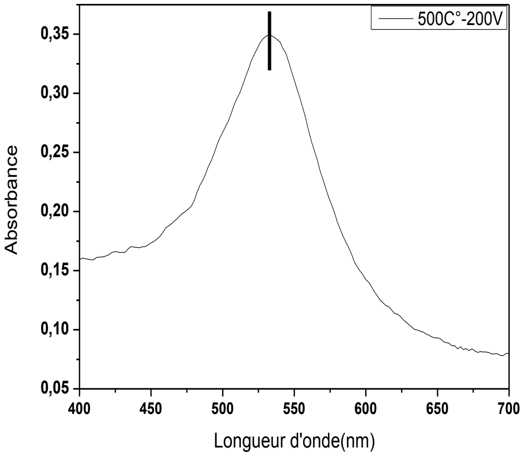

Figure 3: Absorbance spectrum measured through the laser exposed area. The band centered at 530 nm is due to the SPR of gold nanoparticles

The SEM analysis, displayed in fig. 4, clearly reveals the formation of gold nanoparticles of average diameter around 40 nm.

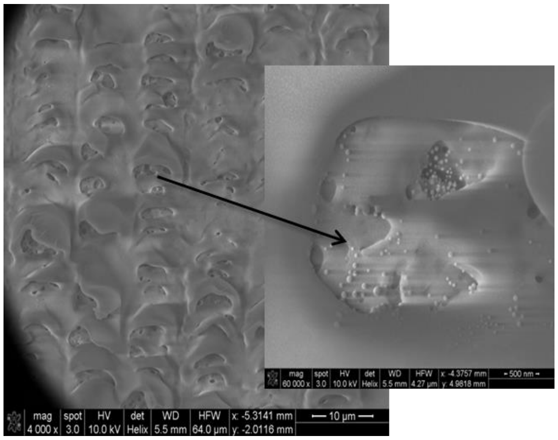

Figure 4: SEM image of the sample poled at 500C° and 200V and laser-exposed. Gold nanoparticles (∅ ~ 40 nm) can be clearly observed.

The mechanisms responsible for the formation of such nanoparticles will be discussed during the presentation, with a particular emphasis on the role of the laser-induced large temperature rise. We will also show that both silver and gold nanoparticles can be formed by laser exposure of a glass, firstly submitted to silver-sodium ion exchange and then to thermal poling.

4 CONCLUSION

We have demonstrated the efficiency of thermal poling and subsequent cw UV laser exposure to grow gold nanoparticles in a soda-lime glass. This technique opens up new perspectives for metallic composite glasses, which are up to now mainly restricted to silver doping.

5 REFERENCES

[1] M. Pelton, J. Aizpurua, and G. Bryant, “Metal-nanoparticle plasmonics,” *Laser Photonics Rev.*, vol. 2, no. 3, pp. 136–159, Jul. 2008.

[2] D. Chakravorty *et al.*, “Novel properties of glass–metal nanocomposites,” *J. Non-Cryst. Solids*, vol. 352, no. 6, pp. 601–609, May 2006.

[3] E. Cattaruzza, G. Battaglin, F. Gonella, S. Ali, C. Sada, and A. Quaranta, “Characterization of silicate glasses doped with gold by solid-state field-assisted ion exchange,” *Mater. Sci. Eng. B*, vol. 149, no. 2, pp. 195–199, Mar. 2008.

[4] J. Gu, W. Fan, A. Shimojima, et T. Okubo, « Microwave-induced synthesis of highly dispersed gold nanoparticles within the pore channels of mesoporous silica », *J. Solid State Chem.*, vol. 181, n° 4, p. 957‑963, avr. 2008.

Politecnico di Bari

UNIVERSITÀ DEGLI STUDI DI PALERMO
DiFC
DIPARTIMENTO DI FISICA E CHIMICA - DiFC

BARI – ITALY
11-13 JUNE
SiO2018

MONDAY

SESSION

FIBERS - SENSORS

UNIVERSITÉ JEAN MONNET
SAINT-ÉTIENNE

UNIVERSITÉ FRANCO ITALIENNE
UNIVERSITÀ ITALO FRANCESE

Anritsu
envision : ensure

ROHDE&SCHWARZ

DEI
DIPARTIMENTO DI
INGEGNERIA ELETTRICA
E DELL'INFORMAZIONE

Phosphosilicate Optical Fibers for Distributed Dose Measurement at CERN

D. Di Francesca[*], G. Li Vecchi[* **], S. Girard[**], Y. Kadi[*], M. Brugger[*]

[*]European Organization for Nuclear Research (CERN), CH-1211 Geneva 23, Switzerland
[**]Univ Lyon, Laboratoire Hubert Curien, UMR CNRS 5516, 42000 Saint-Etienne, France

ABSTRACT

Distributed Optical Fiber (OF) radiation sensing is a dosimetry technique recently developed and adopted at CERN for the monitoring of radiation dose levels in the accelerator complex. The system, called Distributed Optical Fiber Radiation Sensor (DOFRS), is composed of two basic parts: a set of suitably chosen radiation sensitive Optical Fibers (OFs) and an interrogator unit, which is usually an Optical Time Domain Reflectometer (OTDR). Currently, phosphorous-doped OFs are the best candidates for this type of application. The radiation dose measurement relies on the generation of the P1 defect under radiation, which absorbs light in the near infrared domain. To validate the use of the DOFRS in the accelerator tunnels, the radiation response of the OF sensors is tested and calibrated under ^{60}Co γ-rays and X-rays. Subsequently, the same sensors are qualified for employment in mixed field radiation field (typical of accelerator tunnels), at the CHARM facility at CERN. The first operational prototype of DOFRS was installed in the Proton Synchrotron Booster (157 m) in 2017. The same system was implemented in the Proton Synchrotron (628 m) at the beginning of 2018. Both DOFRS system are currently in operation and future deployment in the Super Proton Synchrotron (~7 km) and six regions of the Large Hadron Collider are foreseen during the Long Shutdown 2 (2019/20).

PACS Keywords: Radiation Induced Attenuation, P-doped Silica, Optical Fibers, Dosimetry.

1 INTRODUCTION

CERN (European Organization for Nuclear Research) accelerator complex is rich of electronic components that can be seriously damaged by cumulative radiation effects, such as Total Ionizing Dose (TID), Displacement Damages Dose (DDD) and by Single Event Effects (SEEs). These phenomena can significantly degrade the operability of LHC and the other accelerators by requiring unforeseen beam dumps and maintenance interventions [1,2]. Therefore, it is crucial to qualify the electronic components and system for operation in complex radiation environments, to monitor the radiation levels in the machine tunnels at critical equipment locations, and to put in place mitigation measures whenever possible. The sheer size of CERN accelerator complex requires to use mostly commercial-off-the-shelf (COTS) electronic components, and to develop affordable and performant radiation monitoring tools and, in view of the planned future machine upgrades, carry out detailed simulation studies of all critical areas. These activities are carried out at CERN in the framework of the R2E (Radiation to Electronics) project [3], which, in recent years, has developed and deployed a distributed dosimetry sensor based on radiation sensitive Optical Fibers (OFs) allowing to perform online and distributed dosimetry measurements [4]. The interest in this technological solution is not only due to the possible cost/performance advantages, but also to the technical benefits with respect to the point dosimetry systems currently employed at CERN [4]. The Distributed Optical Fiber Radiation Sensor (DOFRS) is well adapted to be employed in large facilities and especially in long accelerators, where the DOFRS can run parallel to the beam line to provide a linear map of the cumulated radiation dose with a spatial resolution of the order of 1 m.

2 THE OF SENSOR

The OF radiation sensor of choice is a P-doped Single Mode (SM) OF produced by iXBlue Photonics, very similar to the previously investigated sample reported in ref. 5. In the case of distributed OF dosimetry performed with an Optical Time Domain Reflectometer (OTDR) [4], using a P-doped SM OF has some clear implications. For example, the wavelength of interest for the highest radiation sensitivity is at ~1550 nm, a typical operating wavelength for commercially available interrogators. From literature, we know that the absorption band of the radiation induced P1 defects dominates the Near Infrared (NIR) domain and that P1 are thermally stable at room temperature [6]. A number of fundamental tests need to be carried out in order to fully characterize the radiation response of an OF and qualify it for radiation sensing and dosimetry. In detail, we carried out the following tests:

- assessed the RIA dose dependency;
- verifying the RIA dose rate independence;

- verifying the independence of the RIA from the irradiation temperature for room temperature up to 50 °C;
- verifying the absence of spontaneous recovery processes after irradiation;
- studying the radiation response to successive irradiations;
- verifying the absence of possible photo-bleaching effects induced by the ingected light for interrogation;
- qualifying the radiation response of the OF in the mixed field radiation environment by benchmarking with other dosimeters.

3 DISTRIBUTED DOSE MAP IN THE PSD

The first operational prototype was installed in the Proton Synchrotron Booster (PSB) tunnel during 2016/17 end of the year technical stop. The PSB has a total length of 157 m and is made of 16 almost identical periods (see Figure 1). The four superimposed synchrotron rings receive 50 MeV protons from LINAC2 and accelerate them up to 1.4 GeV before extraction. In Figure 1, we report a schematic representation of the OF cable path in the PSB, with the two fiber ends reaching the interrogator rack on ground level. The prototype of DOFSR installed in PSB acquired data during the whole operational year 2017. Some preliminary results (until about half of last year operations) were reported in ref. 4. As an example, in Figure 2, we show the cumulated radiation doses measured along the OF sensor at the end of the operations, about 250 days from the beginning of data acquisition. It is possible to distinguish two large regions where there are measurable radiation levels. The first one, between 70-110 m, corresponds to injection-extraction zone of the PSB. It concerns mainly periods 1, 14, 15 and 16. The second one, between 175 to 210 m, corresponds to periods from 8 to 11. The highest dose peak corresponds to the beginning of period 1, whereas we can link the first peak of area between 70-110 m with the end of period 14.

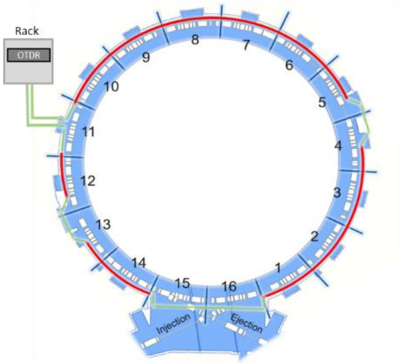

Figure 1: Schematic llayout of the PSB with the 16 periods in evidence. The red line shows the section of the machine where the OF cable lies on the cable tray at 1.5 m from the topmost synchrotron ring.

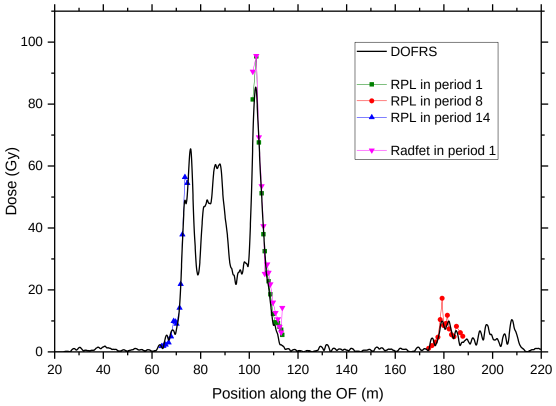

Figure 2: Cumulated radiation dose measured in the PSB at the end of 2017 operations, and comparison with other point sensors.

Unlike the injection/extraction zone, in periods 8, 9 and 10 the OF cable lies on the cable tray at fixed distance from the beamline. Here, the total radiation doses are clearly much lower. In the aim of benchmarking DOFRS measurements with other sensors, several passive Radio-PhotoLuminescent (RPL) dosimeters where attached to the OF sensor in period 1 and beginning of 2, 8 and 14, whereas some RadFETs (radiation-sensing p-channel MOS transistor) were attached only in period 1 and in beginning of period 2. As we can see in Figure 2, the DOFRS radiation map is in good agreement with the passive dosimeters that were exposed to the same radiation field in 2017.

4 CONCLUSION

Nowadays, phosphosilicate OFs are successfully employed to perform online and distributed radiation dose monitoring in two circular accelerators of the LHC injector chain. This technology relies on the radiation induced P1 defect, which is thermally stable and absorbs light in the NIR domain at typical wavelength of OTDR. On the basis of the results obtained in the last two years, the DOFRS should be installed in the SPS and parts of LHC during the Long Shutdown 2 (2019/20).

REFERENCES

[1] A. Apollonio *et al.*, Proc. Int. Particle Accel. Conf. (IPAC), Copenhagen, Denmark, May 2017, pp. 2039–2042, paper TUPVA006.
[2] R. Garcia Alia *et al*., IEEE Trans. Nucl. Scie., vol. 65, no. 1, pp. 448–456, 2018.
[3] M. Brugger, *CERN Yellow Reports*, vol. 2, no. 00, p. 149, 2016.
[4] D. Di Francesca *et al.*, accepted in *IEEE Trans. Nucl. Scie., 2017*. DOI: 10.1109/TNS.2018.2818760
[5] D. Di Francesca *et al.*, *IEEE Trans. Nucl. Scie.*, vol. 64, no. 1, pp. 54-60, Jan. 2017.
[6] D. L. Griscom *et al.*, J. Appl. Phys., vol. 54, no. 7, pp. 3743–3762, 1983.

Low Dose and Low Dose rate measurements of X-rays using Copper-doped Sol-gel Silica Glass

N. Al Helou*, H. El Hamzaoui*, B. Capoen*, G. Bouwmans*, A. Cassez*, Y. Ouerdane**, A. Boukenter**,
S. Girard** and M. Bouazaoui*

* Univ-Lille, CNRS, UMR8523-PhLAM-Physique des Lasers Atomes et Molécules, CERLA/IRCICA,
F-59000 Lille, France
** Laboratoire Hubert Curien, Univ Lyon,
UMR-CNRS 5516, F-42000 Saint-Etienne

ABSTRACT

We report on the low-dose and low dose rate responses of a copper-doped sol-gel silica glass rod, spliced to a fiber-optic, under X-ray irradiation. Both Radioluminescence (RL) and Optically Stimulated Luminescence (OSL) were investigated.

Keywords: Radioluminescence, optically stimulated luminescence, dosimetry, copper, sol-gel silica glass.

1 INTRODUCTION

The use of activated glasses as RL and OSL dosimeter materials is of significant importance and has been investigated in numerous studies [1, 2]. These radiation dosimeters reveal certain characteristic features such as linear dose response and good reproducibility. In principle, these sensors are suitable for environmental measurement requiring monitoring over a long distance, such as in nuclear power plants to control nuclear activities, for protection of workers, in recycling and dismantling operations, in long-term nuclear storage and industrial process controls. They can be also employed for real-time in vivo dosimetry during radiotherapy, thus providing a true and direct feedback dose assessment during clinical radiotherapy. Cu^+-doped glasses are attractive scintillating materials due to their luminescent properties under ultraviolet and X-ray excitation. Consequently, the responses of these materials under low irradiation doses and low dose rates have been investigated. In particular, the studies on an optical fiber radiation dosimeter based on Cu^+-doped fused quartz have shown a linear OSL response between 0.01 Gy and 10 Gy [1].

In this study, the potentiality of a dosimeter system, built with a Cu^+-doped silica glass, to measure low doses and dose rates has been assessed for nuclear domain, where valuable information for low dose areas is imposed. In a previous work, a similar study has been carried out with this kind of Cu-doped silica glass under X-ray beam for high dose rates and high doses measurements [2].

2 EXPERIMENTAL METHODS

A sample of copper-doped glassy rod was synthetized by the sol-gel technique as described elsewhere [3]. The doped glass was drawn down to a millimeter-sized cane and a small portion was fusion-spliced, at its two ends, to a 5 m silica fiber. Figure 1 shows the experimental setup used to characterize the OSL response of the fiber material under X-ray beam. RL measurements were performed using the same setup, except that the spectral filter was removed and the laser diode was switched-off.

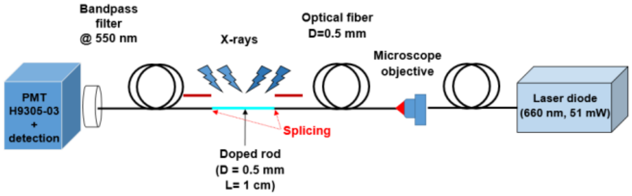

Figure 1: Scheme of the dosimeter system used in RL and OSL measurements.

3 RESULTS

3.1 Radioluminescence measurements

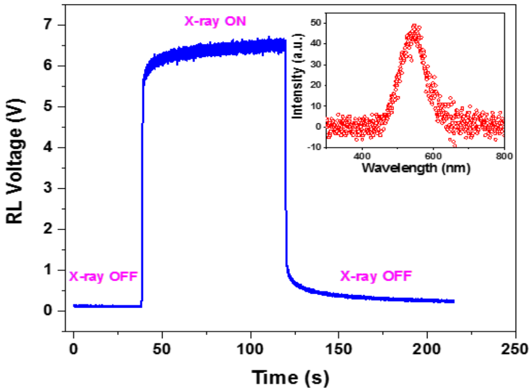

Figure 2: RL response of a Cu^+-doped rod spliced to a fiber under 18 mGy/s X-ray dose rate. The inset shows the RL spectrum under the same dose rate.

Figure 2 shows RL signal versus time at 18 mGy/s. As the X irradiation starts, the RL signal first increases for a few seconds to finally tend toward a plateau. In the inset of Fig. 2, the RL spectrum, taken under the same dose rate, presents a large band centered on 540 nm and attributed to the emission of the Cu^+ doping ions [2].

Figure 3 shows the RL maximum signal of this Cu-doped glass versus dose rate. The presented data are taken on the plateau after a background subtraction. The behavior is obviously linear from 0.256 up to 23.04 mGy/s in silica.

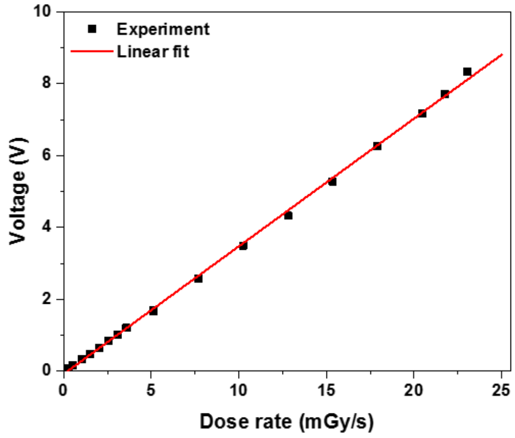

Figure 3: RL response of a Cu^+-doped rod spliced to a fiber as a function of X-ray dose rate.

3.2 Optically stimulated luminescence measurements

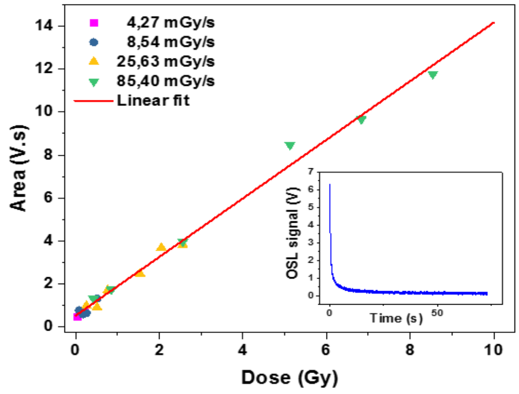

Figure 4: Dose response of a Cu^+-doped rod spliced to a fiber under different X-ray dose rate. Each point presents the integration of the OSL response presented in the inset.

Figure 4 shows the OSL results, defined as the integral over the whole decay time interval until the stabilization of the signal (See inset of Fig. 4). The noise background and the offset due to the residual stimulating laser signal have been subtracted before integration. The copper-doped rod exhibits a linear OSL response from 42 mGy to 12.81 Gy in silica.

3.3 Fading of the OSL signal

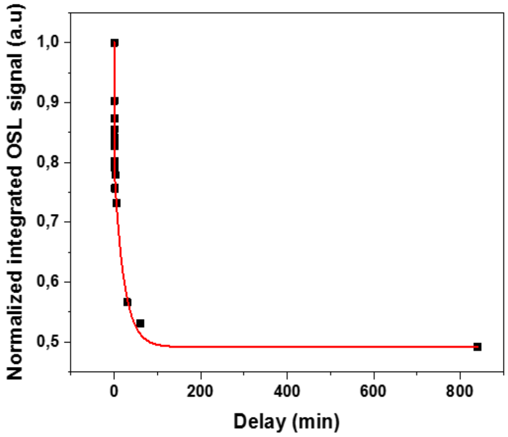

Figure 5: Fading behavior of the integrated OSL signal for an accumulated dose of 17 Gy at a dose rate of 170 mGy/s. The red line is a guide to the eye.

The stability of the measured OSL signal with time, in both short-time and intermediate time scales, has been also studied. Figure 5 presents an example of this fading phenomenon of the OSL signal for an accumulated dose of 17 Gy. The data are normalized to the response, obtained directly after the end of exposure to radiation, at ambient temperature, the sample being kept in the dark. Due to thermal fading, a signal loss of about 50 % of the OSL integrated intensity occurs in 1 hour approximately. After that time, the signal remains stable, which means that the spontaneous depopulation of the trapped levels seems to be completed.

ACKNOWLEDGMENTS

Work performed within the Investments for the future program of the French Government and operated by the French National Radioactive Waste Management Agency (Andra). It was also partially supported by the ANR: LABEX CEMPI (ANR-11-LABX-0007) and the Equipex Flux (ANR-11-EQPX-0017), by The Ministry of Higher Education and Research, the Hauts-de-France Regional Council and the European Regional Development Fund (ERDF) through the Contrat de Projets Etat-Region (CPER Photonics for Society P4S).

REFERENCES

[1] A. Huston, B. Justus, P. Falkenstein, R. Miller, H. Ning, R. Altemus, *Radiat. Prot. Dosim.* vol. 101, no. 1-4, pp. 23–26, 2002.

[2] B. Capoen, H. El Hamzaoui, M. Bouazaoui, Y. Ouerdane, A. Boukenter, S. Girard, C. Marcandella, O. Duhamel, *Opt. Mater.*, vol. 51, pp. 104-109, 2016.

[3] H. El Hamzaoui, G. Bouwmans, B. Capoen, Y. Ouerdane, G. Chadeyron, R. Mahiou, S. Girard, A. Boukenter, M. Bouazaoui, *Mater. Res. Exp.*, vol. 1, no. 2, 026203, 2014.

Investigation by TSL of the properties of some potential fibred-OSL dosimeters

Mourad Benabdesselam*, Franck Mady*, Angela Guttilla*
Hicham El Hamzaoui**, Mohamed Bouazaoui**, Nissrine Al Helou**, Jessica Bahout**, Géraud Bouwmans** and Bruno Capoen**

- Université Côte d'Azur, Institut de Physique de Nice - INPHYNI UMR7010
Parc Valrose, 06108 Nice Cedex 2, France
**Physique des Lasers, Atomes et Molécules - PhLAM UMR8523, Université Lille, F-59000 Lille, France

ABSTRACT

The luminescence properties of some doped materials are explored in many fields of application, including that of ionizing radiation. These luminescence properties are essentially provided by the doping element. In this paper we report some TSL measurements of the trapping and recombination centers involved in the OSL process in sol-gel-derived glasses. Two doped species will be concerned: one transition element (Cu) and one rare earth (Ce) in the sol-gel silica matrix. TSL sensitivity, dose-response, thermal quenching and fading will then be confronted with those of the OSL features of a dosimeter made with the glasses mentioned above.

PACS Keywords: silica, TSL, OSL, doping, radiations

1 INTRODUCTION

Over the last decades, the use of OSL (optically stimulated luminescence)-based dosimeters has proved to be more attractive compared to long-standing solutions based on the principle of TSL (thermally stimulated luminescence) or dosimetric films.

Indeed, OSL dosimetry (OSLD), in particular fibered, has a major advantage since it does not require a thermal energy input of up to a few hundred degrees, which already excludes the implementation of fibred-TSLD solutions. However, there is a direct correlation between the underlying physics of TSL and OSL processes since these two phenomena are inextricably linked. This correlation can assist in determining the presence and influence of shallow traps, identification of optically active or inactive traps, the presence of more than one trap contributing to the OSL signal, and the influence of deep traps.

For this reason, many of the published works about TSL not only guide the search for OSL materials, but they also contribute to their identification. In other words, TSL experiments can provide useful insight into the OSL process. Indeed, almost all the TSL phosphors provide a more or less intense OSL signal and the most iconic of these phosphors is the anion deficient alumina [**1**]. The objective of SURFIN (nouveaux matériaux pour la SURveillance par Fibre optique des Installations Nucléaires) project is to develop new optical materials (glass or fiber) that have been appropriately doped and that are sensitive to the radiation emitted in nuclear power plants being dismantled or on radioactive waste storage sites. This sensitivity is evaluated by both RL (radioluminescence) for dose rate and OSL for dose. TSL investigations will help us in the choice of the solution to be retained for the needs of the project.

2 SAMPLES - EXPERIMENTAL SET UP

Three colorless and transparent doped samples named A, B and C were silica glasses drawn into rods. They all appeared to possess the same optical quality as the undoped specimen. Pure silica xerogels were first stabilized at 1000°C before doping them by impregnation technique and densifying them under He. A piece of each rod was then cut and ground. The amount of obtained powder (#5mg) was then spread on an aluminum cupel for TSL studies. Sample A is Cu-doped, sample B is Ce-doped and sample C is Cu/Ce-codoped, all with contents of about 200 at-ppm.

X-ray irradiations have been performed at room temperature (RT) in air. The tube is a Cu target (30 kV), whose beam is calibrated using an ionization chamber.

The TSL signal was recorded at a linear heating rate of 1 K/s between RT and 773 K by means of a photomultiplier tube (PMT), 2 minutes after the end of irradiation. Spectral distribution of TSL was detected by a spectrograph.

Thermal and optical fading behaviors were studied by storing the previously irradiated samples respectively in the dark and under fluorescent laboratory light.

3 TSL RESULTS

The TSL curve relative to sample A is presented in Figure 1. It is characterized by a main peak at 360 K, which is an overlap of several traps and a less intense one at around 580 K. At the beginning of readout, a significant

part of signal (strong phosphorescence) is due to the release of carriers from shallower traps. These latter and those forming the glow peak 1 can influence the OSL response of the sample at RT.
Initial Rise (IR) method applied to the irradiated sample reveals that the activation energies of the trapping levels corresponding to the set of peaks at 360 K and 580 K are respectively 0,95 and 1,35 eV. These values have been confirmed theoretically by the calculation of DOTS (Density Of Trapping States) [**2**]. The origin of these traps remains unknown even though we also know that the set consisting of shallow traps (phosphorescence) and peak 1 are likely inherent to defects in the silica matrix and that the deepest ones might be induced by the dopant.

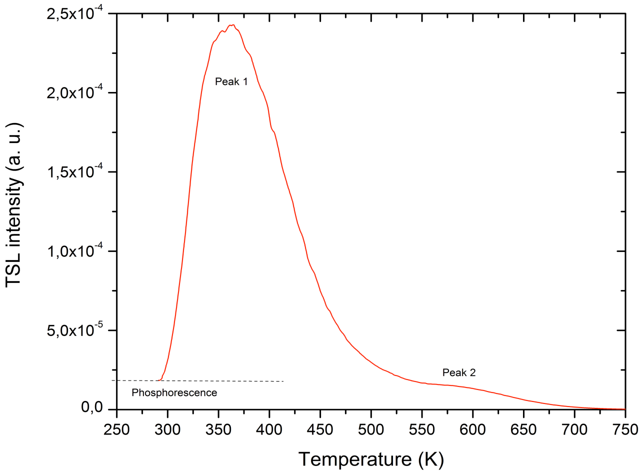

Figure 1: TSL of sample A after X-ray irradiation @ RT

Spectral analysis of TSL shows a single distribution of Cu^+ luminescence centered at 550 nm (Γ=88 nm) all over the temperature range. This emission has already been assigned to the $3d^{10}$-$3d^{9}4s$ transition **[3].** It means that the Cu^+ ions serve as the recombination center for released electrons during readout. These electrons are trapped in two main trapping sites located at around 0,95 and 1,35 eV below the conduction band of the material.

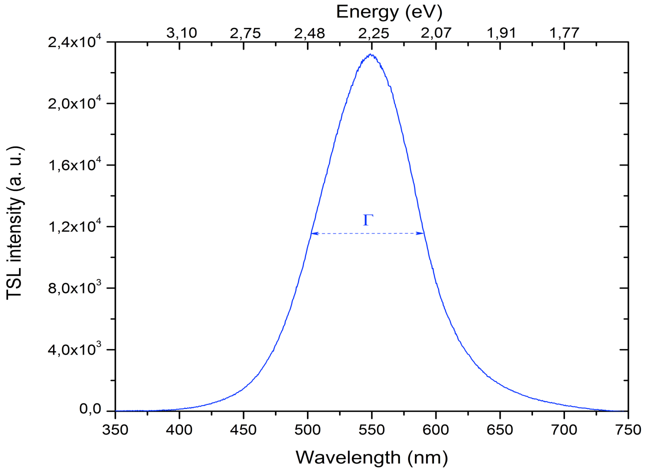

Figure 2: TSL spectral analysis of sample A

Figure 3 represents the amounts of the remaining signal for the two sets of peaks as a function of bleaching with various periods of exposition to ambient light. It shows that the trapping centers responsible for the phosphorescence and the main structure between 300 and 500 K are the most affected by optical stimulation, and are likely the ones mostly contributing to the OSL response. The component named Peak 2 (between 500 and 700 K) also contributes to the OSL sensitivity but more modestly.

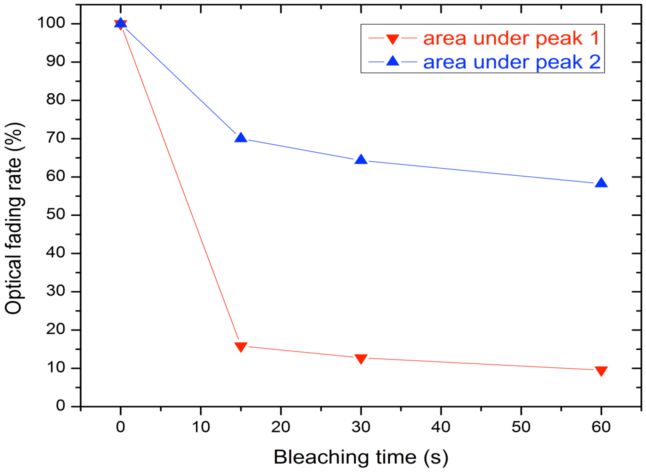

Figure 3: Fading rate for different periods of time bleaching

4 CONCLUSION

By the day of the presentation, we will confirm by OSL measurements if, as the results of TSL seem to indicate, it is the low temperature part (between 300 and 500 K) of the trap distribution that releases electrons and contributes the most to the OSL process whereas the higher temperature traps contribute only moderately to the OSL sensitivity.

Both TSL and OSL results on the two other samples will be presented. They will be compared all together and then, the best solution for OSLD will be proposed.

In addition to the OSLD at RT and in order to take into account the severe operating conditions, TSL investigations on thermal quenching of luminescence are in progress.

REFERENCES

[1] B.G. Markey, L.E. Colyott and S.W.S. McKeever, Radiat. Meas. 24, 457-463, 1995.
[2] F. Mady et al., 12th International Symposium on SiO2, advanced dielectrics and related materials, 11-13th June, Bari, Italy.
[3] B.L. Justus, K.J. Pawlovich, C.D. Merritt and A.L. Huston, Radiat. Prot. Dosim., 8, N°. 1, 5-10, 1999.

ACKNOWLEDGEMENT

This work was carried out within the framework of the SURFIN project, an operation carried out with the assistance of “Programme d’Investissements d’Avenir” (PIA) of the French Government managed by Andra.

Temperature Dependence of Faraday Effect of Germano-silicate Glass Optical Fiber Doped with CdSe and CdMnTe particles

Seongmin Ju[*], Jihoon Kim[*], Yuseung Lee[*], Yong-Tak Ryu[*], Seong Gu Kang[*], Bok Hyeon Kim[**],
Youjin Lee[***], Yong Ho An[***], and Won-Taek Han[*]

[*]School of Electrical Engineering and Computer Science/[**]Advanced Photonics Research Institute,
Gwangju Institute of Science and Technology, 123 Cheomdangwagi-ro, Buk-gu, Gwangju, South Korea
[***]Power System Laboratory, Korea Electric Power Corporation Research Institute,
105 Munji-ro, Yuseong-gu, Daejeon, South Korea

ABSTRACT

We investigated the temperature dependence of Faraday effect of the germano-silicate glass optical fibers doped with CdSe and CdMnTe particles. The Faraday rotation angle measured at 0.142 Tesla upon temperature change from 25 °C to 120 °C of the CdSe and CdMnTe doped fibers were 1.64×10^{-3} degree/°C and -10.49×10^{-3} degree/°C, respectively.

PACS Keywords: Faraday effect; semiconductor particles; optical fiber; magnetic field sensor; temperature dependence.

1 INTRODUCTION

Optical glasses incorporated with binary (e.g., ZnSe, ZnS, CdSe, CdS, ZnTe) and ternary (e.g., CdMnTe, CdZnTe, ZnSSe) semiconductor particles have attracted attention for magneto-optic device applications such as Faraday rotators, optical isolators, optical current sensors, and microwave filters, etc [1]. Especially, optical fibers incorporated with these materials, which are paramagnetic near room temperature, exhibit strong magneto-optic properties. The fiber doped with CdSe particles exhibit giant Faraday rotation upon applying a magnetic field due to yield information on the nature of electronic transitions at the band edge, and on effective masses and g-factors [2]. This can be understood from the information that can be used to explain the electronic states and the effective masses and to understand the theory of matter can be extracted by studying the Faraday effect in semiconductor [1,3]. Earlier the magneto-optic properties of glass doped with binary semiconductor particles have already been extensively studied [1,3-6]. In the case of optical fiber doped with CdMnTe particles, the giant Faraday rotation in the magnetic field come from the Mn^{2+} ion magnetization. The strong spin-spin exchange interaction occurring between the d electrons of the Mn^{2+} ions and the s-like conduction band and p-like valence band electrons affects all physical phenomena that depend on the Zeeman splitting of the band sublevels. This spin-spin exchange interaction leads to the giant Faraday rotation observed at photon energies E near the band-gap resonance [7]. However, the temperature dependence of the Verdet constant of these fibers incorporated with paramagnetic materials depends on the wavelength as well as the composition [8]. Due to the disadvantage of having large temperature sensitivity, a temperature compensation technique is essential for use as a magnetic field sensor.

In this paper, the temperature dependence of Faraday rotation angle (FRA) of the germano-silicate glass optical fibers doped with CdSe and CdMnTe particles was investigated.

2 EXPERIMENTS

The germano-silicate glass optical fiber preforms incorporated with semiconductor particles such as CdSe and CdMnTe in core region were fabricated by the modified chemical vapor deposition (MCVD) process with the solution doping process. A toluene containing CdSe QDs (Sigma-Aldrich: Lumidot CdSe QDs in toluene, peak absorption ~ 650 nm, 7.5 mg in 1.5 ml solution) and a nitric acid solution dissolved with $Cd_{0.5}Mn_{0.5}Te$ powder (Particles size: 0.6 ~ 2.2 μm, International Crystal Lab.) were prepared for solution doping. The porous deposition layers inside the silica glass tube in the form of soot at 1400 °C were soaked with the doping solutions for 1 hour to incorporate CdSe and CdMnTe particles, respectively [9-10]. After draining the solution, the soaked porous layers were dried by flowing Cl_2 and He gases in the tube. Then the tube was sintered at over 2000 °C with chlorine gas that was used as a carrier gas for prevention of the optical absorption by O-H ions. And the tube was collapsed with helium and chlorine gas,and finally sealed to be a fiber preform. Finally, the preform was drawn into fibers with outer diameter of 125 μm at 2150 °C by using the draw tower. The core diameter and the cut-off wavelength of the

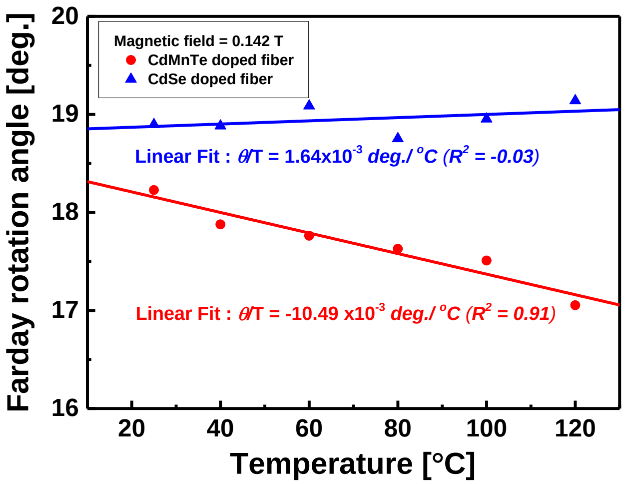

Figure 1: Comparison of the FRA measured at 0.142 Tesla of the CdSe and CdMnTe doped fibers with temperature.

fabricated CdSe and CdMnTe doped fibers were 5.4 µm and 560 nm, and 6.8 µm and 550 nm, respectively.

3 RESULTS AND DISCUSSION

FRA of the fabricated optical fibers of 70 cm length each was measured under magnetic field generated by a direct current (DC) solenoid with inner diameter of 76 mm (Walker scientific INC.) by using a signal light at 650 nm from a superluminescent diode (SLD, power = 1 mW) and a polarimeter (Thorlabs PA510) and recorded in a Poincare sphere. To investigate temperature dependence of FRA, temperature variation was given by the glass tube heater from 25 °C to 120 °C with a precision of 0.2 °C and the fiber was aligned straight inside the glass tube heater under the magnetic field. FRA was measured at 0.142 Tesla (T) under various temperatures from 25 °C to 120 °C. Fig. 1 compares the measured FRAs at 0.142 T of the CdSe and CdMnTe doped fibers with temperature. The change in FRAs of the CdSe and CdMnTe doped fibers from 25 °C to 120 °C were 0.24 degree and 1.18 degree, respectively, indicating that the temperature dependence of the FRA, which is the slope of the line (θ/T), of the CdSe doped fiber (1.64 x 10^{-3} degree/°C) was 6.4 times smaller than that of the CdMnTe doped fiber (-10.49 x 10^{-3} degree/°C). The large temperature dependence of the CdMnTe doped optical fiber compared to the CdSe doped fiber is due to the paramagnetism of the spin-5/2 Mn^{2+} ions, which is temperature dependent [11]. Such temperature insensitive FRA of the CdSe doped fiber would be very useful for magneto-optic devices application. The estimated Verdet constant from the measured FRAs of the optical fibers doped with CdSe or CdMnTe particles at 25 °C ~ 120 °C were 3.34 ± 0.05 rad/T·m or 3.10 ± 0.10 rad/T·m, respectively.

4 CONCLUSIONS

The germano-silicate glass optical fibers incorporated with CdSe and CdMnTe particles for magneto-optic application were fabricated by the MCVD and fiber drawing process. The temperature dependence of Faraday effect of the fibers were investigated from 25 °C to 120 °C. The measured Faraday rotation angle at 0.142 Tesla upon temperature change from 25 °C to 120 °C of the CdSe and CdMnTe doped fibers were 1.64 x 10^{-3} degree/°C and -10.49 x 10^{-3} degree/°C, respectively.

The temperature dependence of the FRA (θ/T) of the CdSe doped fiber (1.64 x 10^{-3} degree/°C) was 6.4 times smaller than that of the CdMnTe doped fiber (-10.49 x 10^{-3} degree/°C). The large temperature dependence of the CdMnTe doped optical fiber compared to the CdSe doped fiber is due to the temperature dependent paramagnetism of the spin-5/2 Mn^{2+} ions. The estimated Verdet constant of the optical fibers doped with CdSe or CdMnTe particles at 25 °C ~ 120 °C were 3.34 ± 0.05 rad/T·m or 3.10 ± 0.10 rad/T·m, respectively.

REFERENCES

[1] P. R. Watekar et al., J. Korean Phys. Soc., 55, 1158-1161, 2009.
[2] M. Balkanski et al., J. Phys. Chem. Solids, 27, 299-308, 1966.
[3] J. H. Kratzer et al., J. Non-Cryst. Solids, 349, 299-308, 2004.
[4] H. S. Bennett et al., Phy. Rev., 137, A448-A461, 1965.
[5] K. Suzuki et al., J. Phys. Chem. Solids, 30, 749-761, 1969.
[6] P. R. Watekar et al., Opt. Express, 17, 3157-3164, 2009.
[7] S. Hugonnard-Bruyère et al., Phys. Review B, 50, 2200-2207, 1994.
[8] M. J. Weber, CRC Handbook of Laser Science and Technology. Supplement 2: Optical Materials. CRC Press, Boca Raton, 372-382, 1995.
[9] P. R. Watekar et al., Phys. Scr., 2010, 014054(1-3), 2010.
[10] M. Jang et al., in Proceedings of Photonics Conference, W2E-IV3, 90-91, 2013.
[11] W. D. Rice et al., Nano Letters, 17, 3068-3075, 2017.

Combined planar-fiber surface plasmon resonance sensor

Tomyshev K.A.[*,**], Tazhetdinova D.K.[*,**], Butov O.V. [*,**]

[*] Kotel'nikov Institute of Radioengineering and Electronics of RAS,
Mokhovaya 11-7, Moscow 125009, Russia
[**]N.M. Emanuel' Institute of Biochemical Physics of RAS
Kosigyna 4, Moscow, 119334, Russia

ABSTRACT

The development and testing results of a new hybrid fiber-planar plasmon sensor design based on tilted fiber Bragg grating (TFBG) are presented. The presented experimental data demonstrate the advantages of such an approach over classical fiber sensor while retaining all its features.

PACS Keywords: surface plasmon resonance, plasmon sensors, tilted fiber Bragg gratings.

1 INTRODUCTION

Surface plasmon resonance (SPR) sensors are an actual trend in modern sensorics and are already actively used as biosensors for immune analysis. Some obvious advantages of fiber sensors are their compactness and convenience of usage. One of the promising designs of a plasmon fiber sensor is a sensor based on a tilted fiber Bragg grating [1]. It has potentially high measurement accuracy. However, in practice it is difficult to reach the high indication stability of such sensors. The main causes for this are propagating light polarization instability and mechanical deformations of the optical fiber during the measurement. Though the first problem was solved using polarization-maintaining fiber [2], the second one remains unresolved until now. A simple two-point sensor mounting does not work well enough, because that makes the sensor a stretched string, sensitive both to the flow velocity of the liquid and to external acoustic and mechanical influences. A single-point sensor mounting does not provide its rigid fixation, which further leads to deformation of the sensor in the flow, and, hence a disruption of its reading stability. In this paper, we propose a possible solution, which allows combining the advantages of stable planar sensors and fiber technologies.

2 EXPERIMENT

2.1 Sample Production

As a basis for the fiber part of the sensor design, we used a well-known technology for obtaining surface plasmon resonance in optical fibers based on a tilted fiber Bragg grating [1]. In our experiments, the Bragg grating was inscribed in a hydrogen-loaded Corning SMF-28 fiber with a tilt angle of 11^0 by means of an ArF-excimer laser radiation and a phase mask [1]. After that, a gold coating with a thickness of the order of 40 nm is deposited on the fiber grating lateral surface by a vacuum evaporation method [2,3].

Separately from the fiber element, a fluid chip was created to conduct experiments in the flow of the liquid under study. The chip represents two parts - a flat base of polycarbonate and a polycarbonate cover, in which the structure of fluid channels is created. On the outer surface of the chip cover, there are also connectors for the input and output of the investigated liquid.

Obviously, TFBG inscribing violates the cylindrical symmetry of the fiber system, thereby making the sensor a flat-symmetrical element. During the grating inscription process, we made special marks, which make it possible to detect the plane of the grating inscription. After the deposition of the gold coating, the fiber sensing element was installed into the base of the fluid chip so that the plane of the base coincided with the plane of the grating. A narrow groove with a depth of about 30 μm was created in advance to provide precise positioning. The profile of the groove completely repeated the longitudinal profile of the fiber sensor (Fig. 1). After fiber sensing element installation into the chip structure, two parts of the chip are glued together and sealed. The liquid is pumped through the system with a syringe pump driven by a stepping motor. Similar system can be used for immune analysis in a small volume of liquids.

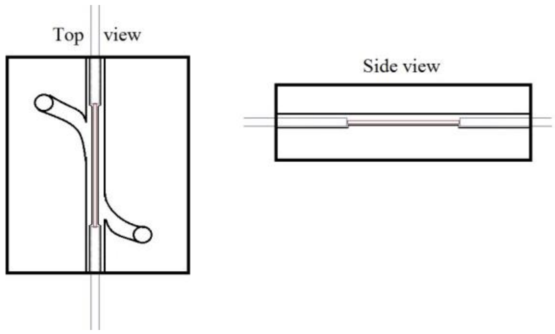

Figure 1: Fluid chip with fiber sensor.

2.2 Experimental Setup

The experimental setup is shown in Fig.2. The sensor (5) is connected via a fiber interface to the two inputs of the multichannel interrogator Micron Optics SM125 (1) with a scan range of 1510-1590 nm. Usually such interrogator is used as a spectrometer of the reflected signal. A feature of this type of interrogator is spectral scanning on all channels simultaneously. This allowed us to use one of the two channels as a scanner of the transmission spectrum of the sensor. For this purpose, an optical isolator (2) is built in the circuit, which blocks the reflected signal readout through channel 2.

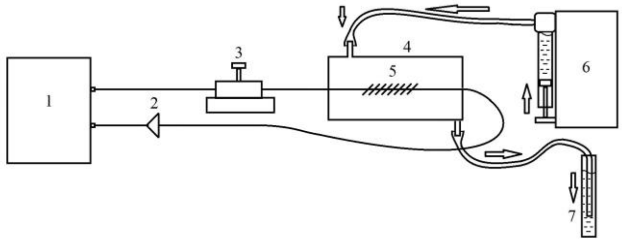

Figure 2: Experimental setup.

As is known, only one of the two orthogonal linear polarizations is suitable for excitation of surface plasmon resonance in a sensor based on TFBG. To adjust the necessary polarization, a mechanical polarization controller (3) is installed directly near the fluid chip (4).

The chip (4) itself is connected to a syringe pump (6). For our experiment, distilled water was used as a test liquid. The water that has passed through the chip is drained into a separate receiving tank (7).

3 RESULTS AND DISCUSSION

The experiments showed that in a similar fiber-planar structure it is possible to obtain a sufficient contrast of the plasmon resonance spectrum (Fig. 3) the wavelength of which is determined by means of a specially developed program.

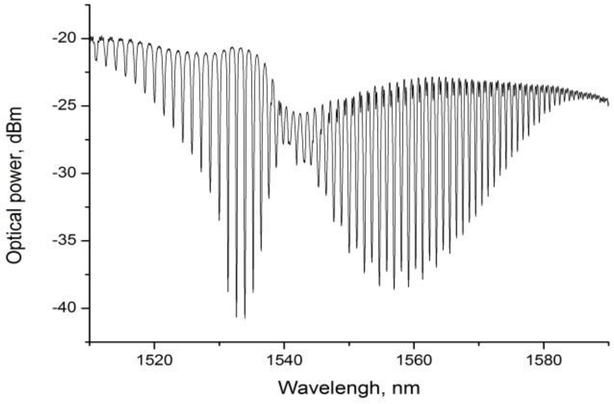

Figure 3: SPR on the transmission spectrum of the combined sensor.

In Fig.4. comparative data for the fiber sensor and the combined one is presented, showing the change in SPR spectral position in the liquid flow during time. As can be seen from the graph, the combined sensor demonstrates a more stable signal in time under the same conditions, which is a consequence of the rigid coupling of the fiber sensing element to the polycarbonate base.

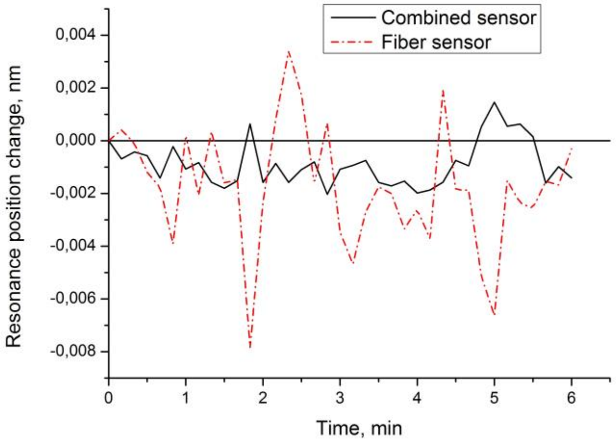

Figure 4: Change in the spectral position of SPR of the combined and standard fiber sensor in the flow of distillate.

4 CONCLUSION

In our work the construction of a combined fiber-planar sensor based on a tilted Bragg grating is proposed. Comparative experiments have shown that such combined sensor is more stable than the fiber one.

ACKNOWLEDGMENTS

The work was supported by the Advanced Research Foundation.

REFERENCES

[1] Jacques Albert, Sandrine Lepinay, Christophe Caucheteur, Maria C. DeRosa, “High resolution grating-assisted surface plasmon resonance fiber optic aptasensor”, Methods 63, 239–254, 2013

[2] Kirill A. Tomyshev, Yuriy K. Chamorovskiy, Vasily E. Ustimchik, Oleg V. Butov, "Polarization stable plasmonic sensor based on tilted fiber Bragg grating", Proc. SPIE 10323, 25th International Conference on Optical Fiber Sensors, 2017

[3] Butov O.V., Golant K.M., Tomyshev K.A. “Recoating of Fiber Bragg Gratings with metals”, 11-th International Symposium on SiO2, Advanced Dielectrics and Related Devices, 2016

MONDAY

SESSION

DEFECTS – MODELING I

Color centers in P-doped silica: generation, conversion mechanisms, and optical properties

Luigi Giacomazzi(1,2), L. Martin-Samos(3), S. De Gironcoli(2), M. Valant(1), and N. Richard(4)

(1) Materials Research Laboratory, University of Nova Gorica
Vipavska 11c, 5270 Ajdovščina, Slovenia
(2)SISSA via Bonomea 265, IT-34136 Trieste (Italy).
(3) CNR-IOM National Simulation Center
c/o SISSA via Bonomea 265, IT-34136 Trieste (Italy).
(4)CEA, DAM, DIF, F-91297 Arpajon (France)

ABSTRACT

In the present work we provide a state-of-the-art first-principles modelling of color centers in P-doped silica mainly based on optical absorption and electron paramagnetic resonance calculations. We provide several insights useful to understand the optical absorption spectra of P-doped silica up to ~7 eV, in particular, the twofold coordinated P is shown to contribute to the optical absorption in the range ~2.5-7 eV. Also, the occurrence of a double phosphorus center $\geq$P-O-P$^+\leq$ is proposed which could allow a ``on site'' interconversion of P_2 centers in to P_1 centers.

PACS Keywords: silica, P-doping, P-centers, P_2O_5, BSE

1 INTRODUCTION

Phosphorus-doped silica is a material of paramount importance in microelectronics, optoelectronics and in fiber optics technology. P-doped fibers not only are employed for the production of fiber amplifiers together with rare-earth elements but are among the best candidate for the development of radiation detectors and dosimeters [1]. Several types of P-centers can be induced under irradiation giving rise to signal attenuation in the visible and infrared part of the spectrum. Although some of these centers (P_1,P_2,POHC,P_4) have been intensively studied using experimental characterization methods such as Electron Paramagnetic Resonance (EPR) and Optical Absorption (OA) spectroscopies, only a few investigations have been dedicated to the study of the diamagnetic defects which are the precursors of the above mentioned ones, and very little is known about the generation and conversion mechanisms among all these centers. A few experimental investigations [2,3,4] show that, under excimer laser irradiation and also by *x*-ray irradiation, the dominant process is the formation of a pair of a phosphorus electron center (an electron trapped at a four-fold coordinated P-atom i.e. a P_2), and a POHC center, suggesting that the following pair generation mechanism may occur:

$$PO_4^+ + [(O-)_3P=O]^0 \rightarrow P_2 + POHC \qquad (1)$$

Furthermore the results of several experimental investigations support the conversion of P_2 (and sometimes also of POHC) to P_1 centers [2]. However a detailed model explanation of the mechanisms lying behind these observations is still lacking. The scope of the present paper is to provide an overview of the state-of-the-art first-principles modelling (OA and EPR) of the above mentioned P-centers, and moreover to discuss of the possible atomic-scale mechanisms behind P-centers generation (under irradiation) and interconversion.

The calculations carried out in this work are based on density functional theory (DFT). In particular, the PBE exchange-correlation functional has been adopted [5]. Norm-conserving Trouiller-Martins pseudopotentials are used and Kohn-Sham wavefunctions are expanded in a basis of plane waves up to a kinetic cutoff of 70 Ry. The codes used for the present structural, nudged elastic band (NEB), and EPR calculations are freely available with the Quantum-Espresso package [6]. Calculations of the quasi-particle energies and of optical absorption spectra have been performed by employing many-body perturbation theory techniques as implemented in the SaX package [7,8]: a Bethe-Salpeter equation (BSE) is solved to obtain the optical excitation energies of singlet excitations. The defect configurations here analyzed have been obtained by using a 108 atoms vitreous silica model previously generated at a density of 2.2 g/cm^3 [9].

2 RESULTS

2.1 Optical absorption calculations

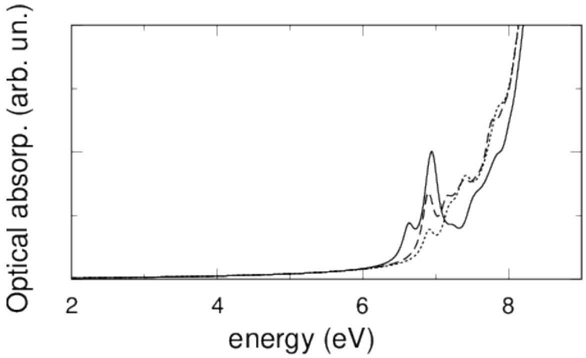

Figure 1: OA spectra of silica models with one, two, four $[(O\text{-})_3P{=}O]^0$ units [8].

In Ref. [8] we presented a study of the optical absorption spectrum of P-related defects in silica. In particular, we have shown that the optical absorption band located at 6.9 eV [Fig. 1] in the absorption spectrum of (non-irradiated) P-doped silica originates from the presence of $[(O\text{-})_3P{=}O]^0$ tetrahedra. In the present work, we extend the investigations of [8] to the diamagnetic twofold-coordinated P atoms (i.e. the precursors of the P_4 centers [2,3]) which are still matter of debate [10]. According to the trapping energies calculations of [11], the most likely precursor of a P_4 center consists of a two-coordinated P atom with two non-bonding orbitals both doubly occupied: a $[(O\text{-})_2P]^-$ center. By contrast the alternative $[(O\text{-})_2P]^+$ is regarded as less likely to occur [11]. The latter center would be the isoelectronic analogue of the twofold Si defect [i.e. the ODC(II)], and in fact the OA spectrum calculated for our silica model including a $[(O\text{-})_2P]^+$ center features an isolated peak at 5.6 eV with an oscillator strength (0.08) comparable to the one (0.11) we calculated for the ODC(II) center [12], and no other absorption peak up to ~7 eV [Fig. 2]. As the experimental OA spectra of P-doped silica [3,4] do not show any strong feature at 5.6 eV we further infer the absence of a precursor such as a $[(O\text{-})_2P]^+$ center. By contrast the calculated OA spectrum of a $[(O\text{-})_2P]^-$ center features several absorption peaks in the range ~2.5–7 eV with major intensity contributions at ~4.8 eV and in the range 5.5–7 eV which appears to be consistent with the findings of [3].

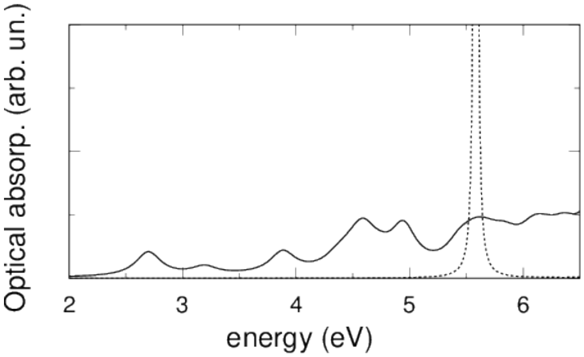

Figure 2: Optical absorption spectra calculated for a silica model containing a twofold coordinated P atom: a $[(O\text{-})_2P]^-$ center (solid) and a $[(O\text{-})_2P]^+$ center (dashed).

2.2 Conversion between P_2 and P_1 centers

The double phosphorus center $\geq P^+\text{-O-}P^+\leq$, by trapping an electron, could give rise to a P_2 center linked to a PO_4^+ or, by breaking of a P-O bond, to a P_1 center with a $[(O\text{-})_3P{=}O]^0$ as a neighbor tetrahedron. We investigated these two possible configurations as hereafter explained. By replacing a SiO_4 tetrahedron with a PO_4 tetrahedron and by cycling over all the 36 available sites in our model it was possible, by means of a first-principles relaxation, to obtain seven P_2 center configurations. We show that for the latter P_2 configurations, a (P_2-PO_4^+) configuration can be obtained by replacing a neighboring SiO_4 tetrahedron with a PO_4^+ and then by performing a first-principles relaxation. Next, the (P_2-PO_4^+) configuration was first positively, so to generate a $\geq P^+\text{-O-}P^+\leq$, and then again negatively charged leading to the formation of a pair of a $[(O\text{-})_3P{=}O]$ and a almost three-coordinated P atom. The latter, provided that the position of the three-coordinated P is reversed with respect to the plane of its three nearest neighbors oxygen atoms can lead to a P_1 center configuration. EPR calculations have been performed to check that the so generated (P_2-PO_4^+) and (P_1-PO_4^+) indeed provide reliable P_2 and P_1 configurations [2,4]. As last step we perform a NEB calculation in order to evaluate the energy barrier separating the configuration showing a P_2 center from the one showing a P_1 center. The NEB calculations show that by overcoming an energy barrier (~0.2-0.5 eV) the former configuration can convert into the latter one, thus providing a tentative model for the observed P_2 to P_1 conversion.

3 CONCLUSIONS

In the present work, together with the results of [8], we provide several insights useful to understand the optical absorption spectra of P-doped silica up to ~7 eV. Furthermore we propose the occurrence of double phosphorus centers $\geq P^+\text{-O-}P^+\leq$ which could allow the interconversion of P_2 centers in to P_1 centers.

REFERENCES

[1] S. Girard *et al*, J. Non-Cryst. Solids 357, 1871, 2011.
[2] D. L. Griscom *et al*, J. Appl. Phys. 54, 3743, 1983.
[3] H. Hosono *et al*, J. Appl. Phys. 91, 4121, 2002.
[4] G. Origlio *et al*, Phys. Rev. B 80, 205208, 2009.
[5] J.P. Perdew *et al*, Phys. Rev. Lett. 77, 3865, 1996.
[6] P. Giannozzi *et al*, J. Phys. Condens. Matter 21, 395502, 2009.
[7] L. Martin-Samos *et al*, Comput. Phys. Commun. 180, 1416, 2009.
[8] L. Giacomazzi *et al*, Opt. Mater. Expr. 8, 385, 2018.
[9] L. Martin-Samos *et al.* Phys. Rev. B, 71, 014116, 2005.
[10] A. Trukhin *et al*, J Non Cryst Solids 462, 10, 2017.
[11] G. Pacchioni *et al*, J. Phys. Chem. 105, 6097, 2001.
[12] L. Giacomazzi *et al*, Nanotech. 28, 195202, 2017.

Modeling of the RIA in silica-based optical fibers: contribution of the photoionization of radiation-induced trapped states

Franck MADY, Mourad BENABDESSELAM, Angela GUTTILLA

Université Côte d’Azur, Institut de Physique de Nice (INPHYNI), CNRS UMR 7010
Parc Valrose, 06108 NICE cedex 2, France

ABSTRACT

The radiation-induced attenuation in silica optical fibers is usually attributed to the formation of color centers. The RIA spectrum is then considered a composition of several characteristic optical absorption bands. We argue, based on experimental and theoretical facts, that the photoionization of radiation-induced bandgap states may also contribute to the RIA. This contribution could notably play a role in the near-infra-red range where silica fibers are frequently operated but the origin of RIA poorly resolved.

PACS Keywords: optical fibers, radiation effects

1 INTRODUCTION

It is widely admitted that radiation-induced attenuation (RIA) of silica optical fibers is due to color centers (CC) formed upon trapping of free carriers excited by the ionizing radiation. RIA spectra are then considered a composition of several optical absorption (OA) bands associated with these CC. Most of the identified intrinsic or Al-, P-, and Ge-related centers were demonstrated to absorb in the UV-VIS ranges [1]. None of them have OA bands in the near-infrared (NIR) region, except self-trapped holes (one band reported at 1.63 eV [2]) that are however unstable above 200 K [2,3]. Lowest energy visible bands are centered at 2 eV (NBOHC and POR [1]) but are characterized by very small oscillator strength compared with UV-VIS OA bands (f = 1–5 x 10^{-4} [1,4]). Therefore, the origin of RIA in the NIR range is poorly elucidated; it is often simply attributed to the tail of visible bands above 2 eV. Yet the NIR RIA well deserves a refined understanding since silica optical fibers are usually operated in this region. We show that photoionization of radiation-induced trapped states by the guided light may contribute to the NIR RIA. This process differs from CC absorption in that it involves the transfer of a carrier from a localized state to a band.

2 EVIDENCE FOR PHOTOIONIZATION

In Fig. 1 we used the setup described in [5] to measure the 980 nm RIA continuously under irradiation. The fiber under test is an aluminosilicate-core fiber (named K04, 1.97 w% Al) fabricated by MCVD and solution doping techniques at INPHYNI, Nice. The optical power launched in the fiber sample was high, about 50 mW. The dose rate was changed at a few times during irradiation. At each dose rate, the RIA reaches a plateau which does not correspond to saturation (RIA takes higher values) but obviously to an equilibrium state. A photo-induced recovery therefore competes with radiation-induced degradation, as confirmed by the fact that lowering the dose rate lowers the RIA equilibrium level. In usual RIA measurements, the probe-light power is much lower so the transient towards equilibrium much longer. Then, saturation is reached before equilibrium. If color centers are trapped carriers, photo-bleaching must follow detrapping and/or recombination. This involves the photoionization of trapped states and the transfer of carriers from localized states to a band. Some light is absorbed in this process that necessarily contributes to RIA. The property illustrated here for an Al-doped fiber is in fact observed for a wide variety of doping conditions.

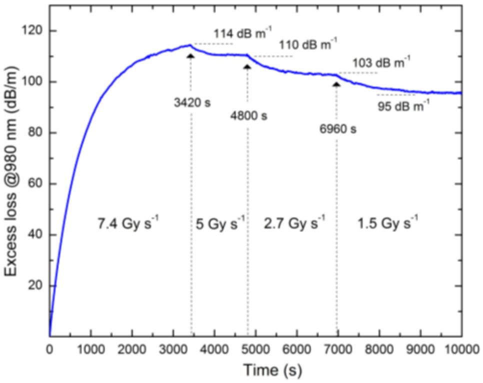

Figure 1: In-line 980 nm RIA of K04 at various dose rates

3 RECOVERY MECHANISM

Recovery was investigated by Thermally Stimulated Luminescence (TSL), a technique where carrier detrapping is due to heating (linear heating ramp applied to the sample [6]). Fig. 2 shows the spectrally-integrated TSL measured at 4 heating rates for K04 and K05 preform samples after a 7.4 kGy(SiO_2) dose. K05 is also an aluminosilicate sample, but with a lower Al concentration (0.53 w% Al). In the inset, the TSL from K04 is plotted versus wavelength and temperature (intensity increases from blue to red). The main TSL emission, around 2.95 eV with FWHM ~1 eV, can be assigned to AlODC centers [7]. AlODC are thus *re-formed* during the TSL readout which relaxes radiation effects: a recombination process reforms AlODC in excited state and produces TSL upon de-excitation. Fig. 3 shows the K05 RIA spectrum and its Gaussian decomposition with well-admitted band features [1]. Radiation-induced CC mainly consist of SiE’, NBOHC, AlE’ and AlOHC. This RIA is completely bleached by TSL readouts stopped at 450 °C. The annealing of AlE’ and AlOHC being accompanied by the reformation of AlODC, it is probable that SiODC are also reformed while SiE’ and NBOHC are annealed, but the SiODC emission at 2.7 eV (459 nm) [1] is weak and hidden by the AlODC emission (it maybe appears as the light-blue tail at 460 nm).

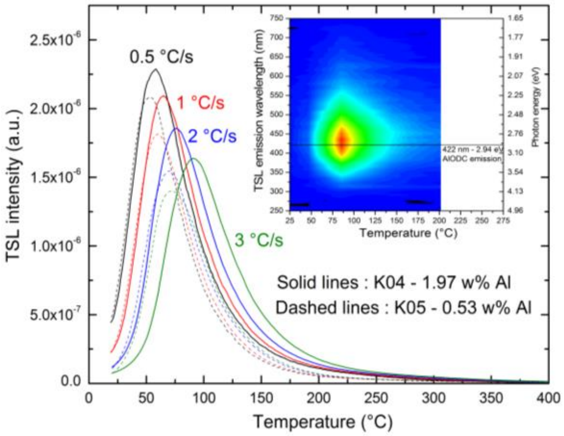

Figure 2: TSL curves from K04 and K05 at 4 heating rates and TSL spectrum of K04 (inset) at 2 °C/s.

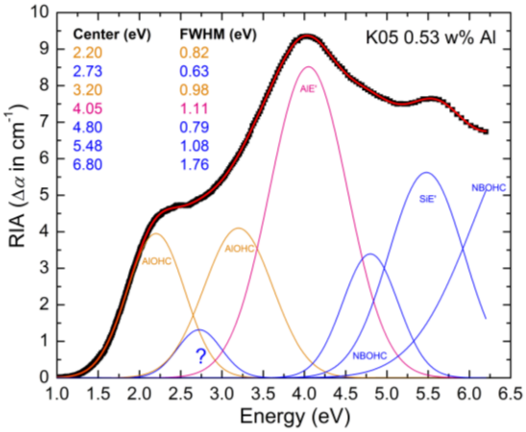

Figure 3: Typical RIA spectrum and its Gaussian decomposition, here for K05.

Fig. 4 presents the thermal bleaching map of K05 during the TSL readout at 2 °C s^{-1} (built following [8]). The color scale gives the percentage of the RIA annealed at given temperature (abscissa) and wavelength (ordinate). AlE’ and NBOHC centers anneal rather continuously up to 350 °C, in a way that parallels TSL and the AlODC emission. Whereas this annealing goes with that of AlOHC around 75°C (main TSL peak), it accompanies the disappearance of SiE’ around 275 °C.

4 MODELING

TSL is usually interpreted through energy level schemes distinguishing “traps” (trapped states that can be thermally emptied within the temperature range of TSL readouts) from “recombination centers” (deeply trapped carriers that can only disappear when a carrier of opposite polarity released from a trap recombines with them). As SiODC, AlODC are associated with an electron occupying a gap level above the valence band [7] and may therefore capture holes during irradiation to form CC. Since AlODC are reformed by recombination during thermal bleaching, the recovery process probably involves the detrapping and recombination of electrons. As the annealing of AlE’ centers parallels this process, the AlE’ seem to serve as the recombination centers (just as free electrons can recombine with SiE’ to form SiODC [1]). Fig. 4 shows that carriers are released around 75 °C with a significant tail up to 300 °C, and around 275 °C. Released carriers are of the same nature in both cases, namely electrons, because we observe the same recombination center throughout the TSL readout. We implemented such a physical picture into the simulation of TSL at various heating rates (first-order TSL analysis). For the preform K05, we obtained a very good agreement with all data using a single set of parameters shown in Fig. 5 (σ_C is the capture cross-section). This figure notably displays the trapped-electron distribution achieved by the 7.4 kGy(SiO_2) dose and its decomposition into two components (red and blue) corresponding to the two above mentioned groups of traps. Simulated TSL curves are validated against data in Fig. 6. The TSL emission from AlODC is submitted to thermal quenching, as proved by the decrease of its intensity observed when the heating rate is increased (this shifts the TSL processes towards high temperature). With the luminescence yield parameters of Fig. 5, it is possible to simulate the TSL that would be obtained without thermal quenching. The renormalized TSL curve at 2 °C s^{-1} corrected from quenching, shown in Fig. 6, reveals hidden TSL components at ~225 and 315 °C. The latter are due to the “blue” density of trapped electrons peaking at 1.25 and 1.44 eV below the conduction band (Fig. 5) and are obviously related to the annealing of SiE’ centers around 275 °C (Fig. 4).

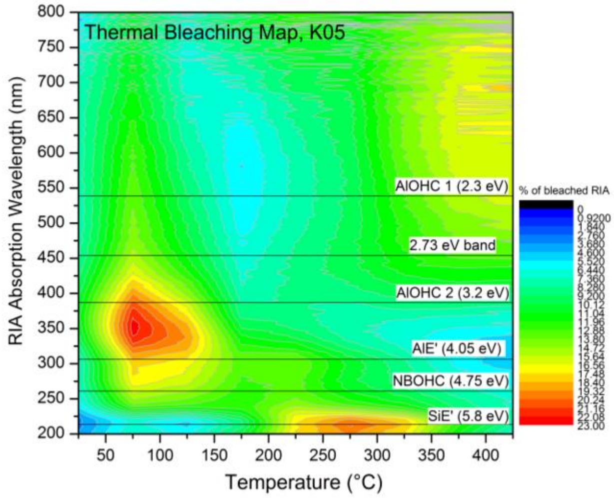

Figure 4: K05 bleaching map during TSL at 2 °C s^{-1}.

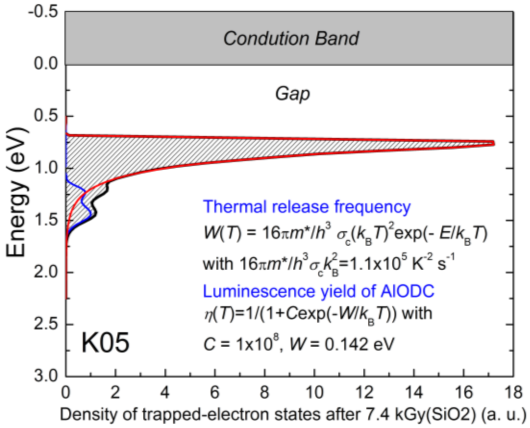

Figure 5: Parameters of the TSL simulation for K05.

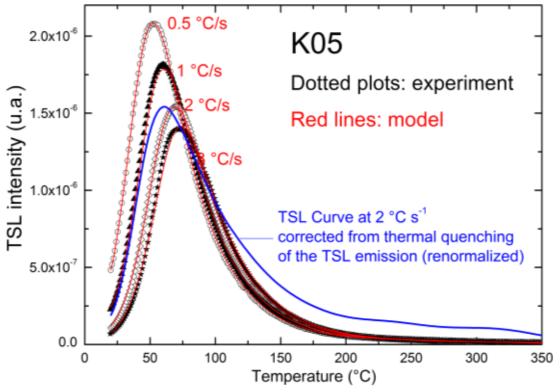

Figure 6: Simulated TSL curves compared to data.

5 PHOTOIONIZATION

Whereas OA bands of CC lie in the UV-VIS regions, trapped electrons of Fig. 5 can be excited to the conduction band by photons whose energy is > 0.7 eV. Each thermal activation energy E is associated with a photoionization cross-section $\sigma(\lambda,E)$ (Lucovsky's or more refined models [9]) so the corresponding absorption coefficient $\Delta\alpha$ is

$$\Delta\alpha(\lambda) = \int n(E)\sigma(\lambda, E)\mathrm{d}E, \qquad (1)$$

where $n(E)$ is the volume density of electrons trapped between E and $E + \mathrm{d}E$. With the density of trapped states of Fig. 5, and considering the intensity of the 0.75 eV peak is 10^{17} cm^{-3}, we can estimate the order of magnitude of $\Delta\alpha$. This also requires gauging $\sigma(\lambda,E)$. Assuming a maximum $\sigma_{\max}(E = 1\text{ eV}) = 10^{-18}$ cm^2 for traps located at 1 eV from the band edge, we obtain the NIR RIA plotted in Fig. 7 for 2 usual models of $\sigma(\lambda,E)$ (see figure). Even with the reasonable estimates of $n(0.75\text{ eV})$ and $\sigma_{\max}(E = 1\text{ eV})$, photoionization can be responsible for RIA levels of a few tens of dB m^{-1}. This contribution to the total RIA should not be neglected.

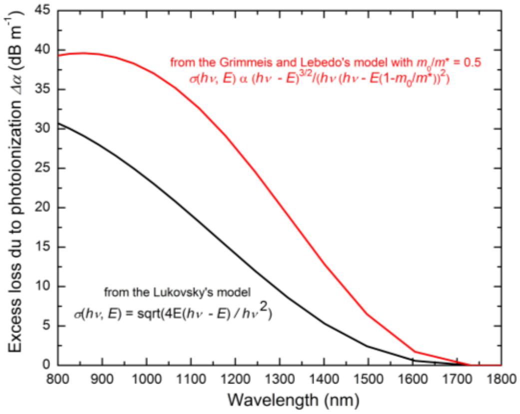

Figure 7: NIR RIA due to photoionization of the electron distribution of Fig 5.

6 CONCLUSION

Photoionization of carriers trapped close to the band edges may induce a significant RIA, notably in the NIR region. This contribution, most often forgotten, should be considered in the RIA modeling. The final paper will give much more experimental details and a clear explanation of the TSL modeling. Various models will be compared, several compositions will be treated to discuss composition and concentration effects.

7 ACKNOWLEDGMENTS

This work is supported by the « Investissements d'Avenir » program of the French government managed by the French National Agency for the Nuclear Waste Management (Andra).

REFERENCES

[1] L. Skuja, J. Non Cryst. Sol., 239, 16, 1998.
[2] D. Griscom, J. Non Cryst. Sol., 352, 2601, 2006.
[3] D. Griscom, J. Non Cryst. Sol., 357, 1945, 2011.
[4] M. Cannas, L. Vaccaro, B. Boizot, J. Non Cryst. Sol., 352, 203, 2006.
[5] F. Mady, J-B. Duchez, Y. Mebrouk, M. Benabdesselam, IEEE Trans. Nucl. Sci., 62, 2948, 2015.
[6] F. Mady, M. Benabdesselam, W. Blanc, Opt. Lett., 35, 3541, 2010.
[7] V. A. Putsovarov *et al.*, J. Exp. Theor. Phys., 111, 989, 2010.
[8] F. Mady, M. Benabdesselam, Y. Mebrouk, B. Dussardier. Proceedings of the RADECS Conference 2010, paper LN2. Download at http://www.radecs2010.ait.ac.at/programme.htm
[9] R. Masut, M. Penchina, Phys. Stat. Sol. (b), 130, 737, 1985

Numerical Modeling of Novel Sensor Element Based on Abnormal Blocking by Periodic Grating Strips over Si/SiO$_2$ wire waveguide

Andrei Tsarev *,**, Eugeny Kolosovsky*, Francesco De Leonardis*** and Vittorio M. N. Passaro***

*Laboratory of Optical Materials and Structures, Rzhanov Institute of Semiconductor Physics, SB RAS, Novosibirsk 630090, Russia
**Laboratory of Semiconductor and Dielectric Materials, Physics Department, Novosibirsk State University, Novosibirsk 630090, Russia
***Photonics Research Group, Dipartimento di Ingegneria Elettrica e dell’Informazione, Politecnico di Bari, Via E. Orabona 4, 70125 Bari, Italy; e-mail: vittorio.passaro@poliba.it

ABSTRACT

The paper discussed the physical nature and the numerical modeling of a novel architecture based on periodic structures for application as photonic sensors. The sensing affect is based on the high sensitivity to the index cover perturbation of the notch wavelength, which takes place in periodic segmented grating over the silica buffer on the conventional silicon wire. The sensing is based on the effect of abnormal blocking of the guided wave propagating along silicon wire with periodic strips overhead. The structure sensing is numerically modeled by 2D and 3D FDTD, taking into account the waveguide dispersion.

PACS Keywords: silicon wire, segmented grating, optical sensing.

1 INTRODUCTION

Grating assisted couplers [1] and segmented waveguides [2] belong to the most popular optical devices utilizing periodic structures. They are used to couple the external optical beam to the guided mode and to construct an optical filter by interaction with the backward-reflected guided mode. Very often, grating is also used to couple the guided modes in two closely spaced optical waveguides which form the optical filter. In all cases the grating periodicity provides the phase-matching between different interacting waves according to the commonly used Bragg condition.

A new outlook on the well known grating filter design [1] is formulated in the present paper, but with the fully etched grating (looks like a periodic structure of the dielectric strip inserts) and constructed near the boundary of the single mode waveguide. Similar polymer segmented grating is previously used to design the wide aperture quasi-single mode strip and grating loaded waveguide [3] on the silicon-on-insulator (SOI) structure. We have proved [4] that the similar segmented grating (see Figure 1), as a set of periodically spaced dielectric strips, could provide strong blocking of a guided wave without the backward-directed guided wave. This unusual feature could be explained by the evanescent coupling of the guided mode with an artificial leaky mode supported by the grating area and which is further radiated from the structure. Thus, the guided wave could be blocked, but this phenomenon will be not supported by the back-reflected guided wave. This abnormal guided wave blocking effect could be used for the construction of notch filters with negligible back-reflection as well as optical sensors.

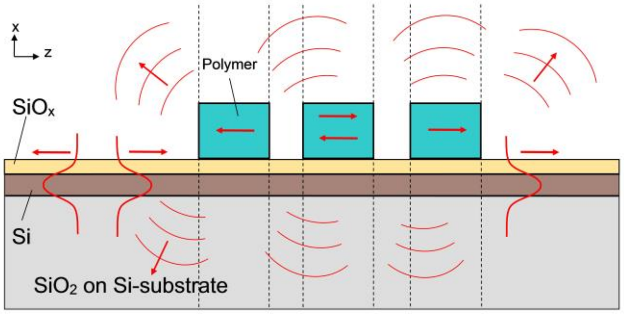

Figure 1: Structure design for modeling of guided wave propagation in the silicon waveguide which is evanescently coupled to the segmented grating. The fundamental TE_0 mode is launched at $Z = 0$ and propagates under the periodic grating formed by multiple polymer strips.

2 STRUCTURE MODELLING

In this paper we considered the demonstration of the previously discovered "abnormal blocking" effect [4] for the creation of optical sensors on the example of weak changes in the refractive index of water. Numerical simulation of such structures is performed using the finite difference time domain (FDTD) method using the commercial software package RSoft-SYNOPSYS [5]. Due to the large size of the computational domain, this kind of problems is usually investigated within a two-dimensional (2D) approximation using the effective index method (EIM) [6]. It was shown that the presence of waveguide dispersion leads to the fact that the direct application of 2D FDTD gives overestimated values of 40% in the sensitivity $Sn=\partial\lambda/\partial n$ (see Fig. 3), which makes unsuitable application 2D FDTD and EIM for accurate analysis of such structures.

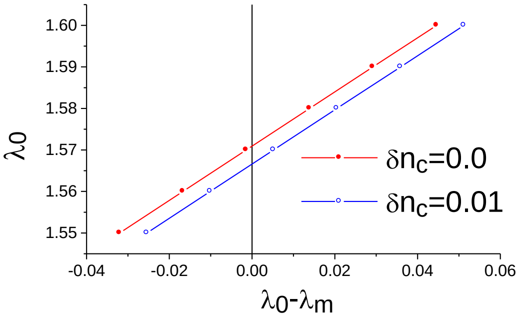

Figure 2: Dispersion compensation algorithm for two-dimensional simulation by FDTD method using EIM.

We found an original solution to this problem. The presence of waveguide dispersion leads to the fact that the wavelengths of anomalous blocking λ_m found using the 2D FDTD modeling depend on the wavelength λ_0, at which the impulse excitation and spectrum analysis of the waveguide structure is carried out. However, for the case $\lambda_m = \lambda_0$ this value is exactly equal to the desired value. Therefore, by constructing the dependence λ_0 on the difference λ_0-λ_m (see Fig.2) and having determined the values λ_0 at the zero coordinate, it is possible to find the wavelengths of the anomalous blocking for different values of the perturbation of the refractive index of the environment and, thereby, find the correct value S_n, which is slightly different (see Fig. 3) from the results of laborious 3D FDTD simulation.

The simulation is performed for the periodic segment structure based on the polymer SU-8 with refractive index of 1.56, grating period of 1.3 µm, thickness and width of 1 µm, separated by using a silicon oxide with a refractive index of 1.4, buffer layer thickness of 0.1 µm from standard silicon waveguide thickness of 0.25 µm and width of 0.45 µm, and buried oxide thickness of 2 µm.

This algorithm opens up the possibility of rapid analysis and optimization of parameters of segment periodic structures and sensors based on them using the EIM and 2D FDTD. Besides, the large-dimensional structures were analyzed by the semi-analytical algorithm of method of lines (MoL), which allows with high accuracy the propagation and reflection of the optical wave to be described in structures with an arbitrary number of periodic segments (2000 or more), not available for the 2D FDTD method (usually no more than 512 segments with reasonable limitations on memory and running time).

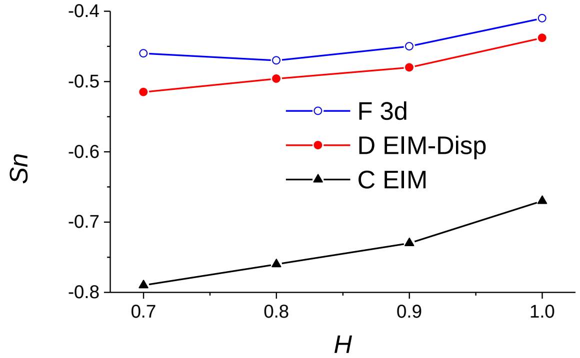

Figure 3: Dependence of the slope change $S_n=\partial\lambda/\partial n$ on the index of medium (water) as a function of the height H of the segmented grating. Calculation by FDTD method for 3D and 2D cases. 2D modeling is accomplished using standard EIM and dispersion compensation algorithm (EIM-Disp).

SUMMARY

We performed numerical modelling which show that the segmented periodic structures, tunnel coupled with an underlying silicon wire, provides high sensitivity $S_n=\partial\lambda/\partial n$ wavelength of the abnormal blocking to the refractive index change of the surrounding space (water, in our case) and can be used for optical sensing. This design provides similar sensitivity as silicon slot sensors [7] but it is based on a more robust technological approach.

REFERENCES

[1] D. Marcuse, "Directional couplers made of nonidentical asymmetric slabs. Part II: Grating-assisted couplers," J. Lightwave Technol., LT-5, no. 2, 268-273, 1987.
[2] R. Halir, et al. "Waveguide sub-wavelength structures: a review of principles and applications," Laser & Photon. Rev. 9, 25–49, 2014.
[3] A. V. Tsarev, "New wide strip and grating loaded quasi-single-mode waveguide on SOI," Opt. Express 17, 13095-13101, 2009.
[4] E. A. Kolosovskii, A. V. Tsarev, "Abnormal blocking of a guided mode propagating in a silicon optical waveguide with periodic tunnel coupling", Quantum Electron., 47, 58–64, 2017.
[5] Rsoft FullWave by SYNOPSYS, single license (2018).
[6] K. S. Chiang, "Dual effective-index method for the analysis of rectangular dielectric waveguides," Appl. Opt., 25, 2169-2174, 1986.
[7] F. Dell’Olio and V. M. N. Passaro, "Optical sensing by optimized silicon slot waveguides," Opt. Express 15, 4977-4993, 2007.

Politecnico di Bari

UNIVERSITÀ DEGLI STUDI DI PALERMO

DiFC
DIPARTIMENTO DI FISICA E CHIMICA - DiFC

BARI – ITALY
11-13 JUNE
SiO2018

TUESDAY

SESSION

NANOSTRUCTURES

UNIVERSITÉ JEAN MONNET
SAINT-ÉTIENNE

UNIVERSITÉ FRANCO ITALIENNE
UNIVERSITÀ ITALO FRANCESE

Anritsu
envision : ensure

ROHDE&SCHWARZ

DEI
DIPARTIMENTO DI
INGEGNERIA ELETTRICA
E DELL'INFORMAZIONE

Charge transport in oxide-in-oxide nanostructured silica-based dielectrics

R. Lorenzi*, J. Remondina*, N. V. Golubev**, E. S. Ignat’eva**, V. N. Sigaev**, A. Sassella*, S. Trabattoni, M. Acciarri*, A. Paleari*

*Department of Materials Science, University of Milano-Bicocca
via Cozzi 55, 20125 Milano, Italy
**P.D. Sarkisov International Laboratory of Glass-based Functional Materials,
Mendeleev University of Chemical Technology of Russia, Miusskaya Square 9, 125047 Moscow, Russia

1 ABSTRACT

We present a novel strategy for the preparation of nanostructured glassceramic thin films based on radio-frequency sputtering of glassy target with tailored composition. The resulting material is a dispersion of Ga-rich oxide nanophase in an amorphous germanosilicate matrix. The investigation of electrical response highlights the presence of percolative processes mediated by hopping and tunneling between semiconductive nanostructures.

PACS Keywords: nanostructured thin films, gallium oxide, germanosilicate glass, impedance spectroscopy

2 INTRODUCTION

Nanostructured oxide-in-oxide glassceramics are a composite materials in which a nanocrystal phase is embedded in an amorphous matrix. These materials possess unique properties since they combine functional properties imparted by the nanocrystals with structural features dictated by matrix composition. Specifically, in photonics and optoelectronics applications the possibility of obtaining a wide-band gap nanocrystal phase homogenously dispersed in a transparent silica-based matrix is the ideal approach for achieving specific optical activities in a transparent glassy material. In this view, germanosilicate glasses embedding nanocrystals of gallium oxide have recently gained attention for their potential use as hosts for rare earth and transition metal ions for tailored optical emission and active window in solar-blind detection, in bulk, fiber and laser-written geometry [1-4]. The opportunity of replicating such materials also in thin film geometry may pay the way to the design of new devices such as electroluminescent thin films, compact UV-detectors, and non-linear electrical components. In fact, the nanoparticle-mediated electrical conduction and charge trapping could, in principle, lead to unexpected results such as a resistance and/or capacitance behavior dependent on the history of applied currents. This effect can, in turn, be exploited for the production of solid state memories in which the 0/1 state can be written by appropriate current history and read by the resulting value of resistance or capacitance [5].

Here we propose a preparation route of such films based on magnetron sputtering of targets made of bulk glasses and we present the collected results concerning optical, morphological and electrical characterization.

3 MATERIALS AND METHODS

Bulk samples to be used as sputtering targets were prepared by melt quenching method with nominal composition: 7.5 Li_2O - 2.5 Na_2O - 20 Ga_2O_3 - 25 SiO_2 - 45 GeO_2 (mol%). Raw materials are amorphous SiO_2 (special purity grade), GeO_2 (special purity), Li_2CO_3 (reagent grade), Na_2CO_3 (reagent grade), Ga_2O_3 (reagent grade). The powders were weighed using an analytical balance with an accuracy of 0.001 g and carefully mixed in an agate mortar. Glass was prepared in air at 1480 °C for 40 min, the melt was poured in a steel form with the size of the target holder (6 cm in diameter) with a final thickness of about 5 mm. Films were deposited at room temperature by radiofrequency sputtering (P_{Ar}~$6\cdot10^{-3}$ mbar, $P_{magnetron}$=250 W, ~1200 V) at a rate of about 3-4 nm/min, either on silica substrate (for optical measurements) or silicon wafer (for complex impedance spectroscopy). In bulk materials the precipitation of gallium oxide nanophase (i.e. the transformation from glass to glassceramic) can be induced by a mild thermal treatment of the glass at 670°C for 30 minutes. As a first approach in the realization of nanostructured glassceramic thin films we deposited films starting from glass targets and we thermally treated them in the same way that we use for the nanostructuring of bulk materials. Film morphology has been evaluated by profilometry, scanning electron microscopy, and atomic force microscopy. Optical properties have been studied by UV-Vis absorption and reflection, ellipsometry and photoluminescence analysis. Electrical characterization and impedance spectroscopy were conducted on metalized

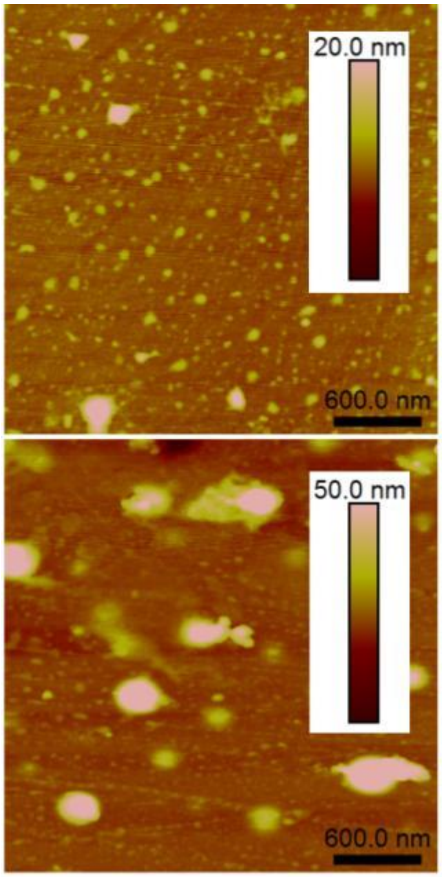

Fig. 1: AFM images of as-deposited (top) and thermal treated (bottom) films.

samples using a LCR-meter and standard i-V characteristic collected as a function of temperature.

4 RESULTS AND DISCUSSION

Morphological characterization evidenced, by variance with bulk materials, nanostructuring features already present in the as-deposited film without the need of further thermal treatment. Thermal treatment of the films only favors the aggregation and coalescence of such structures into bigger agglomerates (see Fig. 1). Compositional analysis of such structures (by Electron Dispersive Spectroscopy) suggest a preferential location of Ga atoms within the structures, confirming the propensity of these systems in the segregation of Ga-rich nanophases. Optical characterization confirms this situation with measured refractive indices and optical band gap comparable with bulk counterparts and slightly modified by thermal treatments. Temperature-dependent electrical measurements show resistivity values order of magnitudes lower than in silicate glasses and a behavior ascribable both to hopping and tunneling. This latter outcome is in agreement with a charge transport mechanism mediated by a dispersion of conductive Ga-rich oxide nanophase embedded in an insulating germanosilicate matrix. Finally, impedance spectroscopy data are compatible with a n-type conduction mechanism probably due to the presence of oxygen vacancies and/or the presence of Si/Ge acting as Ga-oxide nanophase doping agents. The C-V curves present also hysteresis, as observed in memristor technology based on nanostructured thin films, and due to different percolation pathways activated by charging and discharging of the semiconductive nanostructures.

5 CONCLUSIONS

In the present work we realized nanostructured thin films of Ga-oxide rich nanophases, with semiconductive properties, embedded in amorphous and insulating germanosilicate matrix. Electrical characterization of these films in sandwich geometry reveals their potential use as memristor non-linear electrical devices.

6 REFERENCES

[1] Lorenzi R, Paleari A, Sigaev VN, Ignat’eva ES, Golubev VN, ”Augmented excitation cross-section of gadolinium ions in nanostructured glasses”, Optics Letters, 42, 2419, 2017

[2] Sigaev VN, Golubev NV, Ignat’eva ES, Paleari A, Lorenzi R, “Light-emitting Ga-oxide nanocrystals in glass: a new paradigm for low cost and robust UV-to-visible solar-blind converters and UV emitters”, Nanoscale, 6, 1763, 2014

[3] Lotarev S, Lipatiev A, Golubev N, Ignat’eva E, Malashkevich G, Mudryi A, Priseko Y, Lorenzi R, Paleari A, Sigaev V, “Broadband infrared light-emitting patterns in optical glass by laser-induced nanostructuring of NiO-doped alkali-gallium germano silicates”, Optics Letters, 38, 492

[4] Mashinsky VM, Karatun NM, Bogatyrev VA, Sigaev VN, Golubev NV, Ignat’eva ES, Lorenzi R, Mozzati MC, Paleari A, Dianov EM, “Microfluorescence Analysis of Nanostructuring Inhomogeneity in Optical Fibers with Embedded Gallium Oxide Nanocrystals”, Microscopy And Microanalysis, 18, 25, 2012

[5] Dongale, T.D., Shinde, S.S., Kamat, R.K. and Rajpure, K.Y., “Nanostructured TiO2 thin film memristor using hydrothermal process”, Journal of Alloys and Compounds, 593, 267, 2014

A Photoluminescence Study of Microwave Synthesized Carbon-dots Dispersed in Water and in Mesoporous Silica

Carlo Maria Carbonaro[a,] Pier Carlo Ricci[a], Riccardo Corpino[a], Daniele Chiriu[a], Luigi Stagi[a], Maria Francesca Casula[b], Swapneel V. Thakkar[b], Luca Malfatti[c], Kazumasa Suzuki [d]

[a]Department of Physics, University of Cagliari, Campus of Monserrato, sp n8, km 0.700, Monserrato, Italy
[b]Department of Chemical and Geological Sciences and INSTM, University of Cagliari, Campus of Monserrato, sp n8, km 0.700, Monserrato, Italy
[c]Laboratory of Materials Science and Nanotechnology, Chemistry and Pharamacy Department, University of Sassari, CR-INSTM, Via Vienna, 2, Sassari, Italy
[d]Department of Materials Science, The University of Shiga Prefecture, 2500, Hassaka-cho, Hikone-City, Shiga, 522-8533 Japan

ABSTRACT

The optical properties of microwave synthesized Carbon Dots (CDs) dispersed in water and in mesoporous ordered silica are reported. We compare the fluorescence characteristics of bare carbon dots (CDB) nitrogen-doped samples (CDN). Nitrogen doping is exploited to increase the emission efficiency. By exciting the samples in the far UV and in the blue region, we singled out two emission bands in the blue-green region, at about 430 and 520 nm. We discuss the wavelength tunability of CD emission in terms of CDs polydispersity and distribution of green emitting centers. The relative contribution of the green photoluminescence is enhanced once the samples are dispersed in mesoporous silica, suggesting a surface origin of the emitting centers. The presented results offer insights on the parameters affecting the photoluminescence behavior of carbon dots with particular reference to implications on applicability in solid-state photonics.

PACS Keywords: Carbon dot, fluorescence, mesoporous silica

1 INTRODUCTION

Since the discovery of their unexpected efficient luminescence properties in 2004 [1], Carbon-dots (CDs) have emerged as promising fluorescent materials for applications in the photonic, imaging and lightning fields [2-5]. CDs are nanosized particles (dimension lower than 10 nm) with large chemical inertness, low toxicity, high biocompatibility, high water solubility and good photostability. These nanoparticles can be produced with many green chemical and physical, top-down and bottom-up methods. The efficient emission properties of CDs can be tuned either by quantum confinement or surface functionalization, but the very origin of the emissions, their excitation tunability and the role of nitrogen doping are still debated. In this work we investigated the properties of CDs dispersed in water and in mesoporous silica with the idea to clarify the origin of the emissions and possibly exploit the interaction with the host surface to design and control the optical properties of the hybrid system.

2 SAMPLES AND EXPERIMENTS

We prepared bare CDs (CDB) and nitrogen-doped CDs (CDN) by a microwave assisted route, starting either from citric acid or citric acid and urea (reagents were Sigma-Aldrich, analytical grade) in 10 mL of water. The solutions were stirred for 30 min., and then treated in a domestic microwave oven at 700 W. All the samples were purified by centrifuge up to 10k rpm; no effect of centrifuge procedure was obtained on CDB, whilst CDN resulted in purified, concentrated sample (CDNP).

By templated sol-gel synthesis we prepared ordered hexagonal “SBA-15” mesoporous silica powders (MS) exploiting triblock copolymer Pluronic P123 and Tetraethoxysilane (TEOS).

We applied drop casting of a CDs water dispersion upon silica powders to obtain organic-inorganic hybrid samples (MS_CDs). Impregnated powders were left in oven at 40 °C to allow gentle removal of water.

We applied a multi-technique approach to characterize the samples from morphological (TEM), structural (XRD, Raman, FTIR) and optical (absorption, steady state excitation and emission, time resolved spectroscopy) point of view.

3 RESULTS AND DISCUSSION

Figure 1 reports a TEM image of nitrogen doped CD samples. The picture shows quite poor contrast, because we are imaging carbon structures on carbon grids, thus preventing a precise determination of actual CD sizes. As pointed out in the figure, we detected rounded particles with nanosized dimensions (distributed in the 2-7 nm range, with a peak around 3 nm).

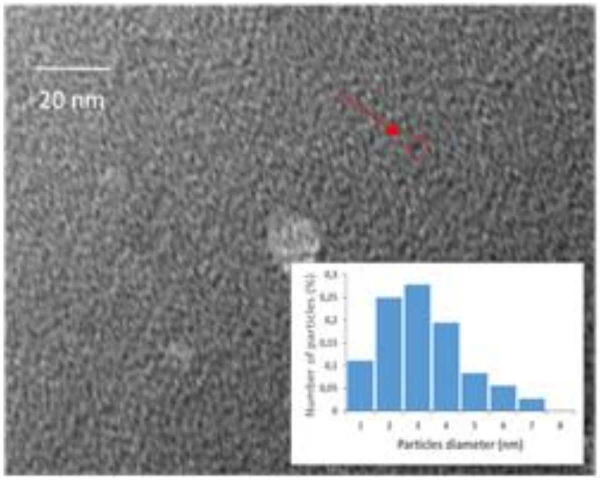

Figure 1: TEM images of CDN samples and size distribution

The absorption spectrum of the CDs is characterized by two large bands in the UV range, at 240 and 340 nm, assigned to the π-π* transitions of aromatic C=C bonds and to n-π* transitions of C=O respectively. Figure 2 reports the emission gathered from CDN when excited at 340 nm. A large asymmetric band peaked at about 420 nm is recorded, with a contribution in the green region. Once the samples are dispersed in mesoporous silica (MS_CDN) we observe a blue shift of about 15 nm of the band and the increase of the relative contribution of the green shoulder. These findings will be discussed with reference to the origin of the blue and green emissions and with respect to the possibility of tuning the optical properties of hybrid systems.

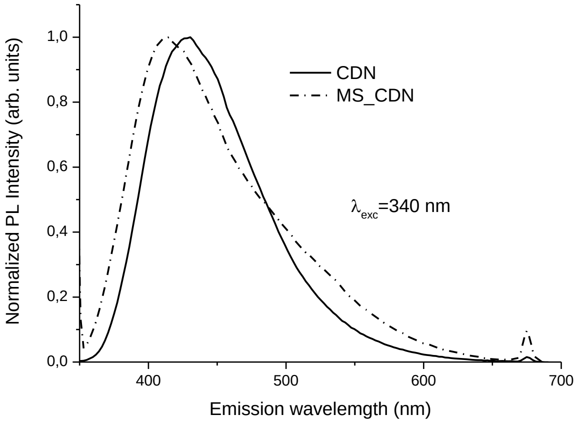

Figure 2: Normalized PL spectra of CDN and hybrid MS_CDN samples excited at 340 nm

REFERENCES

[1] X. Xu, R. Ray, Y. Gu, H.J. Ploehn, L. Gearheart, K. Raker, W.A. Scrivens, J. Am. Chem. Soc. 126, 12736–12737 (2004).
[2] S. C. Ray, A. Saha, N.R. Jana, R. Sarkar, J. Phys. Chem. C 2009, 113, 18546–18551.
[3] H. Li, Z. Kang, Y. Liu, S.-T. Lee, J. Mater. Chem., 2012, 22, 24230.
[4] Y. Wang, A. Hu, J. Mater. Chem. C, 2014, 2, 6921
[5] S. Zhu, Y. Song, X. Zhao, J. Shao, J. Zhang, B Yang, Nano Research 2015, 8(2): 355–381.

Silica coating as “safer by molecular design” strategy to control nano-TiO_2 photoreactivity

Simona Ortelli*, Magda Blosi*, Davide Gardini*, Anna Luisa Costa*

*ISTEC-CNR
Via Granarolo, 64 – 48018 Faenza (RA) Italy

ABSTRACT

The application of a silica coating on TiO_2 nanoparticles (NPs) represents a material design strategy for the purpose of controlling the production and availability of ROS. The SiO_2-modified TiO_2 systems were produced by two different strategies: colloidal hetero-coagulation and chemical synthesis using Stöbert approach.

In this study we evaluated the effect that silica coating had on physicochemical properties, on toxicity drivers such as TiO_2 exogenous production of ROS and on material performances. Merging the experimental results, we demonstrated that the presence of silica coating have an important effect for the control of nano-TiO_2 photoreactivity. In fact, silica acts as dispersing/diluting matrix for TiO_2, decreasing the production of ROS, but improving the photocatalytic performances of pristine sample.

PACS Keywords: SiO_2-modified TiO_2 NPs, safer by design, EPR analysis, ROS production, NO_x abatement

1 INTRODUCTION

Designing intrinsically safer materials (safer by molecular design approach (SbD)) is a big challenge in the world of nanotechnology and nanosafety because is considered the most effective risk management strategy in the production, use and disposal of nanomaterials. Nano-titanium dioxide (TiO_2) is among the materials most investigated for their technological importance and consequent interest in terms of their environment, health and safety (EHS) issues [1]. In particular these particles cause alert for their capacity to produce reactive oxygen species (ROS) that can induce several negative effects, responsible for cytotoxicity. The application of a silica coating on TiO_2 nanoparticles (NPs) represents a material design strategy for the purpose of controlling the production and availability of ROS. In this study we evaluated the effect that silica coating had on physicochemical properties (size, shape and zeta potential), on toxicity drivers such as TiO_2 exogenous production of ROS and in general on material performances. In this way we could address our final aim that was to evaluate if SiO_2 coating matched the objectives of an effective safe by design approach applied to TiO_2: preserving or improving performances but decreasing the availability of ROS [2].

2 MATERIAS AND METHODS

The SiO_2-modified TiO_2 systems were produced using a colloidal hetero-coagulation method expected to give rise to “matrix encapsulation” structure [3]. In order to increase the adhesion of silica on the surfaces of target NPs, hetero-coagulated sols were spray-dried and their behavior on re-dispersion evaluated [4]. The hetero-coagulated structures were compared with core-shell structures obtained by silica chemical nucleation on TiO_2 surface. Diagrams showing the method of production of TiO_2-SiO_2 sols, the selected SiO_2:TiO_2 weight ratio and corresponding nomenclature are reported by Gardini et al. in a previous paper [4].

EPR was used to measure ROS production, particularly the superoxide radicals and hydroxyl radicals, in the pristine and silica-modified TiO_2.

The NO_x abatement test, to assess the photocatalytic performance, was conducted on pristine and silica-modified samples. The analyses were performed by applying nanosuspensions on ceramic tiles with a spray-gun.

3 RESULTS AND DISCUSSION

Merging results of TEM morphological study (Figure 1) and colloidal characterization, we can reasonably confirm that we produced composite structures with SiO_2 NPs surrounding target TiO_2 NPs. The two TEM images of Figure 1 show very clearly the difference between the typical core-shell structure that we obtained by chemical nucleation of SiO_2 on TiO_2 phase by Stöbert method (Figure 1b) and the typical matrix encapsulated structure (Figure 1a) obtained by mixing at colloidal state two hetero-phases in a condition that hetero-coagulation is promoted.

EPR was used to measure ROS production by the pristine and silica-modified TiO_2. The results showed that the silica modified samples only produced fewer ROS in comparison with the samples containing the same total amount of solid. Otherwise, after normalizing to the TiO_2

content, the presence of silica increased ROS generation, given the reported capacity of silica coatings to improve the photoactivity of nano-TiO_2 surfaces.

The reactivity ceramic tile treated with silica-coated nano-TiO_2 was compared with that of unmodified TiO_2 (pristine) to test the NO and NO_x abatement efficiency of the silica coating. We observed the improvement in the photocatalytic performance demonstrated by the enhanced NO_x abatement of the silica-encapsulated TiO_2 samples in comparison with the pristine sample. Combined with the reduction in ROS detected for the silica-modified samples, this last result seems particularly promising as a SbD strategy.

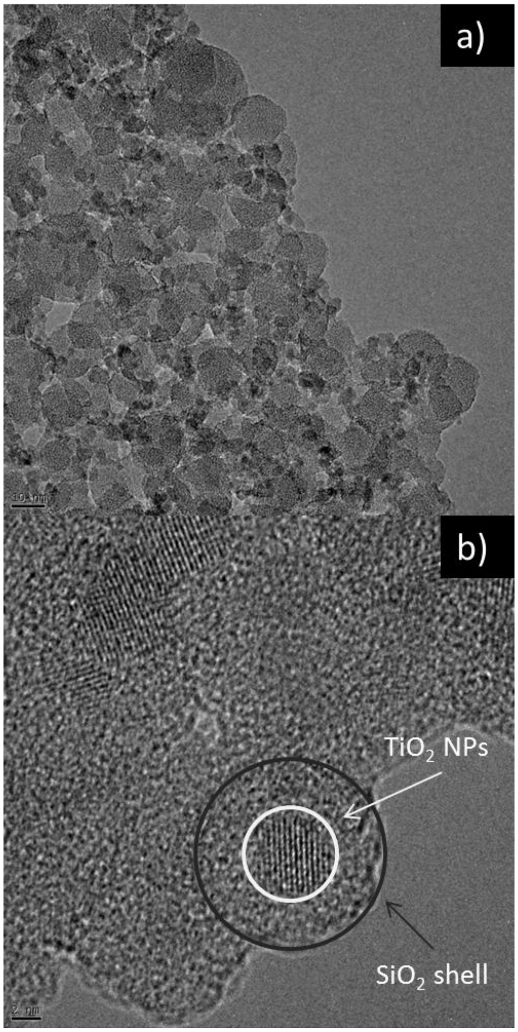

Figure 1: TEM images referred to a) hetero-coagulated and b) chemically synthesized SiO_2-modified TiO_2 NPs.

4 CONCLUSIONS

We investigated silica coating as technique for control two recognised toxicity drivers for nano-TiO_2 as the exogenous production of ROS. We first demonstrated that a matrix of SiO_2 surrounding TiO_2 NPs was formed, even by simply playing with colloidal attraction between the two hetero-phases. The presence of silica coating seems to have an important effect for the control of ROS. In fact, silica acts as dispersing/diluting matrix for TiO_2, decreasing the production of ROS, but improving the photocatalytic performances of pristine sample.

REFERENCES

[1] F. Gottschalk, T. Sonderer, R.W. Scholz, B. Nowack, Environmental Toxicology and Chemistry, 29, 1036–1048, 2010.

[2] S. Ortelli, C.A. Poland, G. Baldi, A.L. Costa, Environ. Sci.: Nano 3, 602–610, 2016.

[3] S. Ortelli, A.L. Costa, Nano-Structures & Nano-Objects 13, 155–162, 2018.

[4] D. Gardini , M. Blosi, C. Delpivo, S. Ortelli, A.L. Costa, Journal of Physics: Conference Series 429, 012052, 2013.

Formation of SiO_2 Dendritic Structures during Annealing of Silicon on Insulator Wafers

Zhigalov V., Novikov S., Korobova N., Vinogradov A., Migunov D., Goryachev A.,
Goryunova E., Timoshenkov S.

National Research University of Electronic Technology, MIET
Bld. 1, Shokin Square, Zelenograd, Moscow, Russia, 124498

ABSTRACT

Dendritic silica formations up to 100 μm in length were built into the silicon surface in the annealing process up to 1000 ^{0}C on the silicon-on-insulator plates. Copper impurity, which acts as a catalyst, played an important role in the formation of dendrites.

PACS Keywords: SOI, dendrite, structure, impurity, defect

1 INTRODUCTION

Recently, in modern technologies of VLSI creation, we can note the tendency to substrates production made using silicon-on-insulator technology (SOI). Unlike the monolithic silicon technology, the electronic systems made using the SOI technology are more resistant to radiation. Also, frequency characteristics with a simultaneous decrease in the power consumption and size of these systems are significantly improved [1-2]. Structural defects significantly affect the yield of suitable products when using silicon-on-insulator (SOI) structures in the production of micro-electromechanical systems (MEMS). We are faced with a large percentage of defective products in the batch of silicon-on-insulator structures during technological development of MEMS production operations [3].

Methods of optical and scanning electron microscopy, energy-dispersive elemental microanalysis (EDA), measurements of electron work function, and secondary ion microscopy were used to determine the causes of defects. EDA was used to determine the elemental composition of the sample on a certain region of its surface applying energy-dispersive spectrometer involved in composition of the scanning electron microscope. Measurements of electron work function [4] showed anomalously low values (<4.0 eV) in comparison with plates without defects. A study of the dependence electron work function after annealing in air at temperatures of 450 ÷ 1000 ^{0}C was made to determine the reasons for such low values. After applying annealing, very interesting structures were visually observed on the plates surface, similar to which were not found in the literature. The paper describes these structures and the patterns of their occurrence on SOI.

2 RESULTS AND DISCUSSIONS

Standard 100 mm silicon (100) - orientation plates were used as the test samples. The initial plates were selected taking into account the minimum deflection (<5 μm) and the non-planarity (<10 μm) of the plates. The substrate, made using silicon technology on the insulator, was a three-layer package consisting of a monolithic silicon wafer with a thickness of 450 μm, a dielectric layer (glass of 8 μm), and a thin silicon surface layer of 30 μm thick placed on it. Structure investigation of electron microscopy methods showed the presence of 5-10 nm thick and 6 micrometers deep cracks in the upper Si layer, which appeared, apparently, at the stage of mechanical grinding of the upper plate. The structures appeared after annealing were localized mainly in these defects.

Spots with a diameter from fractions of mm to 2-3 mm (Fig. 1) were observed on the sample surface after annealing up to 900 ° C in air.

Figure 1: Optical micrograph of a silicon sample surface after 900 ° C annealing.

Such spots sometimes had a dendritic structure in the center (Fig. 2). In addition to these spots, smaller spots with a diameter up to 50 μm were visible. Dendrites were formations growing along the surface, mainly from cracks in the upper layer. They expanded to the end, reaching a width of 10 microns, and usually ended with a cap. Secondary Ion Mass Spectrometry (SIMS) is an extremely powerful technique for analyzing surfaces owing in particular to its excellent sensitivity, high dynamic range, very high mass resolution. In order to get chemical information with a highest sensitivity and highest lateral resolution, we have investigated the feasibility of combining SIMS with Scanning Electron Microscopy (Fig.2a).

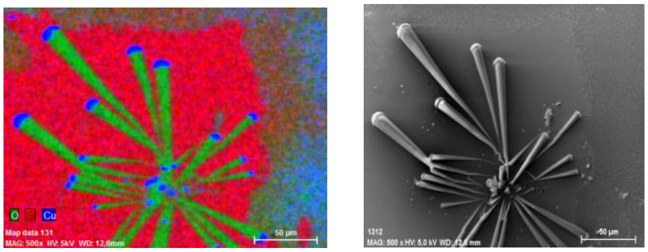

Figure 2: a) Map distribution of oxygen, silicon and copper in the sample; b) SOI image in secondary electrons

Structure elemental analysis by the EDA method showed that dendrites themselves consist of SiO_2, and the caps consist of copper crystals (Fig. 2a, Fig. 3). In addition, the surface of silicon in spots after annealing was covered with a dispersed layer consisting of SiO_2 with copper inclusions.

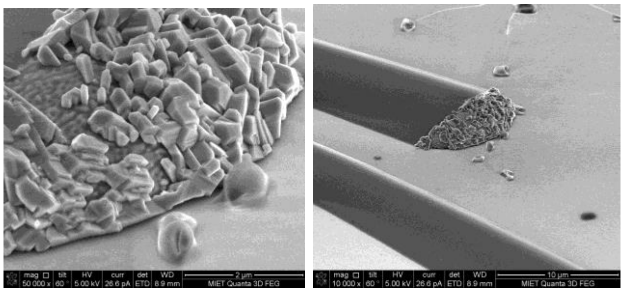

Figure 3: The end of the dendrites and copper crystals on c them.

When annealed at 1000 ° C in air, dendrites occupy an ever larger surface during growth and form a grid (Fig. 4). In addition, interesting features of dendrite growth are revealed:

1) New dendrites grow either from the initial defects of the structure, or from the ends of already grown dendrites;

2) Dendrites never intersect during growth, but are reflected from each other.

When annealing to 1000 °C in an argon medium, dendrites were not formed. Dendrites were formed after annealing in air in a manner similar to the unshielded surface when etched by plasma the upper 10 µm silicon layer. We also have studied the structure of the dendritic germ. The ion beam cross section showed that the germs were fused into the silicon surface at the same approximate depth as the part protruding from the silicon. The section of the dendrite germ thus has the form of a biconvex lens.

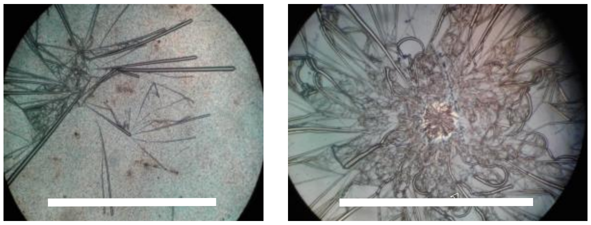

Figure 4: Formation of dendrite grid during annealing at 1000 ^{0}C. The white scale mark has a dimension of 1 mm.

Such interesting structures in defective SOI plates were observed, apparently, for the first time. These results give rise to several questions. The first question is the origin of SiO_2 in germ dendrites. Two basic hypotheses answer this question. The first hypothesis assumes SiO_2 output from the glass layer through defects. The second hypothesis presupposes the oxidation of silicon upon annealing in air. In favor of the second hypothesis is the absence of growing structures upon annealing in an inert medium (argon). The first hypothesis was considered in [4]. However, at present, both hypotheses cannot fully explain the results.

ACKNOWLEDGEMENT

Federal target program (FCP) aimed at "Implementation of applied scientific research and experimental developments aimed at implementing the priorities of the Strategy for Scientific and Technological Development of the Russian Federation"

REFERENCES

[1] Nanotechnology in Electronics. Edited Y.A. Chaplygin. Issue 3. Moscow: Technosphere, 2015, 480 p.

[2] Korobova N. Piezoelectric MEMS technologies" in the book "Advanced Piezoelectric Materials. Science and Technologies". 2-d Ed. Kenji Uchino. Elsevier. 2017. Pp.533-574.

[3] Timoshenkov S., Korobova N., Mikheev A., Timoshenkov A. "Development of MEMS Angular Rate Sensor with Self-calibration Function", Int. Conf. "Actual Issues of Mechanical Engineering" (AIME 2017). Series: Advances in Engineering Research. Vol.133, P.860-865.

[4] Novikov S., Zhigalov V., Korobova N., et al. "Formation of a relief film on the surface of doped monosilicon plates and SOI samples with an anomalously low electron work function". Russ. Journal of Physical Chemistry (in press).

Fumed Silica as Morphological Template for the Synthesis of Luminescent Carbon Nanodots

A.N. Nazarov*, **, A.V. Vasin*, **, D.V. Kysil*, L. Lajaunie***, L. Vaccaro****, G.Yu. Rudko*,
S.V. Sevostianov*****, V.A. Tertykh*****, Yu. P. Piryatinski******, R. Arenal***, *******,
M. Cannas****, and V.S. Lysenko*

*Lashkaryov Institute of Semiconductor Physics NASU,
pr. Nauki 41, 03028 Kyiv, Ukraine
**Igor Sikorsky National Technical University of Ukraine,
pr. Peremogy 37, 03056 Kyiv, Ukraine
***Laboratorio de Microscopías Avanzadas, Instituto de Nanociencia de Aragon, Universidad de
Zaragoza, 50018 Zaragoza, Spain.
****Dipartimento di Fisica e Chimica, Universita degli Studi di Palermo,
I-90123 Palermo, Italy
*****Chuiko Institute of Surface Chemistry NASU
17 Generala Naumova St., 03164 Kyiv, Ukraine
******Institute of Physics NASU
03028, pr. Nauki 46, 03028 Kyiv, Ukraine
*******ARAID, 50018 Zaragoza, Spain

ABSTRACT

Structural and optical properties of carbonized fumed silica nanoparticles (specific area of ≈300 m^2/g) are investigated with the purpose of identifying light-emitting centers that make these materials appealing for applications in nanosensing, photonics, bioimaging. Chemical modification by phenyltrimethoxysilane and thermal annealing in inert atmosphere up to 650 ^oC induce a bright photoluminescence (PL) consisting of two bands: one in the near UV (around 400 nm); another in the visible rang (around 580 nm). The relative contribution of these emissions is studied by steady state and time-resolved photoluminescence spectroscopy; all the obtained results are compared with those observed in fumed silica carbonized using other precursors and treatment procedures. It is found that these two PL bands are observed irrespective of the carbonization procedure and their origin is associated with sub-nanometer carbon particles (nanodots) that can be bonded or adsorbed on the silica surface. Moreover, it is proposed that the energy of emitted photons is determined by the presence or absence of a chemical bond between the emitting clusters and silica surface. These hypotheses are checked by a detailed (S)TEM-EELS study. In fact, we evidence the presence of 2-6 nm carbon dots (CDs), which are not evenly distributed at the surface of the silica nanoparticles. These CDs are mostly amorphous although they possess some degree of graphitization and local order. Finally, the fraction of sp^2 carbon in these nanodots has been estimated to be close to 80 %.

PACS Keywords: carbon dots, fumed silica, photoluminescence

1 INTRODUCTION

At present time, luminescent CDs attract much attention of researchers mainly as novel nanomaterial for bioimaging applications due to absence of citotoxicity and relatively simple synthesis procedures [1]. Nevertheless, identification of physical mechanisms of excitation and light emission in such nanoscale objects is still an outstanding challenge. External quantum yield (QY) of photoluminescence (PL) of CDs diluted in ethanol or aqueous solutions is very high that makes it quite suitable for bioimaging. However, solid state CDs deposited as thin layer or powder by drying procedure exhibits no luminescence. Major mechanism of QY reduction in condensed state is believed to be *aggregation-caused quenching effects* that is well known for conjugated organic molecules dyes. It is suggested that key success to QY enhancement of CDs in solid state lies in the optimization of optical effects in the matrix. Recently, it was reported a QY of CDs in solid state as high as 75% [2], that is comparable to the value typical for commercial inorganic fluorophores on that base of semiconductor quantum dots, thus opening new prospective for CDs in optoelectronic applications. We suggest that proper dispersion of luminescent CDs in nanostructured wide band gap (optically transparent) matrix is one of the ways of avoiding aggregation quenching effects and increasing of PL efficiency. To this aim, fumed silica is a material of choice; its morphological template, characterized by an ultra-high specific surface (up to 500 m^2/g), is believed to be ideal for solid state dispersion of CDs.

2 RESULTS AND DISCUSSION

Fumed silica with specific area of ≈300 m^2/g was carbonized by successive procedures of chemical modification by phenyltrimethoxysilane, propanol or sucrose, followed by thermolysis in the flow of pure nitrogen at atmospheric pressure up to 650 °C for 30 minutes. Structure, morphology and chemical composition were characterized by FTIR spectroscopy, high resolution scanning transmission electron microscopy combined with electron energy loss spectroscopy (STEM-EELS). Emission, excitation, kinetics and photo-induced bleaching of PL were investigated by steady state and time-resolved photoluminescence spectroscopy.

Strong ultraviolet and visible photoluminescence was observed in the samples after chemical modification and thermal annealing (Figure 1). Two types of emission bands were identified depending on the annealing temperature: one is in the near UV and another is in the visible range.

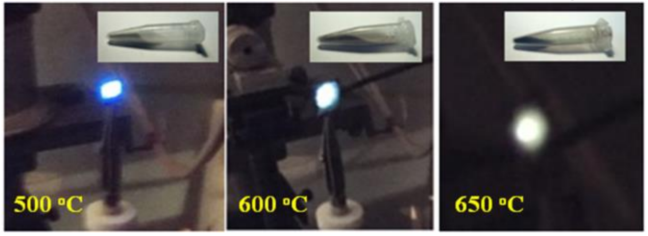

Figure 1. Photo-images of the SiO_2: CDs samples and corresponding light emission under 375 nm excitation.

A detailed (S)TEM-EELS study demonstrates the presence of 2-6 nm carbon nanoclusters distributed at the surface of the silica nanoparticles. These carbon nanoclusters are mostly amorphous although they possess some degree of graphitization and local order; the fraction of sp^2 carbon is estimated to be close to 80 %.

Based on the analysis of emission/excitation of these two bands, as well as on correlations with the synthesis conditions, a structural-energy concept of light-emitting centers has been proposed. According to this model, the light-emitting centers are associated with subnanometer carbon particles (nanodots). It is assumed that the spectral region of radiation is determined by the presence or absence of a chemical bond between the emitting clusters and silica surface: chemical bonding to surface stimulates near UV emission band while weakening of the bonding decreases PL intensity accompanied by red shift of emission spectrum. Such a mechanism of formation of light-emitting centers makes it possible to control the spectral properties of broadband luminescence in the ultra-wide range and further optimization of emission efficiency and stability.

Application perspectives

Optoelectronics SiO_2:CDs under 403 nm excitation originates a bright emission. This finding is promising to develop fluorophores for artificial white light, where the emission properties can be easily tuned by variation of synthesis procedures.

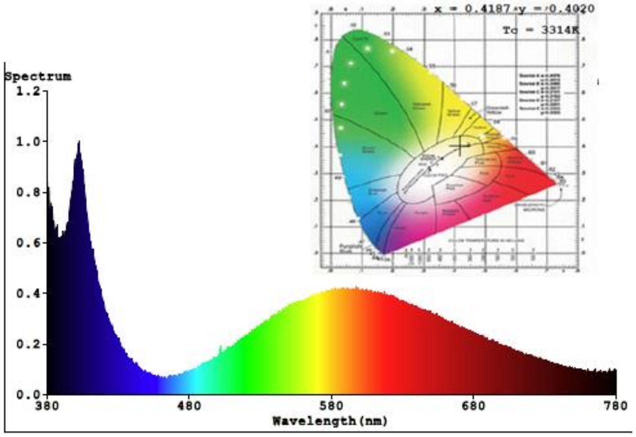

Figure 2. Color properties of light emission of SiO_2:CDs sample (*"phenylsilica"*, ann. 600 °C) under 403 nm excitation: CCT – 3314 K, CRI - 80.

Bioimaging Figure 3 illustrates photo-images of the ethanol solutions of CDs under 409 nm LED. CDs were extracted from suspensions of SiO_2:CDs synthesized at different temperature. Effective multicolor emission is well promising for biomedicine applications as fluorescent nanolabels.

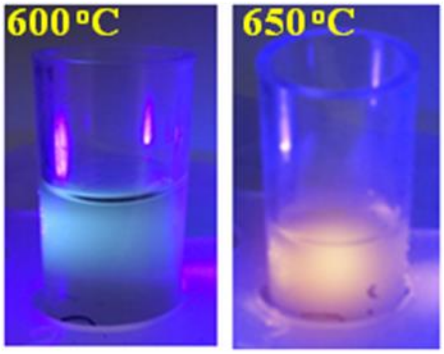

Figure 3. Photo-images of ethanol solution of CDs, extracted from SiO_2:CDs suspension.

REFERENCES

[1] O. S. Wolfbeis, *Chem. Soc. Rev.*, 44, pp.4743 (2015).
[2] L. Pang et al., *Nanotechnology* V.28 p.085305 (2017).

TUESDAY

SESSION

DEVICES – MODELING II

Radiation effects simulation for materials in microelectronics and optoelectronics

Nicolas Richard*, Antoine Jay**, Anne Hémeryck***, Layla Martin-Samos4*, Luigi Giacomazzi5*, Mélanie Raine*, Vincent Goiffon**, Normand Mousseau6*, Sylvain Girard7*, Marc Gaillardin*and Philippe Paillet*

*CEA, DAM, DIF,
F-91297 Arpajon, France.
**ISAE-SUPAERO,
Université de Toulouse, 10 av. E. Belin, F-31055 Toulouse, France
***LAAS/CNRS,
7, av. du Col. Roche, F-31031 Toulouse, France
4*CNR-IOM Democritos
c/o SISSA, via Bonomea 265, IT-34136 Trieste, Italy
5* Materials Research Laboratory, University of Nova Gorica,
Vipavska 11c SI-5270 Ajdovščina, Slovenia
6*Université de Montréal,
C.P. 6128, Succursale Centre-Ville, Montréal, CA-H3C 3J7, Québec, Canada
7*Lab. Hubert Curien,
Université de Lyon F-42000 Saint-Etienne, France.

ABSTRACT

In this talk, we will give an example of study on radiation effects simulation for materials in microelectronics and optoelectronics.

PACS Keywords: silicon, ab initio calculations, multi scale simulation, radiations.

1 INTRODUCTION

In a radiative environment, materials for microelectronics and optoelectronics can suffer different phenomena. Since several years, CEA-DAM-DIF and its partners have studied these phenomena in the materials of interest by coupling experimental characterization with multi-scale simulation in order to make the link between the scale of the phenomena (*i.e.* the atomic scale) and the electrical or optical signals measured in the devices. Here, we give an example of one of the phenomena at stake: the Displacement Damage Dose (DDD). The global simulation project for DDD is given with examples of results and comparison to experiments.

2 DISPLACEMENT DAMAGE DOSE

Displacement Damage Dose (DDD) effects have been studied for a long time, because of historical interest for spatial applications. Numerous studies focused first on image sensors (Charge-Coupled Devices (CCD) and more recently Active Pixel Sensors (APS) or CMOS Image Sensors (CIS)), which dark current distributions directly reflect DDD effects on minority carrier generation rate. Indeed, in recent years, an increasing range of applications for image sensors have appeared, such as high energy physics, fusion, nuclear power plant security, nuclear waste storage security or even medical facilities. That’s why a physical analysis and understanding of these effects have become crucial, in order to deduced mitigating techniques.

2.1 Presentation of the global simulation project

The global simulation project, inspired from the one presented by Srour and Palko in [1], goes from the incident particle interaction in the target material to the resulting electrical effect observed experimentally as shown in Figure 1.

The first step is to simulate the incident particle interaction with the target material using Monte Carlo (MC) to evaluate the energy and the nature of the Primary Knock-On Atom (PKA) in the crystalline structure. The temporal evolution of the resulting defect structure is achieved using two different simulation tools.

First, Molecular Dynamics (MD) simulations are performed to generate the damage structure and to observe its evolution up to nanoseconds. A careful care is given to the consideration of electronic stopping power in the MD simulations, using the Two-Temperature Model (TTM) introduced by Duffy *et al.* [2]. Finally, these simulations are performed on a large number of PKA directions in order to

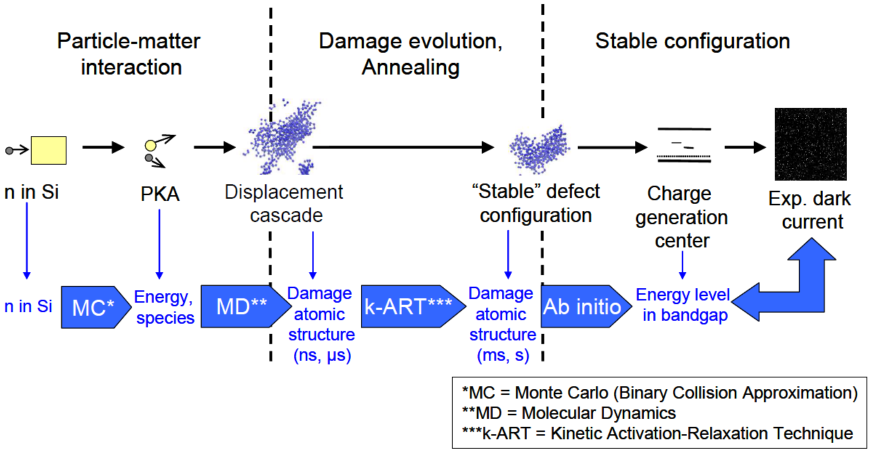

Figure 1: Schematic of the global simulation project.

construct a realistic database of damaged structures. To do so, we also performed simulation on longer timescales than usual studies, i.e. up to seconds and more after the damage generation in order to identify complex defect structures still present in the material after seconds and that could be associated with experimental measurements. These defects structures are then characterized using *ab initio* calculations to achieve this association. This approach and the associated results have been presented in three articles [3,4,5].

2.2 Results

First, the Monte Carlo gives us energies (1 and 10 keV) and species (silicon atoms) of the PKA. Then MD simulations are performed to simulate the displacement cascade and to generate damaged structures after 1 ns as shown in Figure 2.

Starting from these damaged structures, k-ART allows simulating the annealing phase. Examples of the evolution of the defect structures between MD and k-ART is illustrated in Figure 3. The generated clusters are analyzed. We evaluate the atomic structures, the formation energies, the electronic properties, the occupation probability and the lifetimes of the generated defect clusters.

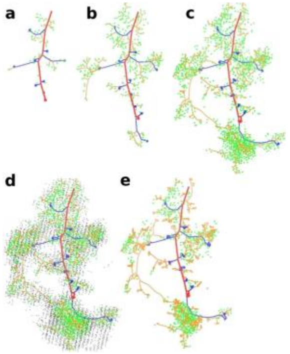

Figure 2: The five characteristic steps occurring during the MD-TTM propagation of the cascade of defects.

One of the important characteristics are the states created by each configuration of a same defect in the band gap of silicon and their associated electronic structure as illustrated in Figure 4.

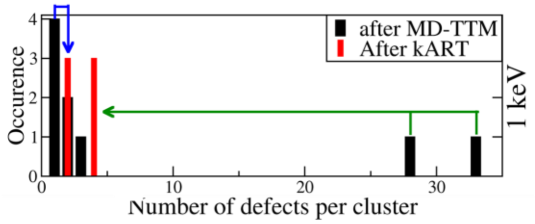

Figure 3: Examples of the variation of the number of defects per clusters for a 1 keV PKA. Black histogram: last step of MD-TTM simulation (1 ns). Red histogram: last step of k-ART simulation (1 min). Blue arrows: agglomeration of point defects. Green arrows: medium clusters total annealing.

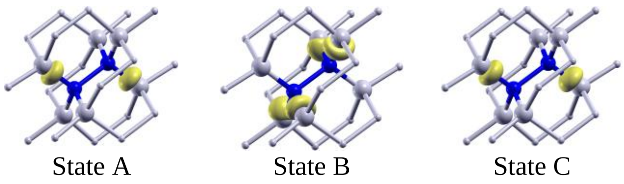
State A State B State C

Figure 4: Electronic wave functions square of the three electronic states A, B, C in the band gap of bulk silicon due to 2Va2 configuration. The yellow surface represents the isovalue for a probability to find the electron in this region equal 50%.

Starting from the generated database, it is then possible to identify the most electronically active defects, that have an negative effect on the performance of the microelectronic or optoelectronic devices, as it will be shown during this talk.

3 CONCLUSION

In order to describe the displacement damage in silicon, we here present our simulation approach. Results and links with experiments will be presented in the talk. Methods to describe other radiation effects such as Total Ionizing Dose will also be discussed and perspectives for future studies will be given.

REFERENCES

[1] J. R. Srour and J. W. Palko, NSREC Short Course, 2013.

[2] D. Duffy and A. Rutherford, *J. Phys.: Condens. Matter*, vol. 19, pp. 016207, 2007.

[3] M. Raine *et al.*, IEEE Trans. Nucl. Sci., vol. 64, no. 1, pp. 133-140, Jan. 2017.

[4] A. Jay *et al.*, IEEE Trans. Nucl. Sci., vol. 64, no. 1, pp. 141-148, Jan. 2017.

[5] A. Jay *et al.*, IEEE Trans. Nucl. Sci., vol. 65, no. 2, pp. 724-731, Jan. 2017.

HEMT Sensitivity to Optical Radiation: Distinguishing Microwave Noise Aspect

Alina Caddemi*, Emanuele Cardillo*, and Giovanni Crupi**

*Department of Engineering, University of Messina, C.da Di Dio, Sant'Agata, 98166 - Messina, Italy
**BIOMORF Department, University of Messina, Via Consolare Valeria, 98100 - Messina, Italy

ABSTRACT

This contribution aims at providing an overview of the distinguishing features of the HEMT performance under illumination. The analysis is carried out in terms of dc, scattering and noise parameters on HEMTs based on GaAs and GaN technologies.

PACS Keywords: III-V semiconductors, field effect devices, processes caused by visible and UV light

1 INTRODUCTION

Due to the material bandgap characteristics and related physical properties, the light sensitivity of III-V compound semiconductor devices is a well assessed feature and several studies have been presented to the scientific community on the influence of light exposure on the dc and small-signal parameters of high electron mobility transistors (HEMT) at microwave and millimeter wave frequencies [1, 2]. Gallium arsenide (GaAs)-based HEMTs are typically employed when demanding low-noise and high frequency gain are needed, whereas Gallium-nitride (GaN) on Silicon Carbide (SiC) substrate HEMT's are used when high power amplification is required in the microwave frequency range. On the other hand, we noticed that not enough works have addressed a careful and complete analysis of the effects of the light exposure on the noise performance of HEMTs [3-5]. During the last years, our effort has been directed towards filling this gap with an extensive experimental activity during which a large amount of data on the noise parameters of illuminated HEMTs has been gathered [6, 7]. Afterwards, a model extraction activity has also been carried out aimed at establishing a compact representation of the observed device behavior [8, 9]. Some comparison with analytical noise models has also been recently presented to account for the most topical aspects of light exposure of HEMTs by using intrinsic noise coefficients [10]. Here, we report and discuss the main findings of our study to provide a clear understanding of the HEMT sensitivity to optical radiation.

2 RESULTS AND DISCUSSION

As far as the GaAs HEMTs are concerned, both lattice-matched and pseudomorphic devices have been tested by using a laser beam exposure in the visible wavelength range. The most frequently chosen wavelength value to work with GaAs HEMTs was 650 nm that can be absorbed by either the undoped (GaAs, InGaAs) layer or the donor layer (AlGaAs) thus stimulating a substantial amount of charge generation triggered by the concurrent photoconductive and photovoltaic processes. Owing to a significant threshold voltage shift generated by the internal photovoltaic effect, for all tested devices an increase of drain current, transconductance, and magnitude of the low-frequency transmission coefficient S_{21} was observed in line with the research findings known to the scientific community. Then, the attention has been focused on the noise parameters of the transistors, typically in the 2-18 GHz frequency range, since very strong variations have emerged in the dark vs. light comparison. All the devices under test exhibited a severe degradation of the minimum noise figure (as shown in Fig. 1(c, d) for three scaled HEMTs) and a decrease of the optimum noise source reflection coefficient, basically attributed to the strong increase of the gate noise current under light exposure. This illustrated in Fig.1 showing that the light exposure leads to a higher gain but a degradation in the noise performance for three GaAs scaled HEMTs.

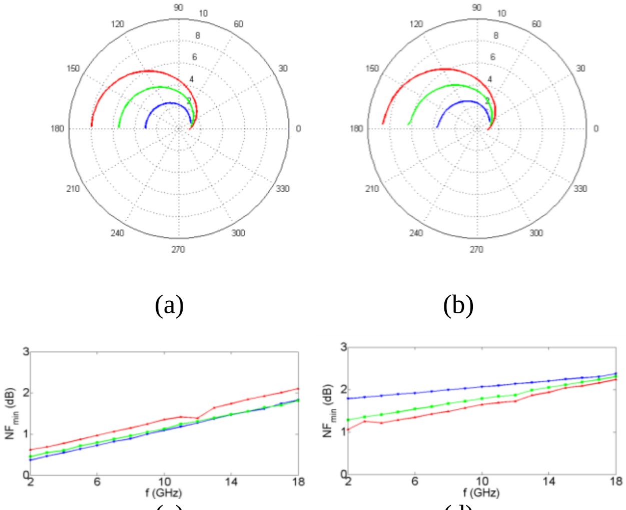

(a) (b)

(c) (d)

Fig. 1 – Measured S_{21} from 0.1 to 26.5 GHz (a, b) and NF_{min} from 2 to 18 GHz (c, d) for three GaAs HEMTs with gate widths of 100 μm (blue line), 200 μm (green line), and 300 μm (red line) without (a, c) and under 650 nm illumination (b, d) at V_{GS} = -0.6 V and V_{DS} = 2.5 V.

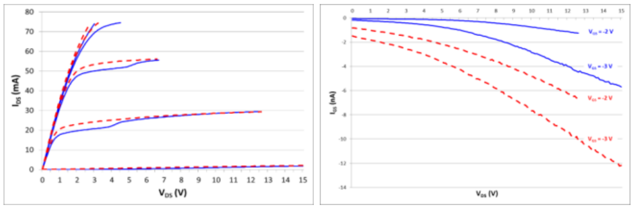

(a) (b)

Fig. 2 - Measured dc behavior of the GaN HEMT without (blue solid line) and with (red dashed line) UV illumination: I_{DS}-V_{DS} a V_{GS} values from −3 V to 1 V with 1 V step (a), I_{GS}-V_{DS} at V_{GS} values of -3 V and -2 V (b).

For the case of GaN HEMTs, an UV light irradiation (375 nm) was employed. The device, having 0.25 μm gate length and 100 μm gate width, was characterized by measuring its dc performance, linear scattering and noise parameters both in dark condition and under CW light exposure [11]. In addition, a circuit model was extracted for a closer analysis of the illumination effects. A slight internal photovoltaic effect and a small photoconductive current were expected because the incident photon energy was too low to interact with the AlGaN material, even for a reduced value of the Al mole fraction (typically, for GaN HEMT an Al content of 0.2 ÷ 0.4 is used). As a result, we could observe only small variations of the dc and the microwave parameters but consistent with the results previously obtained with GaAs devices. In Fig. 2 we report the dc behavior of a GaN HEMT on SiC without (blue solid line) and with (red dashed line) UV illumination, showing a significant increase of the gate current.

Recently, we have performed an application-oriented study where the performance of X-band low-noise amplifiers with HEMTs exposed to laser irradiation has been investigated [12]. Following the theoretical analysis, a pHEMT-based amplifier has been realized and tested with a 635 nm laser beam. The experimental results have confirmed the role played by the light exposure on the noise figure and the gain of the LNA at various bias conditions. By varying the bias point from the standard bias conditions towards the device pinch-off, the light effects change from causing a degradation of the noise figure and the gain towards stimulating a performance improvement. The role played by the increase of the photo-generated gate current on the noise figure degradation is recognizable, but closer to pinch-off this effect is completely canceled by increase of both the transconductance and the drain current due to the optical charge generation.

3 CONCLUSIONS

It has been illustrated that the light exposure might significantly affect HEMT performance. The results of this study can be very useful for communication applications, where transistors are optically controlled to perform various functions of microwave electronic circuits (e.g., gain control of amplifiers, frequency tuning or locking in oscillators, and phase shifting in phase shifters).

REFERENCES

[1] V. Sorianello, L. Colace, S. Rajamani, and G. Assanto, “Design and simulation of optically controlled field effect transistors,” Physica Status Solidi, vol. C11, pp. 81–84, Jan. 2014.

[2] S. Jit, G. Bandhawakar, and B. B. Pal, “Analytical modeling of a DCFL inverter using normally-off GaAs MESFETs under dark and illuminated conditions,” Solid-State Electronics, vol. 49, pp. 628–633, Apr. 2005.

[3] A. Thomasian, A. Rezazadeh, J. Everard, and I. Ipwood, "Experimental evidence for trap-induced photoconductive kink in AlGaAs/GaAs HEMT’s," Electron Letters, vol. 26, pp. 1094–1095, July 1990.

[4] L. Escotte, K. Grenier, J.G. Tartarin, and J. Graffeuil, “Microwave noise parameters of InGaAs pseudomorphic HEMTs under optical illumination," IEEE Trans. Microw. Theory Techn, vol.46, pp.1788-1789, Nov. 1998.

[5] A.A. de Salles, and M. A. Romero, “Al0.3Ga0.7/GaAs HEMT’s under optical illumination,” IEEE Trans. Microw. Theory Techn, vol. 39, pp. 2010-2017, Dec. 1991.

[6] A. Caddemi, G. Crupi, E. Fazio, S. Patanè, and G. Salvo, “Remarks of an extensive investigation on the microwave HEMT behavior under illumination,” IEEE Microw. Wireless Comp. Lett., vol. 24, no. 2, pp. 102-104, Feb. 2014.

[7] A. Caddemi, G. Crupi, and G. Salvo, “A link between noise parameters and light exposure in GaAs pHEMT's,” Solid-State Electron., vol. 105, pp. 16-20, Mar. 2015.

[8] A. Caddemi, E. Cardillo, and G. Crupi, “Microwave noise parameter modeling of a GaAs HEMT under optical illumination,” Microw. Opt. Tech. Lett., vol. 58, no. 1, pp. 151-154, Jan. 2016.

[9] A. Colangeli, W. Ciccognani, E. Limiti, A. Caddemi, G. Crupi, and G. Salvo, “Black-box noise modeling of GaAs HEMTs under illumination,” Int. J. Numer. Modell. Electron. Networks Devices Fields, vol. 28, no 6, pp.698-706, Nov/Dec. 2015.

[10] A. Caddemi, E. Cardillo, and G. Crupi, “Light activation of noise at microwave frequencies: A study on scaled GaAs HEMT's,” IET Circuit, Devices & Systems, DOI: 10.1049/iet-cds.2017.0290 , Available online: 21 Nov. 2017.

[11] A. Caddemi, E. Cardillo, G. Salvo, and S. Patanè, “Microwave effects of UV light exposure of a GaN HEMT: Measurements and model extraction,” Microel. Reliab., vol. 65, pp.310-317, Oct. 2016.

[12] A. Caddemi, E. Cardillo, and G. Crupi, “Comparative analysis of microwave low-noise amplifiers under laser illumination,” Microw. Opt. Tech. Lett., vol. 58, no. 10, pp. 2437-2443, Oct. 2016.

Damping mechanisms of piezoelectric quartz tuning forks used in photoacoustic spectroscopy for gas sensing

Giansergio Menduni[*,**], Pietro Patimisco[*], Angelo Sampaolo[*], Marilena Giglio[*], Vittorio M.N. Passaro[**]
and Vincenzo Spagnolo[*]

[*]PolySense Lab - Dipartimento Interateneo di Fisica, Politecnico and University of Bari,
Via Amendola 173, Bari, Italy
[**]Photonics Research Group, Dipartimento di Ingegneria Elettrica e dell'Informazione,
Politecnico of Bari, Via Orabona 4, Bari, 70126, Italy

ABSTRACT

We reported on a study of the dependence of main loss mechanisms from the geometry of piezoelectric quartz tuning forks (QTFs). The influence of these loss mechanisms on the quality factor *Q* occurring while the QTF vibrates at the in-plane flexural fundamental and first overtone resonance modes is investigated. The resonance frequencies and related *Q*-factors for five different QTFs have been measured. The QTFs response was recorded at different air pressures to investigate the influence of the surrounding medium on the *Q*-factor. A data analysis demonstrated that air viscous damping is the dominant energy dissipation mechanism for both flexural modes. Thermoelastic and support losses are additional contributions that strongly depend on the QTF geometry.

PACS Keywords: quartz tuning fork, quality factor, flexural vibration mode, loss mechanisms.

1 INTRODUCTION

A piezoelectric quartz tuning fork (QTF) is an acoustic resonator in the form of a two-pronged fork. QTFs have proven to be extremely useful as sensors for temperature, mass, pressure and friction. In the last few years, QTFs have been implemented also for several applications, like atomic force microscopy, near-field optical microscopy and quartz-enhanced photoacoustic spectroscopy (QEPAS) for gas sensing applications. For QEPAS, the QTF resonance quality-factor *Q*, defined as the ratio of the total input energy into the device to the energy dissipated within a vibration cycle, is the most important parameter. The QEPAS sensor signal *S* can be expressed as $S \propto (Q \cdot P_L \cdot \alpha)$, where α is the gas target absorption coefficient and P_L is the laser power. Furthermore, a high quality-factor also implies a small resonance bandwidth, which makes the resonator response more selective in detecting external excitations and high *Q*-values correspond to low dissipation losses. To realize custom QTF resonators with a high *Q*-factor, it is important to understand the main physical factors contributing to the energy dissipation.

2 DAMPING MECHANISMS

The main loss mechanisms in a QTF are due to: (i) air damping, related to the transfer of energy and momentum from the QTF prongs to the surrounding medium; (ii) support loss, related to transfer of mechanical energy from the vibrating prong to the support; (iii) thermo-elastic damping, related to coupling between the strain field and the temperature field inside the QTF. Air damping is referred to as an extrinsic loss mechanism, while thermo-elastic and support damping are referred to as intrinsic loss mechanisms. All these loss mechanisms strongly depend on prong size and the dynamics of the vibrational mode under consideration. Several theoretical models have been proposed for each loss mechanism and their dependence on the main physical parameters have been reported. Each loss contribution is independent from the other, but all occur simultaneously for a vibrating QTF prong.

2.1 Air damping

When a QTF vibrating prong is immersed in air, a drag force is exerted on it. In the viscous region, the medium acts as a viscous fluid and the drag force is calculated using fluid mechanics. With the assumption that the length *L* of the QTF prong is much greater than its thickness *T* and crystal width *w*, Hosaka et al. [1] derived a formulation of the quality factor related to fluid damping (Q_{air}):

$$Q_{air} = \frac{4\pi\rho T w^2 f_n}{3\pi\mu w + \frac{3}{4}\pi w^2 \sqrt{4\pi\rho_{air}\mu f_n}} \tag{1}$$

where ρ_{air} is the air density and μ its viscosity; f_n identifies natural resonance frequencies for in-plane flexural mode; ρ = 2650 Kg/m^3 denotes the quartz density. Losses due to the air damping, proportional to the reciprocal of Q_{air}, consists of two terms: one pressure-independent (assuming a negligible dependence of f_n on the air pressure) and the other one pressure-dependent. The Q_{air} depends on the air pressure as well as the resonance frequency and the prong sizes.

2.2 Support losses

Several models have been developed to analyze support loss. The simplest model was developed by Hao et al. [2], in which the prong is supposed to be a rectangular cross-section resonator, attached monolithically to a larger support with the same thickness as that of the prong. The crystal thickness w is assumed to be much smaller than the elastic wavelength λ of the propagating waves. The closed-form expression for the quality factor related to the support loss in a clamped-free cantilever can be expressed as:

$$Q_{\text{sup}} = A_n \frac{L^3}{T^3} \tag{2}$$

with A_n coefficients depending on the resonance mode number and the prong material. Hao et al. estimated A_0 = 2.081 for the fundamental mode and A_1 = 0.173 for the first overtone mode. The straightforward approach for reducing support losses is designing QTFs having prongs with large length-to-thickness aspect ratios. In addition, higher order modes suffer higher support losses

2.3 Thermo-elastic damping

Thermo-elastic dissipation is an intrinsic structural dissipation mechanism of the oscillating elements, which can be expressed using a modelling approach proposed by Zener [3]. The quality factor Q_{TED} related to thermo-elastic loss for an isotropic homogeneous beam can be expressed as:

$$Q_{TED} = \frac{\rho c_T}{E\beta^2\Theta} \frac{1+\left(\dfrac{2\rho c_T T^2 f_n}{\pi\lambda_T}\right)^2}{\dfrac{2\rho c_T T^2 f_n}{\pi\lambda_T}} \tag{3}$$

where λ_T , c_T and β are the thermal conductivity, the heat capacity per unit mass and the thermal expansion of the prong, respectively; Θ represents the prong temperature and $E = 0.72\cdot10^{11}$ N/m^2 is the quartz Young's modulus. Thermoelastic damping decreases as the resonance mode number increases, implying that the fundamental mode is the most affected by this type of loss mechanism.

3 RESULTS

To investigate the dependence of loss mechanisms on the prong size of QTFs vibrating at the fundamental and overtone modes, we designed and realized a set of five different QTFs [4]. The QTF resonance frequencies and quality factors were measured by exciting them electrically with a sinusoidal voltage and by acquiring the QTF response signal with a lock-in amplifier, which demodulates the signal at the same frequency of the excitation voltage. QTF response signals were acquired at different air pressures P, in the range 25-760 Torr. In Table I, the prong sizes (in mm), the resonance frequencies (in kHz) and related Q-factors are reported for the fundamental (subscript 1) and first overtone mode (subscript *2*), for all investigated QTFs, at P = 50 Torr.

QTF	L	T	w	f_1	Q_1	f_2	Q_2
#1	3.5	0.25	0.2	14.07	9100	86.6	18960
#2	10.0	0.25	0.9	7.21	23630	41.0	19180
#3	10.0	0.50	1.0	8.45	36150	51.0	30270
#4	11.0	0.25	0.5	3.45	8850	21.5	32850
#5	17.0	0.25	1.0	2.87	14990	17.7	49490

Table 1: Prong sizes (in mm), resonance frequencies (in kHz) and related Q-factors for the investigated QTFs measured at a 50 torr, in air.

Since the dissipation mechanisms are assumed independent of each other and the resonator quality factor is proportional to the inverse of total energy dissipated, the overall Q-factor can be represented as a reciprocal sum of independent dissipative contributions:

$$\frac{1}{Q(P)} = \frac{1}{Q_{air}} + \frac{1}{Q_{\text{sup}}} + \frac{1}{Q_{TED}} \tag{4}$$

We demonstrated that the dependence of the measured quality factors on air pressure follows the trend of Q_{air} reported in Eq. (1), suggesting that the dominant loss mechanism is air damping for both modes. By using dependences reported in Eq. (2)-(3), we demonstrated that support losses can be neglected at the fundamental mode while they became relevant for the overtone mode [5]. At the fundamental mode, the second dissipation mechanism is related to thermo-elastic damping. In addition, air damping is reduced at the first overtone mode with respect to the fundamental mode and support losses become the relevant mechanism of energy dissipation at low pressures. All these results represent a guideline for the design of QTFs optimized for QEPAS applications.

REFERENCES

[1] H. Hosaka, K. Itao, S. Kuroda, Sensor. Actuat. A-Phys., vol. 49, pp. 87-95, 1995.

[2] Z. Hao, A. Erbil, F. Ayazi, Sensor. Actuat. A-Phys., vol. 109, pp. 156-164, 2003.

[3] C. Zener, Phys. Rev., vol. 53, pp. 90-99, 1930.

[4] P. Patimisco, A. Sampaolo, L. Dong, M. Giglio, G. Scamarcio, F.K. Tittel, and V. Spagnolo, Sensor Actuat. B-Chem., vol. 227, pp. 539-546, 2016.

[5] P. Patimisco, A. Sampaolo, V. Mackowiak, H. Rossmadl, A. Cable, F.K. Tittel, V. Spagnolo, IEEE Trans. Ultrason. Ferroelect. Freq. Control., *submitted* (2018).

The origin of radiation tolerance in amorphous $Ge_2Sb_2Te_5$ phase-change random-access memory material

Konstantinos Konstantinou, Tae Hoon Lee, Felix C. Mocanu, and Stephen R. Elliott

Department of Chemistry,
University of Cambridge
Lensfield Road
Cambridge CB2 1EW
UK

ABSTRACT

Radiation-hardness in amorphous $Ge_2Sb_2Te_5$ phase-change random-access memory (PCRAM) material has been studied by *ab initio* density-functional-theory (DFT) based molecular-dynamics simulations. Ionising radiation events, involving self-ions as the primary knock-on species, have been modelled to study their effect on the atomic and electronic structure of the glass. The simulations reveal a structural recovery of the amorphous network after exposure to the high-energy events modelled in this study. The electronic structure of the modelled system is not significantly affected by the ionizing radiation. These results provide a detailed insight into the atomistic structure of amorphous $Ge_2Sb_2Te_5$ after irradiation and demonstrate the radiation-tolerance of the glass matrix.

PACS Keywords: radiation damage/tolerance, ion irradiation, phase-change memory, *ab initio* molecular dynamics

1 INTRODUCTION

Radiation-hard, non-volatile memories with large capacity, low production cost and small power consumption are in high demand by the space community for use in solid-state data recorders or as boot memories for micro-processors and field-programmable gate arrays [1, 2]. Size down-scaling of silicon complementary metal–oxide–semi-conductor (CMOS) floating-gate (FLASH) memory cells is becoming the crucial obstacle to their use for devices in space [1]. In particular, further thinning of the oxide dielectric layer will result in a reduction of the data-retention capability due to the oxide leakage current [3].

Consequently, alternative data-storage concepts are being actively developed; one of the most promising options is phase-change random-access memory (PCRAM) [4]. PCRAM features high cycling capability, good data-retention characteristics and appreciable scaling potential [5]. The prototypical material employed in PCRAM is the ternary chalcogenide alloy, $Ge_2Sb_2Te_5$ (225GST), which exhibits ultra-rapid (~10ns), reversible amorphous-to-crystalline phase transitions, an appreciable electrical-resistivity contrast between amorphous (a-) and crystalline (c-)phases and good data-storage lifetimes [6].

The potential of PCRAM for radiation-hard applications was recognized early on [7]. In PCRAM, binary data are represented as a structural phase rather than by stored electrical charge; thus, these devices are supposed to be tolerant to ionizing-radiation effects [3]. Radiation-hard memories of relatively small size with 250-nm feature size are already available [8]. BAE systems has been developing a 4-Mbit non-volatile chalcogenide RAM, which is radiation-hard and meets rigorous reliability requirements, making it a promising candidate for spaceship applications [8]. Radiation effects on PCRAM have been addressed in a few experimental studies [2, 3, 5, 8–11]. A PCRAM-cell array with a 225GST film used as the storage medium has been fabricated by a standard CMOS process [12]. X-ray irradiation experiments showed that both the higher and lower resistance states can be maintained, even at large radiation doses, highlighting an overall good radiation-tolerance ability [12]. Total ionizing dose effects and single-event effects on a 64-kbit PCRAM array integrated with radiation-hardened CMOS technology have shown a high resistance against ionizing radiation [10]. Irradiation of 180-nm cells, both with heavy ions and protons, confirmed a good response to irradiation events; the (small) observed degradation was attributed to radiation effects in selection devices and peripheral electrical circuitry [5]. Investigation of single-event effects on 90-nm PCRAM cells in a large array (128-kbit) also verified the radiation-hardness of the cells [2].

In spite of such experiments, no atomistic calculations of ion irradiation in a-225GST have been performed to investigate radiation effects and shed light on the atomistic structure of the irradiated glasses. In this work, DFT-based *ab initio* molecular-dynamics (AIMD) simulations were made to examine the effect of ionising radiation on the atomic and electronic structures of a-225GST. Study of the short- and medium-range order in our simulated glass structures allows us to gain direct insight into the structural evolution and the overall response of the material to radiation. In addition, electronic-structure calculations provide further information about the effect of radiation events on the electronic properties of the glass.

2 METHODS

A 315-atom model of a-225GST, previously generated by AIMD [13], was used to model radiation damage in this study, with the individual number of atoms being Ge = 70, Sb = 70 and Te = 175; the simulation cell size corresponds to the experimental density (5.88 g/cm^3) [14].

Ion irradiation was modelled by carrying out a thermal-spike simulation [15]. A Te primary knock-on atom (PKA) was given initial velocities consistent with kinetic energies of 50, 100 or 200 eV, and the cascade was launched from one corner along the body diagonal of the model to maximize the range. Other atoms were assigned a velocity distribution corresponding to a temperature of 300 K. The system was allowed to evolve, undergoing NVE Born-Oppenheimer AIMD. A damping outer layer of 1.0 Å thickness was placed around the edges of the 21.65 Å simulation box in order to model the dissipation of heat from the irradiated area by using generalized Langevin MD [16]. The total simulation time of the ion irradiation was 12-16 ps, depending on the chosen thermal-spike energy, sufficient for the system to equilibrate at 300 K.

A scheme of mixed NVE Born-Oppenheimer and NVT Langevin AIMD, as implemented in CP2K [17], was used in the simulations. The electronic structure was treated through the Kohn–Sham formulation of DFT using the generalised-gradient approximation with Perdew–Burke–Ernzerhof exchange-correlation functionals. CP2K uses a Gaussian basis set with an auxiliary plane-wave basis set. All atomic species were represented by using a triple-ζ valence-polarised Gaussian basis set, in conjunction with the Goedecker-Teter-Hutter pseudopotential. Four, 5 and 6 valence s and p electrons were used for Ge, Sb and Te, respectively. The plane-wave energy cutoff was set to 250 Ry to efficiently solve the Poisson equation within the Quickstep approach [16].

3 RESULTS

A representative result from our AIMD studies of the effects of ion implantation and the resulting radiation-induced effects in a-225GST is shown in Fig. 1: an image of the PKA trajectory and the secondary cascade.

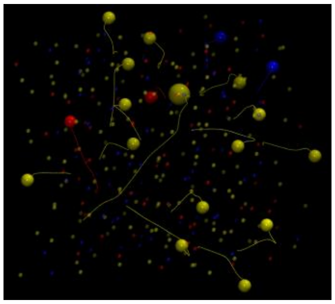

Figure 1: Spatial evolution of the radiation-damage cascade in a-225GST for a 200 eV Te PKA (large yellow sphere) during the first 500 fs. Secondary-cascade Ge atoms, blue; Sb, red; Te, yellow.

It was found that the PKA created transitory large vacancies in its wake, associated with a transient increase and then a decrease in the total number of bonds, and a corresponding diminution of the local medium-range order (e.g. represented by the number of atoms in planes); all these structural changes disappeared after ~10 ps after the launch of the PKA, indicating that the a-225GST structure self-heals after radiation damage.

REFERENCES

[1] Gerardin S, Paccagnella A, IEEE Trans. Nucl. Sci., 57, 3016 (2010).
[2] Gerardin S et al, IEEE Trans. Nucl. Sci., 58, 2755 (2011).
[3] Gasperin A et al, IEEE Trans. Nucl. Sci., 55, 2090 (2008).
[4] Bez R, Pirovano A, Mat. Sci. Sem. Proc., 7, 349 (2004).
[5] Pirovano A et al, IEEE Trans. Dev. and Mat. Reliab., 4, 422 (2004).
[6] Raoux S et al, Chem. Rev., 110, 240 (2010).
[7] Ovshinsky SR et al, IEEE Trans. Nucl. Sci., 15, 311 (1968).
[8] Rodgers J et al, 4-Mb non-volatile chalcogenide random access memory designed for space application, Non-Volatile Mem. Tech. Symp., Pacific Grove, CA (2008).
[9] Bernacki S et al, IEEE Trans. Nucl. Sci., 47, 2528 (2000).
[10] Maimon JD et al, IEEE Trans. Nucl. Sci., 50, 1878 (2003).
[11] Maimon JD et al, IEEE Aerospace Conf. Proc., 4, 2306 (2004).
[12] Wu L-C, et al, Chin. Phys. Lett., 23, 2557 (2006).
[13] Lee TH, Elliott SR, Adv. Mat., 29, 1700814 (2017).
[14] Njoroge WK et al J. Vac. Sci. Tech. 20, 230 (2002)
[15] Prasai K, Drabold D, Nano. Res. Lett., 9, 594 (2014).
[16] Åhlgren EH et al, Appl. Phys. Lett. 100, 233108 (2012).
[17] VandeVondele J et al, Comp. Phys. Comm. 167, 103 (2005).

WEDNESDAY

SESSION

2D AND ADVANCED DIELECTRICS MATERIALS

Graphene – SiO_2 interaction from composites to doping

S. Agnello[*, **], A. Armano[*,***], G. Buscarino[*], M. Cannas[*], F.M. Gelardi[*], F. Giannazzo[****], E. Schiliro'[****], R. Lo Nigro[****]

[*]Dept. of Physics and Chemistry, University of Palermo
Via Archirafi 36, 90123, Palermo, Italy
[**]AteN Center, University of Palermo, Viale delle Scienze - Ed.18, I-90128, Palermo, Italy
[***]Dept. of Physics and Astronomy, University of Catania
Via Santa Sofia 64, 95123 Catania, Italy
[****]CNR-IMM
Strada VIII 5, 95121 Catania, Italy

ABSTRACT

An overview of the interaction between monolayer Graphene and SiO_2 dielectric substrate is reported focusing on the effect this latter has on doping and strain induced by thermal treatments in controlled atmosphere. The disentanglement of strain and doping is highlighted and the comparison with another dielectric substrate of Al_2O_3 evidences the critical role that the substrate has in the electronic properties of Graphene. The reported results pave the way for microelectronic devices based on Graphene on dielectrics and for Fermi level tuning in composites of Graphene and nanoparticles.

PACS Keywords: 78.55.Qr Amorphous materials; glasses and other disordered solids, 74.62.Dh Effects of crystal defects, doping and substitution, 65.80.Ck Thermal properties of graphene

1 INTRODUCTION

Graphene (Gr) is the first two dimensional material ever experimentally discovered [1]. It is composed of a single atomic layer of sp^2-hybridized C atoms in a hexagonal honeycomb structure, derived for the first time from exfoliation of graphite. The Gr high electron mobility and transparency are the basis for its application in optoelectronic devices [2]. In this context, the need for opportune substrates has been shown to be critical since these latter could affect the same Gr properties and, as a consequence, Gr substrate interaction deserves detailed study [3, 4]. In particular, the substrate could enable the trapping of molecules or influence the structural modification of Gr by strain imposed by mechanical mismatch [5, 6].

The SiO_2 is historically the first substrate used to identify Gr but it is also the most used insulator in electronic MOS devices where Gr is of interest for high mobility channel production [2]. By the way, SiO_2 on Si induces both strain and thermal doping of Gr in presence of opportune molecules [5]. These aspects are the focus for research, on the one side, to deepen the possibility to opportunely open a gap in Gr and to pave the way for this latter application and, on the other side, to preserve Gr features during its use in stressed configurations.

In this work a detailed study of the effects of thermal treatments in controlled atmosphere of monolayer Gr transferred on SiO_2/Si is reported, evidencing the efficiency of p-type doping and its reversibility as well as its thermodynamic features. A comparison with Gr transferred on Al_2O_3/Si enabled to highlight the relevant role played by substrate in doping efficiency and stability, showing the better performances of SiO_2.

2 EXPERIMENTAL

Single layer Gr produced by chemical vapor deposition (CVD) on copper and transferred by Poly(-methyl methacrylate) (PMMA) on the final substrate has been investigated. In particular, 300 nm thickness thermal SiO_2 film grown on Si wafer substrate (Gr/SiO_2/Si), and 100 nm thickness Al_2O_3 film grown by atomic layer deposition (ALD) on Si (Gr/Al_2O_3/Si) have been used. Gr deposited on the substrates has been subjected to thermal treatments in controlled atmosphere of N_2, O_2, CO_2, H_2O or vacuum (~10^{-4} mbar) up to 300°C, both exploring the temperature and the treatment time effects. Room temperature MicroRaman measurements with laser excitation at 532 nm as well as Atomic Force Microscopy (AFM) measurements have been carried out to evaluate the structural and morphological changes together with doping effects.

3 RESULTS

Optical microscopy investigation has shown that transferred Gr is constituted by ≥10μm width flakes. The

AFM measurements have highlighted the thickness and typical roughness of distended monolayers of Gr. MicroRaman measurements have been carried out in different points of the flakes to statistically characterize the monolayer properties. As reported in fig.1, both Gr deposited on SiO_2 and Gr deposited on Al_2O_3 have the characteristic bands of monolayer with amplitude ratio of 2D band, at ~2680 cm^{-1}, to G band, at ~1586 cm^{-1}, larger than 2. Furthermore, no relevant D band, at ~1340 cm^{-1}, is found highlighting the low defectiveness of Gr.

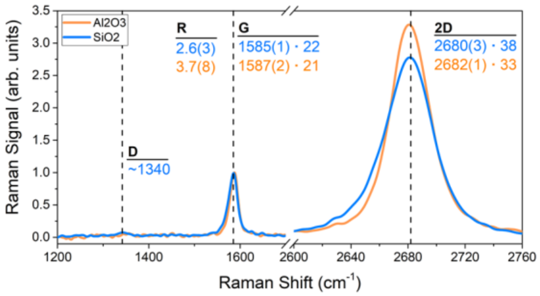

Figure 1: Raman spectra of graphene transferred on SiO_2 (blueline) and on Al_2O_3 (orange line). Numbers in parenthesis refer to the error on the last digit whereas numbers after the dots refer to the full width at half maximum (FWHM).

The thermal treatments of $Gr/SiO_2/Si$ induced the change of the Raman bands already reported in literature [7], featuring a blue shift of 2D and G bands peak positions and a decrease of their amplitude ratio (R) to 1. As shown in Fig.2, the same effects are induced by a thermal treatment in O_2 of $Gr/Al_2O_3/Si$. In particular, the amplitude ratio reaches the value ~1 and a blue shift is found of ~19 cm^{-1} and ~15 cm^{-1} in 2D and G bands, respectively. Furthermore changes in FWHM are found. Overall these changes are in agreement with a Gr p-type doping in contrast to previous findings for Al_2O_3 prepared by sputtering [5]. A similar treatment in N_2 is not effective in doping but induces changes attributable to strain and to some amorphous carbon generation. These results evidence the relevance of substrate preparation in affecting the Gr.

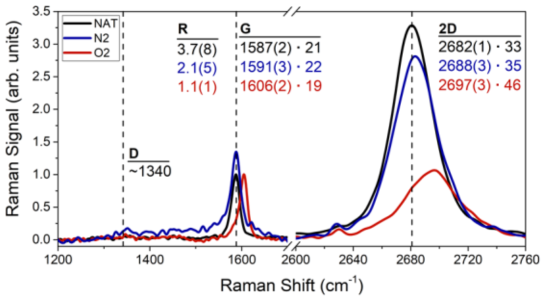

Figure 2: Raman spectra of graphene on Al_2O_3 thermally treated at 300°C in nitrogen (blue line), or oxygen (orange line) and untreated (black line). Numbers in parenthesis refer to the error on the last digit whereas numbers after the dots refer to the full width at half maximum (FWHM).

The detailed study of the different treatments as a function of temperature and time evidences some differences between $Gr/SiO_2/Si$ and $Gr/Al_2O_3/Si$. In particular, it is found that the Al_2O_3 substrate maintains larger strain with respect to SiO_2. Other differences are found in the de-doping effect induced by air moisture. The H_2O molecules affect the doping in both substrates but do not remove strain in the case of Al_2O_3. The doping induced by O_2 at different intermediate temperatures between 150°C and 300°C shows a larger charge concentration in the case of SiO_2 with respect to Al_2O_3. Being the maximum doping level attained at 300°C the same for the two substrates, lower doping activation energy is guessed for SiO_2. Also, the kinetics studies at fixed temperature as a function of time evidence a larger timescale to get equilibrium in the case of Al_2O_3 featuring a lower Gr doping efficiency in the presence of this substrate. Detailed spectroscopic and morphological investigations will be reported to highlight the peculiarities of doping and strain effects induced by the thermal treatments comparing the two substrates.

4 CONCLUSION

We studied the effects of thermal treatments in controlled atmosphere of monolayer graphene deposited on dielectrics substrate grown on Si: SiO_2 and Al_2O_3. The kinetics studies and the equilibrium concentration of doping enabled to evidence that doping is more easily obtained in the case of silica supporting the role of the dielectrics-Gr interlayer in trapping dopant molecules and a prominent role of SiO_2 in tuning the Gr Fermi level. The effect of strain by thermal treatments in inert atmosphere shows also differences between the two substrates evidencing the larger release of strain in the case of SiO_2. The reported results are of relevance for the application of Gr/dielectrics/Si in optoelectronic and microelectronic applications and will be commented also in view of application of Gr composites with nanoparticles.

REFERENCES

[1] K. S. Novoselov, Nobel Lecture, 106-131, 2010.
[2] A.C. Ferrari et al., Nanoscale 7, 4598-4810, 2015.
[3] K. Chen et al., Journ. Phys. Chem. C, 116, 6259-6267, 2012.
[4] I. Calizo et al., Solid State Communications 149, 1132-1135, 2009.
[5] A. Piazza et al., Carbon 107, 696-704, 2016.
[6] S. D. Costa et al., RSC Adv., 6, 72859-72864, 2016.
[7] A. Armano et al., Carbon 127, 270-279, 2018.

Functional Oxides for nano-eletronics and spintronics

A. G. Monteduro[a,b], S. Rizzato[a,b], Z. Ameer[a,b], A. Leo[a,b], F. Sirsi[a,b], C. Leo[a], S. Karmakar[b], V. Tasco[b], A. P. Caricato[a], M. Martino[a], D.D. Sarma[c], G. Maruccio[a,b]

[a] Department of Mathematics and Physics, University of Salento, Lecce, 73100, Italy
[b] CNR NANOTEC - Istituto di Nanotecnologia, Via per Arnesano, 73100 Lecce, Italy
[c] SSSC Indian Institute of Science, Bangalore, 560012, India

e-mail: annagrazia.monteduro@unisalento.it

ABSTRACT

Complex transition metal oxides represent a vast class of materials with fascinating and interesting physical phenomena, such as high dielectric permittivities, ferroelectricity and multiferroicity. Here we report on the preparation, structural and magnetic characterization of BFO in bulk form and on the effect of deposition parameters on the dielectric properties of BFO and YCTO thin films deposited by PLD technique.

PACS Keywords: functional oxides, high-k material, multiferroic material

In resonators, antennas and transmitters, a high dielectric constant and a low dielectric loss are important to miniaturize the devices and reduce the bandwidth. Moreover, novel materials with improved dielectric properties are required to enhance the performance of CMOS field-effect transistors and to allow further miniaturization. In this respect, Y_2CuTiO_6 (YCTO) is a new high-k candidate for technological application, since in its bulk form it was reported to possess a high dielectric constant (ε'=40.3) extremely stable with the frequency, very low losses (Tgδ=0.003) [1, 2] comparable to that of SiO_2 (0.001) and weak temperature dependence. However, to check its technological applicability the deposition and characterization of YCTO thin film is necessary. Here, we report on the first study performed on Y_2CuTiO_6 thin films, deposited by laser ablation. Depending on growth conditions and thickness a dielectric constant up to more than two times higher than in the bulk was found. In particular, the influence of oxygen pressure on the film structural properties and related dielectric behaviour was investigated. For the films with higher dielectric constant value, thickness dependence studies of the dielectric properties have been also carried out. The results show the crucial role played by the oxygen pressure (PO_2) during deposition. By decreasing the O_2 pressure from 0.05 Pa to 1 Pa microstructural evolution has been observed, respectively from rather amorphous to nearly polycrystalline film with an increasing grain size.

Moreover, a reduction of thickness from 335 nm to 50 nm, at lower oxygen pressure, leads to a dielectric constant ε' decrease from 93 to 35, approaching the values reported for the bulk counterpart. The dependence of the dielectric losses with the area of the junction was also investigating, along with the physical origin of the dielectric response [3-5].

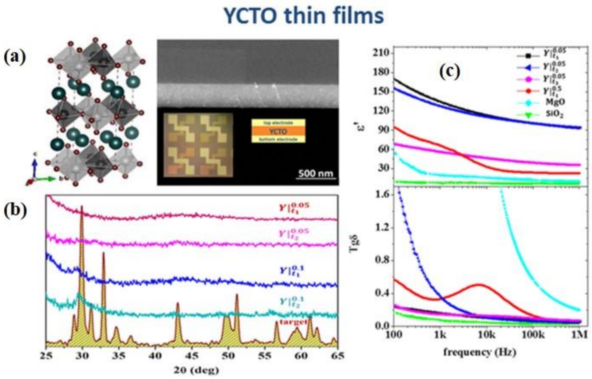

Figure 1. **Y_2CuTiO_6: (a)** the hexagonal unit cell of YCTO with cross sectional SEM image of a typical YCTO thin film deposited by PLD. Inset: electrode architecture employed for the dielectric characterization of the films deposited in arrays of parallel plate capacitors; **(b)** XRD spectra of target and YCTO thin films; **(c)** comparison of dielectric constant and tangent loss among four different YCTO films ($Y_{t_1}^{0.05} Y_{t_2}^{0.05} Y_{t_3}^{0.05}$ and $Y_{t_1}^{0.5}$, where the upper index refers to the oxygen deposition pressure and the lower index to the thickness of the films, t_1=300nm, t_2=150nm and t_3=50nm) and two technologically relevant oxides: SiO_2 and MgO deposited in similar junctions (Figure 1).

On the other hand, $BiFeO_3$ (BFO) is a promising multiferroic material for its high ordering temperatures (Néel temperature T_N = 643K and a ferroelectric ordering below T_c=1103K) [6] far above room temperature which make it suitable for the development of electrically controlled spin devices [7]. Here we report on the synthesis of bulk BFO up to the structural, morphological, dielectric and ferroelectric characterizations of both its bulk and thin film forms. Structural characterization was performed using X-Ray Diffraction and FT-IR spectroscopy. The dielectric constant and tangent loss were found to be ≈ 57.3 and 0.04 at 1MHz for bulk BFO. A systematic study was then performed in order to understand the role of each deposition parameter, such as substrate temperature, oxygen pressure, fluency, number of pulses, on the structure and impure phase formation during BFO film growth. It was found that a non-stoichiometric target is preferable to limit the effect of bismuth losses and contain the impure phase formation. On the other hand increasing the oxygen pressure from 0.5Pa to 1Pa, improved dielectric properties have been observed, due to the decreasing number of the oxygen vacancies (Figure 2).

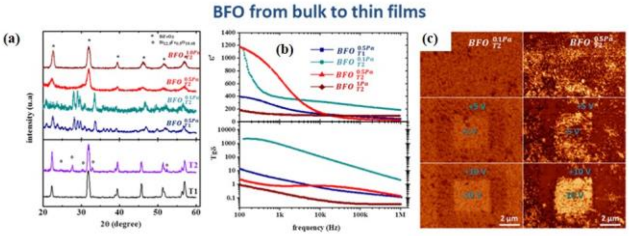

Figure 2. **BiFeO$_3$**: **(a)** XRD spectra of target and BFO thin films; **(b)** dielectric characterization; **(c)** PFM measurements carried out on two films deposited at two different oxygen pressure (0.1Pa and 0.5Pa) varying the polarization bias.

REFERENCES

[1] Choudhury, D., et al., *Electric and magnetic polarizabilities of hexagonal Ln$_2$CuTiO$_6$ (Ln=Y, Dy, Ho, Er, and Yb).* Physical Review B, 2010. 82(13): p. 134203.

[2] Leo, A., et al., *RF and microwave dielectric response investigation of high-k yttrium copper titanate ceramic for electronic applications.* Microelectronic Engineering, 2018. 194: p. 15-18.

[3] Monteduro, A.G., et al., *Dielectric investigation of high-k yttrium copper titanate thin films.* Journal of Materials Chemistry C, 2016. 4(5): p. 1080-1087.

[4] Monteduro, A.G., et al., *Investigation of high- k yttrium copper titanate thin films as alternative gate dielectrics.* Journal of Physics D: Applied Physics, 2016. 49(40): p. 405303.

[5] Ameer, Z., et al., *Dielectrical performance of high-k yttrium copper titanate thin films for electronic applications.* Journal of Materials Science: Materials in Electronics, 2018.

[6] Catalan, G. and J.F. Scott, *Physics and applications of bismuth ferrite.* Advanced Materials, 2009. 21(24): p. 2463-2485.

[7] Chu, Y.-H., et al., *Electric-field control of local ferromagnetism using a magnetoelectric multiferroic.* Nature materials, 2008. 7(6): p. 478-482.

Thermal stability and temperature dependent ESR characteristics of the As acceptor in geological 2H-MoS_2

B. Schoenaers, A. Stesmans, and V. V. Afanas’ev

Department of Physics and Astronomy, University of Leuven
3001 Leuven, Belgium

ABSTRACT

Electron spin resonance (ESR) results are presented on the thermal stability and temperature (T) dependence of the spectral characteristics of the As acceptor dopant (As substituting for S site) in geological 2H-MoS_2. Under sequential isochronal heating in H_2 (1.1 atm), the As dopant density is found to remain unaffected for anneal temperatures (T_{an}s) up to 525 °C, above which the density moderately decreases (~3 times) for $T_{an} \rightarrow 840$ °C. In turn, vacuum annealing is seen to result in a gradual increase (2 – 3 times) of the As acceptor density for T_{an} increasing from 400 °C → 840 °C, pointing to a positive ‘regain’ of misconfigured As impurities in pristine geo-MoS_2. Finally, meticulous monitoring of the ESR signal intensity vs. T at X-band confirms the previously inferred As acceptor activation energy of 0.7 ± 0.2 meV at K-band. In light of these findings, As is exposed as a promising candidate for stable p-type doping of MoS_2.

1 INTRODUCTION

Two dimensional (2D) nanomaterials have arisen as increasingly appealing for pushing the boundaries of current semiconductor technology envisaged by their potential to replace traditional semiconductors in next generation nanoelectronic devices [1-2]. Among the extensive group of 2D transition metal dichalcogenides (TMDs), molybdenite (MoS_2) has been widely studied for its outstanding properties [1-2]: it is a strong, flexible and atomically thin 2D layered semiconductor with a direct band gap of ~ 1.85 eV in covalently bonded S-Mo-S monolayer form and an indirect band gap of ~ 1.3 eV in bulk form.

Evidently, successful exploitation of the outstanding properties of MoS_2 as semiconductor requires dependable controlled doping, preferably achieved by covalent bonding of substitutional impurities. Yet, the current knowledge on dopant characteristics like the dopants nature, concentration and, crucially, corresponding activation energy, is still limited.

The current work reports and expands on the identification by a multi-frequency ESR study of the As acceptor in geological 2H-polytype MoS_2, with the As impurity substituting for an S site. [3] Careful monitoring of the signal intensity over a broad T-range previously revealed the As dopant as a very shallow acceptor with activation energy $E_a = 0.7 \pm 0.2$ meV.

Progressing on these findings, this work presents a detailed analysis of the thermal stability of the As acceptor under heat treatment in H_2 and vacuum, and its stability is compared to that of the N acceptor (in synthetic 2H-MoS_2) [4]. Additionally, the As acceptor activation energy has been separately extracted from X-band ESR to verify the initial assessment based on K-band observations [3].

2 EXPERIMENTAL DETAILS

The material studied is a commercially obtained [5] bulk geological MoS_2 crystal of 2H-polytype (hexagonal symmetry, two MoS_2 layers per repeat unit and Mo in trigonal prismatic coordination bonded to 6 S atoms), from which slices of ~ 2×8 mm^2 main area were cut, with the c-axis along the main face normal **n**, appropriate for ESR study. The latter is performed over the T-range 1.5 – 40 K using conventional cw X- and K-band spectrometers.

3 RESULTS AND DISCUSSION

3.1 Thermal stability

Aiming at a better understating of the dopant stability, the As acceptor has been subjected to two series of thermal treatments, one performed in H_2 (1.1 atm), the other in high vacuum ($< 5 \times 10^{-5}$ Torr). Isochronal thermal steps (~ 45 min) were performed sequentially on two pieces of the same sample, priorly subjected to a ‘reference’ setting treatment in vacuum (~ 400 °C; ~ 21h), referred to as the initial state.

Figure 1 shows the evolution of the As ESR signal intensity (∝ As acceptor density) over the various thermal treatments. Looking at the data corresponding to the vacuum thermal treatments, a first trend is revealed: The signal intensity increases gradually after subsequent thermal steps. This increase can be explained by either additional As atoms moving to the ‘proper’ position, i.e., substituting for S, or alternatively a reactivation effect involving, e.g., defect – H bond breaking.

As to the thermal treatment in H_2, the As signal is seen to remain unaffected, within experimental accuracy, for heating up to ~ 525 °C, to then gradually be decreased by a factor of three at $T_{an} \approx 840$ °C. The latter behavior is in contrast with that of the N acceptor in MoS_2 [4] experiencing a drastic ESR intensity drop by an order of magnitude at T_{an} ≈ 500 °C. Yet, for both acceptors, the intensity decrease can however be tentatively ascribed to the direct passivation (inactivation) of the respective acceptors through defect – H bond formation, similar to previous results for inactivation of point defects, such as, e.g., B acceptors in Si. [6] Contrary to the case of the N acceptor that cannot be reactivated at temperatures up to ~ 740 °C, (partial) reactivation of the As acceptor signal does occur at T_{an} = 840 °C in vacuum (cf. Fig. 1).

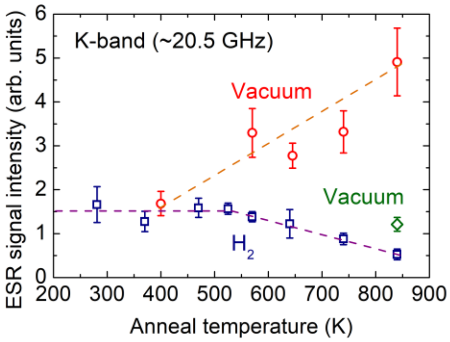

Figure 1: Evolution of the As acceptor ESR signal intensity as a function of isochronal heating in H_2 (blue squares) and vacuum (red circles). The signal intensity increases gradually after sequential thermal treatments in vacuum and decreases after thermal steps in H_2 by a factor of three from ~ 525 °C to ~ 840 °C to be partially recovered after a vacuum anneal at 840 °C (green diamond). The dashed curves guide the eye.

3.2 Temperature dependence

Besides serving as an exclusive technique for atomic identification of dopant impurities, ESR also acts as a unique tool to determine the dopant-type specific activation energy by monitoring the signal intensity vs. T. For an acceptor the activation energy can be written as $E_a = E_A - E_V$ with E_A the acceptor energy level and E_V the valence band (VB) maximum.

Figure 2 shows the normalized X-band ESR signal intensity of the ^{75}As hyperfine (hf) quartet after correction for the admitted Curie-type susceptibility $\chi_C \propto 1/T$ dependence. As demonstrated by the dashed curve, i.e., plot of Eq. (1) for E_a = 0.7 meV, the data reliably confirm the previously obtained activation-driven signal intensity decay of the As acceptor at K-band. The data are interpreted (cf. dashed curve in Fig. 2) using the expression for the ratio of neutral, N_A*, to total, N_A, acceptor densities derived from dopant occupation statistics [7]

$$\frac{N_A^*}{N_A} = 1 - \frac{2}{1+\sqrt{1+Ke^{E_a/kT}}} \, , \qquad (1)$$

where $K = 4g_dN_A/N_v$, with N_v the VB effective density of states, g_d the impurity level spin degeneracy factor inserted for bulk MoS_2 as g_d = 2, [8] and k Boltzmann's constant.

As described before, [3] only 13% of the total As spectrum is composed of the ^{75}As four-peak hf structure, corresponding to dopants residing in the preferred 'isolated' doping state, the major part of the signal being ascribed to exchange-coupled As acceptors. From least-square fitting of the inverse signal intensity of the total As spectrum versus T, a paramagnetic ($\chi \propto (T - T_c)^{-1}$) behavior is observed with a close to zero Curie-Weiss temperature T_C = -1 ± 1 K. The influence of the genuine intensity decrease of the ^{75}As hf quartet on the total intensity appears to be limited.

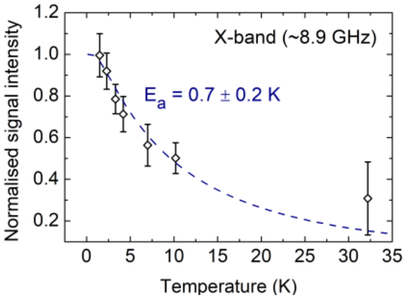

Figure 2: T-dependence of the X-band ESR intensity (double integral of derivative absorption spectra) of the ^{75}As hf ESR pattern originating from single decoupled As acceptors in geo-2H-MoS_2. The dashed curve represents Eq. 1 plotted with E_a = 0.7 meV.

4 CONCLUSIONS

The As acceptor emerges as a quite robust dopant: It sustains annealing in neutral ambient (vacuum) up to 840 °C. When subjected to sequential 'harsh' thermal treatments in H_2 up to this T, some decrease in As acceptor density is observed, but not nearly as drastic as for the N acceptor in synthetic MoS_2.

As to its dopant properties, the previously obtained As acceptor activation energy at K-band has been firmly consolidated by X-band observations while the total As signal exhibits a close to zero Curie-Weiss temperature.

In summary, the current work establishes As as utmost appropriate for stable covalently bonded p-type doping of MoS_2.

REFERENCES

[1] Q. H. Wang, et al., Nat. Nanotechnol. 7, 699 (2012).
[2] D. Voiry, et al., Chem. Soc. Rev. 44, 2702 (2015).
[3] A. Stesmans, et al., Appl. Phys. Lett. 109, 172104 (2016).
[4] B. Schoenaers, et al. (under review).
[5] SPI supplies, West Chester, USA.
[6] J. I. Pankove, et al., Phys. Rev. Lett. 51, 2224 (1983)
[7] J. S. Blakemore, Semiconductor Statistics (Pergamon, Oxford, 1962).
[8] E. Scalise, et al., Phys. E 56, 416 (2014).

Carbon dots dispersed on graphene/SiO_2/Si: a morphological study

G. Faggio[*], A. Gnisci[*], G. Messina[*], N. Lisi[**], A. Capasso[***], G.-H. Lee[***],
A. Armano[****], A. Sciortino[****], F. Messina[****], M. Cannas[****], F.M. Gelardi[****],
E. Schilirò[*****], F. Giannazzo[*****], S. Agnello[****]

[*] DIIES Dept., University “Mediterranea”, Via Graziella, Loc. Feo di Vito, 89122, Reggio Calabria, Italy
[**] ENEA, DTE PCU IPSE, Casaccia Research Centre, Via Anguillarese 301, Rome, Italy
[***] Department of Materials Science and Engineering, Yonsei University, Seoul 03722, Republic of Korea
[****] Dept. Physics and Chemistry, University of Palermo, Via Archirafi, 36, 90123, Palermo, Italy
[*****] CNR-IMM, Strada VIII 5, 95121 Catania, Italy

ABSTRACT

Low-dimensional carbon materials occupy a relevant role in the development of nanotechnology. Herein, we report a study by atomic force microscopy and Raman spectroscopy on carbon dots (CDs) and graphene (Gr) composites deposited on SiO_2/Si substrates aiming to highlight how the surface morphology and the crystalline structure of the Gr change because of its interaction with CDs and substrate. Two dispersion conditions have been explored using different solvents of CDs finding no strong differences in the Gr features apart from some increased defectiveness effects.

PACS Keywords: carbon dots, CVD graphene, AFM, Raman spectroscopy

1 INTRODUCTION

Carbon dots (CDs), carbonaceous nanoparticles with diameter smaller than 10 nm, attract interest because of their interesting optical properties [1] that allow them to be used as building blocks for new optoelectronic and photonic devices [2]. Recent studies have shown that by combining CDs with graphene it is possible to extend their uses in different fields, such as photocatalysis [3] or energy exchange [4] processes. Graphene’s (Gr) high mobility and atomic thickness are key properties that may allow the use of CDs in specific applications.

In this work, we report a systematic study of CDs/Gr nanocomposites deposited on SiO_2/Si substrates. Different CDs solutions were investigated, with the aim of clarifying the modifications induced on graphene grown by Chemical Vapor Deposition. Optical and atomic force microscopy (AFM) were used to study the surface morphology and evaluate the roughness of the nanocomposites. Co-localized Raman spectroscopy highlighted changes in the crystalline structure of graphene.

2 EXPERIMENTAL SECTION

2.1 Sample preparation

SiO_2 was thermally grown with a 300 nm final thickness on a Si wafer. Monolayer graphene was grown on copper foils by CVD at 1000 °C, using a CH_4 carbon source in a gas mixture with hydrogen with ratio 95%/5%, respectively. For the transfer procedure, a layer of Poly(methyl methacrylate) (PMMA) was spin coated onto Gr/Cu and a foil of thermal release tape (TRT) was laminated onto PMMA. The Cu substrate was etched by $FeCl_3$ water solution and the resulting TRT/PMMA/graphene stack was transferred to the final substrate by thermo-compression printing, with the releasing of TRT. Finally, PMMA layer was removed by an ammonium persulfate bath, obtaining the final graphene/SiO_2/Si sample.

Alternatively graphene was grown on copper foils from ethanol precursor at 1070°C [5] and transferred onto the same target substrates using a cyclododecane protective layer [6] after etching in Ammonium persulfate.

CDs were synthesized using citric acid monohydrate (3g), as carbon precursor, and urea (3g) (Sigma-Aldrich) as nitrogen precursor, dissolved in an aqueous solution (10 mL of Milli-Q water). The carbonization process was performed exposing the solution to microwave irradiation until the complete evaporation of water occurs. A first solution was prepared dissolving the as synthesized CDs powder in ethanol. For a second solution, a size exclusion chromatography in Milli-Q water was performed to fractionate the as synthesized sample separating the most luminescent fraction.

Finally, to the realization of CDs/Gr nano-composite, both CDs solutions were diluted by a factor 10^{-4} in volume of the stock solutions and from both of them a 1 μL was withdrawn and deposited on two different graphene/SiO_2/Si samples by drop-casting method.

2.2 Sample characterization

Raman spectra and AFM images were acquired on samples obtained by depositing a drop of an aqueous and ethanol solution of CDs on SiO_2/Si substrates. After drying in a vacuum environment for 2 hours, Raman scattering measurements were carried out at room temperature with a

HORIBA Scientific LabRAM HR Evolution Raman spectrometer with an integrated Olympus BX41 microscope. Laser excitation wavelength of 532 nm (2.33 eV) was focused on the sample surface using a 100× objective with a spot size of approximately 1 µm. Low laser power (below 1 mW) was used to minimize sample heating and possible damages. Spectra were normalized to the Si peak at 520.7 cm^{-1}. Tapping-mode amplitude modulation AFM measurements were performed using a AIST-NT SmartSPM, equipped with a conventional piezoscanner (maximum xy range 100 µm and maximum z range 15 µm) and a four-segment photodetector for cantilever deflection monitoring. We used AppNano Silicon-SPM-probes designed to allow a direct optical view of the AFM tip when imaging for co-localized Raman and AFM measurements, with Al backside reflex coating having a resonance frequency ~300 kHz and a tip apical diameter of 6 nm. All the scans were executed at room temperature. At least three areas for each sample were measured in order to take into account inhomogeneity which might derive from the sample preparation.

3 RESULTS AND DISCUSSION

Figure 1 displays representative optical micrographs of the two different CDs solutions deposited on Gr/SiO_2/Si substrate. CDs deposited in aqueous solution (Fig.1 a) disperse on substrate forming large CDs clusters inside a well-defined circular area. Outside this area, only isolated point-like clusters are observed. Differently, a more uniform dispersion of the CDs ethanol solution is observed on the substrate (Fig.1 b) and no large clusters are present.

The different distribution of CDs solutions on Gr can be ascribed to graphene's hydrophobicity, which leads to the formation of droplets in the case of water dispersion. On the contrary, when using ethanol, the CDs are distributed in a uniform film over the entire surface of the substrate.

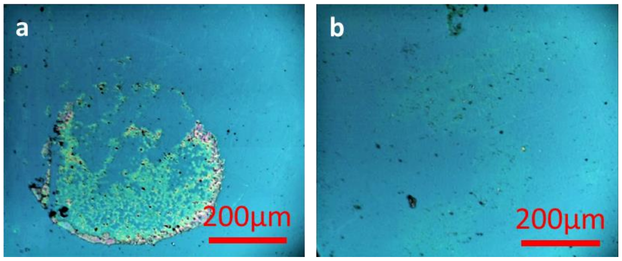

Figure 1: Optical images of CD solution in aqueous (a) and ethanol (b) deposited on SiO_2/Si substrate.

Nevertheless, in both cases it was possible to observe small regions with a homogenous distribution of CDs on graphene. AFM maps were carried out in these small regions, far from the large, droplet related CDs clusters. Figure 2a shows an AFM image acquired near a graphene edge. CDs are uniformly distributed both on SiO_2 and on Gr. Roughness studies were carried out to unveil distortions induced on graphene after the CDs deposition.

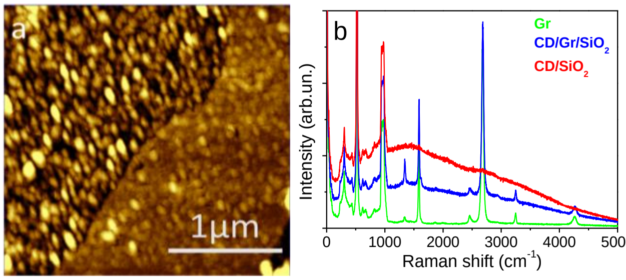

Figure 2: AFM map of ethanol CD solution deposited on SiO_2 and on the Gr (a) and Raman spectra acquired on three different areas of the sample (b).

In Figure 2b are shown the Raman spectra acquired on CDs/SiO_2 and CDs/Gr/SiO_2. The graphene Raman spectrum is also reported. All the spectra showed the typical Raman peaks of the Si substrate in the range between 10 and 1200cm^{-1}. The Raman spectrum of Gr/SiO_2 exhibits the characteristic D, G and 2D peaks respectively at ~1350 cm^{-1}, ~1580 cm^{-1}, ~2700 cm^{-1} [7]. Commonly the D to G (I_D/I_G) and 2D to G (I_{2D}/I_G) intensity ratios provide quantitative information on defect density and thickness of Gr, respectively [5]. I_{2D}/I_G~2 and I_D/I_G~0.05 measured values indicates that Gr is a single layer of high quality. The Raman spectrum of CDs/Gr nanocomposite deposited on SiO_2 showed the graphene peaks superimposed to a large photoluminescence band centered at ~1100 cm^{-1} (2.2 eV) that is seen again in the Raman CDs spectrum, thus confirming its origin. It's interesting to note that the presence of CDs on graphene causes an increase in defect density (I_D/I_G~0.3), leaving its thickness unaltered (I_{2D}/I_G~2). The worsening of Gr quality may be due to effects introduced by CDs.

CONCLUSIONS

CDs/Gr nanocomposites deposited on SiO_2/Si substrate were systematically analysed by AFM and Raman spectroscopy. Our analysis indicates that the use of two different solvents, such as water or ethanol, in the CDs solution does not induce changes on the nanometer scale. However, when using ethanol, the CDs are distributed in a uniform film over the entire surface of the substrate.

REFERENCES

[1] A. Sciortino et al., Phys. Chem. Chem. Phys. 19, 22670, 2017
[2] Li et al.,Adv. Func. Mater. 25, 4929, 2015
[3] X. Zeng et al., Appl. Cat. B Env.202, 33, 2017
[4] A. Raja et al., Nano Lett., 16, 2328, 2016
[5] G. Faggio et al., J. Phys. Chem C, 117, 21569, 2013
[6] A. Capasso et al., Appl. Phys. Lett., 105,113101, 2014
[7] A.C. Ferrari, et al., Phys. Rev. Lett. 97, 187401, 2006

Enhancement of Carbon Dot Emission with Au Nanoparticles

Riccardo Corpino*, Giulia Rossella Delpiano**, Maria Francesca Casula**, Pier Carlo Ricci*, Carlo Maria Carbonaro*

*Department of Physics, University of Cagliari, Campus of Monserrato, sp n8, km 0.700, Monserrato, Italy
**Department of Chemical and Geological Sciences and INSTM, University of Cagliari, Campus of Monserrato, sp n8, km 0.700, Monserrato, Italy

ABSTRACT

We present the study of structure, morphology and emission proprieties of core-shell hybrid systems obtained by combining gold nanoparticles and carbon dots. The gold core, of about 20 nm, is capped by a silica shell with thickness in the 0-20 nm range. The silica surface was decorated with carbon dots. We discuss the interaction of gold nanoparticles with carbon dots in terms of metal enhanced fluorescence due to plasmonic effect. By changing the silica shell thickness, we can modulate the optical properties of the fluorophores.

PACS Keywords: carbon dot, silica shell, metal nanoparticle, photoluminescence.

1 INTRODUCTION

Fluorescent Carbon dots (CDs), discovered in 2004 [1], are gathering increasing attention because of their optical efficiency, chemical inertness and low cost green production. These features make them worthwhile competitors to quantum dots or organic dyes for bioimaging, photocatalysis, sensing and lighting [2-6]. In addition, Carbon sources are naturally abundant and CDs are non-toxic, satisfying market requirements for safety and profit. In general, CDs display an excitation-dependent emission whose peak red-shift by increasing the excitation wavelength. The emission properties, however, strongly depend on the CD structure, namely on the ratio between crystalline and disordered domains due to synthesis procedure (precursors, preparative conditions, post-synthesis conditions). Concerning the quantum yield, the fluorescence of CDs has a high efficiency in the blue-green range, but is quite poor in the red/near-IR, somehow limiting their potential applications. Besides systematic study of synthetic approaches to increase reproducibility and tailor the optical properties, a different strategy is to increase the emission efficiency by means of surface plasmon resonance of noble metal nanoparticles (NP). Metal enhanced fluorescence (MEF) can be achieved by interaction of metal surface plasmons with emitting fluorophores, the critical parameter being the distance between metal NPs and emitting enters. Indeed, both enhancement or quenching of the emission can be produced because of competition between field enhancement and Forster resonance energy transfer (FRET), depending on the NP-fluorophore distance. The nano-architecture of election is a core-shell system, where the core is a gold NP and the shell is silica. Finally, the silica surface is decorated with emitting CDs. Sol-gel technique allows controlling the thickness of the silica shell, thus controlling the distance between NP and CDs. The optical properties of the prepared hybrids are discussed as a function of the silica thickness.

2 SAMPLES AND EXPERIMENTS

We applied a multi-technique approach to characterize the samples from morphological (TEM), structural (XRD, Raman, FTIR) and optical (absorption, steady state excitation and emission, time resolved spectroscopy) point of view.

We prepared bare CDs (CDB) and nitrogen-doped CDs (CDN) by a microwave assisted route, starting either from citric acid or citric acid and urea (reagents were Sigma-Aldrich, analytical grade) in 10 mL of water. The solutions were stirred for 30 min., and then treated in a domestic microwave oven at 700 W.

According to Wu et al. [7], we prepared Au NPs starting from an aqueous solution of gold tetrachloride (HAuCl4) and Au_SiO$_2$ core-shell system following the Stöber method. The shell thickness was varied by changing the reaction time.

Finally, hybrid systems containing CDs on the silica surface (CS_CD) were obtained by mixing an aqueous solution of Au_SiO2 core shell with an aqueous dispersion of CDs at variable concentration.

3 RESULTS AND DISCUSSION

The TEM image of Au_SiO$_2$ core-shell systems displays rounded gold nanoparticles with a diameter of about 20 nm coated with a shell of silica whose thickness is of about 25 nm.

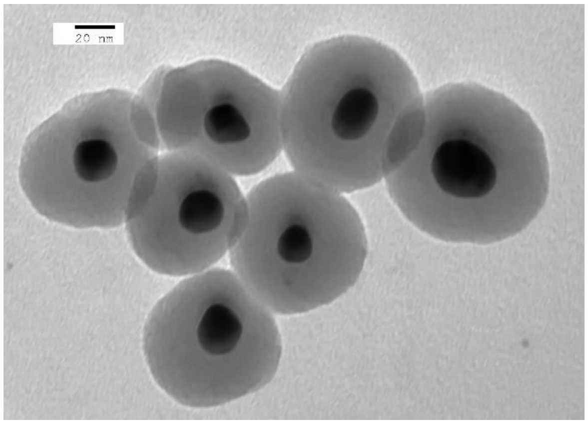

Figure 1: TEM images of Au_SiO2 core shell systems

The absorbance spectra of two hybrid systems (with shell thickness of 25 and 15 nm respectively, CS_CD1 and CS_CD2) are compared to the one of pure CDs in Figure 2.

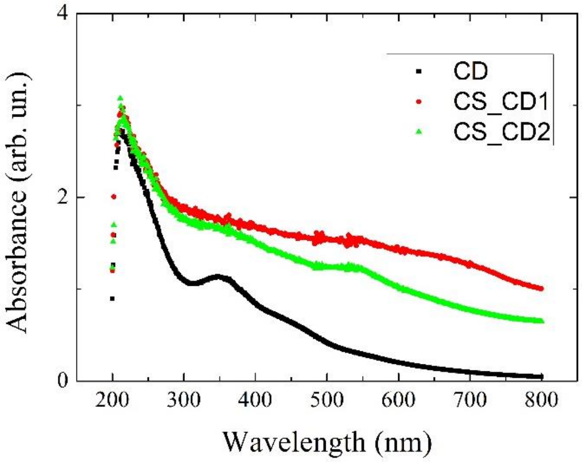

Figure 2: Absorbance spectra of CD and Au_SiO$_2$ core-shell (silica shell is 25 and 15 nm for CS_CD1 and CS_CD2 respectively).

The Au plasmon absorbance peak can be distinguished in the sample with smaller silica thickness (CS_CD2) whilst is merged in a large absorption band extending down to IR region in the CS_CD1 sample.

REFERENCES

[1] X. Xu, R. Ray, Y. Gu, H.J. Ploehn, L. Gearheart, K. Raker, W.A. Scrivens, J. Am. Chem. Soc. 126, 12736–12737 (2004).

[2] Bhattacharyya, S.; Ehrat, F.; Urban, P.; Teves, R.; Wyrwich, R.;Do¨blinger, M.; Feldmann, J.; Urban, A. S.; Stolarczyk, J. K. Nat. Commun. 2017, 8, 1401.

[3] Kang, Y.-F.; Li, Y.-H.; Fang, Y.-W.; Xu, Y.; Wei, X.-M.; Yin, X.-B. Sci. Rep. 2015, 5, 11835.

[4] Zhu, S.; Meng, Q.; Wang, L.; Zhang, J.; Song, Y.; Jin, H.; Zhang, K.; Sun, H.; Wang, H.; Yang, B. Angew. Chem., Int. Ed. 2013, 52, 3953−3957.

[5] Nie, H.; Li, M.; Li, Q.; Liang, S.; Tan, Y.; Sheng, L.; Shi, W.; Zhang, S. X.-A. Chem. Mater. 2014, 26, 3104−3112.

[6] H. Li, Z. Kang, Y. Liu, S.-T. Lee, J. Mater. Chem., 2012, 22, 24230

[7] Z. Wu, J. Liang, X. Ji, W. Yang, Colloids and Surfaces A: Physicochem. Eng. Aspects 392 (2011) 220– 224

Politecnico di Bari

UNIVERSITÀ DEGLI STUDI DI PALERMO
DiFC
DIPARTIMENTO DI FISICA E CHIMICA - DiFC

BARI – ITALY
11-13 JUNE
SiO2018

WEDNESDAY

SESSION

DIELECTRICS MATERIALS FOR HEALTHCARE, ENERGY, ENVIRONMENT

UNIVERSITÉ JEAN MONNET
SAINT-ÉTIENNE

UNIVERSITÉ FRANCO ITALIENNE
UNIVERSITÀ ITALO FRANCESE

Anritsu
envision : ensure

ROHDE&SCHWARZ

DIPARTIMENTO DI
INGEGNERIA ELETTRICA
E DELL'INFORMAZIONE

Integrated photonic and plasmonic microresonators for label-free biosensing and trapping at nanoscale

Caterina Ciminelli, Francesco Dell'Olio, Donato Conteduca, Giuseppe Brunetti, Mario N. Armenise
Optoelectronic Laboratory, Politecnico di Bari, Via Orabona 4, 70125 Bari, Italy
caterina.ciminelli@poliba.it

ABSTRACT

Photonic and plasmonic microresonators are emerging as key building blocks in many application fields especially because they enhance the light-matter interaction and are very sensitive to any change of their physical/geometrical parameters. Two of the most attractive applications of photonic and plasmonic integrated cavities are in the field of biosensing and trapping of biological matter at nanoscale. Both these applications are discussed in this paper with a focus on our recent results.

PACS Keywords: integrated microphotonics, biosensor, plasmonics, Bragg grating, nanotweezer, resonant cavity.

1 INTRODUCTION

In the last few years, integrated photonic and plasmonic microresonators are becoming crucial in new microsystems, instruments, and diagnostic tools for a wide range of biomedical applications including point-of-care diagnostics, new drug development, and proteomics [1,2]. Several resonant label-free photonic and plasmonic biosensors for early diagnosis and monitoring of a wide range of pathologies have attracted a remarkable research interest due to high resolution, small size, immunity to electromagnetic interference, compatibility with the CMOS technology, and strong light-matter interaction.

Recently the great potential of photonic, plasmonic, and hybrid photonic/plasmonic micro and nano-cavities for trapping at nanoscale has been experimentally demonstrated and the interest towards these devices in the field of healthcare is quickly rising [3].

In this paper, recent advances in the field of integrated photonic and plasmonic microresonators for label-free biosensing and trapping at nanoscale are critically reviewed, with a special emphasis on the numerical and experimental results achieved by us in the field of chip-scale multi-analyte biosensing platforms and photonic crystal cavities for nanoparticle trapping. The specific applications of these devices in the field cancer and cardiovascular diseases diagnostics and new antibiotics development are also mentioned.

2 RESONATORS FOR BIOSENSING

In the last two decades, several configurations of photonic and plasmonic resonators at micro- and nano-scale have been investigated and a number of interesting properties for biochemical sensing, including high specificity, high sensitivity, multiplexing analysis capability, and compactness, have been experimentally demonstrated [4]. In particular, several research groups all over the world have demonstrated that the use of planar photonic ring resonators in the field of biosensing is extremely attractive due to their easy fabrication process and the possibility of their monolithic/hybrid integration within complex photonic integrated circuits [5].

A novel resonant multi-analyte biosensing platform with ultra-high resolution (= 0.2 ng/mL) has been recently designed by our group [6]. A silicon nitride ring resonator with a novel waveguide configuration including a hollow region with a reversed T shape having a very large waveguide surface sensitivity (> 0.0001 nm^{-1}) is the key building block of the platform. The device, shown in in Fig. 1, allows the detection of n (number of target molecules to be detected) protein biomarkers dispersed in a biologic fluid and consists of n rings, which are evanescently coupled to a straight bus waveguide. The radius of the rings is scaled so that they resonate at different wavelengths (λ_{r1}, λ_{r2},…, λ_{rn}). Each ring is included in a sensing window filled by the fluid to be analyzed.

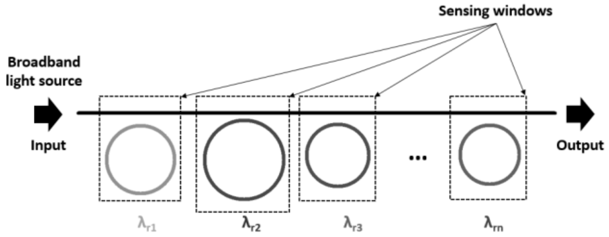

Figure 1: Configuration of the multi-analyte biosensor reported in [6].

The envisaged specific application for the designed platform is the lung cancer early diagnosis though the detection of five proteins, i.e. alpha-1 antitrypsin, cytokeratin fragment 21-1, insulin-like growth factor 1, regulated upon activation normal T cell expressed and secreted, and alpha-fetoprotein, in the human serum.

Aiming at further miniaturizing chip-scale biosensing platforms, planar plasmonic nanocavities can be used as sensing element. According to this approach, we have recently designed an ultracompact resonant plasmonic multi-analyte label-free biosensing platform having a footprint of only 0.011 mm^2 and including 3 nanocavities, each sensitive to a specific protein biomarker [7]. The resonant element of the platform is a plasmonic Bragg grating in a metal-insulator-metal waveguide including a 190 nm-long defect. The surface sensitivity of the nanocavity is equal to 1.8 nm/nm. The platform limit of detection is 128 pg/mm^2 and its target application is the early detection/monitoring of the coronary artery disease through the sensing of 3 protein biomarkers, β_2-microglobulin, C-reactive protein, and adiponectin.

3 RESONATORS FOR TRAPPING

The ability to manipulate biological matter at nanoscale is important in many life science domains, such as single-molecule biophysics, development of new drugs, and cancer detection. To address this key challenge, several types of nanotweezers based on different technologies have recently been demonstrated. In particular, nanotweezers based on integrated photonic and plasmonic resonators are attracting a strong research effort especially because they are efficient and stable, offer fast response time, and avoid any direct physical contact with the target object to be trapped, thus preventing its damage or disruption.

An efficient nanotweezer based on a photonic/plasmonic cavity with a one-dimensional photonic crystal dielectric cavity vertically coupled to a bowtie nanoantenna [8] has been recently demonstrated (see Fig. 2).

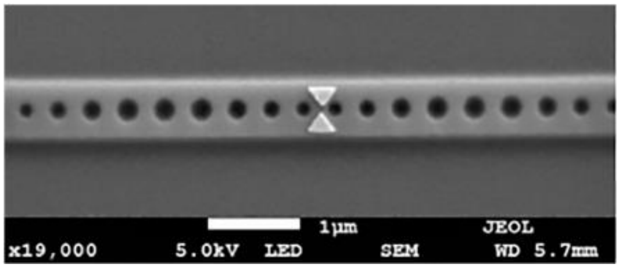

Figure 2: SEM micrograph of the photonic/plasmonic cavity reported in [8].

The ultra-low mode volume of the plasmonic nanoantenna ($5x10^{-4}$ $(\lambda/n)^3$) and the high Q-factor of the PhC cavity ($1.8x10^3$) provide a very strong light-matter interaction with a remarkable energy confinement around the bowtie. The stable trapping of a single 200 nm Au bead for a duration of several minutes ($t_{trap} > 5$ min) and with very low optical power ($P_{in} = 190$ μW) has been achieved by this device.

The target application of the photonic/plasmonic nanotweezer is the rapid and label-free single bacteria detection and monitoring for new miniaturized instruments able to support the research activity on new drugs facing the global challenge of antimicrobial resistance [9].

4 CONCLUSIONS

The unique features of integrated photonic and plasmonic microresonators in the field of biosensing and trapping at nanoscale have been highlighted in this paper, by discussing some recent achievements of our group. Our results show that biosensors with a resolution down to 0.2 ng/mL and nanontweezers able to traps nanobead for a long time (> 5 min) can be obtained by properly designing resonant structure at micron- and nano-scale.

REFERENCES

[1] M.-C. Estevez, et al., “Integrated optical devices for lab-on-a-chip biosensing applications,” Laser Photonics Rev., vol. 6, pp. 463-487, 2012.
[2] C. Ciminelli, et al., “Label-free optical resonant sensors for biochemical applications,” Progress in Quantum Electronics, vol. 37, pp. 51-107, 2013.
[3] D. Conteduca, et al., “Photonic and Plasmonic Nanotweezing of Nano- and Microscale Particles,” Applied Spectroscopy, vol. 71, pp. 367-390, 2017.
[4] F. Vollmer, et al., “Whispering-Gallery-Mode biosensing: Label-free detection down to single molecule,” Nat. Methods, vol. 5, pp. 591-596, 2008.
[5] Y. Sun, et al., “Optical ring resonators for biochemical and chemical sensing,” Analytical and bioanalytical chemistry, vol. 399, pp. 205-211, 2011.
[6] F. Dell’Olio, et al., “New ultrasensitive resonant photonic platform for label-free biosensing,” Opt. Express, vol. 23, pp. 28593-28604, 2015.
[7] F. Dell’Olio, et al., “Design of a New Ultracompact Resonant Plasmonic Multi-Analyte Label-Free Biosensing Platform,” Sensors, vol. 17, art. 1810, 2018.
[8] D. Conteduca, et al., “Ultra-high Q/V hybrid cavity for strong light-matter interaction,” APL Photonics, vol. 2, art. 086101, 2017.
[9] D. Conteduca, et al., “Rapid and label-free single bacteria detection and monitoring by ultra-compact optoelectronic system,” accepted at Biosensors 2018, Miami, FL, USA, 12-15 June, 2018.

Fractional-Calculus-Based electromagnetic tool to study pulse propagation in arbitrary dispersive dielectrics

L. Mescia[*], P. Bia[**], M.A. Chiapperino[*], D. Caratelli[***]

[*]Department of Electrical and Information Engineering, Polytechnic University of Bari
Via E. Orabona 4, 70125 Bari-Italy
[**]EmTeSys S.R.L., Bari, Italy
Via Beata Elia di S. Clemente, 223, 70122 Bari, Italy
[***]The Antenna Company
High Tech Campus 41, 5656 AE Eindhoven, The Netherlands

ABSTRACT

A novel finite-difference time-domain algorithm for studying electromagnetic pulse propagation in arbitrary dispersive dielectric materials is presented. The proposed method is based on the generalization of the Maxwell equations using fractional calculus theory and a general series expansion of the permittivity function. The resulting formulation is explicit, it has a second–order accuracy, and the need for additional storage variables is minimal.

PACS Keywords: dielectric relaxation, dispersive media, fractional derivative, propagation model, computational algorithm

1 INTRODUCTION

In recent years, the feasibility of pulsed electromagnetic fields (PEFs) in RF and mm–wave frequency range, has been investigated in a variety applications. This technology involves the interaction of electromagnetic fields with dielectrics and as a result detailed theoretical modeling and computational techniques are essential to gain insight into the several phenomena occurring within dielectric materials.

It is well know that the Debye model is not able to describe a wide class of relaxation processes occurring complex dielectric materials. As a consequence, spectral models employing fractional power–law should be developed for accurately describing the dielectric response. In particular, taking into account that the dielectric response includes fractional powers of jω the design of the FDTD algorithm requires special treatments [1-2]. To this aim, a novel FDTD approach for simulating ultra-wideband electromagnetic pulses propagating in arbitrary dispersive media is illustrated. In particular, using a general fractional polynomial series approximation, the fractional calculus theory and EMT formulation both the spatial and frequency dispersion characteristics of the dielectric response have been incorporated into the FDTD scheme. The comparison between the numerical results applying both the FDTD code and a fully analytical frequency-based approach demonstrates the accuracy of the proposed FDTD method.

2 FDTD SCHEME

In the developed FDTD scheme, a general relative electric permittivity function having the following fractional polynomial dispersion response has been implemented

$$\varepsilon(\omega) = \varepsilon_\infty + \Delta\varepsilon \frac{1+\sum_{q=1}^{M} b_q \left(j\omega\tau\right)^{\beta_q}}{1+\sum_{p=1}^{N} a_p \left(j\omega\tau\right)^{\gamma_p}} - j\frac{\sigma}{\omega\varepsilon_0} \tag{1}$$

where $\Delta\varepsilon$ and τ are the relaxation strength and time, respectively, ε_∞ is the relative permittivity at high frequency limit, σ is the static conductivity, $\gamma_p, \beta_q \geq 0$, $a_p, b_q \geq 0$ a real coefficients. Moreover, by using an optimization algorithm based on swarm intelligence [4] the parameters $\gamma_p, \beta_q, a_p, b_q$ can be recovered to suitably fit a generic frequency domain permittivity function. Taking into account the complex relative permittivity described by Eq. (1), the Ampere's law in time domain can be written as:

$$\nabla \times \mathbf{H} = \varepsilon_0 \varepsilon_\infty \frac{\partial \mathbf{E}}{\partial t} + \sigma \mathbf{E} + \mathbf{J} \tag{2}$$

where the auxiliary displacement current density $\mathbf{J}$ satisfies the equation

$$\mathbf{J} + D_{\mathrm{t}}^{\mathrm{J}} \mathbf{J} - \frac{\varepsilon_0 \Delta\varepsilon}{\tau} D_{\mathrm{t}}^{\mathrm{E}} \mathbf{E} = \varepsilon_0 \Delta\varepsilon \frac{\partial \mathbf{E}}{\partial \mathrm{t}} \tag{3}$$

with

$$D_{\mathrm{t}}^{\mathrm{J}} = \sum_{\mathrm{p}=1}^{\mathrm{N}} \mathrm{a}_{\mathrm{p}} \tau^{\gamma_{\mathrm{p}}} \mathrm{D}_t^{\gamma_{\mathrm{p}}} \tag{4}$$

$$D_{\mathrm{t}}^{\mathrm{E}} = \sum_{\mathrm{q}=1}^{\mathrm{M}} \mathrm{b}_{\mathrm{q}} \tau^{1+\beta_{\mathrm{q}}} \mathrm{D}_t^{1+\beta_{\mathrm{q}}} \tag{5}$$

Applying a second–order accurate finite–difference scheme at the time instant *t*=*m*Δ*t*, the update equations for both electric and magnetic fields are

$$\mathbf{E}\Big|^{\mathrm{m}+1/2} = \mathbf{E}\Big|^{\mathrm{m}-1/2} + \frac{\Delta \mathrm{t}}{\varepsilon_0 \Delta\varepsilon}\left(\mathbf{J} + D_{\mathrm{t}}^{\mathrm{J}}\mathbf{J} - \frac{\varepsilon_0\Delta\varepsilon}{\tau} D_{\mathrm{t}}^{\mathrm{E}}\mathbf{E}\right)\Bigg|^{\mathrm{m}} \qquad (6)$$

$$\mathbf{H}\Big|^{\mathrm{m}+1} = \mathbf{H}\Big|^{\mathrm{m}} - \frac{\Delta \mathrm{t}}{\mu_0}\left(\nabla\times\mathbf{E}\right)\Big|^{\mathrm{m}+1/2} \qquad (7)$$

where the finite-difference approximation of the generalized fractional derivative operators $\mathcal{D}_{\mathrm{t}}^{\mathrm{J}}, \mathcal{D}_{\mathrm{t}}^{\mathrm{E}}$ has been evaluated by applying the Riemann–Liouville theory [1-2].

3 NUMERICAL RESULTS

To test the developed numerical code, the 1-D layered model illustrated in Fig. 1 is considered. The system is irradiated by a plane wave propagating along the positive x–direction, with electric field linearly polarized along the z–axis and located at a given point x = x_s.

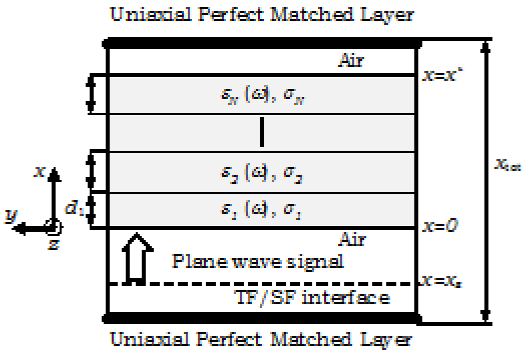

Figure 1: Layered model employed in the simulations.

The first test case pertains a single layer having thickness $d_1 = 10$ mm and relative electric permittivity

$$\varepsilon_1(\omega) = 2 + \frac{60\left[1 + (j\omega\tau)^{0.2}\right]}{1 + 9(j\omega\tau)^{0.3} + 2(j\omega\tau)^{0.5} + 10(j\omega\tau)^{0.9}} \qquad (8)$$

$\sigma = 0.035$ S/m and $\tau = 318$ ps. The second one is a three layer having thickness $d_1 = 10$ mm, $d_2 = 30$ mm, $d_3 = 20$ mm and relative electric permittivity

$$\varepsilon_1(\omega) = 2.4 + \frac{26\left[1 + 2(j\omega\tau_1)^{0.2}\right]}{1 + 5(j\omega\tau_1)^{0.03} + 6.54(j\omega\tau_1)^{0.14} + 0.2(j\omega\tau_1)^{0.8} + 13(j\omega\tau_1)^{0.9}} \qquad (9)$$

$$\varepsilon_2(\omega) = 4 + \frac{44\left[1 + 3(j\omega\tau_2)^{0.3} + 2(j\omega\tau_2)^{0.4}\right]}{1 + 5(j\omega\tau_2)^{0.14} + 8(j\omega\tau_2)^{0.7} + 6(j\omega\tau_2)^{0.8} + 2(j\omega\tau_2)^{0.83}} \qquad (10)$$

$$\varepsilon_3(\omega) = 6 + \frac{60\left[1 + 5(j\omega\tau_3)^{0.3}\right]}{1 + 4(j\omega\tau_3)^{0.29} + 5(j\omega\tau_3)^{0.6} + 6(j\omega\tau_3)^{0.8}} \qquad (11)$$

$\sigma_1 = 0.035$ S/m, $\sigma_2 = 0.05$ S/m, $\sigma_3 = 0.03$ S/m and $\tau_1 = 16$ ps, $\tau_2 = 5.91$ ps, $\tau_3 = 59.1$ ps. Fig. 2 shows the reflectance and transmittance spectra as evaluated by using the proposed FDTD procedure and a fully analytical frequency–domain technique concerning (a) single layer and (b) three layers system. The excellent agreement between them fully validates the developed FDTD formulation.

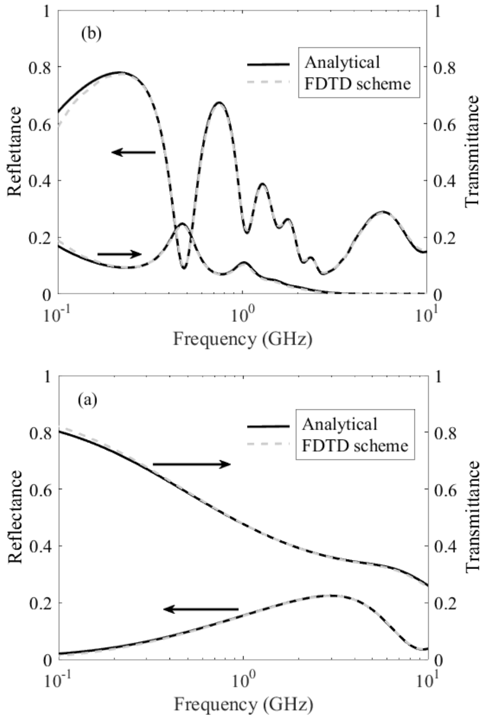

Figure 2:Reflectance and transmittance as a function of frequency of (a) single layer and (b) three layers dispersive media.

4 CONCLUSIONS

An accurate FDTD model for simulating the pulse propagation in arbitrary dispersive media is proposed. Using the fractional derivative operator, the fractional part resulting from a general series expansion of the permittivity function of dispersive materials is directly incorporated into the FDTD scheme, avoiding the use of auxiliary differential equations. The comparison between simulation results and those evaluated by using an analytical method based on the Fourier transformation demonstrates the accuracy and effectiveness of the developed FDTD model.

REFERENCES

[1] L. Mescia, P. Bia, and D. Caratelli, IEEE Transactions on Microwave Theory and Techniques, vol. 62, pp. 1920-1929, 2014.

[2] D. Caratelli, L. Mescia, P. Bia, O. V. Stukach IEEE Trans. Antennas Propag., vol.64, pp. 3533-3544, 2016.

Cosolvent-free synthesis of polysilsesquioxane liquids and polysilsesquioxane-based organic-inorganic hybrid glasses

Koichi Kajihara, Arata Sakuragi, Yuta Igarashi, Yuko Fukuda, Kiyoshi Kanamura

Department of Applied Chemistry, Graduate School of Urban Environmental Sciences,
Tokyo Metropolitan University
1-1 Minami-Osawa, Hachioji, Tokyo 192-0397, Japan

ABSTRACT

A cosolvent-free method to synthesize polysilsesquioxiane (PSQ) liquids from organotrialkoxysilane−water binary systems has been developed. The resultant poly(alkyl-SQ)s and poly(3-sulfanylpropyl-SQ) were viscous liquids except for poly(Me-SQ). They contain a lot of SiOH groups whereas their viscosities are stable over months at room temperature. Poly(Et-SQ) does not contain functional groups that absorb ultraviolet (UV) light and became UV-transparent glasses with an UV absorption edge of ~210 nm by thermal curing. The mixture of poly(3-sulfanylpropyl-SQ) liquid and polyallyl compounds underwent UV-induced thiol-ene reactions and resulted in transparent bulk glasses. These methods are useful in obtaining transparent silicate-based organic-inorganic hybrids.

PACS Keywords: 51.20.+d, 78.40.Pg

1 INTRODUCTION

Silsesquioxanes (SQs) are compounds with the general formula $RSiO_{3/2}$, where R is an organic functional group [1,2]. Hydrolytic polycondensation of organotrialkoxisilanes (sol−gel-based techniques) is widely used for preparing the polymers of SQs (PSQs). These reactions are usually performed in cosolvents, such as alcohols and organic solvents, to homogenize the reaction mixture containing alkoxides and water [3-7]. In addition, complicated multistep processes accompanied by filtration and centrifugation are often employed. The resultant PSQs are typically solids at room temperature, and the synthesis of PSQ liquids has been scarce.

We have developed a facile sol−gel-based technique to prepare PSQ liquids from acid-catalyzed organotrimethoxysilane−water binary systems [8-11]. The properties of PSQ liquids and their conversion to organic−inorganic hybrid glasses will be presented.

2 EXPERIMENTAL PROCEDURE

Trimethoxysilanes $RSi(OMe)_3$ with R = Me, Et, *n*-Pr, *n*-Bu, and 3-SP (3-sulfanylpropyl; HSC_2H_6-) groups were used as silicon sources. A dilute aqueous solution of nitric acid was added at once to each alkoxide at an alkoxide : H_2O : HNO_3 mole ratio of 1 : 3 : 0.002 and stirred for 3 h in a sealed container at 20°C. The solution was aged for 1 d at 25, 60, or 80°C. Then the container was opened, the top layer of the biphasic solution was discarded, and the bottom layer was dried in vacuum for 1 d at 60 or 80°C. The thermal curing of poly(Et-SQ) was conducted by heating for 4 d at 140°C in N_2. Poly(3-SP-SQ) was mixed with triallyl phosphate (TAP) and triallyl isocyanurate (TAIC), and subjected to photocuring with exposure to UV light (λ_{max} ~350 nm, ~2 mW cm^{-2}) for 15 h. This UV irradiation proceeded the thiol-ene reaction [6]:

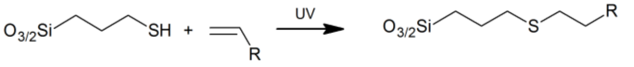

3 RESULTS AND DISCUSSION

Fig. 1 shows the effect of the aging step on the appearance of poly(Pr-SQ). The sample prepared via aging for 1 d at 80°C was a viscous liquid. In contrast, the viscosity was significantly increased by omitting the aging step. PSQ liquid was obtained when R was equal or larger than Et, and the viscosity decreased with an increase in the alkyl chain length. Poly(Me-SQ) was gelled during aging.

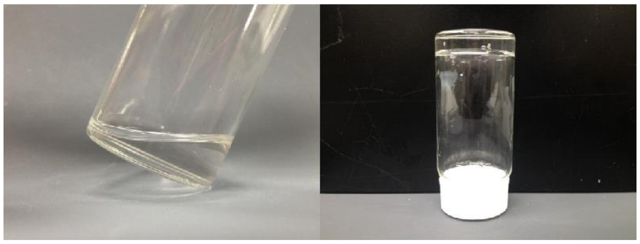

Figure 1: Photograph of poly(Pr-SQ) liquid prepared via aging at 80C (left) and poly(Pr-SQ) obtained without aging (right).

Fig. 2 shows variation of viscosity of poly(Pr-SQ) and poly(3-SP-SQ) during storage at room temperature up to 2 months. The viscosities of PSQs prepared via aging at 80°C were ~4−5×10^3 mPa s at 30°C and their stability was good. It is noteworthy that the fraction of SiOH groups of these samples was as high as ~0.2 whereas the polycondensation during storage at room temperature was slow. In contrast, the viscosities of PSQs prepared via aging at 25°C or without aging were larger, and they gradually increased with time. Thus, the aging step is crucial in obtaining PSQ liquids of lower viscosities by the cosolvent-free hydrolytic polycondensation of organotrimethoxysilanes. The relatively low viscosity of poly(3-SP-SQ) liquid is suitable for mixing with TAP and TAIC to prepare photocurable organic-inorganic hybrids.

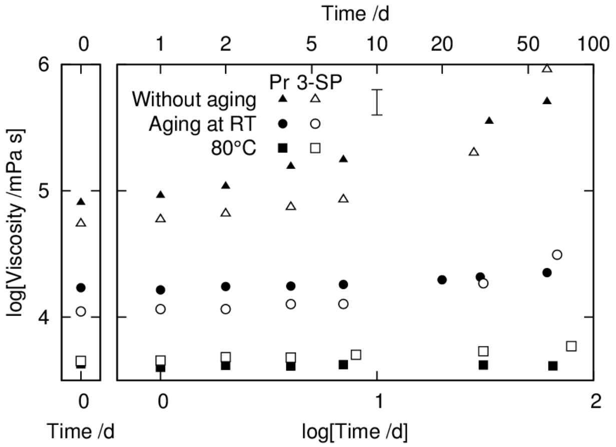

Figure 2: Viscosity of poly(Pr-SQ) and poly(3-SP-SQ) measured at 30°C for the as-prepared ones (left panel) and those stored up to 2 months at room temperature. The error bar represents the experimental uncertainty.

Fig. 3 shows optical absorption spectra of a poly(Et-SQ) glass prepared by thermal curing and composites of poly(3-SP-SQ) with TAP and TAIC obtained by UV-induced thiol-ene reaction. Poly(Et-SQ) glass exhibited a good UV transparency. The UV absorption edge was located at ~210 nm and it was shorter than that of conventional optical polymers (>260 nm). The density, refractive index (n_D), and Abbe number ($\nu_D = (1 - n_D)/(n_F - n_C)$) of poly(Et-SQ) glass were ~1.22 g cm^{-3}, ~1.44, and ~50, respectively. The density was comparable to conventional optical polymers, and n_D was lower than that of silica glass. The UV absorption edge of poly(3-SP-SQ) hybrids were located at ~300−350 nm. The good agreement of the absorption spectra between poly(3-SP-SQ)−TAIC hybrid and TAIC indicated that TAIC determines the UV absorption edge of poly(3-SP-SQ)−TAIC hybrid. The UV absorption edge of poly(3-SP-SQ)−TAP hybrid was located at shorter wavelength side of that of poly(3-SP-SQ)−TAIC hybrid because UV transmittance of TAP was better than that of TAIC. The UV absorption edge of poly(3-SP-SQ)−TAP hybrid was determined by the optical absorption of sulfide ($-CH_2SCH_2-$) and unreacted thiol (−SH) groups. The densities of these hybrids were both ~1.33 g cm^{-3}. The values of n_D and ν_D were ~1.531 and ~49, respectively, for poly(3-SP-SQ)−TAP hybrid, and ~1.556 and ~45, respectively, for poly(3-SP-SQ)−TAIC hybrid. The relatively high n_D values were due to the presence of sulfur in the composite.

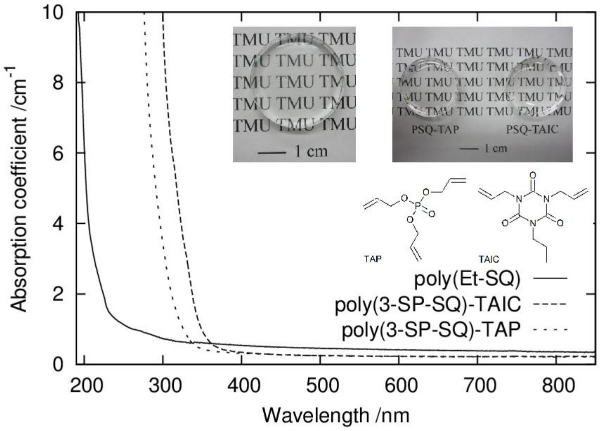

Figure 3: Photograph and optical absorption spectra of poly(Et-SQ) glass prepared by thermal curing, and poly(3-SP-SQ)-TAP and poly(3-SP-SQ)-TAIC hybrids cured by UV-induced thiol-ene reactions. The precursor PSQs were prepared via aging at 60°C.

REFERENCES

[1] R. H. Baney, M. Itoh, A. Sakakibara, T. Suzuki, Chem. Rev. 95, 1409 (1995).
[2] Y. Abe, T. Gunji, Prog. Polym. Sci. 29, 149 (2004).
[3] K. Katagiri, K. Hasegawa, A. Matsuda, M. Tatsumisago, T. Minami, J. Am. Ceram. Soc. 81, 2501 (1998).
[4] H. Masai, M. Takahashi, Y. Tokuda, T. Yoko, J. Ceram. Soc. Jpn. 113, 259 (2005).
[5] L. C. Klein, A. Jitianu, J. Sol-Gel Sci. Technol. 55, 86 (2010).
[6] K. Matsukawa, T. Fukuda, S. Watase, H. Goda, J. Photopolym. Sci. Technol. 23, 115 (2010).
[7] H. Kakiuchida, M. Takahashi, Y. Tokuda, H. Masai, M. Kuniyoshi, T. Yoko, J. Phys. Chem. B, 110, 7321 (2006).
[8] K. Kajihara, A. Sakuragi, Y. Igarashi, K. Kanamura, RSC Adv. 2, 8946 (2012).
[9] Y. Igarashi, K. Kajihara, K. Kanamura, Bull. Chem. Soc. Jpn. 86, 880 (2013).
[10] A. Sakuragi, Y. Igarashi, K. Kajihara, K. Kanamura, Dalton Trans. 45, 3151 (2016).
[11] Y. Fukuda, K. Kajihara, S. Kakinoki, J.-H. Jang, H. Yoshida, K. Kanamura, Dalton Trans. 45, 15532 (2016).

WEDNESDAY

POSTER SESSION

Relaxation of the UV-induced defects in H_2-loaded Er-doped fibers

A.P. Bazakutsa*, K.M. Golant*, O.V. Butov*

* Kotel’nikov Institute of Radioengineering and Electronics of RAS,
Mokhovaya 11-7, Moscow 125009, Russia

ABSTRACT

Twofold (0.9 dB/cm to 0.45 dB/cm) 1.55 μm gain decrease of Er-doped active fiber was observed as a result of molecular hydrogen loading and subsequent 193 nm excimer laser radiation exposure. Gain was partially restored to 0.65 dB/cm by lapse of time after UV exposure. Such a process is appearingly caused by dissociation of H_2-associated photoinduced defects.

PACS Keywords: UV-induced defects, Er-doped active fiber, hydrogen loading

1 INTRODUCTION

Hydrogen loading of optical fibers followed by UV exposure is used for fiber Bragg gratings (FBG) production [1]. When used for distributed feedback fiber laser (DFB) [2] fabrication FBG is inscribed directly in heavily-doped by active dopant fiber. It was reported [3] that H_2 loading affects the luminescent properties of active fibers negatively. By lapse of time, unbounded H_2 molecules escape from the glass, but H_2-associated UV-induced defects stay in fiber. Our work is concerned on investigation of such defects and their influence on active fiber gain.

2 SAMPLES

We used a single mode Er-doped active optical fiber, drawn from the SPCVD [4] fabricated preform. Fiber core was co-doped with aluminum. Refractive index profile is shown in Fig. 1.

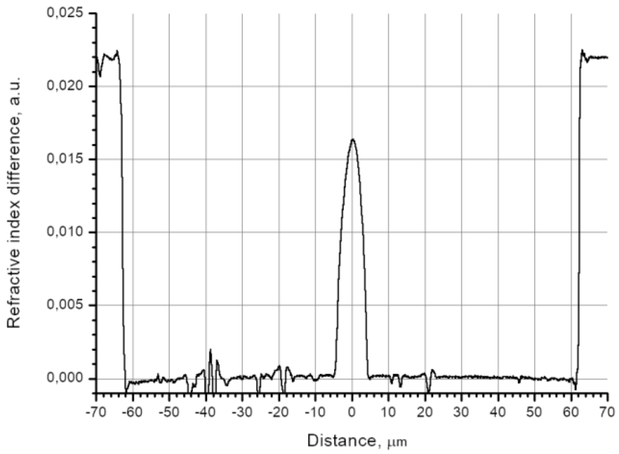

Figure 1: Refractive index profile.

The rare-earth element concentration of 0.3 mol.% of Er_2O_3 in the optical fiber core was determined with the help of X-ray structure analysis. Absorption spectrum of the active fiber under investigation is shown in Fig. 2. It is necessary to note that high absorption and a rather low «gray loss» level were achieved thanks to SPCVD method application.

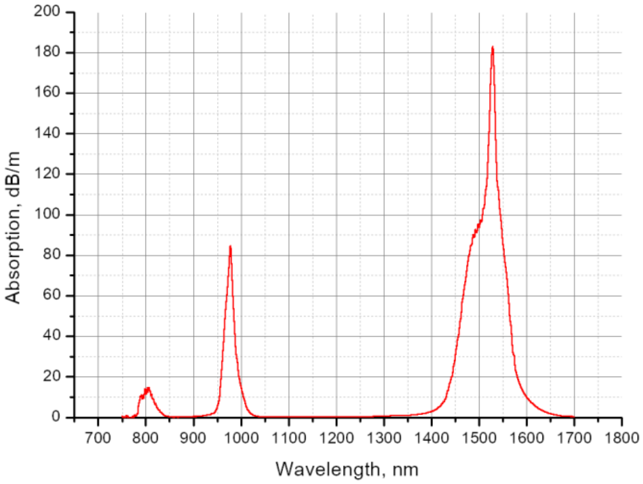

Figure 2: Er^{3+}-doped fiber absorption spectrum.

The main parameter investigated in our experiments was 1.55 μm gain. Gain was measured with the help of ordinary cut-back method [2]. Experimental setup is shown in Fig. 3.

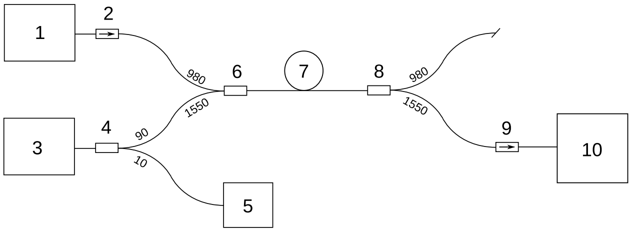

1 – tunable 0 – 620 mW 980 nm pump, 2 – 980 nm ISO, 3 – tunable 0 – 3 mW input signal source, 4 – 10/90 1550 nm coupler, 5 – power meter, 6 and 8 – 980/1550 nm WDM-couplers, 7 – Er doped active fiber, 9 – 1550 nm ISO, 10 – optical spectrum analyzer.

Figure 3: Experimental setup**.**

We used fiber coupled 1550 and 980 nm semiconductor lasers as signal and pump source correspondingly. Pump power, launched into the active fiber varied from 0 to

620 mW. WDM-coupler was used for multiplexing – demultiplexing of source and pump signals. Sample fiber length was 8 cm and in the course of cut-back method it decreased to 4 cm. Active fiber sample under investigation was located in water filled vessel to improve cooling and minimize the effect of temperature dissociation of photoinduced defects under high pump power. FBG was inscribed in one of the samples to determine temperature changes during the experiment. While monitoring the Bragg wavelength of the FBG we found that temperature increase of the fiber core was only 15 ^{0}C at the maximum pump power. Optical spectrum analyzer Agilent 86140B was used for amplified signal registration. Most of the samples were loaded with molecular hydrogen with the help of special high pressure chamber at 12 MPa and 100 ^{0}C temperature during 24 hours. 193 nm radiation of ArF-excimer laser was used for UV exposure of the samples. Radiation power density was 75 mJ/cm^2, the repetition rate was 10 Hz. To ensure uniform irradiation of the long section, the fiber was uniformly moved across the laser beam. Total UV exposure dose was of about 0.27 kJ/cm^2.

3 RESULTS

In the course of the measurements, the change in the gain value of the sample under investigation was studied as a function of the time elapsed after UV irradiation. Results are shown in Fig. 4:

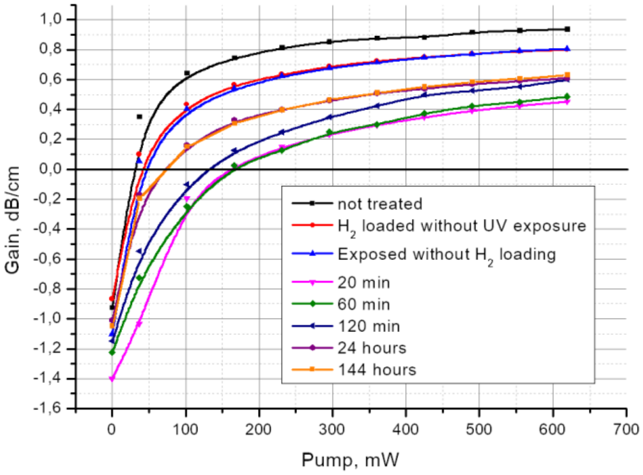

Figure 4: Er-dopped fiber gain after H_2 loading and UV exposure.

Low signal (1 μW) gain of hydrogen loaded / not loaded, UV exposed / not exposed active fiber is shown in Fig. 4. As one can see, both H_2-loading without UV exposure and UV exposure of not loaded fiber results in rather weak ~10% gain decrease, while UV exposure of H_2-loaded fiber leads to twofold (0.9 – 0.45 dB/cm) decrease of the gain at the maximum pump power. Over time the gain is partially restored to 0.63 dB/cm. The major part of the gain restoration occurs in the first hours after irradiation. Such a process can be explained as a dissociation of H_2-associated photoinduced defects, responsible for gain decrease. In addition, the effect of a sufficiently rapid change in the amplified signal transmitted through the sample was observed under the influence of 980 nm radiation (Fig. 5).

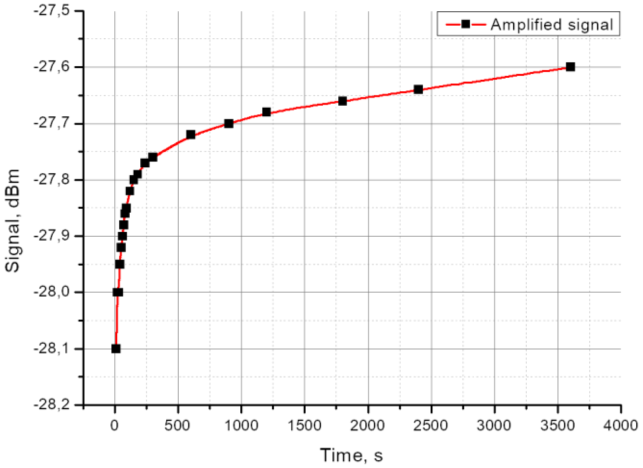

Figure 5: Amplified signal after 8 cm of H_2 loaded UV exposed Er-doped active fiber change at 165 mW 980 nm irradiation over time.

This effect was irreversible and could be observed both immediately after UV exposure and after a time sufficient for unbond H_2 escape from fiber core glass.

ACKNOWLEDGEMENT

This work was supported by Russian Foundation for Basic Research (RFBR) (project 17-07-01388).

REFERENCES

[1] M. Sejka, P. Varming, J. Hubner, and M. Kristensen, “Distributed feed-back Er^{3+}-doped fibre laser,” Electron. Lett., vol. **31**, no. 17, pp. 1445–1446, Aug. 1995.

[2] Oleg V. Butov, Andrey A. Rybaltovsky, Alexey P. Bazakutsa, Konstantin M. Golant, Mikhail Yu. Vyatkin, Sergei M. Popov, Yuriy K. Chamorovskiy, “1030 nm Yb^{3+} distributed feedback short cavity silica-based fiber laser”, Journal of the Optical Society of America B, Vol.**34**, No.3, pp. A43-A48, 2017

[3] A.P.Bazakutsa, K.M.Golant "Quenching of erbium and ytterbium luminescence by the random walk of H_2 and D_2 molecules in the silica glass of active optical fibers", Journal of Non-Crystalline Solids Vol. **411**, pp. 68 – 75, 2015

[4] Golant, K. M., “Surface plasma chemical vapor deposition: 20 years of application in glass synthesis for lightguides (a review)," XXI International Congress on Glass (International Commission on Glass), 2007

Synthesis and optical properties of Bismuth-doped sol-gel derived phosphosilicate glasses

Hicham El Hamzaoui, Christophe Kinowski, Igor Razdobreev, Andy Cassez, Géraud Bouwmans, Benoît Prochet, Bruno Capoen, and Mohamed Bouazaoui

Univ-Lille, CNRS, UMR 8523 - PhLAM - Physique des Lasers Atomes et Molécules, F-59000 Lille, France

ABSTRACT

We report on Bi-doped phosphosilicate glasses fabricated via the sol-doping technique in combination with shaping using cold isostatic pressing process. After a first drawing of the bulk glass, the obtained glass cane presents a wide near infrared (NIR) photoluminescence band under visible excitation. We have shown that this NIR emission, connected to a phosphorus center, has been preserved after a second drawing of the cane into a conventional optical fiber.

PACS Keywords: sol-gel processing, glasses, silica, bismuth, photoluminescence

1 INTRODUCTION

Bi-doped silica glasses exhibit a wide near infrared (NIR) photoluminescence (PL) that can be tailored depending on the co-doping element (Al, P, Ge) [1, 2]. However, due to the dependence of the optical activity on bismuth valence state, the incorporation and the preservation of optically active bismuth centers into silica optical fibers constitute an actual challenge in materials science. Particularly, a bismuth active center related to phosphorus (P-BAC) presents promising potential for the development of new tunable laser sources and amplifying media in the spectral range of the second telecommunication window. In this spectral window around 1300 nm, indeed, active fibers adapted to common silica-based telecommunication fibers are missing. Bi-doped phosphogermanosilicate glasses have been already prepared using conventional modified chemical vapour deposition (MCVD) technique [3]. Moreover, the optical activity of Ge-free Bi-doped phosphosilicate glasses prepared using MCVD process has been recently reported [4].

In this paper, we report on P/Bi-co-doped silica glasses prepared *via* the sol-doping route. We synthesized Bi-doped phosphosilica powder using the sol-gel method. Then, the obtained powder was compressed into cylinders before being sintered and drawn into samples presenting NIR PL connected to P-BAC.

2 EXPERIMENTAL METHODS

Bi-doped phosphosilica powder was prepared using a sol-gel process starting from tetraethylorthosilicate (TEOS), triethyl phosphate, and bismuth nitrate as Si, P, and Bi precursors, respectively (with concentration ratios [P]/[Si] = 30 at.% and [Bi]/[Si] = 0.25 at.%). After gelation, the obtained gel was dried and powdered. The powdered sample was then compressed into cylinders using cold isostatic pressing. The obtained cylinders were then subjected to dehydration and densification as described elsewhere [5]. Finally, one of these doped glass rods was drawn into 1.7 mm diameter cane. The elongated cane has been sleeved into a Suprasil F300 tube and drawn into an optical fiber at about 2000 °C. The P/Bi-co-doped fiber had an outside diameter and core diameter of about 130 and 12 µm, respectively.

The atomic concentration in the glass was measured by Electron Probe Micro-Analysis (EPMA) using a CAMECA SX 100 microprobe.

The radial RI of the drawn fiber was profiled using a IFA-100 fiber index profiler.

The luminescence properties were studied by PL measurements at room temperature in the infrared region, using a HORIBA Jobin Yvon IHR550 spectrometer coupled with a nitrogen-cooled linear InGaAs array detector. The PL was collected transversely and the 514.5 nm line of an Ar^+ laser served as excitation source.

3 RESULTS

The average doping levels of P and Bi, measured by EPMA, were 2.1 and 0.023 at.%, respectively. Hence, in comparison with the amount of P and Bi initially incorporated in the starting sol, a significant loss of these species can be noticed inside the doped glasses. The loss of phosphorus, of about 77 %, could be explained by the low reactivity of triethylphosphate with TEOS [6]. On the other hand, the leakage of bismuth, estimated to 70 %, could be attributed to its high volatility at the dehydration stage. Such a leakage has been previously observed also in the processing of preforms fabricated with MCVD technology. However, in our case, the obtained bismuth doping level is higher when compared to the one reported in optical preforms fabricated using MCVD method [3].

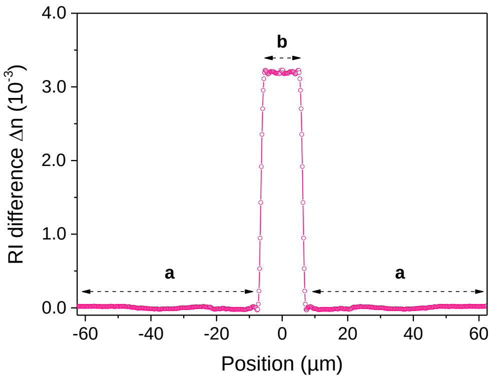

Figure 1: Relative refractive index profile (RIP) of P/Bi-doped silica fiber. Profile was taken at a wavelength of 960 nm.

Figure 1 shows the relative RIP of the obtained fiber. As can be seen, the presence of phosphorus and Bi inside the sol-gel silica glass (zone b) leads to a refractive index higher than the one of Suprasil (zones a). A quite homogenous index was measured in the fiber core of about 11 µm diameter. The refractive index difference with undoped silica glass (Suprasil F300) was about 3.2×10^{-3}. This value is very close to the one estimated from the measured average phosphorus content in the cane sample and using the data relating the RI difference (Δn) to P molar concentration of binary SiO_2-P_2O_5 glasses, reported in [7].

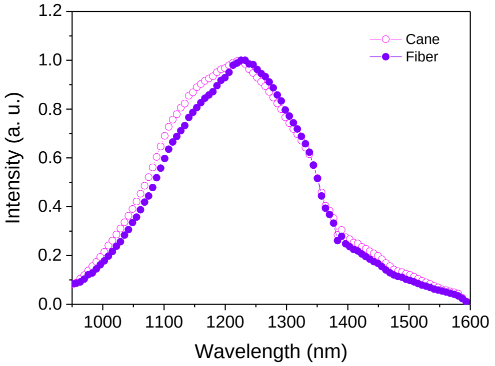

Figure 2: Normalized CW PL spectra of elongated cane and its corresponding P/Bi-doped silica fiber under excitation at 514.5 nm.

Figure 2 shows the normalized NIR PL spectra of the glassy cane and of the corresponding optical fiber under excitation at 514.5 nm. Both samples presented wide NIR PL bands centered around 1225 and 1230 nm for the cane and fiber, respectively. The corresponding full widths at half maximum (FWHM) were estimated to about 282 and 266 nm, respectively. This band is attributed to a bismuth active center associated with phosphorus [1].

4 CONCLUSION

In conclusion, we demonstrated the possibility of producing, by the sol-doping process in combination with cold isostatic pressing process, Bi-doped phosphosilicate optical fibers exhibiting high doping homogeneity, uniform RIP and a NIR PL connected to phosphorus center with a maximum intensity in the region of 1230 nm and a FWHM of about 266 nm. This emitting center is very stable during the fiber drawing process.

ACKNOWLEDGMENTS

This work has been partially supported by IRCICA and CERLA institutes of University of Lille.

Funding: This work was supported by the French Agence Nationale de la Recherche: the LABEX CEMPI (ANR-11-LABX-0007) and the Equipex Flux (ANR-11-EQPX-0017); The Ministry of Higher Education and Research, the Hauts-de-France Regional Council and the European Regional Development Fund (ERDF) through the Contrat de Projets Etat-Region (CPER Photonics for Society P4S).

REFERENCES

[1] E. M. Dianov, "Bismuth-doped fiber lasers - promising tunable and new wavelength lasers," in Laser Congress 2017 (ASSL, LAC), OSA Technical Digest (online) (Optical Society of America, 2017), paper ATh4A.1.
[2] E. M. Dianov, Light Sci. Appl. 1(5), e12, 2012.
[3] E. M. Dianov, M. A. Mel'kumov, A. V. Shubin, S. V. Firstov, V. F. Khopin, A. N. Gur'yanov, and I. A. Bufetov, Quantum Electron. 39(12), 1099-1101, 2009.
[4] N. K. Thipparapu, A. A. Umnikov, P. Barua, and J. K. Sahu, Opt. Lett. 41, 1518-1521, 2016.
[5] H. El Hamzaoui, L. Courthéoux, V. Nguyen, E. Berrier, A. Favre, L. Bigot, M. Bouazaoui and Capoen B, Mater. Chem. Phys. 121, 83-88, 2010.
[6] H. El Hamzaoui, M. Bouazaoui, and B. Capoen, J. Mol. Struct. 1099, 77 (2015).
[7] C. R. Hammond and S. R. Norman, Opt. Quantum Electron. 9(5), 399-409, (1977).

Multiphysics Numerical Model of Rare Earth-Doped Cladding-Pumped Fiber Amplifiers for Space Missions

M.A. Chiapperino, C. Campanella, P. Bia, L. Mescia

Department of Electrical and Information Engineering, Polytechnic University of Bari
Via E. Orabona 4, 70125 Bari-Italy

ABSTRACT

In this paper, a multiphysics numerical model based on the spatial-dependent rate equations and 3-D thermal analysis has been developed to investigate the cladding pumped Er^{3+}/Yb^{3+}-codoped fiber amplifiers (EYDFAs) for space applications. Using the developed numerical code, the temperature field inside the fiber have been calculated and the temperature-dependent optical amplifier behavior have been analyzed.

PACS Keywords: Er^{3+}/Yb^{3+}-codoped fiber amplifier, space optical communications, thermal analysis, computational model.

1 INTRODUCTION

In the context of space optical communications rare-earth-doped fiber amplifier (REDFA) is the most sensitive part of the whole system [1]-[2]. As consequence REDFA design has to consider spectroscopic, fiber, operative and radiation parameters as well as temperature effects. Existing temperature-dependent models of REDFA are typically restricted to special cases and approximations, such as radial two-dimensional (2-D) heat flux and heat source into the fiber core. Based on these considerations, a numerical algorithm combining the 3-D non-homogeneous heat conduction equation with nonlinear rate equations, has been developed to study the cladding pumped Er^{3+}/Yb^{3+}-codoped fiber amplifiers for space missions. The developed numerical code makes possible the calculation of the temperature field inside the fiber and a correct understanding of the temperature-dependent optical amplifier behavior. Moreover, it is a useful tool to obtain reliable qualitative and quantitative predictions for the design and optimization of the amplifier performance in a large variety of operative configurations.

2 THEORETICAL MODEL

The proposed numerical algorithm combines the 3-D non-homogeneous heat conduction equation with nonlinear rate equations. Using the staircase approximation of the refractive index profile along the longitudinal z-direction, the whole fiber length has been sampled in N slots and an electromagnetic analysis has been performed for each longitudinal step. The calculated modal amplitudes are used to evaluate the z-dependent overlap factor which is used in the rate equation model. The light amplification has been studied using a semiclassical approach based on the most general rate equations for the pump, signal, and amplified spontaneous emission (ASE). The numerical code solves a coupled nonlinear differential equations system constituted by Er^{3+}/Yb^{3+} multilevel rate equations and the general evolution equations describing the longitudinal propagation of pump, signal, forward and backward ASE powers in both pump and signal wavelength bands. A comprehensive and detailed description of the developed and experimentally validated numerical algorithm is given in [3]. Such algorithm is characterized by many degrees of freedom pertaining to the fiber parameters (fiber length, overlapping factors, intrinsic losses), the operative parameters (input pump and signal powers, pumping configuration, signal and pump wavelengths, number of signal channels), the spectroscopic parameters and irradiation parameters (radiation induced attenuation, RIA). The resulting, pump, amplified and ASE signals as well as the population inversion along the fiber are used to calculate the heat load. The integral transform technique is implemented to solve the thermal problem and the resulting temperature field is then used to update the refractive index distribution. Then, this new 3-D model offers a very useful tool to well understand the impact of the thermally induced refractive index changes on the performance of high-power fiber amplifiers.

3 NUMERICAL RESULTS

A double cladding Er^{3+}/Yb^{3+}-codoped fiber prototype having an inner cladding diameter equal to 125 µm, has been considered. The core, inner cladding and coating are made of phosphosilicate glass, silica glass and acrylate, respectively. By using the multiphysics numerical code based on nonlinear multilevel rate equations and the 3-D non-homogeneous heat conduction equation, the effects of the fiber length on temperature distribution and optical gain have been analyzed. The results concerning the study performed by changing the fiber core diameter, d, for a fiber amplifier 20 m long are reported in Fig. 2 and Fig. 3. A backward pumping scheme has been employed.

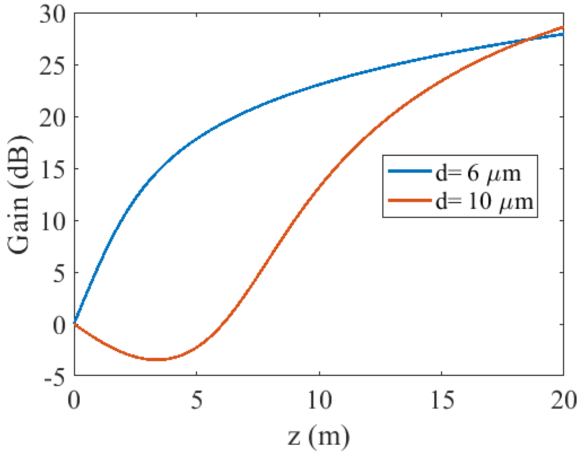

Figure 1: Gain versus fiber length, z, for two values of fiber core diameter, d.

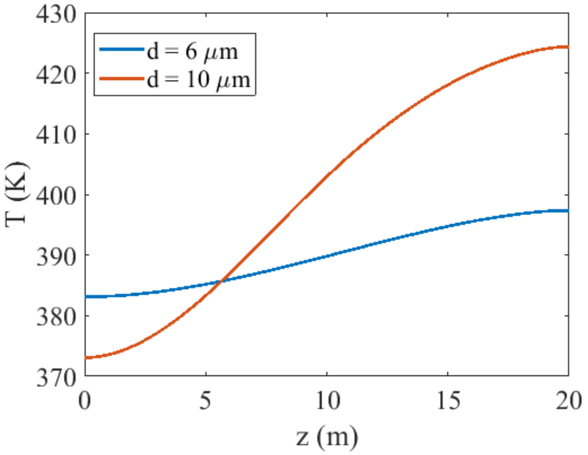

Figure 2: Temperature, T, versus fiber length, z, for two values of fiber core diameter, d.

Fig. 1 shows the gain inside the fiber for two values of core diameters. As expected, the gain increases by increasing the fiber length. Moreover, for the considered fiber length, a similar gain has been calculated for the two amplifier configuration. In fact, the larger pump absorption characterizing the fiber having larger core diameter gives an optimal fiber length lower than 20 m. As illustrated in Fig. 2, the temperature has a maximum value corresponding to the fiber end where the pump is injected decreasing toward the fiber end where the signal is injected. The higher temperature of the amplifier having core diameter equal to 10 µm can be justified by considering that it exhibits an higher pump absorption. As a result, the best performance in terms of high gain and low temperature is obtained using the fiber with the smallest fiber core diameter.

4 CONCLUSION

In this paper, a numerical algorithm combining the 3-D non-homogeneous heat conduction equation with nonlinear rate equations, has been developed to predict the temperature-dependent performance of cladding pumped Er^{3+}/Yb^{3+}-codoped fiber amplifiers. The temperature distribution and optical gain versus the fiber length have been calculated for two values of fiber core diameter. The obtained numerical results underline that the best gain and temperature performance is obtained when the fiber core diameter is the smallest.

REFERENCES

[1] S. Girard, J. Kuhnhenn, A. Gusarov, B. Brichard, M. V. Uffelen, Y. Ouerdane, A. Boukenter, and C. Marcandella, “Radiation effects on silica-based optical fibers: Recent advances and future challenges,” IEEE Trans. Nucl. Sci., vol. 60, pp. 2015–2034, 2013.

[2] S. Girard, Y. Ouerdane, B. Tortech, C. Marcandella, T. Robin, B. Cadier, J. Baggio, P. Paillet, V. Ferlet-Cavrois, A. Boukenter, J.-P. Meunier, J. R. Schwank, M. R. Shaneyfelt, P. E. Dodd, and E. W. Blackmore, “Radiation effects on Ytterbium- and Ytterbium/Erbium-doped double-clad optical fibers,” IEEE Trans. Nucl. Sci., vol. 56, pp. 3293–3299, 2009.

[3] Ladaci, S. Girard, L. Mescia, T. Robin, A. Laurent, B. Cadier, M. Boutillier, Y. Ouerdane, and A. Boukenter, “Optimized radiationhardened erbium doped fiber amplifiers for long space missions,” J. of Applied Physics, vol. 121, p. 163104, 2017.

Structural Evolution in Thermally Treated Preforms of Slip Cast Silica Ceramics as Revealed from FTIR Reflectance Study

Alexandre Chmel, Rustam Mamalimov, Alfred Sinani

Ioffe Institute, 26 Polytekhnicheskaya, 194021 St. Petersburg, Russia

ABSTRACT

The FTIR reflection spectra of a commercial silica ceramics, which is used in laser pump systems, were recorded at three stages of the thermal treatment of its cast preform: after drying at 100°C; sintering at 1200°C; and firing. The spectroscopic data evidenced the presence of a considerable amount of non-bridging Si–O bonds in the primary material (before high-temperature heat treatment); this is a favorable factor for doping the ceramics by Eu, Ce, Sm oxides in order to transform the UV radiation from pump lamps into the visible luminescent radiation. The non-bridging bonds did not manifest themselves in a final product but the IR spectroscopic data evidenced the presence of residual strain in the finished silica ceramics

PACS keywords: 81.40.-z, 81.06.Je, 78.30.-j

INTRODUCTION

First commercial applications of cast fused silica appeared in sixties of the last century [1, 2], and the technology of manufacturing various ceramic products continues to be developing up to now [3, 4]. The silica cast ceramics is used in chemical industry (reactors, lining, etc.), in foundry (molds for precision casting), in aircraft industry (radomes) etc.; however, there is little information on the structural evolution of cast preform to refractory ceramics at successive stages of thermal treatment. In this communication we present results of the IR study of silica ceramics made by water slip casting of finely dispersed synthetic silicon dioxide. This commercial ceramic is produced in Russia under the trademark Kersil™. Each newly-cast preform passes through a few stages of heat treatment: conditioning, drying, sintering, and firing. Every thermal cycle produces some changes in the structure of silica network, which lead to the consummation of target properties of a final product. The performed spectroscopic analysis showed some particular features in the structure of both intermediate and finished products, the knowledge of which would be useful for controlling the product properties at all stages of thermal processing.

EXPERIMENTAL

The Kersil™ ceramics was made by the water slip forming of the fine powder of high chemical purity SiO_2. A newly-cast preform shaped to 50 mm disc of 15 mm in thick was conditioned at room temperature during two days with subsequent drying at temperature of 100°C for 2 hours. The dried preform was sintered in an electric furnace at temperature of 1200°C. The final firing was performed to protect the porous material from the water penetration. Some characteristics of the product are given in Tables 1, 2. The obtained ceramics was close in physical and mechanical properties to the material Corning 7941.

The FTIR reflection spectra of the sample taken after drying, sintering, and firing were recorded with a spectrometer IR Prestige 21.

Table 1. Some properties of Kersil^{TM}.

Characteristics	Magnitude
Density, g/cm^3	1.9–2.1
OH^- content, ppm	10^3
Porosity, %	10

Table 2 Vickers hardness of Kersil^{TM}.

Treatment	Vickers hardness *, GPa
Drying at 100°C	0.29 ± 0,02
Sintering at 1190°C	4.6 ± 0.6
Firing	8 ± 1

*Indentation load is of 98 N.

RESULTS AND DISCUSSION

Figure 1 presents the reflection spectra of a cast preform of silica ceramics recorded after its drying at 100°C; after sintering at 1200°C; and after firing. One can distinguish certain trends when comparing the band positions and relative intensities in the spectra of heat treated samples. In the dried preform, the most intensive band belonging to the vibrations of an oxygen atom in Si-O-Si groups is situated at 1122 cm^{-1}. This peak position is characteristic for the reflection spectrum of fused SiO_2. However, the feature shifts to 1118 cm^{-1} in the sintered sample and reach 1115 cm^{-1} after firing. The variation of the vibration frequency of oxygen atoms in Si-O-Si bridges in fused SiO_2 subjected to uniaxial tensile/compressive stress was reported in Ref. [5]; the peak shifts due to change in the value of Si–O–Si angle. In our case, the band shift signalized that the sintering and firing procedures induced the internal stress in the slip-cast-derived ceramics.

As a rule, the high-temperature annealing results in the stress relaxation that is it leads to more equilibrium state of a solid. However, in the case of water-saturated porous SiO_2, its heat treatment caused the intensive water yield from the sample bulk. This process gives rise to the increase of the silica network connectedness but a certain tensile stress appears.

The presence of Si-OH end-groups in the primary substance was evidenced by the presence of a wide band in the range of 600-700 cm^{-1} in the spectrum of dried sample. This band had been assigned [6] to atomic groups containing one or two non-bridging oxygen atoms, such as HO-Si-OH. One can see in Fig. 1a, that in the spectrum of dried sample this band is close in its intensity to the intensity of the band at 790 $см^{-1}$, which belong to bridging structural groups; The intensity of the band at ~670 cm^{-1} decreases significantly after sintering the preform at 1190°C (Fig. 1b), and the feature almost disappears at (Fig. 1c). The presence of a great deal of non-bridging oxygen atoms in the preform before the high-temperature treatment is explained by the intensive hydrolytic reactions in SiO_2 particles in the primary water slurry. The sintering carried out at 1190°C resulted in dehydration of the OH^--saturated silica product with forming vitreous substance between compacted particles [7].

The presence of multiple end groups in the anionic glass network of the primary substance is a favorable factor for obtaining the doped ceramics. For example, the using of $Kersil^{TM}$ for fabrication of reflecting elements for high-power laser pumping systems was quite productive due to its high capacity to accept rare-earth dopants, such as Eu, Ce, and Sm oxides, which gain the transformation of the UV radiation from pump lamps into the desired luminescent radiation [8].

CONCLUSION

The IR spectroscopic data evidence the presence of residual strain in the finished silica ceramics, which appears as a result of fast yield of combined water at the stage of high-temperature treatment of a cast preform. This factor reduces mechanical strength of the ceramics.

At the same time, the great amount of the end-groups in the silica network of the primary product gains the capacity of the studied ceramics to accept dopants; this property is useful in some specialized applications.

REFERENCES

[1] J.D. Wallton, Ceramic Age, 76, 33–39, 1960.

[2] J.W. Lindenthal, US Patent 3163688 A, 1962.

[3] V.V. Vikulin, I.L. Shkarupa, S.M. Itkin, F.Ya. Borodai, Patent RU 2385850, 2008.

[4] A.U. Kumar, S.S. Kumar, Patent US 20120098169 A1, 2012.

[5] M. Tomozawa, Y.-K. Lee, Y-L. Peng, J. Non-Cryst. Solids, 242, 104–109, 1998.

[6] P.H. Gaskell, D.W. Johnson. J. Non-Cryst. Solids, 20, 171–191, 1976.

[7] A. Chmel, T. Pesina, V.S. Shashkin, J. Non-Cryst. Solids 210, 254–260, 1997.

[8] V.V. Kornev, I.A. Pavlova, S.S. Pivovarov, Inorg. Mater. 23, 145–147, 1987.

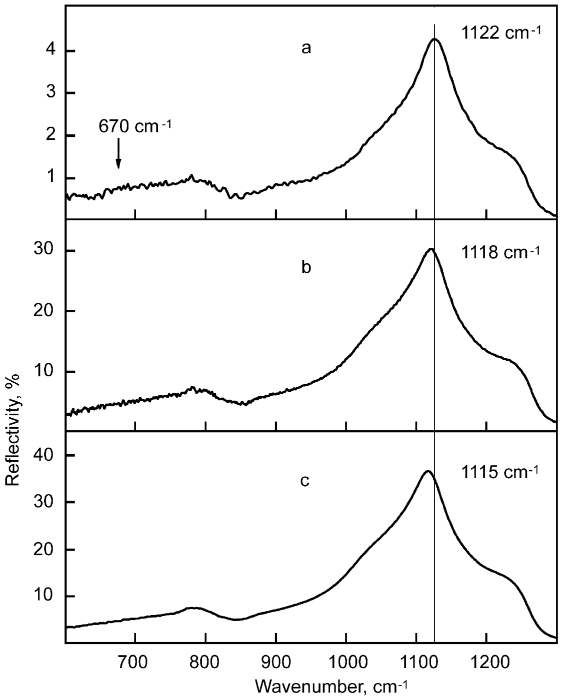

Figure 1: FTIR reflection spectra of a cast preform of silica ceramics recorded after its drying at 100°C (a); after sintering at 1200°C (b); and after firing (c).

Proton radiation responses of pure or doped multimode optical fibers

S. Girard*, P. Paillet**, M. Trinzcek***, C. Marcandella**, A. Alessi*, A. Morana*, A. Boukenter*,
Y. Ouerdane*

*Univ Lyon, Univ Saint-Etienne, Laboratoire Hubert Curien, UMR CNRS 5516, Saint-Etienne, France
**CEA, DAM, DIF, Arpajon, France
***TRIUMF, Vancouver, Canada

ABSTRACT

Radiation-induced attenuation (RIA) spectra in pure (PSC)- and doped-silica core multimode fibers (MMFs) are measured in the spectral range 300 – 900 nm during and after steady state 105 MeV proton exposure. The RIA growth and decay of two F-doped optical fibers are compared with those of a "dry" PSC and a germanosilicate fibers. F-doping reduces the UV-RIA related to SiE' centers whereas it can be associated with a RIA increase in the visible-near-IR through the generation of self-trapped holes.

PACS Keywords: Radiation effects, optical fibers, protons, self-trapped holes

1 INTRODUCTION

The most extensively researched area of radiation effects on photonic component concerns optical fibers [1]. For space applications, γ-rays are commonly used for qualification due to their low-cost and more readily availability compared to proton facilities. However, for earth-bound applications, Boucher *et al.* showed that the environment seen by photonic components, such as fiber-optic gyros or data links, will be dominated by energetic protons [2]. Previous studies showed that pure-silica-core (PSC) and F-doped-core fibers are the most radiation-resistant waveguides to high dose levels [3-6] in the Telecom windows (850, 1310 and 1550nm). However, some of these fibers exhibit high RIA levels at lower doses, especially after exposure to a high dose rate and low dose (<20 krad) X-ray pulse [7]. Their unexpected behaviors can be explained by room-temperature (RT) unstable defects: the self-trapped holes (STHs) [8,9]. In this work, we investigate the effects of 105 MeV protons on the transmission properties of radiation hardened fibers to detect if these unstable defects can influence their proton radiation responses for space applications.

2 EXPERIMENTAL DETAILS

We characterized a set of 4 MMFs. Fibers #1 and #2 are step-index (200/250 µm) prototype fibers made by VAD process. As previous studies [10,11] showed that the F-level inside the glass matrix strongly affects the point defect generation mechanisms, we used two samples with either low (*Fiber #1; few hundreds of ppm*) or high *(>2 wt.%)* F-doping of the cores. Both fibers have low Cl and hydroxyl groups (OH, <2 ppm) concentrations. According to [12], the different F amounts result in different incorporation mechanisms associated with different degradation mechanisms [11]. Fiber #3 is a commercial PSC MMF made by MCVD process with low level of OH groups but quite large amount of Cl. Fiber #4 (50/125 µm), made by OVD process, has a Ge-doped core (>4 wt.%). Proton irradiations were performed at RT at TRIUMF PIF, Canada [13]. The 105 MeV proton fluence was measured using a calibrated ion chamber and converted into dose through the factor 1 p/cm²= 8.9×10^{-8} rad(Si). The light from a DH-2000 source is injected in the sample under test and the transmission spectra from 300 to 900 nm are recorded by a HR4000 spectrometer (Ocean Optics).

3 EXPERIMENTAL RESULTS

Fibers #1, #2 and #3 have been submitted to a total fluence of 2.2×10^{11} p/cm^2 [~20.1 krad(Si)] whereas fiber #4 has been exposed to ~25.6 krad [2.8×10^{11} p/cm²]. Fig. 1 illustrates the RIA growth at several wavelengths during the proton exposure (flux ~10^8 p cm^{-2} s^{-1}) and its decay after the irradiation ends. Our results show a large dispersion in the sensitivity of the different fiber types, highlighting that specific defects seem involved in the fiber #2 response. Fig. 2. gives the spectral dependence of the RIA for the four fibers for a fluence of 5×10^{10} p/cm² (~5 krad). Fibers #1 and #2 are characterized by the lowest RIA level in the spectral range 300-500 nm. The two fibers exhibit a strong difference in radiation sensitivity at larger wavelengths (500-900 nm) with a factor ×10 of RIA increase in the highly F-doped sample #2. For fiber #2, the induced losses in the Vis/near-IR are maximum around 675 nm. Fiber #1 also exhibits an optical absorption (OA) in the visible part of the spectrum with a peak around 620 nm. Fiber #4 with the Ge-doped core has the largest RIA level for λ<550 nm but has lower RIA at greater wavelengths than fiber #2.

4 DISCUSSION

Previous studies showed that F-doping of silica reduces the generation of SiE' centers and non-bridging oxygen hole centers (NBOHC) under γ-rays [15] or fluorine-dimer-excimer laser radiation [10]. PSC fiber #3 is characterized by larger RIA at λ<550 nm (>2.25 eV) than the two F-doped samples. At larger wavelengths, its low RIA is comparable to the one of fiber #1.

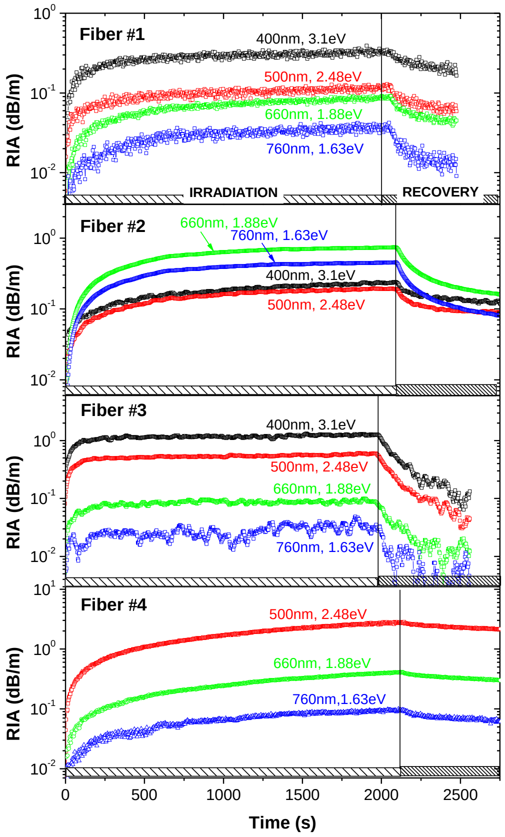

Fig.1. RIA growth and decays kinetics during and after a 105 MeV proton exposure at RT.

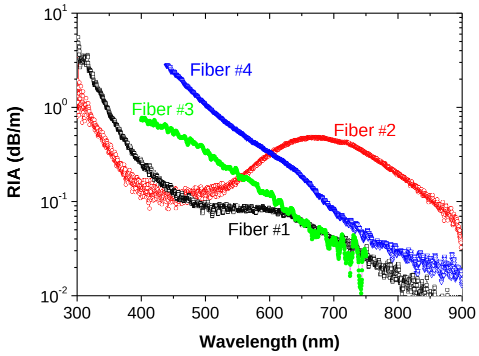

Fig.2. RIA spectral dependence during 105 MeV proton exposure. Spectra acquired at ~5×1010 p/cm^2 [5 krad(Si)].

It was proposed [16] that F acts by limiting the number of precursors (*such as strained bonds*) for radiation-induced defects. These defects are associated with this UV/visible OA bands: SiE' (5.8 eV, FWHM= 0.8 eV) and NBOHC (4.8 eV, FWHM= 1.07 eV; 1.97 eV, FWHM= 0.17 eV) [17]. This positive influence of the F-doping on SiE' and NBOHC centers explains the reduced contribution of UV absorbing species in fibers #1 and #2 compared to PSC fiber #3. This positive effect of F-doping in the UV range is counterbalanced by a large increase of RIA in the Vis/near-IR range for the highly F-doped sample. The RIA in the Vis/near-IR seems related to OA bands at 660 nm and 760 nm that are associated to the self-trapped holes (STHs) [9], either STH1 or STH2 [9]. Previous work [11,18] provided evidence that their amount seems not directly linked to the F or OH group concentrations [9] but rather to the glass fictive temperature, with an increase of STH's optical absorption in fibers in comparison with bulk samples. These large 660 nm and 760 nm OA bands, observed in some PSC [19] and F-doped fibers may be related to uniaxial strain and/or abnormally high fictive temperatures during the fiber drawing process. For the Ge-doped fiber #4, RIA spectrum can be reproduced by the same three defects: NBOHC (1.97 eV, FWHM=0.26 eV), Ge(1) (4.41 eV, FWHM=1.1 eV) and GeX (2.61 eV, FWHM=0.82 eV) than the ones proposed by D.L. Griscom to explain the γ-ray response of this class of fibers [19] or by our group for 14 MeV neutron irradiation [20]. Other defects are also present [21] but did not affect the transmission in our radiation test conditions.

5 CONCLUSION

The vulnerability of F-doped MMFs depends on both the F amounts and on the signal wavelength. Even at low F-levels, the doping of silica allows to reduce the UV-RIA. However, it seems that for the AVD manufacturing process, the increase of F-levels results in the appearance of STHs. That means that some F-doped and some PSC fibers that are radiation-tolerant to high doses (> 1 Mrad) can present large Vis/near-IR RIA levels due to these defects at lower dose levels representative of space missions. This can potentially limit the use of such "radiation hardened" fiber for data transmission in the 1st Telecom window (850 nm).

6 REFERENCES

[1] F. Berghmans, Opto&Laser Europe, 25 (1995).
[2] R.H. Boucher, *et al.*, Opt. Eng. 35(4) 955 (1996)
[3] E. J. Friebele, "Photonics in the space environment", NSREC Short Course, San Diego III-1 (1991).
[4] D.L. Griscom, *et al.*, Appl. Phys. Lett. 69(3), 322 (1996).
[5] D.L. Griscom, Appl. Phys. Lett. 71(2), pp. 175 (1997).
[6] T. Shikama, *et al.*, Fus. Eng. Design 51-52, 179 (2000).
[7] S. Girard, *et al.*, J. Non-Cryst. Solids 352, 2637 (2006).
[8] D.L. Griscom, J. Non-Cryst. Solids 349, 139 (2004).
[9] D.L. Griscom, J. Non-Cryst. Solids 352, 2601 (2006).
[10] H. Hosono, *et al*, Appl. Phys. Lett., 74(19), 2755 (1999).
[11] R.P. Wang, *et al.*, J. Appl. Phys. 98, 023701 (2005).
[12] R.E. Youngman *et al.* J. Non-Cryst. Solids 337, 182 (2004).
[13] E. Blackmore, IEEE REDW Record, Reno, Nevada, 1 (2000).
[14] H. Anderson, *et al.*, "Hydrogen –Stopping Powers and Ranges in All Elements", Pergamon Press, New York (1977).
[15] K. Awazu, *et al.*, J. Appl. Phys. 73(4), 1644 (1993).
[16] K. Awazu, *et al.*, J. Appl. Phys. 94(10), 6243 (2003).
[17] L. Skuja, in Proceedings of the NATO Advanced Study Institute, Pacchioni G. et al. Eds, 73 (2000).
[18] Y. Sasajima, *et al.*, Phys. Rev. B 68 014204 (2003).
[19] D.L. Griscom, J. Appl. Phys. 80(4) 2142 (1996).
[20] S. Girard, *et al.*, IEEE Trans. Nuc. Sci., 53(6), 3750, (2006)
[21] S. Girard, *et al.*, Appl. Phys. Lett., 83(2), 219 (2003).

Non-Conductive Graphene-Based Derivative as Interlayer in Graphene/n-Si Schottky Barrier Solar Cells

A. Gnisci*, G. Faggio*, R. Carotenuto*, G. Messina*, L. Lancellotti**, E. Bobeico**,
P. Delli Veneri**, A. Capasso***, T. Dikonimos****, N. Lisi****

* DIIES Dept., University “Mediterranea” of Reggio Calabria
Via Graziella, Loc. Feo di Vito, Reggio Calabria, Italy
** ENEA, Portici Research Center, P.le E. Fermi 1, Portici (Naples, Italy)
*** Department of Materials Science and Engineering,
Yonsei University, Seoul 03722, Republic of Korea
**** ENEA, DTE PCU IPSE, Casaccia Research Centre
Via Anguillarese 301, Rome, Italy

ABSTRACT

In Schottky barrier solar cell (SBSC), the interface between semiconductor absorber and metal front electrode plays an important role for reducing the dark current, blocking the majority carriers injected into the electrode at forward bias, reducing surface recombination, improving the device performance. We realize stacked structures combining n-type crystalline silicon with graphene and graphene-based derivative (GBD) with different structure, work function and electrical conductivity, obtained by varying the temperature in ethanol chemical vapor deposition (CVD). The device with the GBD interlayer exhibits promising performances in terms of external quantum efficiency (EQE, ~60%) and power conversion efficiency (PCE, ~5%). Doping treatments with nitric acid vapor was performed and improved the cell PCE up to 6.7%.

PACS Keywords: Graphene-based derivative, Photovoltaics, Solar cell, CVD graphene.

1 INTRODUCTION

In the last few years, a great deal of interest has been focused on the graphene-on-silicon (Gr/n-Si) Schottky barrier solar cell cells (SBSC), due their easier and much less expensive fabrication in comparison to traditional Si solar cells based on p-n junctions. In Gr/n-Si SBSC the graphene serves as a transparent conductive electrode and contributes as an active layer for carrier separation and hole transport [1]. The performance of Gr/n-Si SBSC is highly affected by the recombination of the charge carriers at the interface due to a low Gr/n-Si Schottky barrier height (SBH) (~0.6–0.7 V), smaller than the traditional Si solar cells. To reduce charge recombination and improve the performance, an insulating interfacial layers can be added between Gr and n-Si [2]. This interlayer works as an electron blocking layer preventing the diffusion of electrons from n-Si to Gr and thus reducing the carrier recombination. The interlayer should be very thin (down to atomic thickness) and uniform to avoid increasing the series resistance (R_s).

In this work we use a graphene based derivate (GBD) as interlayer, realized by chemical vapor deposition (CVD) of ethanol on copper. SBSC with single and double GBD interlayers were fabricated and tested. A molecular p-doping treatment (by HNO_3 vapors) was performed on the SBSC with single interlayer, showing an increment of cell’s PCE from 4.8 % to 6.7 %.

2 EXPERIMENTAL SECTION

Conductive Gr and GBD interlayer were grown by ethanol CVD onto copper substrate respectively at 1070°C and 790°C. After growth the films were transferred by using cyclododecane [3] onto polished Si substrates ([100]-oriented, n-doped, 1 Ω cm), with thermally grown SiO_2 layer (300 nm) patterned by photolithography and with an active area of 0.09 cm^2. The scheme of the solar cell is shown in Figure 1.

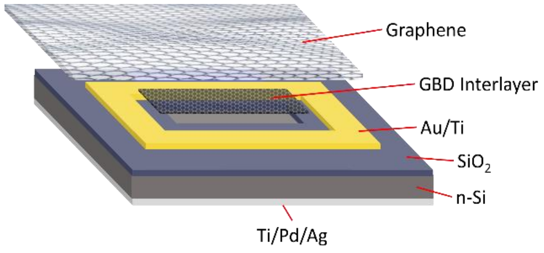

Figure 1. Schematic illustration for 1L-SBSC

SBSC with single-layer GBD between single-layer Gr and n-Si (1L-SBSC), and with double-layer GBD between double-layer Gr and n-Si (2L-SBSC) were fabricated. Molecular p-doping was performed by exposing the top part of the cell to HNO_3 vapor (from a 70 % solution diluted 1:1 in deionized water) for 3 min [4].

The sheet resistance of the Gr was measured by four-point probe method in Van der Pauw configuration. Raman spectra were acquired on samples transferred onto Si/SiO_2 substrates. Laser excitation wavelength of 532 nm was focused on the sample surface using a 100× objective with a spot size of approximately 1 µm and a low laser power (below 1 mW) was used to minimize sample heating and possible damages. The solar cells were characterized by means of external quantum efficiency (EQE) and current density–voltage (J-V) measurements. Illuminated J-V characteristics were performed in standard test conditions (25° C, AM1.5G, 1000 W/m^2).

3 RESULTS AND DISCUSSION

The Raman spectrum of Gr (Fig. 2a) exhibits D, G and 2D peaks respectively at ~1350 cm^{-1}, ~1580 cm^{-1}, ~2700 cm^{-1} [5]. The 2D to G intensity ratio (I_{2D}/I_G) less than 1 and the D to G intensity ratio (I_D/I_G) of 0.13 indicate the formation of multilayer Gr [5] with low defect density [6]. In the Raman spectrum of GBD (Fig. 2b), the D peak strongly intensifies and the defect-related D’ peak at ~1620 cm^{-1} appears. The high I_D/I_G (~3.2) is typical of defective carbonaceous film [5] or hydrogenated Gr [7]. The sheet resistances of the Gr and GBD films are 0.5 and 124 kΩ/sq, respectively.

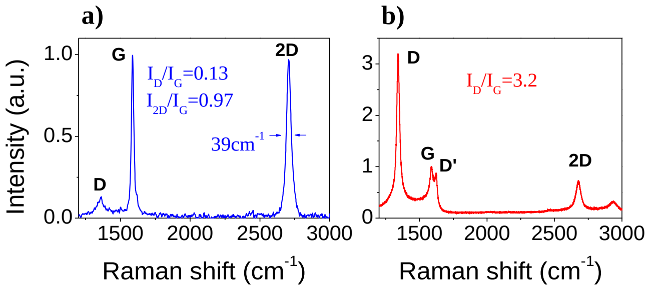

Figure 2. Raman spectra of a) conductive graphene, b) GBD interlayer

The diode characteristics were extracted from the dark ln(J)-V curves (Fig. 3): 1L-SBSC shows the lower reverse saturation current, the ideality factor (η) is reduced from 2.15 to 1.6 while reaches 3.5 in 2L-SBSC, the SBH increases from 0.78 to 0.87 V and R_s decreases from 216 Ω to 178 Ω. EQE curves were acquired with and without optical bias (OB). Without OB all cells show an EQE ~60 % in the wavelength range 650 nm < λ < 800 nm. Differently from SBSC and 2L-SBSC, for 1L-SBSC the EQE curves acquired with OB result unchanged. The higher EQE observed for the 1L-SBSC with OB is due to more efficient charge separation and charge collection as a result of increased SBH and reduced recombination centers at the interfaces, which also reflect in reduced R_s. These results reveal a lower interface recombination and hence better junction quality with the introduction of single GBD layer, while with double GBD layer a large quantity of trap states between stack interfaces is present.

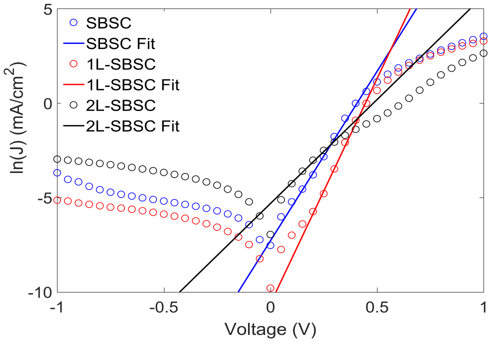

Figure 3. Dark ln(J)-V characteristics

The molecular p-doping treatment was performed on 1L-SBSC and the J-V characteristics under illumination were acquired just after the fabrication and after each doping process step (HNO_3 doping, ageing and recovery). The doping improves the cell performance in particular in term of PCE and fill factor (FF), while reducing the R_s. The FF increases from 39.4% to 54.2%, with a consequent increment of PCE from 4.8% to 6.7%. The R_s decreases from 17.5 to 7.8 Ω. After 2 hours, FF and PCE decrease respectively at 32.7% and 3.5%, increasing the S shape of the curve with R_s=32.3 Ω. A quasi-complete recovery of photovoltaic parameters is possible upon repeating the exposure to HNO_3. This effect is due to the instability of the doping obtained by volatile acid compounds.

CONCLUSION

SBSC based on few-layer Gr/n-Si junction with single and double GBD interlayers were fabricated and characterized. J-V curves and EQE confirm that a single GBD layer improves the Schottky junction, by reducing the inhomogeneities at interface that work as recombination centers. In 1L-SBSC, the saturation current and R_s are lowered, while the SBH increases from 0.78 to 0.87 V in comparison with SBSC. η was reduced from 2.15 to 1.6, as indicator of reduction of interface recombination centers. The EQE curves confirm the improvements derived by the insertion of single GBD interlayer in Gr/n-Si junction, in particular for measurements acquired in OB conditions. Doping treatment with HNO_3 vapor was performed on the 1L-SBSC, whose PCE reached 6.7%.

REFERENCES

[1] Li, X. et al., Adv Mater, 22, 25, 2743–8, 2010.
[2] Ye, Y. et al., J Mater Chem, 22, 46, 24224–9, 2012.
[3] Capasso, A. et al., Appl Phys Lett, 105, 11, 113101, 2014.
[4] Lancellotti, L. et al., 2014 Fotonica AEIT Ital Conf Photonics Technol, p. 1–3.
[5] Ferrari, A.C., Solid State Commun, 143, 1, 47–57, 2007.
[6] Pimenta, M.A. et al., Phys Chem Chem Phys, 9, 11, 1276–90, 2007.
[7] Wang, Y. et al., ACS Nano, 4, 10, 6146–52, 2010.

Glass Formation Ability and Glass Structure of Chalcogenide Systems

Minaev V., Timoshenkov S., Korobova N.

National Research University of Electronic Technology, MIET
Bld. 1, Shokin Square, Zelenograd, Moscow, Russia, 124498

Preference: poster presentation

ABSTRACT

The relationship between the glass formation ability, covalent ionic bonding, entropy of melting, evaporation, melt dissociation and chalcogenes entering into it has been analyzed. The formula of glass-forming ability was specified. Ways of a correct comparison of this value for alloys with various chalcogenes were indicated. Conclusion was made about the possibility of glass formation only in liquids that are capable for dissociation (non-molecular) and subsequent polymerization. A simbatic relationship was established between the energy of atom covalent ionic bonding and the softening temperature, micro-hardness, and the specific electrical glass resistance. Glass structure model was proposed.

PACS Keywords: glass formation, structure, system, composition.

1 INTRODUCTION

Chalcogenide glass semiconductors are widely used in the production of electrical switches, memory elements, acousto-optic devices. Glassy materials used in electronic devices are divided into two types: (1) structurally stable materials, in which structure does not change during device operation, (2) structure-reversible materials which structure varies in a controlled and reproducible manner. A number of methods for evaluating the glass-forming ability of alloys are known. The most physically justified is the comparison of the glass-forming ability with the chemical bonding energy and the liquidus temperature [1-3]. It is difficult not to agree with the opinion of Rawson [1] that the greater energy of the chemical bond between oxide melt atoms, the more difficult to rearrange and order them at the time of melt solidification, i.e. the greater the glass-forming ability. On the other hand, the lower the melting point of the oxide, the less rupture of the chemical bonds and the restructuring of the melt atoms into the crystal lattice, i.e. the greater the glass-forming ability. In [2], the San-Rawson criterion was modified in such way that its application can be extended to multi-component glasses, which makes it possible to predict and explain a number of regularities of glass formation in chalcogenide systems. The usual way to improve the rules, criteria, regularities lies in the direction from the particular case to the general. The existing regularity is supplemented, expanded and transformed into a more general pattern. We proposed a formula that, under certain conditions, becomes a "glass formation criterion" (GFC). It is directly proportional to the average energy of the chemical bond and the average effective coordination number, but inversely proportional to the liquidus temperature.

2 RESULTS AND DISCUSSIONS

We propose to take into account also unaccounted factors of glass-forming in the form of a certain multiplier. On the basis of numerous studies [2-4], knowledge of glasses entropy of evaporation was established in addition to the energy of chemical bonds and liquidus temperature. In Rowson's works [1], the melting entropy was considered as a criterion for the stability of phases with a certain degree of disordering. It is noted that the proposed "glass formation criterion" works well inside telluride systems and gives much worse results when comparing these systems with selenide systems. The reasons are: (1) the difference in the heat and entropy of sublimation and, correspondingly, the evaporation temperatures of selenium and tellurium alloys; (2) the melting entropy of the chalcogenes themselves. It is known that the melting entropy is a periodic function of the element number and "practically a function of the chemical bond". The magnitude of the entropy is determined primarily by the degree of change in the chemical bond during melting. All substances that change the type of chemical bond during melting are characterized by an increased value of ΔS_{melt}. The melting entropy of chalcogenes according to the data [5] is in entropy units (cal· mole^{-1} ·K^{-1}): oxygen 0.92; selenium 3.25; tellurium 5.78. As we see, with a decrease in the atomic element number, its melting entropy in the VIA group decreases. In accordance with [2 and 5] works, this is explained by the conservation (complete or partial) of the molecular structure during melting.

For oxygen, these are O_2 and O_3 molecules; these are Se8 molecules and chains of different length for selenium, i.e. there are already more broken bonds than in selenium, where Van der Waals bonds are torn during melting. For tellurium, the destruction of chains is characteristic for solid phase up to the formation of Te_2 and Te, also as significant increase in the concentration of free electrons. In order for different chalcogenides to participate in the same degree in glass formation with a certain element, it is necessary that they have the chemical bonds "chalcogen - chalcogen" severed to the same extent, i.e. so that they are equally dissociated. Only in this case their glass-forming ability will be comparable.

Studies of glass formation and glass properties in the Ga-Tl-Te system have been made. Glasses rich in thallium (up to 40 at.%) were distinguished by a unique specific electrical resistance (up to 1.3 ohm ·cm) with an activation energy of electrical conductivity ~ 1.3 eV. The current-voltage characteristic of these glasses reflects their varistor properties. Glasses poor in thallium (≤ 12 at.%) had I-V characteristic for threshold switches with memory and were suitable for manufacturing memory elements.

Minaev [2-4] noted an interesting feature of the change in such glasses properties as the softening temperature T_g, micro-hardness H and resistivity ρ in sections with a constant gallium content: $Ga_4Tl_xTe_{96-x}$ (A), $Ga_{15}Tl_xTe_{85-x}$ (B), $Ga_{20}Tl_xTe_{80-x}$ (C), $Ga_{22}Tl_xTe_{78-x}$ (D). As Tl content in the glass increases, the values of these properties decrease in the glasses of section A, remain approximately at the same level in section B and increase in sections C and D. To explain this behavior of T_g, H and ρ, the covalent ion bonding energy of the glasses was calculated for all four sections and for cases of single- and trivalent thallium. The calculation using a modified glass formation criterion which takes into account the liquidus temperature showed that the glass-forming ability in the binary Ga-Te system increases with increasing distance from the eutectic towards an increase in the gallium concentration and has a maximum 0.279 kJ/(mol· K) at 24-25 at.% Ga , which was confirmed experimentally [2]. Accounting for the energy of covalent ionic (chemical) bonding and liquidus temperature gives a more objective assessment of the glass-forming ability.

In this paper we estimated the amount of covalent - ion binding (CIB) energy in order to predict (quantify) glass properties E_{cib}. This value reflects the dependence of composition properties and glasses structure. For over than twenty ternary telluride systems the quantitative ratio of T_g and E_{cib} , it means $T_g/E_{cib} = (2.3 \pm 0.3)$ K· kJ ·mol^{-1} on the basis of glass softening temperature analysis data (at the cooling melt rate around 180 $K{\cdot}s^{-1}$) has been obtained. The maximum deviation from the average value was ± 14.0%. Obtained relation allows predicting T_g for telluride glasses. All synthesized new ternary telluride glasses in accordance with the forecast were semiconductors with p-type conductivity and $\sigma = \sigma_o \cdot \exp(-E_\sigma /kT)$. Glasses have resistivity in the range 1.3 - 1.0 ·10^7 ohm ·cm and activation energy of conductivity E_σ from 0.1 to 1.0 eV. Most of the glasses have electrical switch memory effect. They can be used as electric storage devices, as well as bit-optical recording media. Structural analysis results confirmed the presence of fine crystals mixture of tellurium and glassy phase near the crystallization temperature. The crystalline tellurium causes the resistivity decrease at this temperature for several orders. Slow cooling results in the eutectic crystals precipitation which having a low resistivity at room temperature. It was shown that the structural transformation can be controlled by heating and different cooling rates [6].

Structural-chemical and energetic factors of glass-formation, together with the relaxation conditions of glass-forming ability with increase in atomic numbers of elements have been considered as a starting point for the development of the structural- energetic concept of glass formation.

ACKNOWLEDGEMENT

Our deep gratitude to Viktor Minaev for his dedication to the Science of Glass.

Federal target program (FCP) aimed at ”Implementation of applied scientific research and experimental developments aimed at implementing the priorities of the Strategy for Scientific and Technological Development of the Russian Federation”

REFERENCES

[1] Rowson H. “Inorganic glass forming systems”, Academic Press, London and New York, 1967. 553p.

[2] Minaev V.S., [Semiconducting Chalcogenide Glass. Series Semiconductors and Semimetals , Elsevier Academic Press. Amsterdam, New-York, Tokio, 139 – 179 p. (2004).

[3] Minaev V.S., Timoshenkov S.P., and Kalugin V.V., “Some features of the glass transition process by the example of chalcogenide glass systems”, J. Optoelectron. Adv. Mater. 13(11-12), 1393 - 1399, 2011.

[4] Minaev V.S., Timoshenkov S.P., Vassiliev V.P., Aleksandrovich E.V., Kalugin V.V., Korobova N.E. “The concept of polymer nano-heteromorphic structure and relaxation of the glass-forming substance by chalcogenides, oxides and halides example. Some results and perspective //J. Optoelectron. Adv. Mater., 18 (1–2), 10–23pp., 2016.

[5] Rinzler Charles Cooper “Quantitatively Connecting the Thermodynamic and Electronic Properties of Molten Systems”. Thesis of Ph.D. Massachusetts Institute of Technology, 166p. 2017.

[6] Minaev V.S., Timoshenkov S.P., Korobova N.E., Kalugin V.V. “Some important aspects in the glass structure of chalcogenide systems”, Proceedings of SPIE –The International Society for Optical Engineering. 10224, 02240G.

First Principles Study of the Influence of the Local Steric Environment on the Incorporation and Migration of NO in a-SiO_2

M. V. Mistry*, J. Cottom*, K. Patel*, A. M. El-Sayed*, A. L. Shluger*

*Department of Physics and Astronomy, University College London
Gower Street, London WC1E 6BT

ABSTRACT

In this work the NO incorporation energies and migration barriers are correlated with the morphology of the a-SiO_2 lattice, showing a clear dependence of the local steric environment to both the incorporation of NO and its migration. This explains the observed ease with which NO is incorporated into and moves through a-SiO_2. Additionally, the importance of the model building and sampling methodology is illustrated as it has the potential to dramatically influence the results obtained, giving a range of incorporation energies of 2.5 eV and range migration barriers in excess of 3 eV.

PACS Keywords: DFT, defect diffusion, passivation, structure sampling, molecular dynamics.

1 INTRODUCTION

Amorphous materials present a formidable modelling challenge, requiring large cells and extensive statistics to allow structures within an a-SiO_2 network to be described. To capture a representative range of structural motifs requires the construction of statistical ensembles before defect concentration and kinetics can be studied. A widely accepted modelling approach relies upon using a continuum random models generated *via* molecular dynamics (MD) based melt-quench.[1] As the method has been developed and computational power has increased, the small cells of the early studies have been replaced by larger cells that are better able to describe the range of motifs that may reasonably be expected to be found in the bulk a-SiO_2 samples. In each case, a large number of test systems is required to build a statistically representative population. To understand how these different structural motifs, influence the formation energies of defects, and the barrier heights for diffusion, is of vital importance in understanding how these systems are formed and ultimately breakdown.

In this work, the diffusion of NO within amorphous SiO_2 is used as a test case. NO is an important passivation agent used to reduce the density of interface traps (D_{it}), predominately in silicon carbide-based devices, although NO based anneals have been tested with some success on Si / SiO_2 devices. The experimental work shows an accumulation of N at the interface and no significant N-incorporation into the body of the oxide. It has been found that the NO anneal passivates about 99% of the defects present in the SiC bandgap. From this, the assumption is that the NO diffuses through the oxide intact to the interface where the passivation and accumulation is observed.

Previous studies by Bakos *et al.*[2], Munde *et al.*[1], and Orellana[3] have investigated the diffusion of O_2, H_2O, V_O, N_2 and NO. Each of these studies describe a range of barriers and formation energies that can be correlated to the local steric environment. In the Bakos *et al.* study, they describe an inversely proportional relationship between the ring size and the barrier height. This study was conducted in 72 atom cells, which can lead to limited structure sampling. The work of Munde *et al.* observes that this trend can in general be extended to the migration of vacancies. The Orellana study forms a baseline for comparison as it describes NO diffusion in α-SiO_2. This work shows there is little interaction between neutral NO (NO^0) and the lattice, which supports the view that NO remains intact while diffusing through a-SiO_2, reinforcing the picture presented in the experimental studies. In this work, these strands are combined, presenting a picture of NO^0 diffusion in a-SiO_2.

2 METHODOLOGY

To conduct this study 30 amorphous structures were produced, which form an ensemble representative of the parent population (in this case a-SiO_2). Each of these structures were generated by performing an MD-melt quench on a 216-atom cell of β-cristobalite. The models generated here used the ReaxFF force field as implemented in the LAMMPS code[4,5], with a cooling rate of 1 Kps^{-1} and the NPT ensemble. The ion positions and lattice parameters of the MD structures were then relaxed with CP2K using the PBE0-TC-LRC functional to give the final test structures.[6–9] The DZVP-MOLOPT basis set was selected and a converged plane wave cutoff of 550 Ry was used. To allow the efficient calculation of the exact exchange, the ADMM approximation is used. [6]

The experimental density of a-SiO_2 is 2.2 gcm^{-3}[1], the models generated have a range of densities of between 2.1 gcm^{-3} and 2.3 gcm^{-3}. From these we take 3 samples so that the median density is 2.2 gcm^{-3} in agreement with the experimental oxide density. Figure 1 shows the distribution of bond lengths (1a), and angles (1b).

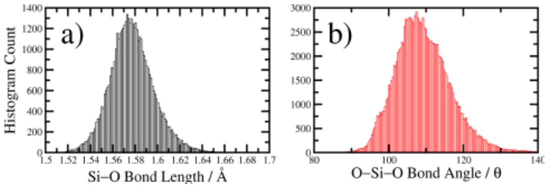

Figure 1: a) The Si-O bond angle distribution and b) the O-Si-O bond angle distribution.

NO is introduced to each of the faces of the SiO_4 tetrahedra in the above models. This forms the initial sampling of the NO_i configurations, these structures are then geometry optimized and the incorporation energy calculated. The transitions states are identified *via* climbing image nudged elastic band as implemented in CP2K, with the functional and basis set previously described.

3 RESULTS

3.1 Interstitial NO

To sample the range of incorporation energies for NO a series of initial configurations were generated with the NO in differing steric environments. From these structures the effect of the local steric environment on NO_i incorporation energy was explored and is presented in figure 3.

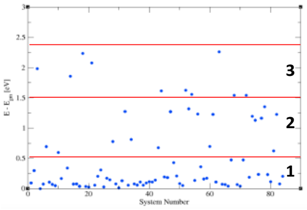

Figure 2: NO incorporation energy in a-SiO_2. The three regimes indicated relate to the degree of steric crowding the NO molecule feels. 1, representing the least (near zero interaction case), and 3 the most sterically hindered.

It is clear from figure 2 that the incorporation energies can be divided into 3 regions; the first (1) sitting between 0.0 - 0.5 eV of the lowest energy configuration of the system. This represents the case with negligible steric crowding, the NO_i sits approximately 4 Å away from the lattice. The second region (2) between 0.5 - 1.5 eV, the steric crowding is more significant with the NO_i forced into closer proximity with the lattice, with an average separation of 3 Å. The final region (3) above 1.5 eV is the point where the steric crowding is most acute and the NO_i is forced into close proximity to the lattice with an average separation of 2 Å. In each case there is a direct correlation between the size of the rings making up a given cage and the degree of steric crowding and ultimately the incorporation energy.

3.2 NO_i Migration

Using the interstitial configurations characterised in section 3.1 to form the starting points for a series of NEB calculations, these allow the effect of morphology on the NO_i migration barriers to be explored. From these results it is possible to divide these barriers into two main categories. The first relates to the migration of NO across the cage, not passing through a ring of any size, these transitions have barriers of 0.1 eV or lower and reflects the non-interacting nature of NO_i with the a-SiO_2 lattice. In the second category, the NO moves through rings connecting these cages. This is shown in figure 3, for a 6-membered ring. A representative sample of rings between 4 and 7 members, gave barrier heights of between 0.8 and 3.0 eV. The magnitude of the barrier is wholly dependent on the size of the ring the NO passes through, smaller rings leading to larger barriers.

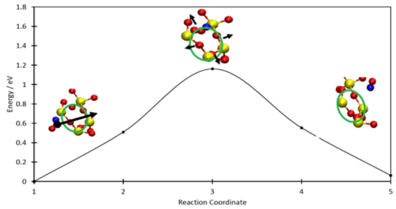

Figure 3: Migration barrier associated with NO passing through a 6-membered ring. The arrows represent the reaction coordinate and the lattice displacements at the transition state. The green circle indicates the ring that the NO is migrating through.

4 CONCLUSION

In this work the NO incorporation energies and migration barriers are correlated with the morphology of the a-SiO_2 lattice. Showing a clear dependence of the local steric environment to both the incorporation of NO and its migration. This offers an atomistic explanation of the ease of NO incorporation and migration in a-SiO_2 that is observed experimentally. This illustrates the importance of the model building and sampling methodology as it has the potential to dramatically influence the results obtained, giving a range of incorporation energies of 2.5 eV and range migration barriers of over 3 eV in the case of NO.

REFERENCES

1. M. S. Munde, D. Z. Gao, and A. L. Shluger, J. Phys. Condens. Matter **29**, (2017).
2. T. Bakos, S. N. Rashkeev, and S. T. Pantelides, Phys. Rev. Lett. **88**, 55508 (2002).
3. W. Orellana, Appl. Phys. Lett. **84**, 933 (2004).
4. S. Plimpton, J. Comput. Phys. **117**, 1 (1995).
5. A. C. T. van Duin, A. Strachan, S. Stewman, Q. Zhang, X. Xu, and W. A. Goddard III, J. Phys. Chem. A **107**, 3803 (2003).
6. M. Guidon, J. Hutter, and J. Vandevondele, J. Chem. Theory Comput. **6**, 2348 (2010).
7. J. Hutter, M. Iannuzzi, F. Schiffmann, and J. Vandevondele, Wiley Interdiscip. Rev. Comput. Mol. Sci. **4**, (2014).
8. S. Goedecker, M. Teter, and J. Hutter, Phys. Rev. B **54**, 1703 (1996).
9. M. Guidon, J. Hutter, and J. VandeVondele, J. Chem. Theory Comput. **5**, 3010 (2009).

Spatial distributions of NBOHCs in electron and γ-ray irradiated germanosilicate optical fibers

I. Reghioua*, S. Girard*, A. Alessi*, M. Fanetti **, D. Di Francesca***, M. Raine****,
L. Martin-Samos**, N. Richard****, A. Boukenter* and Y. Ouerdane*

*Univ-Lyon, Laboratoire H. Curien, UMR CNRS 5516, 18 rue du Pr. Benoît Lauras,
42000 Saint-Etienne, France.
**Materials Research Laboratory, University of Nova Gorica, Vipavska 11c 5270-Ajdovscina,
Slovenija.
***European Organization for Nuclear Research, CH-1211 Genève 23, Switzerland.
****CEA, DAM, DIF, F-91297 Arpajon, France.

ABSTRACT

We investigate the electron or γ-ray induced defect spatial distributions in the transverse cross-sections of a 4-steps Ge-doped multimode optical fiber. The measured Confocal-Micro luminescence (CML) cartographies of the Non-Bridging Oxygen Hole Centers (NBOHCs) differ between the fiber samples irradiated with electrons (~100 MGy) and those exposed to γ-rays (9 MGy).

PACS Keywords: optical fiber, point defects, electron radiation, photoluminescence.

1 INTRODUCTION

Silica-based optical fibers (OFs) are nowadays considered as important components among the various photonic devices. In addition to their basic telecom applications, and thanks to their unique properties, they can be used for intrinsic fiber-based sensing in environments associated with severe conditions (radiations, temperature...) [1]. Radiations cause a degradation of the transmission properties of the OFs, mainly through the generating of absorbing point defects [1]. It is mandatory, as a consequence, to deeply study these different generation mechanisms, as well as the bleaching and conversion processes for their radiation induced point defects. One of the most studied point defects in silica is the Non-Bridging Oxygen Hole Center (NBOHC). NBOHC consists in a paramagnetic defect with a dangling oxygen bond ($\equiv$ Si — O•) [2]. NBOHC is characterized by an absorption band at ~1.97 eV and others in the range from 4 to 8 eV [2, 3]. Furthermore, this defect is responsible for an emission band centered at ~1.91 eV (~650 nm) [2, 3]. It has been demonstrated in [4] that these centers are already present, at low concentration, in the pristine (non-irradiated) samples and they are generated by the various types of irradiation (X-rays, γ-rays, neutrons…).

In this abstract, we present a Confocal Micro-Luminescence (CML) investigation of the spatial distributions of these defects in a germanosilicate optical fiber exposed either to electrons of various energies or to γ-rays.

2 EXPERIMENTAL DETAILS

The selected sample for this study is a 4-steps Ge-doped multimode optical fiber, fabricated by the MCVD (Modified Chemical Vapour Deposition) by iXBlue photonics division. Its chemical composition measured by EDX (Energy Dispersive X-ray), reveals the presence of 4 different Ge doped zones in its core (pure silica cladding). These zones are Ge-doped at 11, 8, 4.4 and 2.2 wt% (from the center of the core till the core/cladding interface). Such doping profile was achieved to investigate the influence of this dopant concentration on the generation and bleaching mechanisms of point defects. Samples of this fiber have been used for CL imaging measurements at three different energies 5, 10 and 20 keV, all the other parameters that determine the irradiation dose were kept fixed. The used apparatus for CL and EDX measurements is a field-emission Scanning Electron Microscope (SEM) (JSM 7100f JEOL) that includes both (X-Max 80, OXFORD) and (GTAN MONOCL4) detectors for EDX and CL measures respectively.

After being exposed to CL electron beam, the samples were characterized *post mortem* by CML using an Aramis (Jobin-Yvon) at the excitation line of 633 nm (HeNe laser) with a ×50 objective that allows ~2 µm of lateral resolution.

3 RESULTS

We report in Table 1 the calculated doses after the electron exposure at the three energies as well as their interaction volumes. We can see that higher is the energy, deeper is the electron range and lower is the accumulated dose.

	Electron range (µm)	Dose (MGy)
5 keV	0.5	320
10 keV	1.3	150
20 keV	4	90

Table 1: Electron irradiation characteristics as a function of the energy.

Figure 1 shows the 2D CML cartographies of the NBOHC emission band at 650 nm in the samples irradiated with electrons of different energies. We can easily distinguish the traces of the electron irradiation (the squares with higher NBOHC signal), and it seems that higher is the Ge concentration (the center of the core) lower is the generated NBOHC signal.

We remind that the electron irradiation is characterized by its limited interaction volume that increases at higher energies [5], so the reported CML cartographies are affected by these interaction volumes. As an example, for E = 5 keV and although the highest associated accumulated dose, the NBOHC signal appears lower. This is probably due to the fact that the measured NBOHC signal results from the contributions from both the 0.5 µm of the irradiated material and the pristine zone located just below.

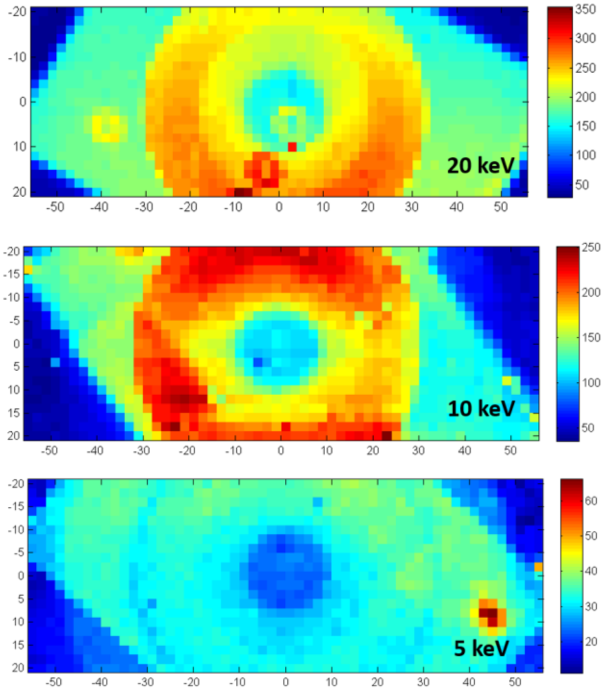

Figure 1: CML cartographies of the NBOHC at 650 nm of the electron irradiated Ge-doped samples.

The above reported cartographies are compared with the one obtained in the same experimental condition for another sample of the same OF γ-ray irradiated up to 9 MGy. The observed spatial distribution of NBOHCs in this fiber is shown in figure 2.

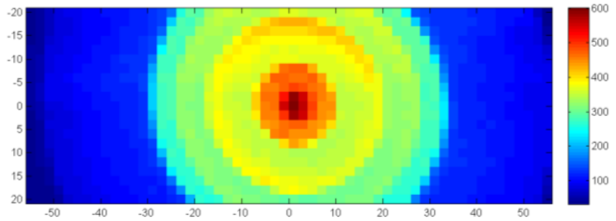

Figure 2: CML cartography of the NBOHC in the γ-ray (9 MGy) irradiated Ge-doped sample.

In this case, intensity of the NBOHC signal has an opposite trend as a function of the Ge concentration: larger is the Ge content higher is the NBOHC intensity.

Such differences between the signal distributions of the NBOHCs as a function of the Ge content could be due to the different doses, larger in the cases of electron irradiations. We remind that in the presence of Ge, new Ge-related defects are generated, such as Ge-NBOHC in which the central position of its emission band (~660 nm) is very close to the Si-NBOHC (~650 nm) [6]. This complicates further our analysis since both features are existing in the core of the OF and it is very hard to separate both signals, hence the difficulty to affirm if one defect or another is more responsible of such difference.

4 CONCLUSION

This abstract deals with the electron irradiation effects on the NBOHC up to hundreds of MGys of deposited dose. Our results show that the NBOHC signal follows different trends, as a function of the Ge concentration, if irradiated with electrons compared with γ-rays. This difference could be due the nature of the irradiation, considering that the electrons are more aggressive and higher doses are easily reached using them. Further *in-situ* CL results concerning the evolution of the NBOHC as a function of the electron irradiation will be presented in the final paper.

REFERENCES

[1] S. Girard et al, IEEE. Trans. Nucl. Sci., 60, 2015 - 2036, 2013.

[2] G. Pacchioni, L. Skuja, and D. L. Griscom, Eds., Defects in SiO2 and related dialectrics: science and Technology. Dordrecht: Springer Netherland, 2000.

[3] M. Cannas and F. M. Gelardi, Phys. Rev. B, 84, 153201, 2004.

[4] S. Girard et al, App. Phys. Lett, 84, 4215 - 4217, 2004.

[5] I. Reghioua et al, IEEE Trans. Nucl. Sci., 64, 2318 - 2324, 2017.

[6] L. Skuja and A. Naber, Nucl. Instrum. Methods Phys. Res. B, 116, 549 – 553, 1996.

P10

Heavily Er^{3+}-doped distributed feedback silica-based fiber laser

A.M. Smirnov[*], A.P. Bazakutsa[*], Y.K. Chamorovskiy[*], K.M. Golant[*], O.V. Butov[*]

[*]Kotel'nikov Institute of Radioengineering and Electronics of RAS,
Mokhovaya 11-7, Moscow 125009, Russia

ABSTRACT

Heavily Er-doped Yb-free silica optical fiber for laser application was fabricated by the SPCVD method. An ultrashort cavity distributed feedback (DFB) fiber laser based on this fiber was developed and studied. A single-mode passively Q-switched with up to 750 kHz 70 ns's pulses repetition rate and CW at liquid nitrogen temperature oscillation regimes of the DFB laser core-pumped at a wavelength of 976 nm was obtained.

PACS Keywords: distributed-feedback fiber lasers, Q-switched

1 INTRODUCTION

The development of new fiber optic laser systems is of interest in the optical field. Erbium-doped fiber lasers demonstrate lots of potential applications, such as sources for telecommunication and sensing systems.

In recent years, much attention has been paid to develop of various methods to create Q-switched erbium-doped fiber lasers. Passive Q-switching on erbium-doped lasers was realized by using a saturable absorber co-doping with rare earth elements such as samarium, thulium, or by chalcogenides of tungsten and molybdenum. Active Q-switching was realized for example by using an acousto-optic modulator (AOM), a piezoelectric acousto-optic modulator and an electro-optic modulator.

Progress in fabrication of distributed feedback (DFB) lasers [1-3] and the ability to change a wavelength generation by stretching or compression of the distributed resonant cavity allows to use them in a sensitive element of the compact high-speed fiber sensors. Q-switched DFB fiber laser is a good candidate as a light source for distributed sensor systems.

2 EXPERIMENTAL

The active fiber was drawn from a preform with SiO_2:Al_2O_3/Er_2O_3 core glass and undoped silica cladding. The core glass was synthesized by plasma-chemical reactions in the gas phase at a low pressure via SPCVD [4], vapors of anhydrous metal halides being utilized as raw materials. The Plasma-chemical synthesis permits us to fabricate a heavily Er-doped silica glass fiber (absorption at 1530 nm ≈180 dB/m, 0.3 mol.% Er_2O_3) with a low level of erbium clustering.

The cavity of the fiber DFB being formed by active fiber with a special π-shifted fiber Bragg grating which was inscribed by means of phase mask technique and a radiation of an ArF-excimer laser.

The emission spectra and radiation dynamics of the investigated DFB fiber lasers were measured by a scheme presented in Fig. 2. We used an additional FBG (976 nm) as a pump mirror to increase a pump absorption efficiency.

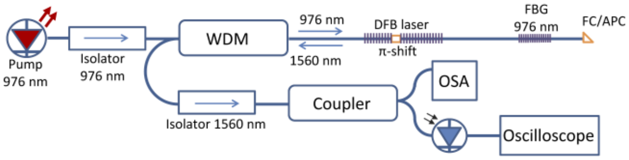

Figure 1: Experimental setup of the DFB fiber laser. OSA – optical spectrum analyzer, WDM - Wavelength division multiplexing splitter

3 RESULTS AND DISCUSSION

Recently we demonstrate a generation of ultrashort (24 mm in length) cavity DFB fiber laser [3]. In this work 50-mm cavity lasers have been used for our experiment. We experimentally observed a stable single-mode passively Q-switched laser generation with up to 750 kHz pulses repetition rate with 70 ns pulse duration (Fig.2).

Q-switched regime was realized due to presence of Er ion pairs that apparently are responsible for saturation of the absorption [5,6]. The measured increasing pulses repetition rate (Fig.2b) and simultaneous decreasing pulse duration (Fig.2c) at pump power magnification can be explained by the dynamics of the saturation process and relaxation of the excited state. Excited state lifetimes in its turn depend on the pump power, including because of the nonlinear optical up conversion process. High repetition rate was reached, most likely, due to the high Er-concentration in the fiber core.

Stable CW oscillation regime of heavily-Er-doped DFB laser was realized at liquid nitrogen temperature (Fig. 3). It can be explained by the decreasing of up-conversion effect in erbium ion pairs and increasing lifetime of excited states.

Unstable CW, sinusoidal and self-pulsing regimes at heavily erbium-doped DFB fiber lasers were observed at room temperature (Fig. 4).

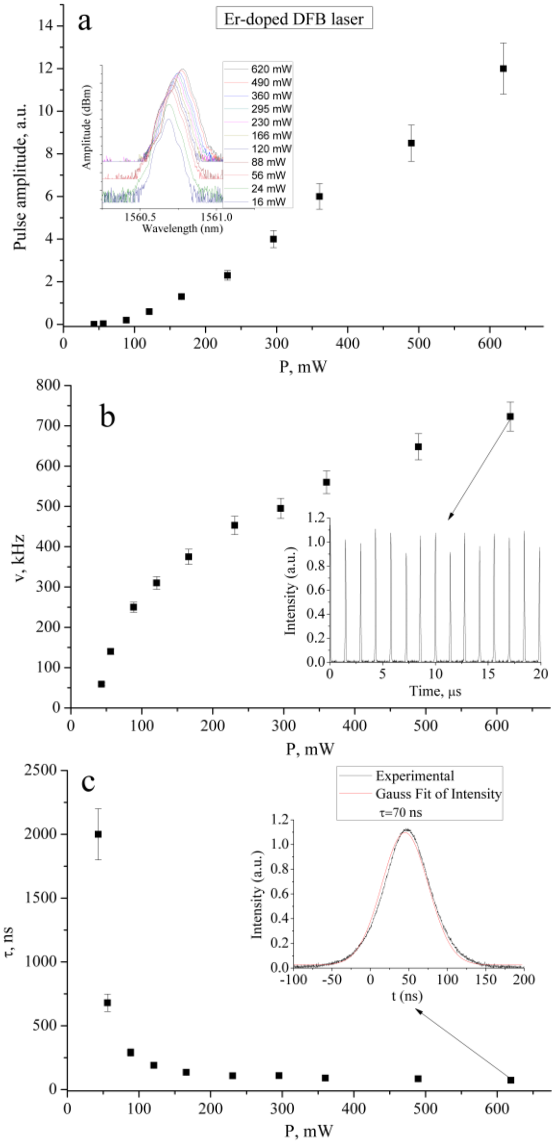

Figure 2: Characteristics of passively Q-switched DFB laser generation regimes. Amplitude (a), frequency (b) and pulses duration (c) dependencies on the pump laser power.

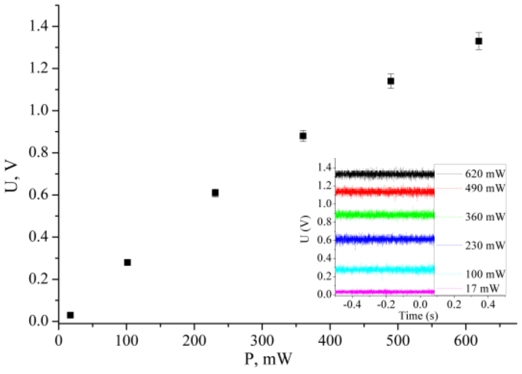

Figure 3: Erbium-doped DFB laser radiation power at CW generation regime at 77K dependence on the pump laser power.

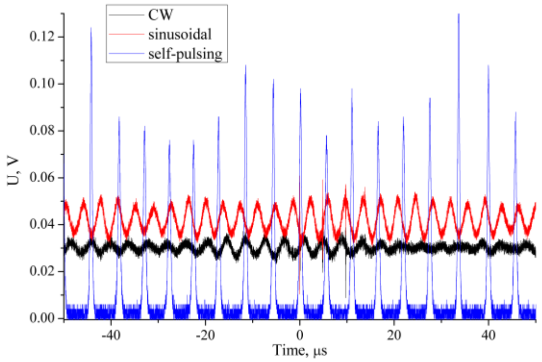

Figure 4: CW, sinusoidal and self-pulsing heavily erbium-doped DFB fiber lasers regimes.

Experimental results can be explained by the dynamics of the excited states that is strongly dependent on the ion-pair concentration (erbium clustering) [5]. At high erbium concentrations (>0.1%wt) fluorescence lifetime is reduced and competing effects like cooperative up-conversion can occur to reduce the amplifier's efficiency [7,8].

4 CONCLUSION

We have fabricated Yb-free heavily-Er-doped DFB fiber laser. There was experimentally observed single-mode a CW laser oscillation at 77K and passively Q-switched oscillation with up to 750 kHz pulses repetition rate and 70 ns pulse duration by core-pumped at a wavelength of 976 nm of the DFB laser.

This work was supported by Russian Foundation for Basic Research (RFBR) (project 17-07-01388).

REFERENCES

[1] O.V. Butov, A.A. Rybaltovsky, A.P. Bazakutsa, K.M. Golant, M.Yu. Vyatkin, S.M. Popov, and Y.K. Chamorovskiy, JOSA B **34**(3), A43-A47, 2017.

[2] Varming. J. Hubner and M. Kristensen, ELECTRONICS LETTERS **31**(17) 1445, 1995.

[3] O. V. Butov, A. A. Rybaltovsky, M. Yu. Vyatkin, A. P. Bazakutsa, S. M. Popov, Yu. K. Chamorovskiy, and K. M. Golant, PIERS - Spring, 1594-1597, St. Petersburg, 2017

[4] Golant, K. M., "Surface plasma chemical vapor deposition: 20 years of application in glass synthesis for lightguides (a review)," XXI International Congress on Glass (International Commission on Glass), 2007.

[5] F. Sanchez, P.L. Boudec, P.-L. Frangois, G. Stephan, Phys. Rev. A., 48(3), 2220-2229, 1993.

[6] W. H. Loh, OPTICS LETTERS 21 (10) 734, 1996

[7] A. Bellemare, Progress in Quantum Electronics 27, 211–266, 2003.

[8] P.W. France, CRC Press, Boca Raton, 259, 1991.

Electronic structure and optical absorption in Gd-implanted silica glasses

A.F. Zatsepin[1], Yu.A.Kuznetsova[1], D.A. Zatsepin[1,2], N.V. Gavrilov[3], M.S.I. Koubisy[1], S.P. Vyatkina[1]

[1] Ural Federal University, Mira Street 19, 620002, Ekaterinburg, Russia
[2] Institute of Metal Physics, Ural Branch of the Russian Academy of Sciences,
Kovalevsky Street 18, 620137, Ekaterinburg, Russia
[3] Institute of Electrophysics, Ural Branch of the Russian Academy of Sciences, Amundsen Street 106,
620016, Ekaterinburg, Russia

ABSTRACT

We studied the electronic structure and optical properties of silica glass implanted with Gd-ions. The effect of limiting of oxygen transport due to the gadolinium passivation was found. The optical absorption bands corresponding to the transitions in Gd^{3+} ions and ODC intrinsic defects of matrix were detected. Spectral dependences of exponential tails of absorption edge have the fan-like behavior due to «quasi-dynamic» disordering caused by ion implantation. According to the principle of static and dynamic disorder equivalence, ion fluence corresponds to a certain temperature of structural silica glass disordering.

PACS Keywords: silica, ion implantation, gadolinium, optical absorption, quasi-dynamic disorder

1 INTRODUCTION

Ion implantation into SiO_2 host matrix has been receiving considerable attention of materials scientists because it is a powerful method to re-build the electronic structure and physical properties of this practically significant wide-gap transparent insulator [1]. Rare earth ions are promising dopant elements for optoelectronics and spintronic applications, due to their intra *f*-shell transitions and high orbital angular momentum. Gadolinium ions are of particular interest because of its strong paramagnetic behavior resulting from the presence of seven unpaired electrons on the *4f* valence shell that provides opportunities for a wide application in biomedical fields (MRI, bioimaging, drug delivery). In addition, Gd^{3+} ions have a variety of energy levels in the region of optical transparency of SiO_2 host matrix, so one can expect the emission in VUV spectral region caused by direct transitions from high-energy excited states and the visible orange/red luminescence due to the quantum cutting [2].

Optical properties of solid-state systems is largely influenced by the degree of structural disorder. In accordance with additivity principle, the structural disorder in solids can be represented as a sum of two components: static disordering caused by lattice imperfections and dynamic disordering resulting from thermal lattice vibrations [3]. The contributions of both disordering types lead to appearance of localized states tails in electronic band structure. The ion implantation affects both type of disordering which leads to a modification of electronic structure and, as a consequence, to a change in the optical properties. One of the powerful approaches to quantitative estimation the structural disordering in solids is the analysis of exponential tail of absorption edge on the basis of the Urbach rule [3-5].

In the present work, the materials under investigation were glassy SiO_2 host lattices implanted with Gd^{3+} ions at different fluences. The two main questions were considered: (*i*) the spectral properties of gadolinium ions embedded in an insulator and (*ii*) an influence of ion implantation on the electronic structure and optical characteristics of a SiO_2 matrix.

2 MATERIALS AND EXPERIMENTAL METHODS

The samples of quartz SiO_2 glass of KUVI-type were square plane-parallel plates with an area of 1 cm^2 and a thickness of 1.5 mm. KUVI glass is a high-purity optical glass of type IV with a minimum concentration of metal impurities and hydroxyl groups. This provides high radiation-optical stability and high transparency in the UV, visible and IR spectral ranges. The glassy samples were implanted by Gd-ions with fluences of $5{\cdot}10^{16}$ and 10^{17} cm^{-2} using a metal-vapor vacuum arc ion source (pressure in chamber was $2{\cdot}10^{-3}$ Pa). The ion energy was set to 30 keV, the pulse duration was 0.4 ms with a current density of 17 $\mu A/cm^2$. Thermal annealing of the implanted samples was made at 1000°C within 1 h.

The study of the electronic structure was performed by X-ray photoelectron spectroscopy (XPS) measurements with using a Thermo Scientific™ *K*-Alpha+™ XPS spectrometer. Photoluminescence (PL) and PL excitation spectra were obtained on a Perkin Elmer LS 55 spectrophotometer. Optical absorption spectra within the interval of 2.5-11.3 eV photon energies were measured on a McPherson VuVAS PL 1000 spectrometer.

3 RESULTS AND DISCUSSION

The results of XPS Valence band mapping for not-implanted host KUVI-SiO_2 matrix and for sample implanted with Gd-ions are presented in Fig. 1. The most distinctive feature of obtained XPS VB spectral data is the absence of dive-down effect on O 2s and Si 3s electronic states intensity for implanted sample, which was observed in the case of SiO_2 implantation by other ions. Indirectly, it indicates the limiting and oxygen transport caused by implantation (Gd passivation).

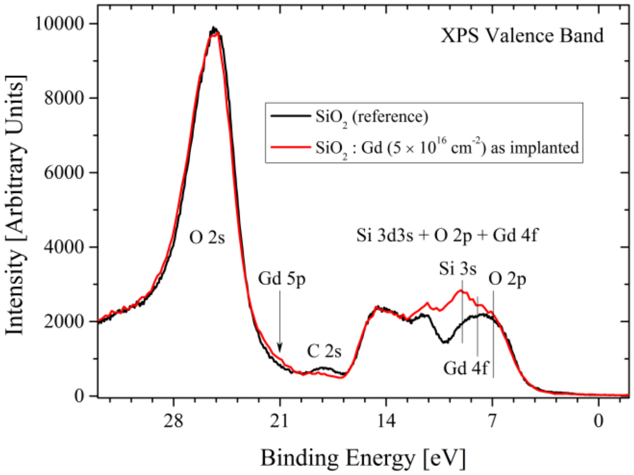

Figure 1: XPS Valence band mapping for KUVI-SiO_2:Gd implanted under 5×10^{16} fluence and not-implanted KUVI-SiO_2 host matrix.

For implanted sample, a weak luminescent band at 4 eV was observed corresponding to the radiative ${}^6P_J \rightarrow {}^8S_{7/2}$ transition in Gd^{3+} ion. This emission is excited by the intracenter mechanism and results from the relaxation of high-energy ${}^6D_J$ state of gadolinium ion. After annealing there are no any PL bands were found. It is a consequence of a change in structure of host lattice induced by thermal treatment. Annealing can cause the formation of non-luminescence gadolinium compounds or centers acting as quenchers of Gd^{3+} emission.

In optical absorption spectra, there are four regions: (i) interband absorption of host lattice at energies up to 8.3 eV; (ii) exponential tail of absorption edge at energies of 7.9-8.3 eV; (iii) band at 7.5 eV corresponding to the absorption in oxygen-deficient center ODC (I); (iv) band at 5.5 eV, close to the energy of transition in Gd^{3+} ion from the ${}^8S_{7/2}$ ground state to the ${}^6D_J$ excited state. The intensity of bands at 5.5 eV and 7.5 eV is higher for the sample with a large fluence of gadolinium ions. A decrease in intensity of absorption band assigned to the ODC (I) centers after thermal treatment indicate the decrease in a concentration of intrinsic defects in matrix due to the well-known effect of thermal annealing of defects.

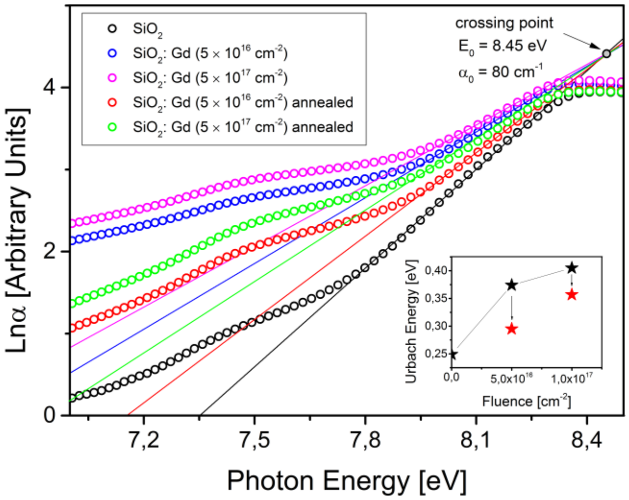

Figure 2: Spectral dependences of logarithmic absorption coefficient for not-implanted SiO_2 matrix, implanted SiO_2:Gd samples with fluences 5×10^{16} and 10^{17} cm^{-2} before and after thermal annealing. Solid lines show the approximation of linear spectral regions. Inset: Urbach energy as a function of the Gd ions fluence (red stars correspond to data for annealed samples).

The most attention was paid to the region (ii), where spectral dependence of absorption coefficient obeys to the Urbach rule [3]. The linear dependences of logarithmic absorption coefficients on photon energies in the region 7.9-8.3 eV for all samples under investigation are fan-shaped and converge to the crossing point that corresponds to the crystal-like Urbach rule (Fig. 2). A similar behavior of absorption edge was observed with a temperature change for non-implanted SiO_2 [6], which indicated a predominance of dynamic type of disorder under the static one. In our case, all measurements were at room temperature, so the change in slope of spectral dependences is due to the change in static disordering induced by ion implantation, so-called «quasi-dynamic disorder». The Urbach energy that reflects the overall structural disorder increases with increasing of fluence (Fig. 2, Inset). Thermal annealing causes ordering of the structure as indicated by decreasing in Urbach energy. Modification of optical spectra under ion implantation allow to conclude that the ion fluence correspond to a certain temperature of structural disordering.

ACKNOWLEDGEMENTS

This work was supported by the Ministry of Education and Science of the Russian Federation (Government Task No. 3.1485.2017/4.6).

REFERENCES

[1] A. F. Zatsepin et al., J. Alloy. Compd., 728, 2017.
[2] R. T. Wegh., Phys. Rev. B, 56, 21, 1997.
[3] F. Urbach, Phys. Rev., 92, 1324, 1953.
[4] A. F. Zatsepin et al., J. Lumin., 183, 135, 2017.
[5] A. F. Zatsepin et al., J. Nanopart. Res., 19, 111, 2017
[6] I. Godmanis et al., Phys. Status Solidi, 116, 1983